

**OBSERVATION OF THE GZK SUPPRESSION WITH THE  
TELESCOPE ARRAY FLUORESCENCE TELESCOPES  
AND DEPLOYMENT OF THE TELESCOPE  
ARRAY EXPANSION**

by

Greg David Furlich

A dissertation submitted to the faculty of  
The University of Utah  
in partial fulfillment of the requirements for the degree of

Doctor of Philosophy

in

Physics

Department of Physics and Astronomy

The University of Utah

August 2020

Copyright © Greg David Furlich 2020

All Rights Reserved

**THE UNIVERSITY OF UTAH GRADUATE SCHOOL**

**STATEMENT OF DISSERTATION APPROVAL**

This dissertation of

Greg David Furlich

has been approved by the following supervisory committee members:

Douglas R. Bergman

, Chair

April 28, 2020

Date Approved

Gordon B. Thomson

, Member

April 28, 2020

Date Approved

Robert Wayne Springer

, Member

April 28, 2020

Date Approved

Yan Sarah Li

, Member

April 28, 2020

Date Approved

Miriah Dawn Meyer

, Member

April 28, 2020

Date Approved

and by Christoph Boehme, Chair of

the Department of

Physics and Astronomy

and by David B. Kieda of the Graduate School.

## ABSTRACT

The Telescope Array (TA) Cosmic Ray Observatory, located in Millard County, Utah, is the largest cosmic ray detector in the northern hemisphere. TA was built to study the highest energy particles in the universe, Ultra-High Energy Cosmic Rays (UHECRs) with energies above  $10^{18}$  eV. TA is a hybrid detector that consists of three fluorescence detector (FD) stations overlooking a ground array of 507 scintillating surface detectors (SDs).

TA is currently undergoing an expansion known as TAx4, to quadruple the detection aperture with the addition of 500 SDs with a northern and a southern extension to the main array. The SD array expansion is accompanied by 4 new fluorescence telescopes at the Middle Drum (MD) FD station and 8 new fluorescence telescopes at the Black Rock (BR) FD station. The new fluorescence telescopes are comprised of refurbished and upgraded detectors from the HiRes-II experiment. The TAx4 FD expansion looks out over the TAx4 SDs to allow for hybrid energy calibration of the new surface array. TAx4 MD FD began operation in 2018. In this dissertation, we calculate a preliminary energy spectrum using the first year of data from the new TAx4 MD FD. This preliminary spectrum is in agreement with previous TA measurements.

In the main effort for this dissertation, we calculate a combined cosmic ray energy spectrum using reconstructed monocular events with energy above  $10^{17.5}$  eV from the Black Rock (BR) and Long Ridge (LR) FD sites using 10 years of data, from 2008 to 2018. We implement a novel weather classification method using machine learning to increase the quality of the BR and LR FD data. We observe excellent agreement comparing the combined fluorescence spectrum to the TA SD measurement, as well as the HiRes experiment fluorescence measurement. We fit the monocular combined spectrum with a series of broken power law fits and found the spectrum fit well with three breaks in the spectrum. We claim the fourth observation of the GZK suppression with the combined fluorescence energy spectrum with a significance above  $4\sigma$ .

To my companion in this great adventure and love, Kiley.

“As for me, I am tormented with an everlasting itch for things remote. I love to sail forbidden seas...”

-Herman Melville, *Moby Dick*

# CONTENTS

<b>ABSTRACT</b> .....	<b>iii</b>
<b>NOTATION</b> .....	<b>vii</b>
<b>PREFACE</b> .....	<b>viii</b>
<b>CHAPTERS</b>	
<b>1. AN INTRODUCTION INTO ULTRA-HIGH ENERGY COSMIC RAY PHYSICS</b> .....	<b>1</b>
1.1 A Brief History of Cosmic Radiation .....	1
1.2 Theories of Cosmic Ray Acceleration .....	3
1.3 Cosmic Ray Propagation and the Greisen-Zatsepin-Kuzmin (GZK) Suppression ..	5
1.4 Cosmic-Ray-Induced Extensive Air Showers .....	6
1.5 Models of Cosmic Ray Extensive Air Showers .....	7
1.6 Cascade Equation .....	12
1.7 Shower Development.....	13
1.8 Atmospheric Fluorescence and Light Propagation .....	13
<b>2. COSMIC RAY DETECTION AND THE TELESCOPE ARRAY PROJECT</b> .....	<b>23</b>
2.1 Direct versus Indirect Detection of Cosmic Rays .....	23
2.2 The Telescope Array Cosmic Ray Observatory .....	24
2.3 Telescope Array Black Rock and Long Ridge FD Stations .....	26
2.4 TAx4, the Telescope Array Project Expansion .....	30
2.5 The TAx4 MD and BR Fluorescence Detectors .....	33
2.6 TAx4 First Light .....	37
2.7 MD TAx4 Operation Epochs .....	37
<b>3. MONOCULAR RECONSTRUCTION OF COSMIC RAY FD EVENTS</b> .....	<b>52</b>
3.1 DST Files .....	52
3.2 Data Collection .....	53
3.3 Intermirror Timing.....	53
3.4 Geometry Reconstruction .....	54
3.5 Calorimetric Energy Reconstruction .....	56
3.6 Missing Energy Correction .....	57
3.7 Data Selection and Quality Cuts.....	57
3.8 Python Processing Pipelines and Pandas DataFrames .....	58
3.9 Distance to Shower Max, $R_{X_{\max}}$ .....	58
3.10 TAx4 MD FD Reconstructed Good Event .....	59
3.11 LR Highest Energy Reconstructed Event .....	59
<b>4. WEATHER SELECTION CUTS USING MACHINE LEARNING</b> .....	<b>68</b>
4.1 Impact of Weather on Observation and FDEvent Reconstruction .....	68
4.2 Current Weather Recording at the MD Station .....	69
4.3 FD Pedestal Snapshots of the Night Sky.....	69

4.4	Weather Classification Using Neural Networks . . . . .	70
4.5	BR Neural Network Weather Classification Results . . . . .	73
4.6	LR RCNN Weather Classification Results . . . . .	73
4.7	Machine Learning Weather Cuts . . . . .	74
4.8	Other Interesting Optical Events Seen in FD Pedestals . . . . .	74
<b>5.</b>	<b>COSMIC RAY EVENT MONTE CARLO SIMULATIONS . . . . .</b>	<b>91</b>
5.1	Telescope Array Monte Carlo Programs . . . . .	92
5.2	TAX4 FD Observed Data versus Monte Carlo Comparison . . . . .	94
5.3	TAX4 FD Monte Carlo Reconstruction Resolution . . . . .	94
5.4	BR and LR FD Monte Carlo Weather Cuts . . . . .	95
5.5	BR and LR FD Observed Data versus Monte Carlo Comparison . . . . .	95
5.6	Bad Weather Observed Data versus Monte Carlo Comparison . . . . .	97
5.7	BR and LR FD Monte Carlo Reconstruction Resolution . . . . .	98
<b>6.</b>	<b>TAX4 MD FD PRELIMINARY COSMIC RAY ENERGY SPECTRUM . . . . .</b>	<b>120</b>
6.1	Event Distribution . . . . .	120
6.2	Thrown Monte Carlo Event Distribution . . . . .	121
6.3	Weather Cuts . . . . .	121
6.4	Ontime . . . . .	122
6.5	Detector Acceptance and Aperture . . . . .	122
6.6	Detector Exposure . . . . .	122
6.7	Preliminary Cosmic Ray Energy Spectrum . . . . .	123
<b>7.</b>	<b>TA 10-YEAR MONOCULAR FD COSMIC RAY ENERGY SPECTRUM . . . . .</b>	<b>132</b>
7.1	Coincidence FD Events between the BR and LR Stations . . . . .	132
7.2	Event Distribution . . . . .	133
7.3	Monte Carlo Event Distribution . . . . .	133
7.4	Ontime . . . . .	133
7.5	Detector Acceptance . . . . .	134
7.6	Detector Aperture . . . . .	134
7.7	Detector Exposure . . . . .	135
7.8	Combined Cosmic Ray Spectrum . . . . .	135
7.9	Broken Power Fits to the Combined Spectrum . . . . .	136
7.10	Observation of the GZK Suppression . . . . .	137
7.11	Integral Flux and $E_{1/2}$ . . . . .	138
<b>8.</b>	<b>CONCLUSIONS . . . . .</b>	<b>150</b>
<b>APPENDICES</b>		
<b>A.</b>	<b>US STANDARD ATMOSPHERE 1976 . . . . .</b>	<b>152</b>
<b>B.</b>	<b>TA TOPOGRAPHIC AND RELIEF MAPS . . . . .</b>	<b>154</b>
<b>REFERENCES . . . . .</b>		<b>156</b>

## NOTATION

### Telescope Array and Physics Notation

---

TA	Telescope Array Project, an international collaboration for studying UHECRs with the Telescope Array Cosmic Ray Observatory
TAX4	The quadruple expansion of the Telescope Array cosmic ray observatory
TALE	Telescope Array Low Energy extension.
UV	Ultraviolet spectrum of light.
FD	Fluorescence Detector
SD	Surface Detector
UHECR	Ultra-High Energy Cosmic Rays ( $E > 10^{18}$ eV)
MD	Middle Drum site
BR	Black Rock Mesa site
LR	Long Ridge site
CLF	Central Laser Facility site
FOV	Field of View
eV	Electron volts, a standard unit of energy in high energy physics
EAS	Extensive airshower, sometimes shortened to shower
PMT	Photomultiplier Tube
GZK	Greisen-Zatsepin-Kuzmin (suppression)
SDP	Shower Detector Plane
MC	Monte Carlo
FADC	Fast Analog Digital Converts
$R_p$	Impact Parameter, closest approach of the shower core to the FD site
$X_{\max}$	Parameter where the shower is maximally developed
$R_{X_{\max}}$	The distance from the FD site to the shower maximum
ICRC	International Cosmic Ray Conference

---

### Machine Learning Notation

---

NN	Neural Network
DNN	Dense Neural Network
RNN	Recurrent Neural Network
CNN	Convolution Neural Network
RCNN	Recurrent Convolution Neural Network

---

## PREFACE

This dissertation presents two measurements of the ultra-high energy cosmic ray flux with the Telescope Array (TA) Project. One measurement uses the preliminary data of the new fluorescence detectors installed for the expansion of TA (known as TAx4), and the other measurement uses data collected over 10 years with the Black Rock (BR) and Long Ridge (LR) fluorescence detectors. The experimental apparatus of TA, methods of this analysis, measurement of the cosmic ray flux, and the significance of the results are described at length in this work.

The field of cosmic rays employs several acronyms and significant amount of jargon. For the convenience of the reader a notation guide is tabulated at the beginning of this thesis. Important terms in cosmic rays and this analysis are introduced in italics. Chapter 1 introduces the field of cosmic radiation, includes a brief history of these observations, and highlights the important physical considerations in their analysis. Chapter 2 provides a description of the detectors used to observe the particle cascade created by cosmic rays in the atmosphere at TA. Chapter 3 explains the reconstruction of cosmic ray events using the fluorescence detectors in monocular mode. Chapter 4 describes the novel machine-learning weather classification used to select good weather data in further analysis. Chapter 5 describes the Monte-Carlo simulation used to generate cosmic ray events and to analyze the detection aperture and event reconstruction resolution. Chapter 6 describes the preliminary TAx4 MD FD cosmic ray spectrum measurement. Chapter 7 describes the 10-year monocular combined spectrum measurement. Chapter 8 provides a conclusion.

I would like to express my gratitude to the following people for all they have done to support me in this endeavor. I would like to thank my advisor, Douglas Bergman, for his support and guidance in this herculean labor. I am very appreciative of his insight and patience.

I would like to thank the many members of the Telescope Array Collaboration<sup>[1]</sup>. A special thanks to the Co-Spokespersons, Charlie Jui and Shochi Ogio, for their support in my research; John Matthews and Frank Misak for their organization; Stan Thomas and Jeremy Smith for their assistance in understanding the detectors and help with the TAx4 refurbishment and deployment; Robert Cady for teaching me to operate the FDs and how to maintain the SDs; Tom Stroman for all his assistance, insight, and patience with the many BR and LR analysis scripts; Dmitri Ivanov for his assistance with the spectrum fitting and TAx4 FD analysis; Tareq Abu Zayyad for his assistance with the TAx4 FD analysis and monte carlo scripts, Jon Paul Lundquist for his machine learning

profile recognition algorithm and for the lecture on the many genres of metal music; JiHee Kim for answering many of my questions about the analyses of cosmic rays and teaching me to maintain the SDs; Gary McDonough and Patrick Wright for their help with the TAx4 deployment; Matt Potts, Gordon Thomson, Pierre Sokolsky, Bill Hanlon, Yoshiki Tsunesada, Toshihiro Fujii, Eiji Kido, and many more. I would like to thank the hardworking undergraduates that assisted me in testing and refurbishing the TAx4 FDs: Zane Gerber, Isaac Buckland, and Mark Hayward. I would like to acknowledge the University of Utah Center for High Performance Computing (CHPC) for the use of their CPU and GPU nodes in my machine learning weather classification project.

I would like to thank my many friends at the University of Utah, especially Flo Doval, Nels Evenson, Rosa (the dog) Doval-Evenson, Paul Bergeron, Jessica Galbraith-Frew, JiHee Kim, and Jackson Remington. Thank you for being supportive, great friends, and for all the board games we played and gatherings to help mediate the stress of graduate school. I would like to thank my family: Stephan, Paula, Jon, Emily, Chris, Lily, Eric, Bonnie, Ginny, Freddy, Skip, Cheryl, Oliver, Robert, Valerie, Sonny, and in memory of Frank and Vicky. Most importantly, I would like to thank my wife, Kiley, for her support, encouragement, and patience.

Thank you to the many that supported this work, especially to those that continued to assist until the end, through the March 18<sup>th</sup>, 2020 Salt Lake City earthquake, and the social distancing of the 2020 global COVID-19 pandemic.

# CHAPTER 1

## AN INTRODUCTION INTO ULTRA-HIGH ENERGY COSMIC RAY PHYSICS

Cosmic radiation, commonly known as *cosmic rays*, is atomic nuclei moving across the universe with tremendous energies. Cosmic rays have been studied for more than a century. However, there remain many open questions about their nature, especially at the highest energies, where they are called *Ultra-High Energy Cosmic Rays* (UHECRs). At these energies, they exceed the energies of particles produced in modern particle accelerators. Observing UHECRs presents significant technical challenges, requiring both a large detection area and observations over an extended period of time.

The study of cosmic rays has had an impact across many other fields in physics. The methods and analyses developed in cosmic ray research have been transferred to the later-developed fields of gamma-ray observations and astrophysical neutrino observations. Even particle physics traces its beginning to the study of the exotic particles created in the atmosphere by cosmic rays.

This chapter will provide a brief overview of the physics of cosmic rays: from understanding their possible sources, through their propagation through the universe, to what happens once the cosmic ray interacts with the Earth's atmosphere.

### 1.1 A Brief History of Cosmic Radiation

The history of cosmic rays begins in the study of ionizing radiation. The theory of electromagnetism was developed in the middle of the 19th century. Many experiments were carried out to test and understand this revolutionary new theory. These experiments lead to the development of the charge-detecting electroscope and the cathode ray tube. These instruments were used in understanding and probing the newly-discovered ionizing radiation. While studying ionizing radiation, scientists observed a puzzling sudden discharge in electroscopes when they were moved away from known radiation sources. This discharge indicated that there was an unknown source of ionizing radiation.

Victor Hess<sup>[2]</sup> proposed a novel experiment to determine if the Earth was the ultimate source of ionizing radiation in the air. Hess took an electroscope up in a hot air balloon to test this hypothesis.

If the Earth was the source of radiation, he would observe the radiation levels going down as he rose up in the balloon. He did observe a slight dip in the radiation levels before an increase as his balloon traveled up to 5 km in altitude. This experiment was the first indication of radiation from above, with cosmic origins. The term “cosmic ray” was coined by Robert Millikan in the 1920s as more physicists were drawn to this exciting new field.

Another prominent discovery in cosmic rays was the *extensive air shower (EAS)* by Bruno Rossi<sup>[3]</sup> and again independently by Pierre Auger<sup>[4]</sup>. These extensive air showers were the result of a cascade of particles initiated high in the atmosphere. The source of this cascade was a cosmic ray *primary* entering the atmosphere and interacting with an air molecule. The initial interaction caused by a cosmic ray creates further interactions that can continue to develop and spread over an extensive area. By using Geiger counters, Auger was able to detect coincidences within microseconds with separations of up to 300 meters. Auger postulated, given the density of detection at different separations, that these extensive air showers consisted of more than  $10^6$  particles, and that the initial cosmic ray had an energy  $E > 10^{15}$  eV. This was the first experiment to study cosmic rays using an array of detectors spread over a large area. This design remains the basis for modern cosmic ray detector arrays.

The particles produced in these EASs were some of the first observations of new fundamental particles. Physicists were able to observe the tracks of unknown fundamental particles now known as types of mesons using cloud chambers housed at the top of mountains<sup>[3]</sup>. Eventually, human-made synchrotrons and particle accelerators became the more convenient way of producing and understanding these fundamental particles. The fields of modern particle physics and cosmic rays then split.

The field of cosmic-ray research transitioned from using cosmic-ray induced extensive air showers to understand fundamental particles to studying the nature, sources, and arrival rates of cosmic rays themselves. In order to study and detect cosmic rays at higher energies, given the lower fluxes, it is convenient to observe them through their interactions in the Earth's atmosphere indirectly. This detection requires vast arrays of detectors to observe a significant portion of the EAS. One such method involves detecting the cascade of particles indirectly via their excitation of the nitrogen molecules in the atmosphere. The excited nitrogen molecules return to lower energy by losing energy through scintillation, where the nitrogen molecules produce light in the UV<sup>[5]</sup>. This method, developed by a group lead by Kenneth Greisen, is known as *fluorescence detection*. Another method, derived from Auger's experiment, involves the placing of an array of particle detectors out over a large area. Cosmic ray events are observed through the coincidence signals in multiple detectors. The number of and location of triggered detectors and signal strength in each provides a

sampling of the footprint of the particle cascade. This method is called *surface detection*.

The University of Utah has a long history in cosmic-ray research. This history began with Jack Keuffel and his detector deep underground in the Silver King Mine, located in Park City, UT<sup>[6]</sup>. A group of scientists from the University of Utah were the first to successfully detect a cosmic-ray event using the fluorescence detection method at Volcano Ranch<sup>[7]</sup>. This working fluorescence detector prototype was developed into the Fly's Eye fluorescence detector<sup>1</sup> array at Dugway Proving Grounds in Utah<sup>[8]</sup>. Fly's Eye collected data for 10 years and added a second station named Fly's Eye II, allowing for coincident observation of an event between the two sites. This was the first *stereo* fluorescence observation. Stereo detection, compared to *monocular* (single observer) detection, improves the ability to reconstruct a cosmic ray event. Fly's Eye was replaced by its upgraded successor called HiRes (High Resolution Fly's Eye). HiRes was named for its bigger collection mirrors and better angular resolution, with a  $1^\circ \times 1^\circ$  pixel resolution on the night sky<sup>[9]</sup>. HiRes also operated two detector stations, HiRes-I and HiRes-II, collecting data from 1997 and 1999, respectively, until 2006. The latest cosmic ray detector operated by the University of Utah is known as the Telescope Array (TA) Cosmic Ray Observatory. The TA Project is an international collaboration with the University of Utah as the home institution. TA will be discussed further in Chapter 2.

## 1.2 Theories of Cosmic Ray Acceleration

As cosmic rays have only been studied in the Earth's atmosphere or from Earth's orbit, their sources in the cosmos are still highly debated. Cosmic rays have only been observed after they have propagated over possibly vast distances. Since cosmic rays are charged particles, they undergo deflection from magnetic fields in the solar system, galaxy, and intergalactic medium. This magnetic deflection tends to isotropize the direction of cosmic rays moving across the universe. Magnetic deflection makes pointing cosmic rays back to their sources impossible.

Magnetic fields can also trap cosmic rays in a given region. These regions may be the location of cosmic-ray acceleration. A criterion for the minimum energy of cosmic ray to escape the region, given the size and average magnetic field strength of the region, was formulated to understand the size and magnetic field characteristics of possible cosmic ray sources. This criterion, known as the Hillas criterion<sup>[10]</sup>, is

$$E_{\text{escape}} \propto qBR, \quad (1.1)$$

where  $E_{\text{escape}}$  is the escape energy,  $q$  is the cosmic ray charge,  $B$  is the average magnetic field, and  $R$  is the size of an astrophysical object. This criterion allows an evaluation of possible sources

---

<sup>1</sup>Named for the way the hexagonal PMT, when projected onto the sky, resembles a fly's eye.

where cosmic rays can be accelerated to the energies we observe. The Hillas criterion also allows one to rule out of sources if they are too small or do not have sufficiently strong magnetic fields.

Even though cosmic ray sources are not well understood, some acceleration methods are postulated, given a cosmic ray's charged nature and observations of the dynamic systems present in the universe. Two possible mechanisms for cosmic ray acceleration are *first* and *second-order Fermi acceleration*<sup>[11]</sup>. Both involve the interaction of charged particles with plasma clouds.

### 1.2.1 First-Order Fermi Acceleration

First-order Fermi acceleration is an acceleration method that considers a charged particle transiting across the shock front of a moving plasma cloud multiple times. Such shock fronts occur in Supernova remnants and jets of Active Galactic Nuclei. As the particle crosses the shock front, it interacts and scatters with the plasma flow downstream of the front. This interaction isotropizes the direction of the particle in the frame of the downstream plasma. For a particle that returns upstream of the shock front, given the relative motion of the plasma upstream, the particle gains energy when isotropized upstream. The particle is again scattered, possibly crossing downstream, and will again gain energy when isotropized downstream. This process will continue back and forth with the particle gaining energy upon each crossing. The energy after  $n$  interactions,  $E_n$ , is expressed as

$$E_n = E_o(1 + \langle \xi \rangle)^n \quad \langle \xi \rangle \approx \frac{4}{3}\beta \quad (1.2)$$

where  $\xi$  is the energy gained in each interaction which depends on the relative motion between the particle and the moving shock front,  $\beta$ .

Eventually, after crossing back and forth across the shock front many times, the cosmic ray gains enough energy to escape to the region. First-order Fermi acceleration is illustrated in Figure 1.1. First-order Fermi acceleration is the favored method of explaining cosmic ray energy distribution.

### 1.2.2 Second-Order Fermi Acceleration

Second-order Fermi acceleration involves a cosmic ray interacting with multiple, different moving plasma clouds as it propagates through the universe. Again as the particle interacts with the moving plasma cloud, depending on its direction, its energy changes. Given the random motion of the plasma clouds, on average, the net acceleration will be positive. However, second-order Fermi acceleration is too slow to explain cosmic rays at the highest energies<sup>[12]</sup>. Second-order Fermi acceleration is illustrated in Figure 1.2.

### 1.2.3 Cosmic Ray Energy Spectrum and Power Laws

Fermi acceleration leads to a power law form of the differential flux of cosmic ray with respect to energy, called a *cosmic ray energy spectrum*. The cosmic ray energy spectrum, considering the

number of particles observed at energy,  $N(E)$ , has the form

$$N(E)dE \propto E^{-\gamma}dE. \quad (1.3)$$

The observed cosmic ray energy spectrum follows a power law<sup>[13]</sup>. Equation 1.3 illustrates that the distribution of cosmic rays,  $N(E)$ , falls off as energy increases by the rate of a spectral index,  $\gamma$ . The spectral index,  $\gamma$ , has a value of  $\gamma \approx 3$  over tremendous ranges of energies.

### 1.3 Cosmic Ray Propagation and the Greisen-Zatsepin-Kuzmin (GZK) Suppression

Besides the magnetic deflection of cosmic rays due to their charged nature, as illustrated in Figure 1.3, there are also particle interactions that a cosmic ray will undergo as it propagates through the universe.

In 1965, Arno Penzias and Robert Wilson observed a dominant noise source emanating from space with a noise temperature of 2.73 K<sup>[14]</sup>. This observation was the discovery of the *cosmic microwave background (CMB)*. Soon after, Kenneth Greisen<sup>[15]</sup> and independently Georgiy Zatsepin and Vadim Kuzmin<sup>[16]</sup> recognized that this isotropic and homogeneous sea of photons left over from the early universe would interact with proton with enough energy to form a  $\Delta^+$  particle resonance. The  $\Delta^+$  particle is unstable and decays into a nucleon (proton or neutron) and the appropriate pion to conserve charge. In this process, some of the kinetic energy of the proton goes into the rest mass of the created pion, and the resultant nucleon has less kinetic energy than the initial proton. The critical energy of the proton is the energy needed to form the  $\Delta^+$  given the energy of the CMB photons. This critical energy is  $E_{\text{GZK}} = 6 \times 10^{19}$  eV. This interaction will quickly reduce the number of protons observed above the critical energy. This suppression is named the *Greisen-Zatsepin-Kuzmin (GZK) suppression* after the three physicists who suggested it. The possible interactions are



The Feynman diagram of one of these interactions is shown in Figure 1.4. A proton above the critical energy, interacting with the sea of CMB photons, has a mean free path of about 50 Mpc. A proton originating from a source beyond 50 Mpc, with energy above the GZK critical energy, will lose energy and be observed at an energy lower than the critical energy.

At high energies, the rigidity of the cosmic rays increases. However, the GZK suppression limits the ability to point back UHECRS to sources beyond 50 Mpc. Cosmic rays *have* been detected above the GZK critical energy. Most famous is a particle observed by the Fly's Eye I detector that

is the highest energy particle ever detected. In October 1991, Fly's Eye I observed a particle with  $E = (3.2 \pm 0.9) \times 10^{20}$  eV, referred to as the *Oh-My-God particle*<sup>[17,18]</sup>.

## 1.4 Cosmic-Ray-Induced Extensive Air Showers

When a cosmic ray enters the Earth's atmosphere, it will interact with an air molecule at a high altitude. This interaction produces a cascade of secondary particles that are imparted with tremendous energy from the *primary cosmic ray particle*. A depiction of the *first interaction* in Figure 1.5.

After the first interaction, the secondary particles interact with other air nuclei, and this develops into a chain reaction of particles. This cascade of particles can grow to be extensive in number, depending on the energy of the primary cosmic ray. This cascade of particles is called a cosmic-ray-induced extensive air shower, which discovery was discussed in Section 1.1. The term EAS is often shortened to *shower* or *cascade*. A schematic representation of a cosmic ray EAS is shown in Figure 1.6.

An EAS has three main components, named due to the types of particles produced and the available particle interactions they go through. These three components are highlighted in Figure 1.7. The *hadronic component*, shown in Figure 1.7a, consists of baryons and mesons, and provides the core of the EAS as it develops. As the particle cascade continues to interact with air nuclei, the hadrons will spallate off groups of nucleons and produce mesons. The baryons and mesons continue the development of the hadronic component in the EAS while some of the mesons, being unstable, decay, and develop into the other components of the EAS.

Neutral pions generated in the hadronic component begin the *electromagnetic (EM) component*, shown in Figure 1.7b. The neutral pions decay into two photons,

$$\pi^0 \rightarrow \gamma + \gamma. \quad (1.6)$$

The photons undergo pair production,

$$\gamma \rightarrow e^+ + e^-. \quad (1.7)$$

The electrons then undergo bremsstrahlung,

$$e^\pm \rightarrow e^\pm + \gamma. \quad (1.8)$$

Through the interactions in Equations 1.7 and 1.8, the EM component becomes self-sustaining while there is enough energy for the interactions above. The EM component becomes the dominate component of the EAS, and is important for the fluorescence detection of cosmic rays (to be discussed later in Section 1.8.1).

The final component of the EAS is the *muonic component*, shown in Figure 1.7c. The hadronic component produces charged pions, and they may decay into muons and their associated neutrino.

$$\pi^+ \rightarrow \mu^+ + \nu_\mu \quad (1.9)$$

$$\pi^- \rightarrow \mu^- + \bar{\nu}_\mu \quad (1.10)$$

Relativistic muons are stable relative to the timescale of the EAS and survive to the ground. Neutrinos interact only via the weak interaction and are nearly massless. Thus, the muons neutrinos carry off energy from the air shower. The charged pions can also decay into electrons, but this is much less likely to happen, given *helicity suppression*.

Eventually, the energy is so dispersed amongst the multiplicity of particles that the EAS stops developing. The EAS is the result of the primary cosmic ray depositing energy in the Earth's atmosphere and gives us the ability to observe the primary cosmic ray particle indirectly.

## 1.5 Models of Cosmic Ray Extensive Air Showers

Several EAS models have been created to gain insight into the development and evolution of the particle cascade. Two illustrative models are the Heitler model, concentrating on the EM component, and the Heitler-Matthews model, which also incorporates the hadronic and muonic components.

### 1.5.1 Heitler Model

The Heitler Model<sup>[19]</sup> describes the electromagnetic component in an EAS. The Heitler model starts the particle cascade with a high energy photon of energy  $E_0$ , which undergoes pair production of electrons ( $e^\pm$ ) as described in Equation 1.7. The electrons then undergo bremsstrahlung, producing more high energy photons as described in Equation 1.8. The interactions repeat from this point.

The Heitler model assumes the interaction lengths,  $\lambda$ , of the pair production and bremsstrahlung are equal, which is a good approximation at high energy for ionizing particles. After each interaction length, the cascade branches in two-body splitting, and the energy is assumed to be evenly split. The model assumes the interactions are spaced at each interaction length, instead of a distribution over each interaction length. This cascade is illustrated in Figure 1.8.

The particle multiplicity,  $N_{\text{particles}}$ , and the energy of each particle in the cascade can then be described after  $n$  branchings as

$$N_{\text{particles}} = 2^n \quad (1.11)$$

$$E_n = \frac{E_0}{2^n}. \quad (1.12)$$

The distance over which the shower has developed is expressed as

$$X_n = n\lambda \quad (\lambda = x_e \ln(2)) \quad (1.13)$$

$$= nx_e \ln(2), \quad (1.14)$$

where  $x_e$  is the radiation length of an electron in air.

Eventually the energy of the particles falls below a critical energy,  $E_n < E_{\text{critical}}^e$ . At this point, the cascade stops as the interactions are no longer sustained. Empirically, The critical energy is observed to be  $E_{\text{critical}}^e \approx 85$  MeV. The shower creates  $N_{\text{max}}$  particles after  $n_{\text{critical}}$  iterations,

$$N_{\text{max}} = \frac{E_0}{E_{\text{critical}}^e} = 2^{n_{\text{critical}}}. \quad (1.15)$$

The depth at which the particles stop interacting and the shower reaches its maximum size is

$$X_{\text{max}} = n_{\text{critical}} x_e. \quad (1.16)$$

Thus  $n_{\text{critical}}$  becomes

$$n_{\text{critical}} = \frac{1}{\ln(2)} \ln \left( \frac{E_0}{E_{\text{critical}}^e} \right) \quad (1.17)$$

and  $X_{\text{max}}$  can be expressed in terms of the primary energy,

$$X_{\text{max}} = x_e \ln \left( \frac{E_0}{E_{\text{critical}}^e} \right), \quad (1.18)$$

illustrating the maximum depth of the particle cascade grows logarithmically with  $E_0$ . Higher energy cosmic rays develop deeper into the atmosphere.

Another important characteristic of particle cascades illustrated with this model is the *elongation rate*,  $\Lambda$ . The elongation rate is the rate at which  $X_{\text{max}}$  changes with respect to the energy of the shower. The elongation rate is defined as

$$\Lambda \equiv \frac{dX_{\text{max}}}{d \log_{10}(E_0)}. \quad (1.19)$$

Thus, using Equation 1.18, the elongation rate becomes

$$\Lambda_{\text{Heitler}} = x_e \ln(10) \quad (1.20)$$

Using the radiation length of electrons in air<sup>[13]</sup>, the elongation rate has a value of

$$\Lambda_{\text{Heitler}} \approx 85 \text{ g/cm}^2. \quad (1.21)$$

For every increase of a power of ten (referred to as a decade on a log scale) in energy, the EM particle cascade develops roughly 85 g/cm<sup>2</sup> further into the atmosphere. The Heitler model emphasizes how the depth of the EM particle cascade develops as a function of the primary cosmic ray energy.

### 1.5.2 Heitler-Matthews Model

Matthews has developed an extension to the Heitler model that includes the consideration of the hadronic cascade by adding pion interactions<sup>[20]</sup>. This model considers a primary cosmic ray *proton* with energy  $E_0$ , which begins a particle cascade that, like the Heitler model, branches every interaction length,  $\lambda$ . However, the Heitler-Matthews model primarily considers the generation of pions ( $\pi^0\pi^\pm$ ) as the secondary particles. Figure 1.9 illustrates the development of the particle cascade.

After each interaction length, a given number of pions are generated, evenly distributed amongst the flavors:  $N_{\text{ch}}$  charged pions and  $\frac{1}{2}N_{\text{ch}}$  neutral pions, with the additional assumption that the energy is distributed evenly amongst the generated pions. Since the neutral pions are unstable relative to the interaction length scale and decay into photons as described in Equation 1.6, only the charged pions split as described above. Thus, at each interaction,  $\frac{2}{3}E$  goes into the charged pions, and the remaining  $\frac{1}{3}E$  goes into the neutral pions. The neutral pions then feed into the electromagnetic component of the particle cascade, providing a link between the two components. The hadronic component continues through the charged pions, which continue to interact with air molecules after each interaction length producing more pions. The hadronic component stops developing when the charged pions drop below the critical energy,  $E_{\text{critical}}^\pi \approx 20$  GeV, where it is more probable the pions decay into muons and neutrinos as described in Equation 1.10 than interact with air molecules, incorporating the last component of the EAS in the muonic component.

After  $n$  interactions the energy split between the hardonic and electromagnetic component of the shower is described as

$$E_{\text{hadronic}} = E_{\pi^\pm} = \left(\frac{2}{3}\right)^n E_0 \quad (1.22)$$

$$E_{\text{EM}} = E_{\pi^0} = \left[1 - \left(\frac{2}{3}\right)^n\right] E_0. \quad (1.23)$$

As the number of interactions increases, more energy is transferred into the electromagnetic component of the cascade.

Using energy conservation, the multiplicity of particles in the cascade can be calculated. The initial energy of the primary cosmic ray is divided into the electromagnetic component and the remaining hadronic component. For the electromagnetic component we consider the particles at maximum development. For the hadronic component, we consider all the pions converted into muons. Thus, we have,

$$E_0 = N_\mu E_{\text{critical}}^\pi + N_{\text{max}}^e E_{\text{critical}}^e. \quad (1.24)$$

To account for other interactions outside of the Heitler model such as multiple photon generation in bremsstrahlung and the absorption of electrons in the air, a correction factor is added to better

estimate the number of electrons generated in the electromagnetic component of the EAS. This correction is given by

$$N_e = \frac{N_{\max}^e}{g}, \quad (1.25)$$

where a correction of  $g = 10$ . Using this correction in Equation 1.24,

$$E_0 = N_\mu E_{\text{critical}}^\pi + g N_e E_{\text{critical}}^e \quad (1.26)$$

$$= g E_{\text{critical}}^e \left( N_e + \frac{N_\mu E_{\text{critical}}^\pi}{g E_{\text{critical}}^e} \right). \quad (1.27)$$

Putting in known critical energy values,

$$E_0 \approx (0.85 \text{ GeV}) \times (N_e + 24 N_\mu). \quad (1.28)$$

Equation 1.28 shows how sampling the multiplicity of the electrons and muons is a good estimator for the initial energy of the cosmic ray primary that created the cascade. When the particles in cascade reach a critical energy,  $E_{\text{critical}}^\pi$ , the hadronic component stops and the charged pions decay. When the hadronic component stops, the energy split amongst all the particle is

$$E_n = E_{\text{critical}}^\pi = \frac{E_0}{(\frac{3}{2} N_{\text{ch}})^{n_{\text{critical}}}}. \quad (1.29)$$

Solving for  $n_{\text{critical}}$ ,

$$n_{\text{critical}} = \frac{\ln(\frac{E_0}{E_\mu})}{\ln(\frac{2}{3} N_{\text{ch}})}. \quad (1.30)$$

The multiplicity of muons can be determined by assuming that at  $n_{\text{critical}}$ , the charged pions decay to muons

$$N_{\pi^\pm} = N_\mu = (N_{\text{ch}})^{n_{\text{critical}}}. \quad (1.31)$$

Using Equation 1.30 the multiplicity of muons becomes

$$\ln(N_\mu) = \frac{\ln(N_{\text{ch}})}{\ln(\frac{2}{3} N_{\text{ch}})} \ln\left(\frac{E_0}{E_\mu}\right). \quad (1.32)$$

To simplify, a  $\beta$  factor is introduced where

$$\beta = \frac{\ln(N_{\text{ch}})}{\ln(\frac{2}{3} N_{\text{ch}})}. \quad (1.33)$$

The multiplicity of muons at the end of the particle cascade is proportional to the energy of the primary cosmic ray,

$$N_{m\mu} \propto E_0^\beta. \quad (1.34)$$

This can be used to evaluate the energy that is converted from the hadronic component to the muonic component. The energy of the mouns is important as it reveals how much energy is carried away

from the EAS in stable muons and weakly interacting neutrinos, both of which do not interact strongly with the atmosphere. The energy left in the charged pions when the cascade drops below critical energy is

$$E_{\text{critical}}^{\text{hadronic}} = N_\mu E_{\text{critical}}^\pi = N_{\text{ch}}^{n_{\text{crit}}} E_{\text{critical}}^\pi. \quad (1.35)$$

Using Equation 1.23 at  $n_{\text{critical}}$  where  $E_{\text{hadronic}} = E_{\text{critical}}^\pi$ ,

$$E_{\text{hadronic}} = E_{\text{critical}}^\pi = \left(\frac{2}{3}\right)^{n_{\text{critical}}} E_0. \quad (1.36)$$

The fraction of the energy converted into the muonic component using Equation 1.35 in Equation 1.36 gives the muon fraction as

$$f_\mu = \frac{E_{\text{hadronic}}}{E_0} = \left(\frac{2}{3}\right)^{n_{\text{critical}}}. \quad (1.37)$$

At each interaction, one-third of the energy remaining in the hadronic component goes into the neutral pions which feed into the electromagnetic component. Therefore, the missing energy carried away by the muonic component decreases as the number of interactions increases.

The depth at which the proton-induced EAS reaches its maximum,  $X_{\text{max}}^p$ , is determined by when the EM component maximum occurs. The highest energy photons are generated in the first interaction of the model,  $X_0$ . These photons contain energy,

$$E_{\text{EM}} = \frac{E_0}{3N_{\text{ch}}}. \quad (1.38)$$

Using this energy in the Heitler model maximum in Equation 1.18, with  $E_0 = E_{\text{EM}}$ , the photons generated in the first interaction reach a maximum at

$$X_0^{\text{EM}} = X_{\text{EM}} \ln \left( \frac{E_0}{E_{\text{critical}}^e} \right) = X_{\text{max}}^{\text{EM}} - X_{\text{EM}} \ln(3N_{\text{ch}}). \quad (1.39)$$

Thus, the shower maximum for the Heitler-Matthews particle cascade initiated by a proton is

$$X_{\text{max}}^p = X_0 + X_0^{\text{EM}} = X_0 + X_{\text{max}}^{\text{EM}} - X_{\text{EM}} \ln(3N_{\text{ch}}). \quad (1.40)$$

Determining the elongation rate using Equation 1.19,

$$\Lambda^p = \frac{d(X_{\text{max}}^p)}{d \log_{10}(E_0)} = \frac{d(X_0)}{d \log_{10}(E_0)} + \Lambda^{\text{EM}} - X_{\text{EM}} \frac{d(\ln(3N_{\text{ch}}))}{d \log_{10}(E_0)}. \quad (1.41)$$

The last term in Equation 1.41 shows the multiplicity of pions created in the hadronic component reduces the elongation rate of the EAS.

The Heitler-Matthews model describes a proton starting the hadronic component of the EAS, which generates the EM and muonic components. The model illustrates how missing energy depends on how many charged pions are left after the air shower stops. The model also illustrates how the elongation rate depends on the pion generation as well. Accurately determining the missing energy of an EAS is essential to calculate the energy of the primary cosmic ray.

### 1.5.3 Superposition Model

The composition of primary cosmic ray particles extends beyond protons. To describe heavier nuclei with  $A$  nucleons, the particle cascade is modeled as initiated by  $A$  protons, each of which each creates its own cascade. The energy of the initial nuclei is assumed to be evenly distributed in each nucleon

$$E_{\text{nucleon}} = \frac{E_0}{A}. \quad (1.42)$$

A hardonic shower initiated by a nuclei with atomic number  $A$ , creates  $A$  identical showers, each with the energy given in Equation 1.42. Including the superposition model and the Heitler-Matthews model, the multiplicity of muons produced by the nuclei, using Equation 1.34, is

$$N_\mu^A \propto A \left( \frac{E_0}{A} \right)^\beta = A^{(1-\beta)} E_0^\beta = N_\mu^p A^{(1-\beta)}. \quad (1.43)$$

In Equation 1.33,  $\beta > 1$ , thus  $N_\mu^A$  decreases with  $A$ . The shower maximum in Equation 1.40 for the nuclei becomes

$$X_{\max}^A = X_0 + X_{\text{EM}} \ln \left( \frac{E_0/A}{E_{\text{critical}}^e} \right) \quad (1.44)$$

$$= X_{\max}^p - X_{\text{EM}} \ln(A) \quad (1.45)$$

The superposition model illustrates the expectation that heavy nuclei cosmic rays should develop higher in the atmosphere than lighter nuclei and produce fewer muons. Thus, the maximum depth of the shower is an estimator for the composition of a primary cosmic ray particle.

## 1.6 Cascade Equation

For a better understanding of the development of an EAS th provided by the EAS models, one can model the shower with a *cascade equation*. The cascade equation<sup>[21]</sup> has the form

$$\frac{dN_i(E_i, X)}{dX} = -\frac{N_i(E_i, X)}{\lambda_i} - \frac{N_i(E_i, X)}{d_i} + \sum_{j=1}^J \int_E^\infty \frac{F_{ji}(E_i, E_j)}{E_i} \frac{N_j(E_j, X)}{\lambda_j} dE_j. \quad (1.46)$$

The cascade equation describes the rate of change of the number of particles of species  $i$  with depth. The first term on the right hand side is the particle loss via interaction with the medium in one interaction length,  $\lambda_i$ . The second term is the particle loss due to decay in one decay length,  $d_i$ . The last term is the particle yield that creates the particle species  $i$  from particle species  $j$ , in interactions given the interaction cross section of particle  $j$  with the air. The cascade equation neglects energy loss due to ionization of the air, but this term can be neglected for hadrons and high energy electrons. The cascade equation can be used to describe all the various components of the air shower.

The variables  $X$ ,  $\lambda$ , and  $d_i$  have units of depth, the integration of the density of air through which the particles traverse to account for the matter that they can interact with. This integration along the path  $r$  of the medium density  $\rho$  is the *interaction depth*  $X$ ,

$$X = \int \rho(r) dr. \quad (1.47)$$

When the particle is traveling at an angle through a nonuniform medium, this is called *slant depth*. The standard units of depth and slant depth are g/cm<sup>2</sup>.

## 1.7 Shower Development

As the EAS develops in the atmosphere, the number of charged particles at a given slant depth can be described by the phenomenological form of the *Gaisser-Hillas function*<sup>[22]</sup>

$$N_{\text{ch}}(X) = N_{\text{max}} \left( \frac{X - X_0}{X_{\text{max}} - X_0} \right)^{\left( \frac{X_{\text{max}} - X_0}{\lambda} \right)} \exp \left( \frac{X_{\text{max}} - X}{\lambda} \right). \quad (1.48)$$

The number of charged particles,  $N_{\text{ch}}(X)$ , is described by the maximum number of particles the shower creates,  $N_{\text{max}}$ , at the depth of shower maximum,  $X_{\text{max}}$ .  $X_0$  is the approximate start of the shower and  $\lambda$  is the shower decay length.  $X_0$  and  $\lambda$  are phenomenological variables rather than physically relevant parameters. The distribution of charged particles is used to calculate the calorimetric energy deposition of the shower in the atmosphere via the mean ionization loss<sup>[23]</sup>

$$\frac{dE_{\text{dep}}(X)}{dX} = \alpha(X)_{\text{eff}} N_{\text{ch}}(X). \quad (1.49)$$

$\alpha(X)_{\text{eff}}$  can be parameterized in terms of shower age,

$$s = \frac{3X}{X + 2X_{\text{max}}} \quad (1.50)$$

and  $\alpha$  is given by<sup>[23]</sup>

$$\alpha(s)_{\text{eff}} = \frac{c_1}{(c_2 + s)^{c_3}} + c_4 + c_5 s. \quad (1.51)$$

The parameters used in Equation 1.51 are listed in Table 1.1.

Integrating over the profile in Equation 1.48, and using it in Equation 1.49 yields the energy deposited in the atmosphere by the EAS, and includes all of the primary energy except for the missing energy carried off in the muonic component.

## 1.8 Atmospheric Fluorescence and Light Propagation

As the electromagnetic component of the EAS grows in the atmosphere, it excites the nitrogen molecules, producing fluorescence light. The EAS can also generate light in the form of *Cherenkov radiation* if the charged particles travel faster than the speed of light through air. The Cherenkov

light is emitted in a narrow cone in the direction of the charged particle's velocity. Both forms of light production are dependent on the number of charged particles in the EAS. The fluorescence light produced by the EAS dominates over the amount of Cherenkov light in most cases. These effects allow for the observation of the development of an EAS induced by a cosmic ray with fluorescence telescopes. The amount of light an observer receives is dependent on the light scattering off air molecules or aerosols, and light absorption due to ozone as the fluorescence light propagates from the source to the observer.

### 1.8.1 Atmospheric Fluorescence and Light Production

The molecular nitrogen in the atmosphere,  $N_2$ , becomes ionized by the charged particles of the EAS. The nitrogen recombines and the electrons de-excite. By doing so, the nitrogen emits light in the near UV spectrum between 300-400 nm<sup>[5]</sup>. This light emitted by the nitrogen is called *fluorescence*<sup>2</sup>. The amount of fluorescence light emitted at a position along the EAS track is proportional to the number of charged particles in the EAS, as well as the temperature and pressure of the air.

A number of experiments have been conducted to determine the air fluorescence yields, such as Kakimoto<sup>[24]</sup>, FLASH<sup>[25,26]</sup>, Nagano<sup>[27]</sup>, and AIRFLY<sup>[28]</sup>. The fluorescence light is emitted isotropically by the molecular nitrogen and the number of photons generated is

$$\frac{d^2N_\gamma}{dld\Omega} = \frac{YN_e}{4\pi} \quad (1.52)$$

where  $Y$  is the fluorescence yield in photons per electron per meter and  $N_e$  is the number of electrons at that position in the EAS. Kakimoto<sup>[24]</sup> created a model for the air fluorescence yield depending on pressure and temperature

$$Y = \frac{\frac{dE}{dX}}{\frac{dE}{dX}_{1.4\text{MeV}}} \rho \left( \frac{A_1}{1 + B_1\rho\sqrt{T}} + \frac{A_2}{1 + B_2\rho\sqrt{T}} \right) \quad (1.53)$$

where the parametrization constants are given in Table 1.2.

The EAS also emits Cherenkov radiation for the charged particles exceeding the speed of light in the air. Charged particles with velocity  $v$  in the EAS produce Cherenkov light if the particle's velocity exceeds

$$v > \frac{c}{n(h)} \quad (1.54)$$

where  $c$  is the speed of light and  $n(h)$  is the index of refraction at altitude  $h$ . The minimum energy at which the particles with mass  $m$  produce Cherenkov light is

$$E_{\min} = \frac{mc^2}{\sqrt{2(n - 1)}}. \quad (1.55)$$

---

<sup>2</sup>Fluorescence is a misnomer, technically the light is created via scintillation.

The Cherenkov radiation is emitted within a cone with a maximum angle of  $\cos(\theta_{\max}) = \frac{1}{n}$ . The Cherenkov light generated per particle with energy  $E$  per unit length  $l$  is

$$\frac{dN_\gamma}{dl} = 4\pi\alpha \left(1 - \left(\frac{E_{\min}}{E}\right)^2\right) \int \frac{1-n}{\lambda^2} d\lambda \quad (1.56)$$

where  $\alpha$  is the fine structure constant. The  $\lambda^{-2}$  factor dependence causes a majority of the Cherenkov light to be in UV wavelength. The angular distribution of the Cherenkov light is

$$\frac{d^2N_\gamma}{dld\Omega} = \frac{dN_\gamma}{dl} \frac{e^{-\theta/\theta_0}}{2\pi \sin(\theta)}. \quad (1.57)$$

where  $\theta_0 = 0.83E_{\min}^{-0.67}$ .

Both methods of light production by the EAS are considered when reconstructing the cosmic ray event. This reconstruction is described further in Chapter 3.

### 1.8.2 Light Propagation

The atmospheric fluorescence light is attenuated as it propagates through the atmosphere by Rayleigh scattering, Mei scattering, and Ozone absorption. Rayleigh scattering is the case when light is scattered by an object much smaller than the wavelength of the light. This scattering is primarily due to air molecules. Mei scattering is the case when light is scattered by an object with a similar or greater size than the wavelength of light. This scattering is due to suspended particulates in the air such as dust, sand, or pollutants. Ozone,  $O_3$ , does absorb the near UV but not as much compared to the far UV spectrum. This makes the fluorescence light observation possible. In addition, most atmospheric ozone is in the ozone layer.

The amount of light scattered per unit length due to Rayleigh scattering is

$$\frac{dN_\gamma}{dl} = -\rho \frac{N_\gamma}{x_R} \left(\frac{400}{\lambda}\right)^4 \quad (1.58)$$

where  $\rho$  is the atmospheric density,  $x_R$  is the mean free path for the scattering at 400 nm, and  $\lambda$  is the wavelength of scattered light in units of nm. The angular scattering distribution due to Rayleigh scattering is

$$\frac{d^2N_\gamma}{dld\Omega} = \frac{dN_\gamma}{dl} \frac{3}{16\pi} (1 + \cos^2(\theta)). \quad (1.59)$$

The transmission of photons from a point on the sky through the atmosphere to an observer at distance  $\Delta x$  is

$$T_{\text{Rayleigh}} = \exp\left(-\frac{\Delta x}{x_R} \left[\frac{400}{\lambda}\right]\right) \quad (1.60)$$

where again  $\lambda$  is given in nm. This shows a strong dependence on the wavelength over the distance between the source and observer.

The amount of light scattered per unit length due to Mei scattering is dependent on the scatterer shape and their density in the atmosphere. The angular scattering distribution due to Mei scattering is

$$\frac{d^2N_\gamma}{dld\Omega} = -\frac{N_\gamma}{L_M(\lambda)} \rho_{Aero}(h) \varphi(\theta) \quad (1.61)$$

where  $L_M(\lambda)$  is the horizontal extinction length as a function of wavelength,  $\rho_{Aero}(h)$  is the density of aerosols as a function of altitude, and  $\varphi(\theta)$  is the scattering phase function of the scatterer. Different aerosols have a different scattering phase functions. Mei scattering is much harder to model due to dependence of the quantities of aerosols and type which can vary night to night. However it is not strongly wavelength dependent and scatters mostly in the forward direction<sup>[29]</sup>. The transmittance of Mei scattering is phenomenologically modeled as

$$T_{Mie} = \exp \left( \frac{H_M}{(h_2 - h_1) L_M} \left( e^{\frac{-h_1}{H_M}} - e^{\frac{-h_2}{H_M}} \right) \right) \quad (1.62)$$

where  $H_M$  is the characteristic height, also called scale height of the aerosol density, and  $h_1$  and  $h_2$  are the altitude of the scatterer and the observer respectively.

The absorption due to Ozone per unit length is

$$\frac{dN_\gamma}{dl} = -N_\gamma A_{O_3}(\lambda) \rho_{O_3}(h) \quad (1.63)$$

where  $A_{O_3}(\lambda)$  is the absorption coefficient as a function of wavelength and  $\rho_{O_3}(h)$  is the density of Ozone as a function of altitude. The transmittance due to ozone is

$$T_{O_3} = \exp(-X A_{O_3}(\lambda)) \quad (1.64)$$

where  $X$  is the slant depth the light propagates through.

Combining all the scattering and absorption effects, the total transmittance of the air fluorescence light propagating to the observer is then

$$T_{Tot} = T_{Rayleigh} \times T_{Mie} \times T_{O_3}. \quad (1.65)$$

These scattering and attenuation effects are important for reconstructing the EAS accurately in Chapter 3.

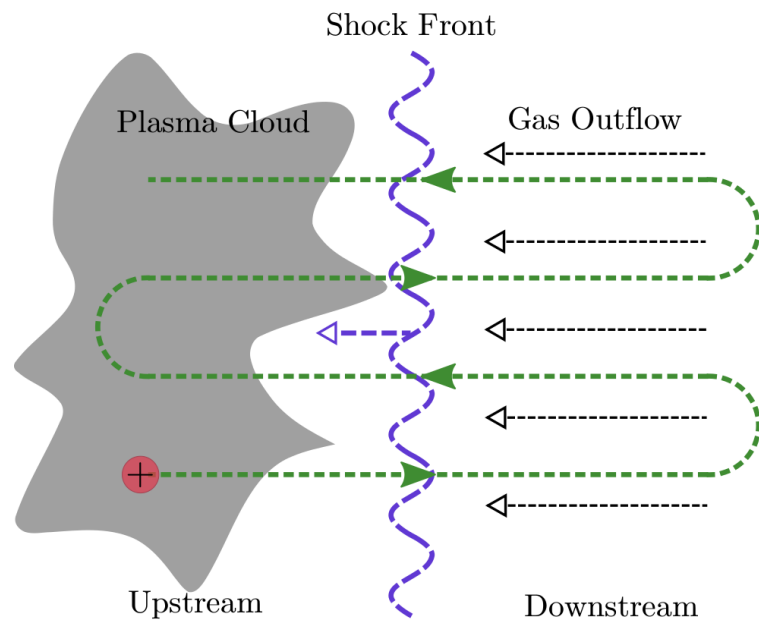


**Figure 1.1:** First-order Fermi acceleration with a cosmic ray crossing shock front multiple times.

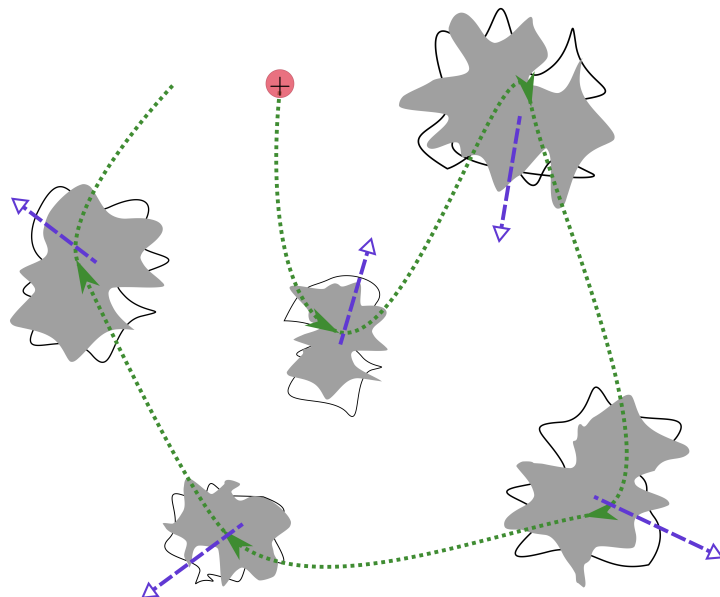


**Figure 1.2:** Second-order Fermi acceleration with a cosmic ray interacting with multiple moving plasma clouds.

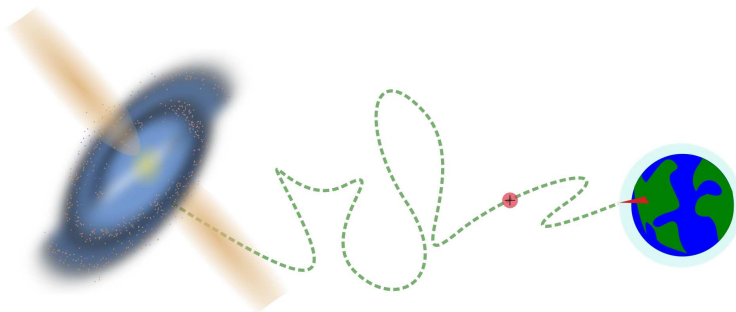


**Figure 1.3:** A cosmic ray propagating through the universe in a chaotic path due to its interaction with magnetic fields until intersects with the Earth's atmosphere and creates a cascade of particles.

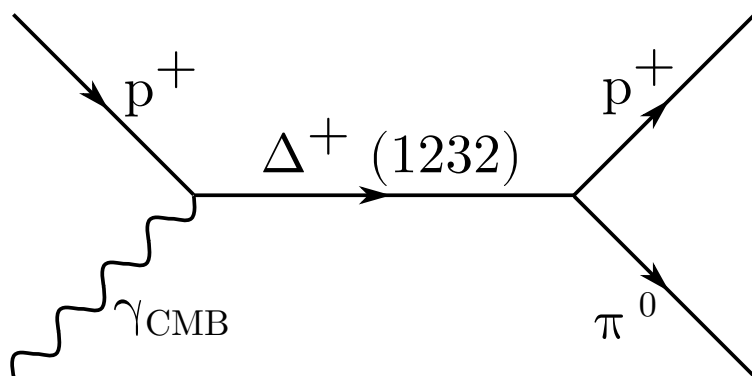


**Figure 1.4:** Feynman diagram of the proton interaction with the cosmic microwave background in the GZK suppression.

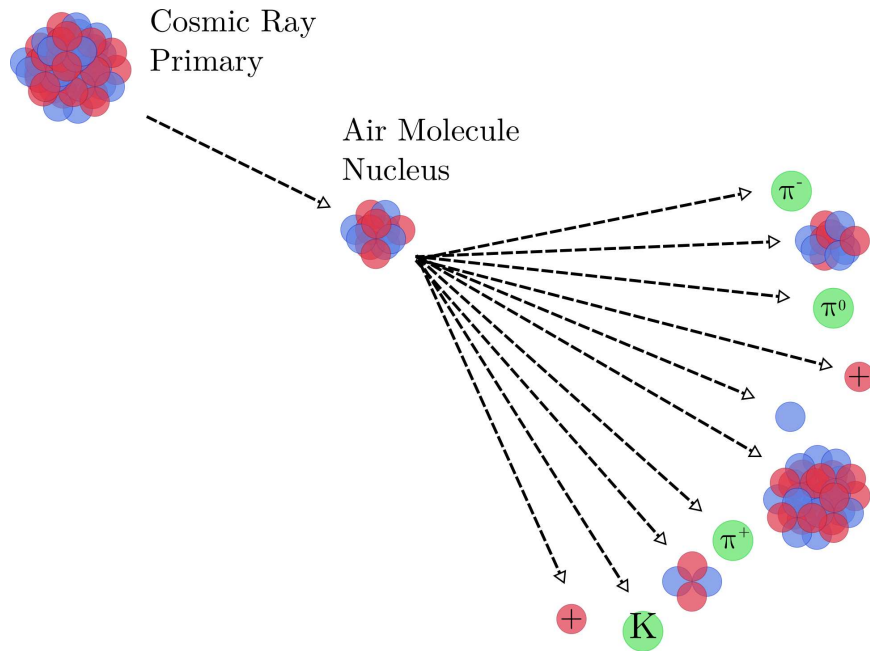


**Figure 1.5:** The first interaction of a cosmic ray with the nucleus of an air molecule.

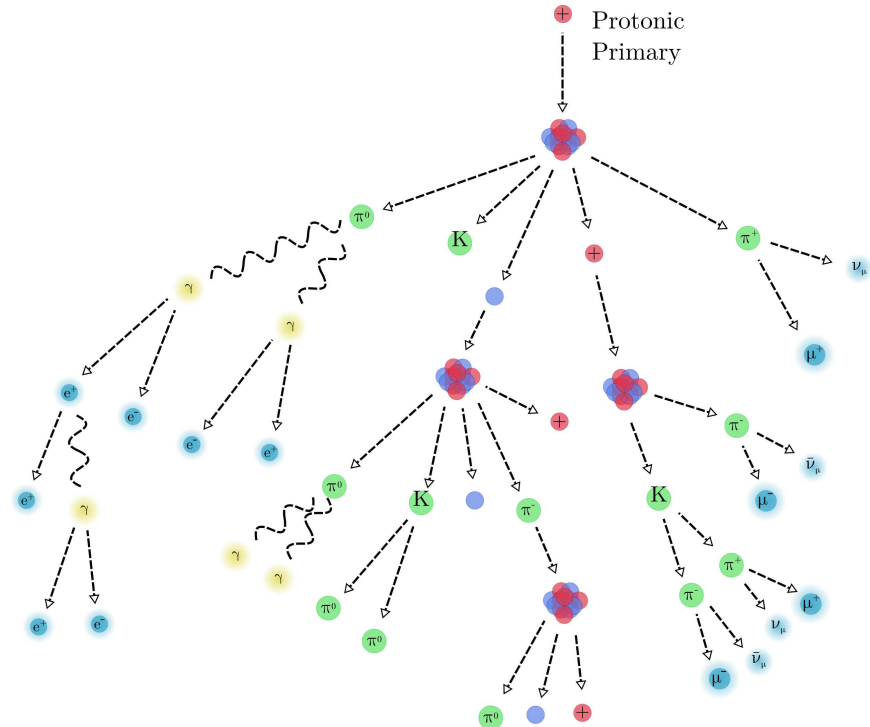


**Figure 1.6:** An extensive air shower generated by a protonic primary cosmic ray and some of the particle interactions that develop.

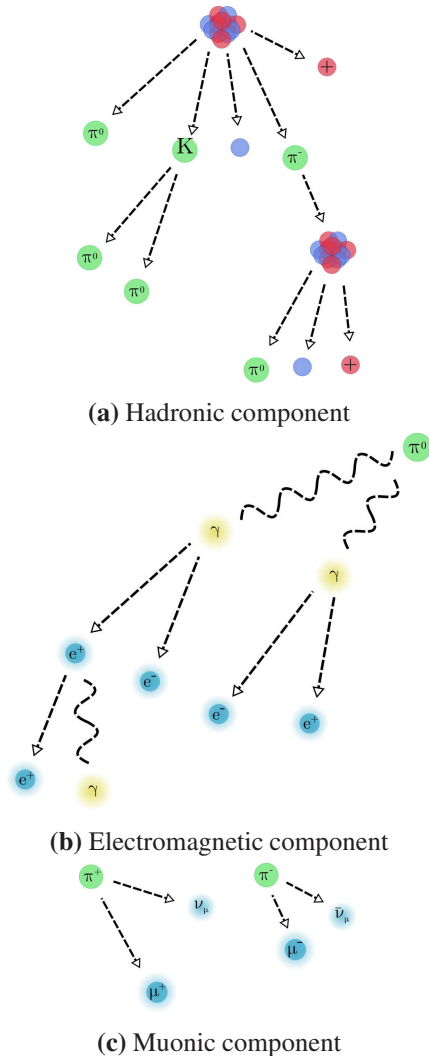


**Figure 1.7:** The three main components of particle interactions of an extensive air shower.

**Table 1.1:** Parametrization constants of  $\alpha(s)_{\text{eff}}$  in Equation 1.51 taken from<sup>[23]</sup>.

Parameter	Value
$c_1$	3.90883
$c_2$	1.05301
$c_3$	9.91717
$c_4$	2.41715
$c_5$	0.13180

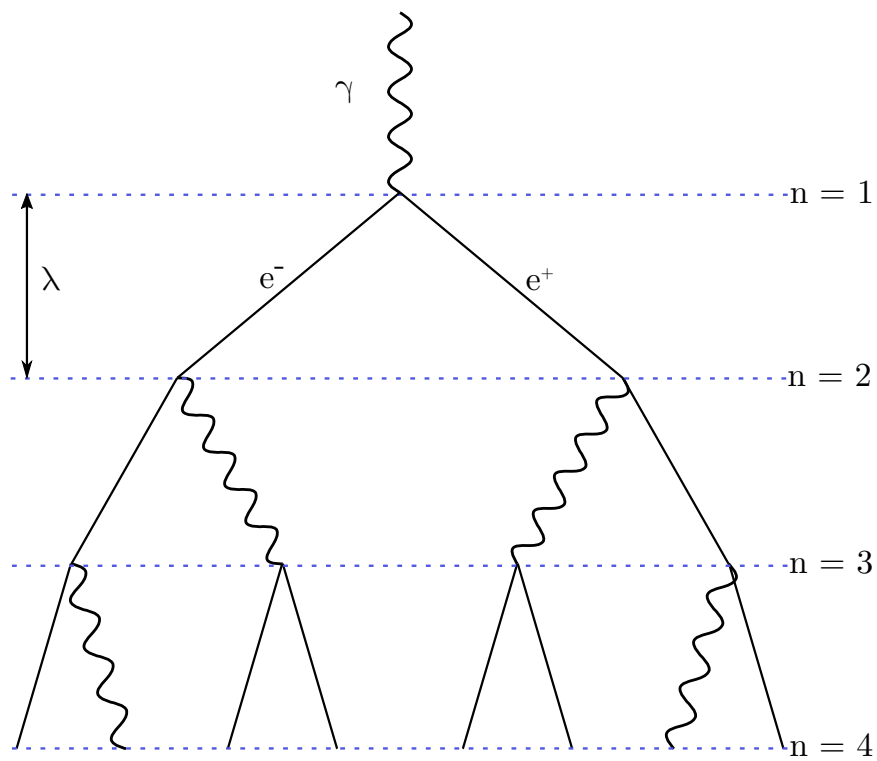


**Figure 1.8:** The development of an electromagnetic shower in the Heitler model.

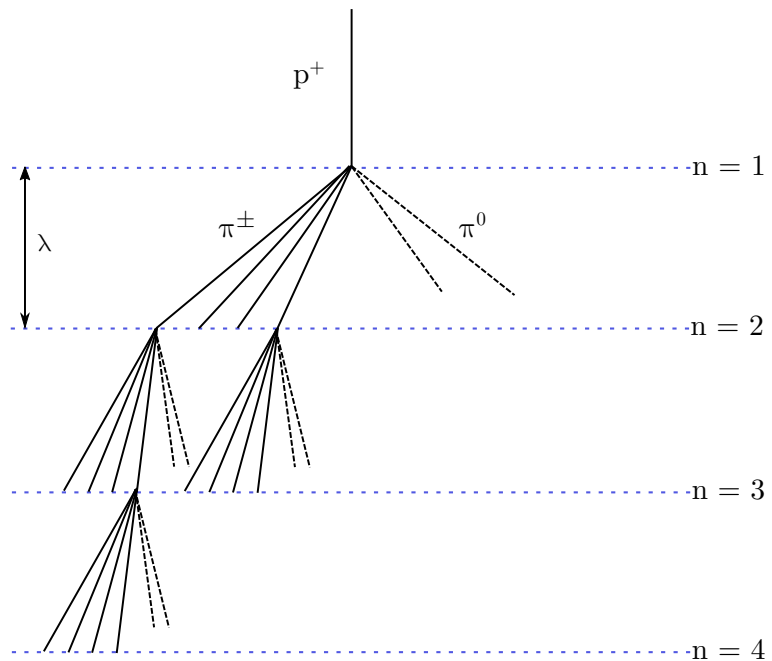


**Figure 1.9:** The development of a hadronic induced air shower in the Heitler-Matthews model.

**Table 1.2:** Air fluorescence yield parametrization constants for Equation 1.53 taken from<sup>[24]</sup>.

Parameter	Value
$A_1$	$8.09 \pm 1.7 \text{ m}^2 \text{ kg}^{-1}$
$A_2$	$55.0 \pm 2.2 \text{ m}^2 \text{ kg}^{-1}$
$B_1$	$1.85 \pm 0.04 \text{ m}^3 \text{ kg}^{-1} \text{ K}^{-\frac{1}{2}}$
$B_2$	$6.50 \pm 0.33 \text{ m}^3 \text{ kg}^{-1} \text{ K}^{-\frac{1}{2}}$

## CHAPTER 2

# COSMIC RAY DETECTION AND THE TELESCOPE ARRAY PROJECT

The observation of cosmic rays uses similar concepts of particle detectors at modern particle colliders. Both make use of *calorimeters*, which detect the deposition of energy in a medium, *scintillators*, which detect ionizing radiation, and *cherenkov* detectors, which detect the light emitted by particles moving faster than the speed of light in the medium. These detectors are employed to directly or indirectly detect the cosmic ray primary via their interactions. The fundamental questions about cosmic rays are: what is their composition, what is their source, and what is their energy density in the universe? These questions are analyzed over a vast range of energies to understand the different populations of cosmic rays.

This chapter will cover the use of indirect detection of UHECRs with the Telescope Array Cosmic Ray Observatory, and the expansion of Telescope Array Cosmic Ray Observatory known as TAx4.

### 2.1 Direct versus Indirect Detection of Cosmic Rays

Experiments such as SUPERTIGER<sup>[30]</sup>, CALET<sup>[31]</sup>, AMS-02<sup>[32]</sup>, and CREAM<sup>[33]</sup> are space or high altitude based *direct detectors* designed to detect the primary cosmic ray particle via its interaction within the detector. These experiments have a different scientific significance as they can measure the energy, charge, and composition of cosmic rays directly. The SUPERTIGER experiment was designed with a unique focus on cosmic ray composition by observing *Ultra-Heavy Cosmic Rays* compositions beyond Iron from galactic origins. The Voyager probes<sup>[34]</sup> also have direct cosmic ray detectors to make measurements as they were sent out on their journey of the edges of the solar system and beyond. However, these detectors only measure cosmic rays up to about TeV in energy.

At the energies levels of UHECRs, direct detection becomes unfeasible where the expected number of observed events is one event per square kilometer per century. In order to detect UHECR, *indirect detectors* are used to study the primary cosmic ray particle via its interaction with an external medium. As discussed in Chapter 1, a cosmic ray creates an extensive airshower. This interaction

is detectable by two general methods: either by using the atmosphere as a calorimeter and detecting the fluorescence light produced via the deposited energy or by sampling the particle footprint on the ground with scintillators or other particle detectors. Indirect detection via particle interactions is also used in the fields of gamma rays with HAWC<sup>[35]</sup> and neutrinos with IceCube<sup>[36]</sup>. There are also proposed space-based indirect detectors, such as JEM-EUSO<sup>[37]</sup>, which look down at the atmosphere with an increased aperture compared to ground-based cosmic ray observatories. A space-based prototype of this concept, Mini-EUSO<sup>[38]</sup>, was launched to the ISS in August 2019 and is currently taking data.

## 2.2 The Telescope Array Cosmic Ray Observatory

The Telescope Array (TA) Cosmic Ray Observatory<sup>[39]</sup> is located in Millard County, Utah. TA is an international collaboration with members from the USA, Japan, South Korea, Russia, Belgium, and the Czech Republic. TA was formed out of the two previous cosmic ray experiments of HiRes, which specialized in fluorescence detection, and the Akeno Giant Air Shower Array (AGASA)<sup>[40]</sup>, which specialized in surface detection. TA was built using both detection methods forming a *hybrid detector* for detecting UHECRs.

The location of TA was chosen for its dry desert air and distance from significant light pollution sources. TA is roughly 1370 m above sea level with roughly  $876 \text{ g/cm}^2$  of atmosphere above it. There are three atmospheric fluorescence detector (FD) stations at TA looking out over the surface array, as shown in Figure 2.1. The Black Rock (BR) and Long Ridge (LR) stations are identical stations on the southeast and southwest portions of the array. The Middle Drum (MD) station located in the northern portion of the array was built from refurbished equipment from TA's predecessor, the HiRes experiment with Hires-I sample-and-hold electronics. Reusing the HiRes equipment allows for cross-calibration between the HiRes analysis and the new BR and LR FD stations. The surface array of TA consists of 507 surface detectors (SDs) arranged in a grid with 1.2 km spacing covering 700 km<sup>2</sup> in area to detect the footprint of the cosmic ray EAS. TA is the largest cosmic ray observatory in the northern hemisphere. The Pierre Auger Cosmic Ray Observatory<sup>[41]</sup>, named after Pierre Auger, introduced in Section 1.1 and referred to as simply *Auger* or PAO, is the largest cosmic ray observatory located in the southern hemisphere. There is a slight overlap in sky coverage between the two observatories.

In the middle of TA is the *Central Laser Facility* (CLF), which houses a vertical laser source. The CLF was placed to be roughly equidistant between all 3 FD stations. The CLF laser emits light at 355 nm and has a maximum energy of 10 mJ. The CLF laser is fired in pulses every 30 min at night. The CLF is used for cross-calibration between the different FD sites, and for measuring

the *vertical aerosol optical depth (VAOD)* to understand the atmospheric conditions throughout the night and variation with the seasons.

### 2.2.1 Surface Detectors

TA's surface detector array<sup>[42]</sup> is arranged in a roughly square grid on United States public land managed by the Bureau of Land Management (BLM) and the Utah School and Institutional Trust Lands Administration (SITLA). The array is bounded by the geographical features of Long Ridge to the west, the Little Drum Mountains, Big Drum Mountains and Smelter Knolls to the North, the towns of Delta, Hinckley, and the Black Rock Mesa to the east, and the Sevier Lake to the south giving the array it's deformed oval as shown in Figure 2.1.

A surface detector (SD) contains two plastic sheets of  $3 \text{ m}^2$  surface that are 1.2 cm thick of scintillating organic compound (Polyvinyl toluene, PVT) covered in light-shielding material. These two scintillating sheets are placed one on top of the other. As a charged particle passes through the scintillating plastic, it excites the organic compound, which then emits light as it returns to a ground energy state. The light is collected by wavelength shifting optical fibers, which guide the light onto two *Photomultiplier Tubes (PMTs)*. The PMT converts the light into a voltage pulse. This voltage pulse is converted to a time sequence of digital signals via a *fast analog digital converter (FADC)*. The SD monitors the signal from the ionizing particles passing through both layers for the trigger condition to record data. The trigger is handled by an onboard data acquisition electronics. The SD triggers if it detects a pulse of 3 *minimum ionizing particles (MIP)*. The SD reports a good signal to one of 3 radio communication towers (CTs) around the array via a radio wide local area network (WLAN). If three adjacent SDs each report a trigger within an  $8 \mu\text{s}$  time window, the CTs send an event trigger to record data from any SD in the array with a 0.3 MIP signal within the coincidence window. Each radio tower records data for one of three subsections of the array and saves the data to an operations computer at each tower. The SD contains two layers in order to reduce noise by requiring a coincidence signal between the two layers. The internal composition of the SDs is shown in Figure 2.2.

The SDs are powered by a battery that is charged during the day by a solar panel. The metal covering the SD was galvanized so as not to reflect sunlight off the SD surface into airplanes as they fly over. An SD in the field is shown in Figure 2.3.

The SD detectors sample the lateral particle density of the EAS. The number of SDs triggered by an event depends on the cosmic ray particle type and energy. SDs have the advantage of operating nearly 100% of the time and therefore gather more cosmic ray events. The SDs at TA differ from PAO, which uses water tanks to detect Cherenkov radiation emitted by particles moving faster than the speed of light through the water tank to sample the lateral particle density.

### 2.2.2 Fluorescence Detectors

As discussed in Chapter 1, the EAS excites nitrogen molecules in the atmosphere. The excited nitrogen molecules produce light in the near UV and a little in the blue (300-420 nm). This process is illustrated in Figure 2.4. An array of telescopes is used to collect the light from the atmosphere onto a camera to detect the fluorescence light. This is illustrated in Figure 2.5. The EAS will appear as a track along the focal plane of the camera. Using the light profile of the track, the calorimetric energy that was deposited in the atmosphere can be determined.

#### 2.2.2.1 Photomultiplier Tubes

A *photomultiplier tube* (PMT), sometimes shortened to *tube*, is a photon sensitive detector. It is a device used to turn photons into an electrical signal and is used in low light signal analysis. A photon hits the photocathode at the front of the PMT and emits an electron due to the photoelectric effect. This free electron, called a *photoelectron* given the process which creates it, is directed by an electric potential onto a linear array of dynodes. As the electron strikes the first dynode, the dynode releases multiple secondary electrons. Within the linear series of dynodes, the number of electrons continues to build. The anode on the far end collects the electrons to produce a significant signal in the form of an electrical current. A general schematic of a PMT is illustrated in Figure 2.6.

The design of a PMT allows for the generation and amplification of a significant electrical signal, allowing for the sensing of individual photons. Important characteristics of a PMT are the *quantum efficiency* (QE) and the *collection efficiency* (CE). Both of these effects can be incorporated together into the *QECE*. The quantum efficiency is the efficiency that a photon with wavelength  $\lambda$  produces an electron in the photocathode. The collection efficiency is the efficiency in collecting the photoelectron emitted by the photocathode onto the dynode. Understanding these quantities, and taking into account the known electron multiplicative factor of the linear series of dynodes, allows for calculating the photon flux hitting the photocathode from the electrical signal. These effects are taken into account in the fluorescence detector analysis in Chapter 3.

## 2.3 Telescope Array Black Rock and Long Ridge FD Stations

Data used in the analysis of this dissertation was collected from the Black Rock (BR) and Long Ridge (LR) stations. The BR and LR FD station<sup>[43]</sup> are each composed of an array of 12 FD telescopes with a field of view (FOV) of about  $118^\circ$  in azimuth and from  $3^\circ$  to  $33^\circ$  in elevation. Each telescope consists of a segmented spherical mirror 3.3 m in diameter, and the primary mirror is comprised of 18 hexagonal segments, shown in Figure 2.7c, that focuses onto a 16x16 cluster of hexagonal PMTs, shown in Figure 2.7b called the camera. This configuration creates a Schmidt Camera optical system, except the focal surface is flat to provide a wide field of view while limiting

the aberration. The telescopes are arranged in two stacked rows of six telescopes divide into three bays, as seen from the outside in Figure 2.7a to form the FOV. Each telescope has a FOV of roughly  $15^\circ$  in elevation by  $18^\circ$  in azimuth given, thus each PMT has an approximate  $1^\circ \times 1^\circ$  view on the sky. The stacked rows of telescopes are called *ring one* for the lower row and *ring two* for the higher row. The PMTs used for BR and LR are Hamamatsu R9508.

The fluorescence light produces a signal that is dependent on the mirror reflectivity, the transmittance through a protective cover over the camera made of Paraglas acrylic, the BG3 bandpass filters that cover the PMTs, and the QECE of the PMTs. These are all wavelength dependent and taken into account in the fluorescence event reconstruction described in Chapter 3. TA's FDs are sensitive between 290-420 nm, the range of fluorescence light produced by the excited nitrogen.

### 2.3.1 FADC Electronics

To read out the signal of each 3072 PMTS, sometimes referred to as *channels*, at each FD station, *fast analog digital converters (FADCs)* are employed. The analog electric signals from a column of PMTs is digitized and monitored by the *signal digitizer/finder (SDF)* circuit for a significant signal above the background. Each SDF has 16 FADCs, one for each channel. Each channel is read out with four consecutive 40 MHz sampled FADC digitization sets, which are summed together over to produce an effective 10 MHz sampling. This summation of four consecutive sets is done to improve the signal-to-noise and lessen the size of the raw data. The FADC samples the analog signal value and converts it to discrete values called *counts* that can be stored in a digital value. This signal summation is recorded out in a 14-bit time series value. The signal time series of read out values is referred to as a *waveform*. The clock for each SDF at a station is synchronized by a distributed count signal from a central clock called the *central timing and trigger distributor (CTD)*.

### 2.3.2 Triggering System

To trigger the data acquisition (DAQ) system and record out the data, the first step is calculating the significance of the PMT signal above the background. The significance is determined in a series of sliding windows<sup>[44]</sup>. Each sample out of the FADC is grouped into a time series of 256 samples called a *frame*. Given the 10 MHz sampling, a 100 ns cadence, this frame corresponds to  $25.6 \mu s$  time window. The frame is divided sums over 8, 16, 32, 64, 128, and 256 (0.8, 1.6, 3.2, 6.4, 12.8, and  $25.6 \mu s$ ) samples, which are compared to the appropriate sample-size threshold value. This threshold value is determined by the SDF, which monitors the background mean and variance. The threshold value is computed as a signal  $6\sigma$  above the mean background accounting for the samples in the sum window. Any PMT with a value higher than the threshold is considered a *hit tube or good tube*. If there is no hit PMT, the frame advances another 128 samples to overlap with the half of the

last frame. Then the same procedure of sampling over the frame for significant values is repeated.

The next level of the trigger is the recognition of a track pattern of hit PMTs. A *track finder* (*TF*) module scans a 5x5 subcluster across the PMT array and searches the hit PMTs for a match in a series of defined track patterns stored in a *fast programmable gate array* (*FPGA*). If five contiguously touching PMTs form a track that is found in the scanning 5x5 subcluster within a  $25.6\mu\text{s}$ , the TF issues a trigger code to the CTD. The CTD, in turn, issues a station wide trigger command where all the FADC waveforms from each PMT over a  $51.2\mu\text{s}$  span is recorded to disk by the DAQ. This  $51.2\mu\text{s}$  span will capture the entire track in the station's FOV, assuming the EAS propagates close to the speed of light. An example EAS track and the possible track patterns recognized are illustrated in 2.8.

To allow for intermirror triggers in the case that an EAS track was to start at the edge of one camera and appear in another, a 4x4 subcluster scans along the edge of a mirror looking for a track of 3 contiguous hit PMTs. If two neighboring mirrors with the correct corresponding edges report this condition to the CTD, a station wide trigger is also issued. These two trigger methods are assigned a code in the system to track which type of trigger was achieved. A track of 5 hit PMTs is denoted as a trigger code 1, and an intermirror track of 3 hit tubes is denoted as a trigger code 2. An example of an intermirror EAS track and the possible track patterns recognized are illustrated in 2.8.

### 2.3.3 Calibration

To calibrate the PMTs of the FD system, TA utilizes the following calibrations methods<sup>[45]</sup>. These methods account for PMT environmental and geometry factors and track the PMT's performance throughout the operation of the TA experiment over 10 years of operation. The factors such as the temperature and position of the PMT in the cluster change the FADC readout. These are accounted for with sensors and active calibration method. The nominal initial PMT gain was also tested with a small subset of the PMTs. A PMT's *gain* is the conversion measurement of one incident photon on the PMT to ADC counts. To account for other long or short term factors that change the nominal gain of the PMT, other systems of active and passive calibration were used.

Two PMTs in each camera were absolutely calibrated to get a baseline performance of the PMTs placed in a camera cluster. These PMTs can then be compared to the other PMTs in the cluster for a relative calibration. This calibration allows for an understanding of every PMT without having to absolutely calibrate every PMT in a cluster. To get the absolute calibration of those PMTs, TA set up an experiment named *calibration with rayleigh scattering (CRAYS)*<sup>[46]</sup>. Using a pulsed laser beamed through a chamber filled with gases, the Rayleigh scattered light at  $90^\circ$  was detected by a PMT. The PMT high voltage was adjusted to achieve a nominal value, which corresponded to 2.3

337 nm photons per FADC count. This ratio of adjusting the signal out of a PMT before the signal is sent into the FADC to adjust the FADC count value is called *gain balancing*. Gain balancing is a method used across many different means of calibration. CRAYS also determined the temperature dependence of a PMT as -0.72% per degree Celsius. The temperature of the PMTs is monitored by a sensor in each camera to account for this effect.

A radioactive  $\alpha$  emitter inside a scintillator was attached to the center of each CRAYS calibrated PMT in a camera to understand long term changes to the PMTs over time. The radioactive source of  $^{241}\text{Am}$  (Americium 241) with a half-life of 242.2 years and emits  $\alpha$  particle(helium nuclei). A Yttrium Aluminum Peroxide (YAP) scintillating crystal ( $\text{YAlO}_3$ ) is placed between the  $\alpha$  emitter and the PMT. When a  $\alpha$  particle passes through the YAP scintillator, photons with a peak at 370 nm are produced near the PMT. A mirror is placed over the  $\alpha$  emitter and YAP scintillator to ensure the light produced in the scintillator passes into the PMT. The YAP is used as a known light source that has no temperature dependence to check the PMT response. The YAP is used to monitor the PMT QECE, which will gradually decrease with age due to the chemical break down of the photocathode. The YAP is only 4 mm in diameter and has a negligible effect on the fluorescence light into the PMT.

A Xenon UV Flasher (XF) was placed in the center of the mirror segments of each telescope and pointed toward the camera to understand the gain balance drift while operating the FDs at night. Every hour of operation, the night sky DAQ is stopped, and a series of flashes from the XF is produced. The XF is analyzed to understand, given the known rate of UV photons produced by the XF, to understand how the system's conversion of photons to FADC counts. The Xenon flasher is covered with a 355 nm narrow pass filter with a Teflon diffuser to produce a diffuse monochromatic source for the PMTs to measure. Then the HV for each PMT is adjusted until the FADC conversion of photoelectrons to counts is uniform across the camera. The XF is operated throughout the night to monitor the PMT gain balance drift. The position of the PMT in the cluster is accounted for in the XF calibration by the light diffusion difference between the center of the cluster and the edges with a  $\cos^4\theta$  factor.

Using the XF and the YAP, the PMTs' performance is analyzed in both the short and the long term. The CRAYS calibration gives the nominal response of select PMTs when the experiment first began to get the relative calibration of the other PMTs in a camera. Also, the temperature dependence of the PMTs was determined using CRAYS. These calibration factors are used when reconstructing the EAS track. The FADC counts from each hit PMT in a track are adjusted by these factors to gauge the light produced by the EAS accurately. These calibration methods provide a more accurate measure of the calorimetric energy of the cosmic ray, as discussed in Chapter 3. These calibration factors are also used when simulating the response of the detector to simulated

EAS, as discussed in Chapter 5.

## 2.4 TAx4, the Telescope Array Project Expansion

Hints of anisotropy of UHECRs in the northern hemisphere has been observed<sup>[47]</sup>. Using the SD data, 72 events have been found with  $E > 57$  EeV. A significance of  $3.4\sigma$  was observed in pointing back these events and observing a clustering of events assuming an isotropic background. In order to better observe this clustering, coined the *hotspot*, TA is quadrupling its size. This expansion is appropriately named *TAx4*. This expansion of the detector will increase the detection aperture and increase the amount of detected cosmic ray events. With more events, the statistical significance of this hotspot will be better resolved. The TAx4 expansion will bring TA's size to be comparable to the size of PAO. The proposed TAx4 map is shown in Figure 2.10.

### 2.4.1 Surface and Fluorescence Detection Expansion

The surface and fluorescence detector station expansions are divided into a northern and southern region branching out from the current TA array around the city of Delta, UT. This location gives the benefits of the remoteness to the new FDs for decreased light pollution while allowing the SDs to be placed near enough to Delta to be accessible in need of repairs. The deployed TAx4 SDs and FDs as of summer 2019 are shown in Figure 2.11.

The new surface array will consist of 500 new SDs divide into the northern and southern lobe<sup>[48,49]</sup>. The spacing in the SD array was increased to 2.08 km to cover more area but not so much as to drastically decrease the efficiency of observing UHECRs of energy greater than 57 EeV. The new SDs have the same design concepts of the current TA SDs with a double layer of  $3 \text{ m}^2$  scintillating plastic beds. The new SD array is divided into six subarrays with the accompanying radio WLAN CTs.

To allow for calibration of the SD detectors, new FDs were added to the BR and MD FD stations to look out over the new surface array. These two detectors will allow for hybrid analysis of events where the events are reconstructed using both detectors. Twelve new fluorescence telescopes will be added, four at MD and eight at BR. Each telescope views about  $3^\circ - 17^\circ$  in elevation and  $15^\circ$  azimuthal with a roughly  $1^\circ \times 1^\circ$  pixel size. These new telescopes were recycled from the HiRes experiment with upgrades to the data trigger electronics system.

TAx4 FD FOV is not as extensive as the TA FD FOV for BR, LR, or MD. However, the focus of TAx4 FD is for hybrid detection with the SDs to allow for energy calibration of the SDs. The TAx4 SD expansion is the focus of novel physics results in anisotropy.

### 2.4.2 Construction, Testing, and Deployment of Fluorescence Expansion

The refurbishment, testing, and deployment of the new FDs for TAx4 was a significant component of this dissertation. The electronics, PMT clusters, and segmented mirrors, as was for the *TA Low Extension (TALE)*<sup>[50]</sup>, is comprised of parts from the HiRes Experiment<sup>[51]</sup>. TAx4 is reusing the “clover-leaf” 4 segments mirror of the Hires experiment. These are *ring one* mirrors that look from  $3^\circ - 17^\circ$  in elevation and have a collection area of roughly  $5 \text{ m}^2$ . The PMT clusters are the same Columbia University Nevis Labs designed 16x16 cluster of hexagonal Philips XP3062/FL that connect to the FADC electronics system for readout. The FADC electronics systems were refurbished, and some electronics were upgraded and swapped for newer components.

A HiRes-II FADC electronics rack houses the electronics for two telescopes. Seven HiRes-II racks were refurbished and upgraded for the 12 new telescopes that were to be deployed at BR and MD. The remaining rack is to be used as a spare. A new link module that connects the racks to the CTD for synchronizing the clock at each rack was installed. A new networking system was installed to connect each rack to the operations computer. A new low voltage (LV) system was installed for powering the FADC racks. The remote relay power supply was upgraded from 120 VAC to 220 VAC. To test that the electronic racks were working correctly, they were powered up remotely using the TAx4 operations software. The TAx4 operations software was based on the TALE operations software and uses the same Skynet server<sup>[50]</sup>. The operations software would report out issues with the electronics systems if anything was not working correctly during bootup and configuration.

Once the LV and HV were tested to be working properly, the upper and lower FADC readout racks were connected to a known working PMT cluster. A 355 nm UVLED, shown in Figure 2.12a, was placed at the end of a light cone connected to the front of the PMT cluster. This system was tested in a dark room as not to destroy the PMTs when the HV was turned on. The UVLED was flashed on the PMT cluster using a gain balancing program in the TAx4 operation software. This gain balancing differs from the BR and LR FADC gain balancing. This gain balancing test adjusts the value of variable gain amplifier connected to the tail of each PMT to create a uniform readout of FADC counts. Using the *real time event display* of the gain balancing, an example is shown in Figure 2.12b, bad columns of PMTs were recorded. Since an FADC board in the FADC rack of the electronics rack corresponds to a column of PMTs, missing columns in the known working PMT cluster corresponded to a bad FADC board. FADC boards were swapped until all worked properly for the gain balancing. This operation was repeated for all seven racks.

Next, the 14 PMT clusters that were going to be deployed were also tested with the same setup as the FADC racks with a known working electronics rack. Two clusters were tested for working spares. Each PMT cluster was set up with the UVLED in the light cone. The gain balancing

software was again run. A bad PMT was shown in the event display. Each bad PMT was first reseated, then replaced until the PMT worked. This was done until all PMTs in the cluster were working properly. With the PMT clusters and upgraded electronic racks tested, they were then backed up to be deployed at MR and BR stations.

A series of connected sheds were constructed at the MD and BR stations to house the new TAx4 FDs. Four sheds were built with connecting wedges, as shown in an ariel photo from an unmanned drone in Figure 2.13a. The new TAx4 MD telescope bays were connected to the TALE building to allow operators to walk through the whole station to check all telescopes. Eight connected sheds were built at the BR station, as shown in Figure 2.13b. Since the BR TA FD is currently being operated remotely, the BR TAx4 FD is planned to be as well.

Once the housing was finished, the telescopes went in. The TAx4 MD FD was installed in the spring of 2018, while TAx4 BR FD was installed late summer 2019. First, the electronics rack went in the wedges between the two sheds for operating the two telescopes on either side. Next, the segmented mirrors were installed and focused. With the mirrors installed, the rough pointing direction of the mirrors was surveyed. The mirror pointing direction was more rigorously calculated using the stars that passed across the camera face<sup>[52]</sup>. Then the PMT cluster stand was installed. Lastly, the PMT cluster was placed in the stand, shown in figure 2.14a, locked upright, and then wired up to the electronics rack shown in Figure 2.14b. In the center of the connected bays is the CTD that uses a GPS to distribute the clock to each electronics rack. The finished installation of the MD TAx4 FD is shown in Figure 2.14c. What was left was to turn on the FDs and achieve first light of a cosmic ray event with the new fluorescence telescopes.

#### **2.4.3 Deployment of the Surface Detector Expansion**

The new SDs for TAx4 were constructed in Japan, shipped to Delta, UT, and finished at the Lon and Mary Watson Cosmic Ray Center. The SDs were then placed at selected staging areas in the field. Given the restriction of the SDs being on US public land, the new SDs were flown by helicopter to their sites. A ground team assisted the helicopter in placing the roughly one-ton detector at the assigned GPS location and aligning the SD in a north-south direction for the solar panel to charge the internal battery. A picture of the detector being guided in is shown in Figure 2.15. 257 SDs (more than half of the proposed TAx4 SDs) were deployed in February and March of 2019. The SDs started recording data in the summer of 2019.

## 2.5 The TAx4 MD and BR Fluorescence Detectors

### 2.5.1 Fluorescence Telescope system

The telescope system of the FDs for the TAx4 are refurbished from the HiRes experiment. The telescopes collect fluorescence light from the excited nitrogen in the atmosphere onto a PMT cluster camera. The mirror is comprised of 4 spherical mirrors segments that together have a clover-leaf shape, which has a collection area of about  $5 \text{ m}^2$  as shown in Figure 2.16a. Light from the mirror is focused on a flat PMT 16x16 (256) hexagonal PMT cluster camera shown in Figure 2.16b. Like the BR and LR fluorescence telescopes, this forms a Schmidt Camera optical system with a flat focal plane. The reflectivity and curvature of the mirrors, the shadowing of the PMT cluster stand and shed doorway, the transmittance of the camera UV 300 - 420 nm passband filter, the spacing of between the PMTs, and the quantum efficiency of the PMTs are optical and system effects that need to be taken into account for accurately understanding the light produced by the EAS exciting the nitrogen.

### 2.5.2 Electronics and FADC Readout

The TAx4 readout system that converts the continuous analog signal from the PMTs to a discrete-time series digitized waveform is an FADC system. This system is the same type of system that is employed at BR and LR, but the exact electronics are different. The TAx4 FADCs are the electronics from the HiRes-II. The HiRes-II electronics were built to controls two telescopes from one rack, which stems from HiRes-II sheds housing two telescopes side by side while TAx4 is housed in connected bays. This system still is convenient as the electronics racks were placed in the wedges between the telescope bays and serve both bays cutting down on space needed for an electronics system for each telescope.

The electronics racks are shown front and back in Figure 2.17. The electronics racks are operated remotely with an operation software and server on the operations computer. The electronic racks, most importantly, provide, monitor, and control the HV and LV provided to the FADCs and the PMT clusters. The electronics rack also links to the CTD for clock counts and the operations PC that provides operational procedures from startup, calibration, DAQ, and shutdown scripts and saving the triggered data. The electronics racks also monitor the temperature and humidity within the rack and run a heat distribution system on top of the electronics rack to keep the electronics from overheating. The electronics racks also control the doors to open the telescopes to the night sky. There is a system of rain monitors on each PMT cluster that will trip in the presence of moisture. If the rain system trips, to protect the HV electronics, the electronics rack goes into an automatic shutdown procedure.

Within each electronics rack are two FADC racks, each FADC corresponding to a telescope. Each FADC rack has a *trigger-host board* monitoring 16 FADC boards. Each FADC board reads out and digitizes the signal of each PMT in a vertical column of the 16x16 PMT camera. Each FADC in the rack also performs a summation of the channels in the column. In addition, each FADC board also performs a summation of one of the rows in the PMT cluster. The row summation is done as each channel in a row is connected to a corresponding FADC board via a ribbon cable on the front of each FADC rack. These two summations are done twice with different gains: once with a high gain setting and again with a low gain setting for greater signal range in case of saturation in the high gain. Thus each FADC has 20 channels: the 16 PMT waveforms and the four summations. The FADC converts the 16 PMT signal channels in a column over a timescale of 100 ns (10 MHz sampling) and stores the output to an 820  $\mu$ s buffer called M1. The high gain row and column sums are used as the input for the triggering conditions. If the high gain sum is 12 ADC counts above the set pedestal value, the signal is discriminated to a high value, which is passed along to the trigger-host board via the backplane of the FADC rack. If this threshold value is not met, the signal is discriminated to a low value to the trigger-host board. This effectively passes a binary value along to the trigger board of if the condition is met or not. It is similar to the hit condition of the TA BR and LR PMTs but done on the row or column level. This allows for parallel pre-processing of the trigger reducing the burden on the trigger-host board.

### 2.5.3 Trigger

The TAx4 trigger condition for EAS tracks in the camera is the same as that for TALE. The trigger-host board at the end of the FADC rack contains four *programmable logic devices (PLDs)* and a *digital signal processor (DSP)* which scan the input trigger information from the row and column sums of the FADCs.

The primary trigger condition for TAx4 is finding a three-fold coincidence in the vertical or horizontal sums. Two of the PLDs handle this calculation, one for the 16 vertical sum channels and one for the 16 horizontal sum channels. The PLD scans across the channels in positional order to reconstruct channel position in the PMT cluster.

The PLD first looks for a two-fold coincidence between a high value in one channel and a high value in at least one of the next two sequential channels. This two-fold coincidence is performed using the boolean AND operation between the first channel and the boolean OR operation of the next two sequential channels. The two-fold coincidence is shown in the boolean equation for the  $i^{\text{th}}$  channel

$$\text{2Fold}_i = \text{Channel}_i \wedge (\text{Channel}_{i+1} \vee \text{Channel}_{i+2}) \quad (2.1)$$

where  $\wedge$  is the boolean AND operator, and  $\vee$  is the boolean OR operator. So if either of the two following channels and the first channel have a high trigger value from the FADCs pre-processing, a two-fold coincidence is found. The scan then proceeds to the next channels and performs the same logic operation.

The next level is a three-fold coincidence. This is performed using the values of the two-fold coincidence in the same manner as above. This is shown in the boolean equation

$$3\text{Fold}_i = 2\text{Fold}_i \wedge (2\text{Fold}_{i+1} \vee 2\text{Fold}_{i+2}). \quad (2.2)$$

This allows for a logical check of what should be a sufficiently long EAS track.

If the three-fold condition is met, the trigger host board issues a store command to the FADC boards, which dump M1 to another buffer called M2. The time window of the waveform from M1 that is dumped to M2 is  $2t_{coinc} + 10\mu\text{s}$  with a max of  $200\ \mu\text{s}$  where  $t_{coinc}$  is the time difference between the times in the three-fold coincidences. If the trigger condition is not met, the FADCs overwrite M1 with new data.

After a store command, the M2-waveform is scanned for a pulse above threshold. If a sufficient pulse is found, the time corresponding to the start and stop of the pulse, as well as the integral of the FADC waveform, are sent back to the trigger host board. If the FADC boards report a track-like series of pulses in space and time, a readout command is issued to the FADC boards to send the significant-pulse waveforms to be recorded.

However, this trigger system does not work well with events near vertical. These events might pass only one or two columns and not meet the three-fold coincidence described above. A horizontal track would have the same issue, but near-horizontal EASs are less likely to be observed, given the amount of atmosphere they would travel through.

A column thickener daughter board was added to the trigger board to counter this effect.<sup>[53]</sup> The column thickener board has two complex programmable logic devices (CPLDs) that widen the high values of a column into two columns. Each CPLD handles the modification one-half of the 16 column channel bits before the channels are processed by the column PLD for a three-fold coincidence. One CPLD handles the channels 0-7 but reads channel 8 (to allow crossover), and the other handles channels 8-15 plus channel 7. The CPLD on the column thickener is programmed with three modes that are set by two jumpers. The CPLD modes are :

**Straight Through:** The CPLD leaves the column values unchanged. This mode is set by two closed jumpers. The channels 0-7 are passed through as:

$$\text{Channel}_i^{\text{out}} = \text{Channel}_i^{\text{in}} \quad (2.3)$$

**Thicken All:** The CPLD thickens all high values columns. This mode is set by two open jumpers. The out channels 0-7 are thickened by in channels 0-8 (where 8 is the crossover channel) as:

$$\text{Channel}_i^{\text{out}} = \text{Channel}_i^{\text{in}} \vee \text{Channel}_{i+1}^{\text{in}} \quad (2.4)$$

with the special case for channel 1 to account for the edge:

$$\text{Channel}_1^{\text{out}} = \text{Channel}_0^{\text{in}} \vee \text{Channel}_1^{\text{in}} \vee \text{Channel}_2^{\text{in}} \quad (2.5)$$

**Hybrid:** The CPLD only thickens one high value channel if and only if the rest of the channels have low values. If there are more channels with high values, the channels are passed straight through. This mode is set with an open and closed jumper. The single high channel is thickened by :

$$\text{Channel}_i^{\text{out}} = \text{Channel}_{i+1}^{\text{out}} = \text{Channel}_i^{\text{in}} \quad (2.6)$$

with the special case for channel 1 to account for the edge:

$$\text{Channel}_1^{\text{out}} = \text{Channel}_0^{\text{out}} = \text{Channel}_1^{\text{in}} \quad (2.7)$$

else the channels are sent straight through as in Equation 2.3.

The CPLD that reads channels 8-15 inverts the order, so channel 15 is read as channel 0 and so on to apply the same logic described above. That way, both CPLDs run the same program. The column thickener is shown in Figure 2.18.

An intermirror trigger was set for the TAx4 FDs later in operation. The data used in further analysis in this dissertation does not contain this data; thus, the intermirror trigger will not be discussed in detail.

#### 2.5.4 Calibration

For purposes of calibration, a UV LED was placed at the center of the segmented mirror pointing at the camera is. The UV LED is pulsed to calibrate the signal read out of the PMTs and FADC signal conversion<sup>[54]</sup>. The UV LED photons are passed through a diffuser before hitting the camera. Using photon statistics which models the flux of photons produced by the source hitting the camera, the variable gain amplifier attached to the PMT is adjusted so that all the FADC channels have a nominal gain of one photoelectron to one ADC count. This UVLED calibration is done once at the beginning of the night and once at the end to record the drift of the gain balance.

## 2.6 TAx4 First Light

To illustrate the operational status of the TAx4 FD, *first light* of a cosmic ray event for both station expansions has been achieved.

### 2.6.1 TAx4 MD FD First Light

The first light of the MD expansion was achieved on February 16<sup>th</sup>, 2018. The FD was run for about 2 hours that night. A good cosmic ray event is shown in Figure 2.19 with an extended track on a time scale over about 5  $\mu\text{s}$ . TAx4 MD began full operation and collecting data in the summer of 2018. This data was used for a preliminary spectrum to confirm that the new FD was working and observing cosmic ray events properly. This will be discussed further in Chapter 6.

### 2.6.2 TAx4 BR FD First Light

The first light for the BR expansion was achieved on October 22<sup>nd</sup>, 2019. The FD was again run for about 2 hours that night. A good cosmic ray event is shown in Figure 2.20 with an extended track on a time scale over about 10  $\mu\text{s}$ . TAx4 BR FD is not collecting good data yet as the remote operations procedures are being worked out.

## 2.7 MD TAx4 Operation Epochs

TAx4 MD FD is split into three distinct time periods, called a *epoch*, due to upgrades to the hardware and software in the triggering mechanism. These distinct epochs are important as they affect the amount of data collected and change the analysis reconstruction and how the simulated events need to be handled. The different epochs are:

**Epoch 0 (2018/06/08 - 2019/04/09):** The initial TAx4 MD FD epoch since the FD became fully operational and started collecting data every night.

**Epoch I (2019/04/24 - 2019/06/08):** The column thickener daughter board was added to the trigger-host board for each telescope. The column thickener was set to the thicken all mode. The trigger rate of the telescopes increased.

**Epoch II (2019/06/25 - Present):** The current TAx4 FD epoch. The intermirror trigger was enabled in the TAx4 operations software. The trigger rate of the telescopes increased further.

For this dissertation, only data from epochs 0, and I were analyzed further.

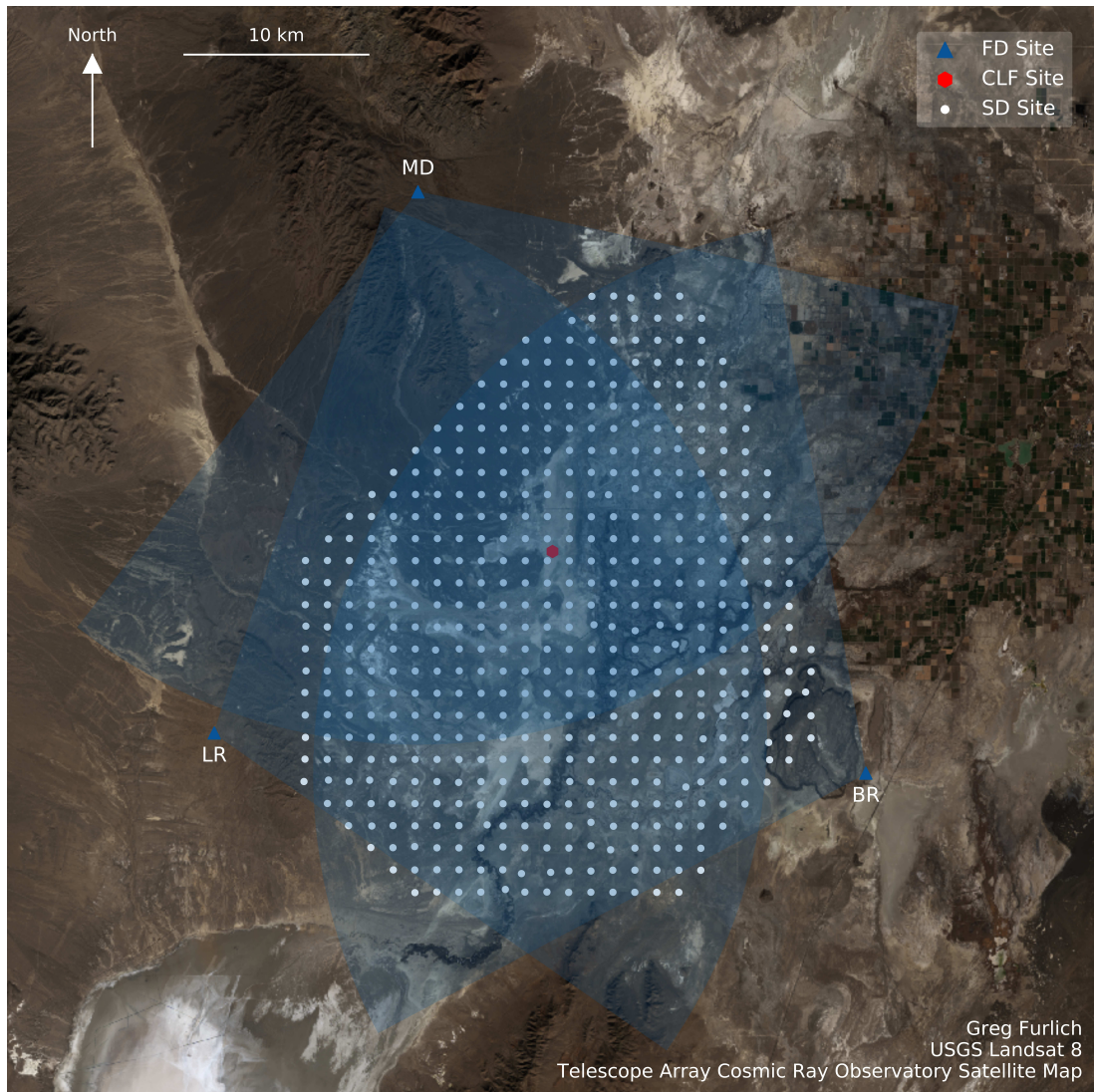


**Figure 2.1:** Satellite map of the Telescope Array Cosmic Ray Observatory with an overlay marking the FD stations with a 30 km FOV ring in blue, the SD array in white, and the CLF in red. Centered roughly around  $112.9^\circ$  W,  $39.3^\circ$  N.

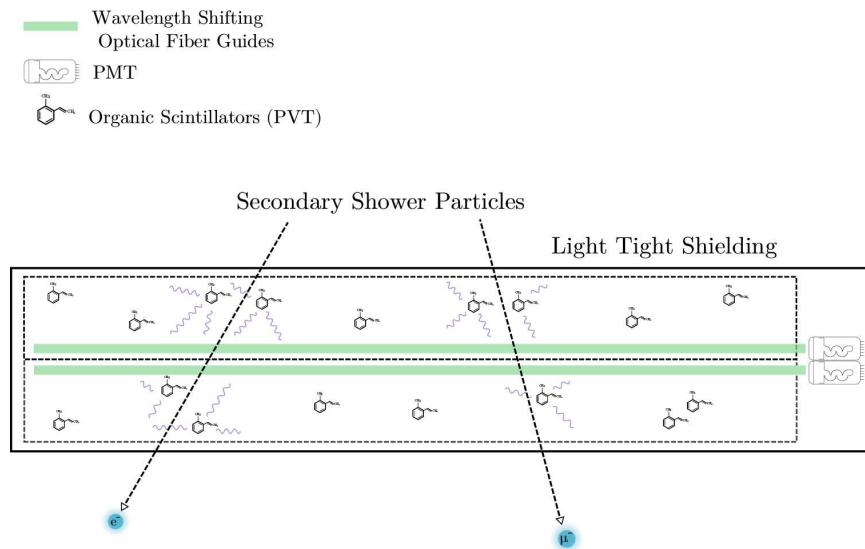


**Figure 2.2:** The inside of a surface detector (SD) with secondary particles generated in the EAS passing through the organic scintillation material which emits light.



**Figure 2.3:** A surface detector in the field.

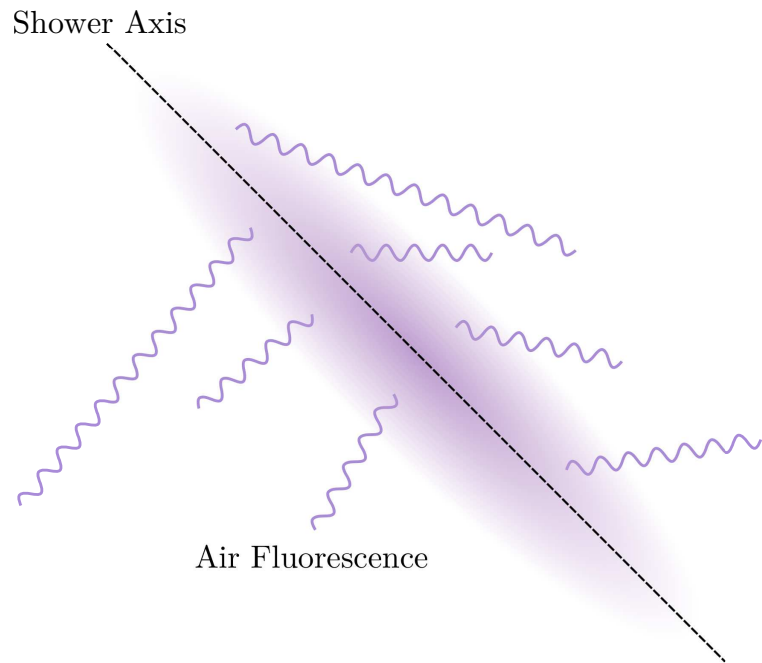


**Figure 2.4:** The EAS generated by the cosmic ray excites air molecules along its path which emit light.

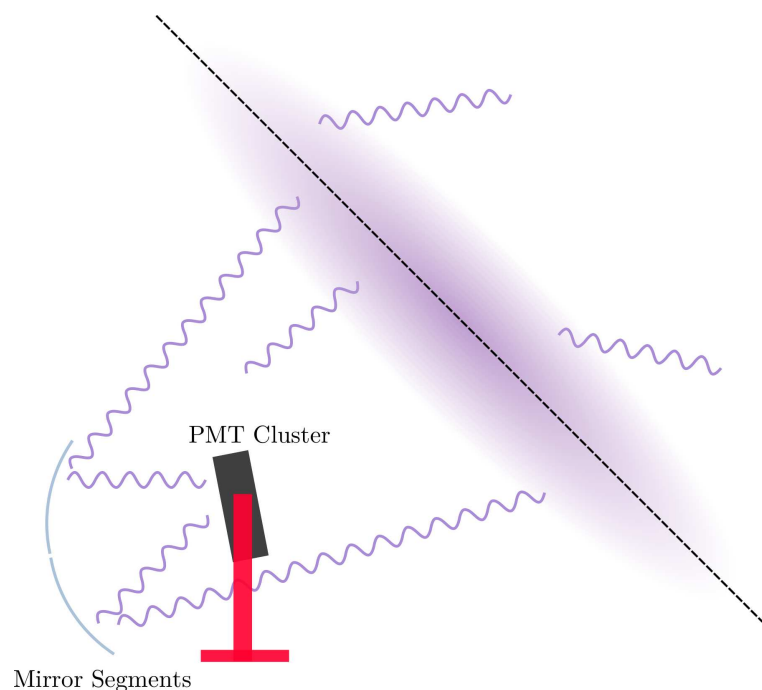


**Figure 2.5:** Fluorescence light from the excited air collected onto a camera.

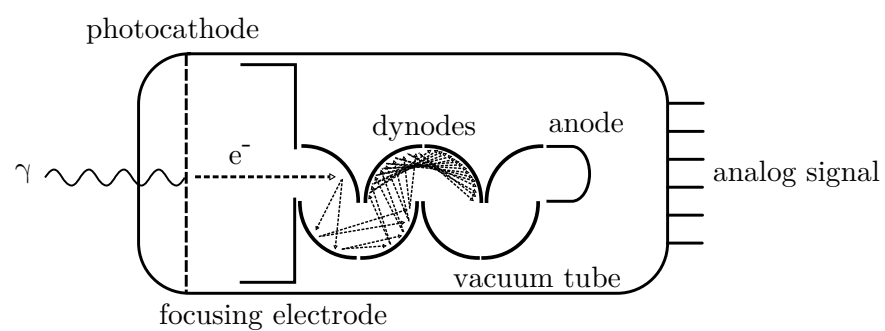
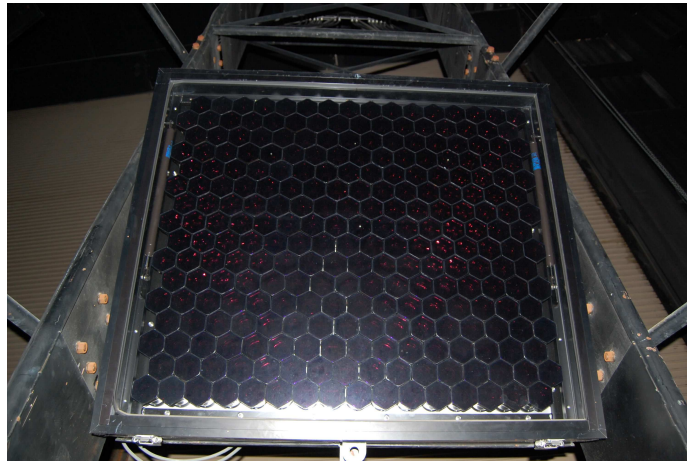


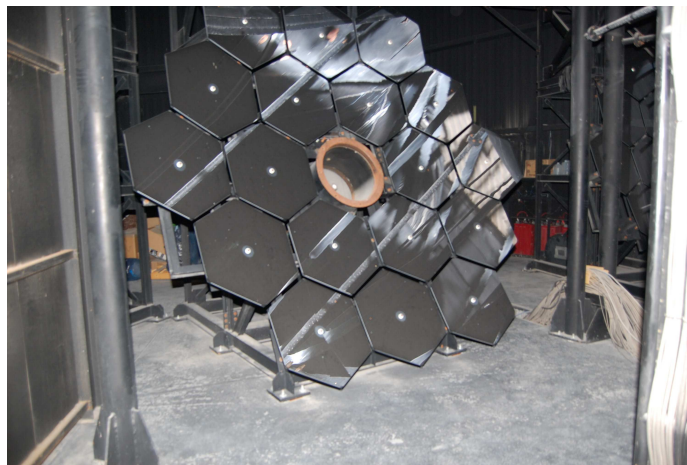
**Figure 2.6:** Basic photomultiplier tube schematic.



**(a)** The BR FD from the outside. The TA-EUSO<sup>[55]</sup> shed in the foreground. The Shed housed a the JEM-EUSO FD prototype for joint analysis of FD events between the TA and EUSO FDs. The TAx4 BR fluorescence telescope sheds are behind the BR FD on the left.

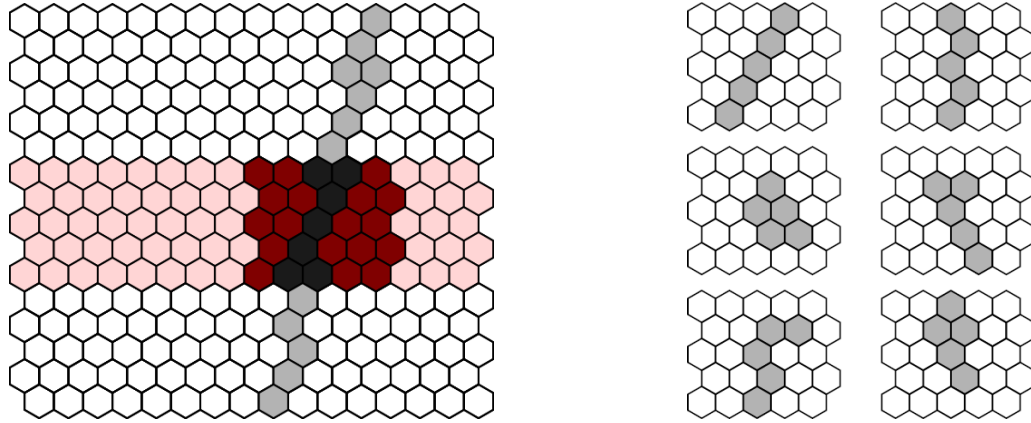


**(b)** A BR FD 16x16 hexagonal PMT camera.



**(c)** A BR FD segmented mirror. The Xenon Flasher is in the center of the segments.

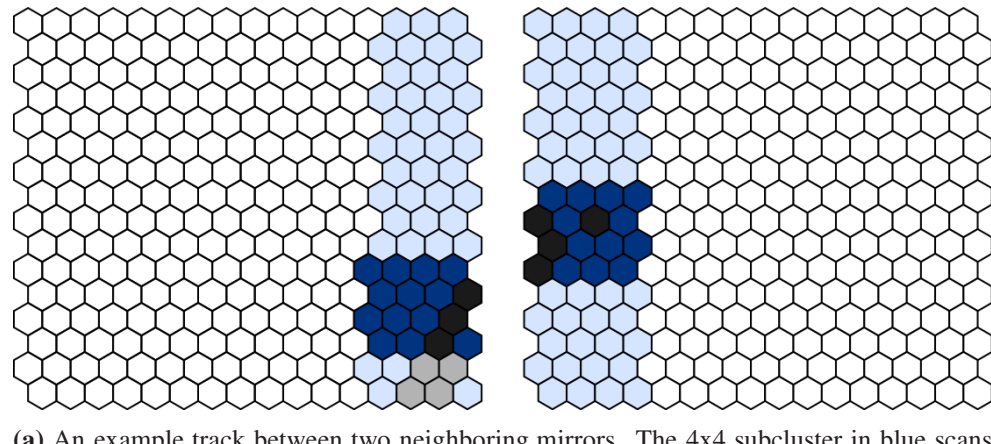
**Figure 2.7:** Pictures of the inside and outside of the BR FD station.



**(a)** An example EAS track with hit PMTs darkened in the 16x16 camera cluster. The 5x5 subcluster, in red, scans across the camera cluster looking for a track pattern.

**(b)** Example track patterns the TF will recognize of a 5 contiguous PMT track.

**Figure 2.8:** Trigger code 1 example and a subset of the possible track patterns found in the 5x5 subcluster.



**(a)** An example track between two neighboring mirrors. The 4x4 subcluster in blue scans across the 16x16 camera cluster edge in neighboring telescopes looking for a 3 contiguous PMT track pattern to allow for an intermirror trigger.

**(b)** Example track patterns the TF will recognize on the edge.

**Figure 2.9:** Intermirror trigger code 2 example and a subset of the possible track patterns found in the 4x4 subcluster along the camera edge.

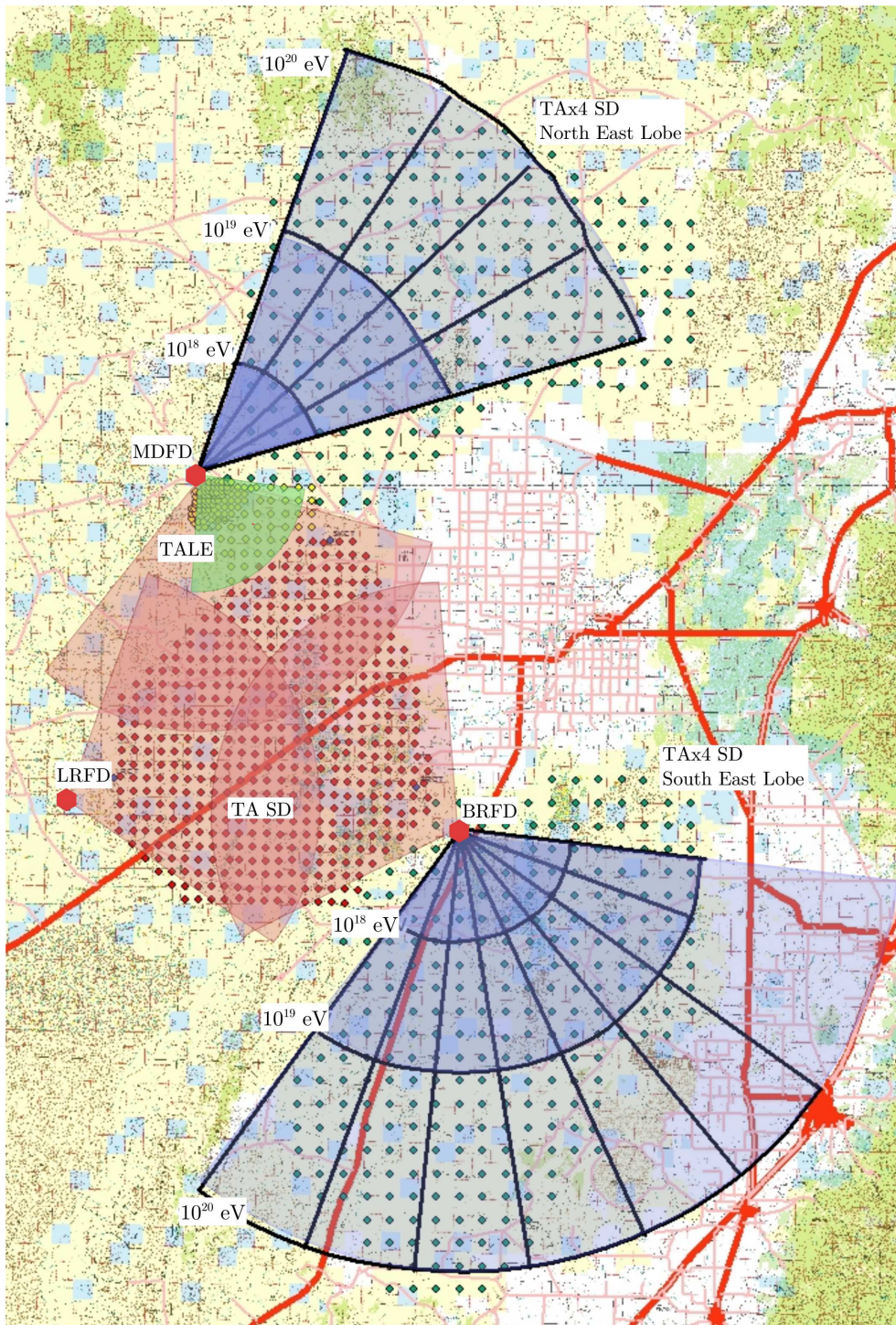


**Figure 2.10:** Political map of Telescope Array cosmic ray observatory expansion. TAx4 SD sites are green dots, TA sites in red, and TALE sites in yellow. Reproduced and adapted with permission from Robert Cady. Adaptions to this map include labels to the sites and shaded approximate FOV arcs:  $\approx 10$ ,  $20$ , and  $30$  km for the TAx4 FD sites in blue,  $\approx 20$  km for the existing TA sites (BR, LR & MD) in red, and  $\approx 10$  km for TALE site in green.<sup>[56]</sup>

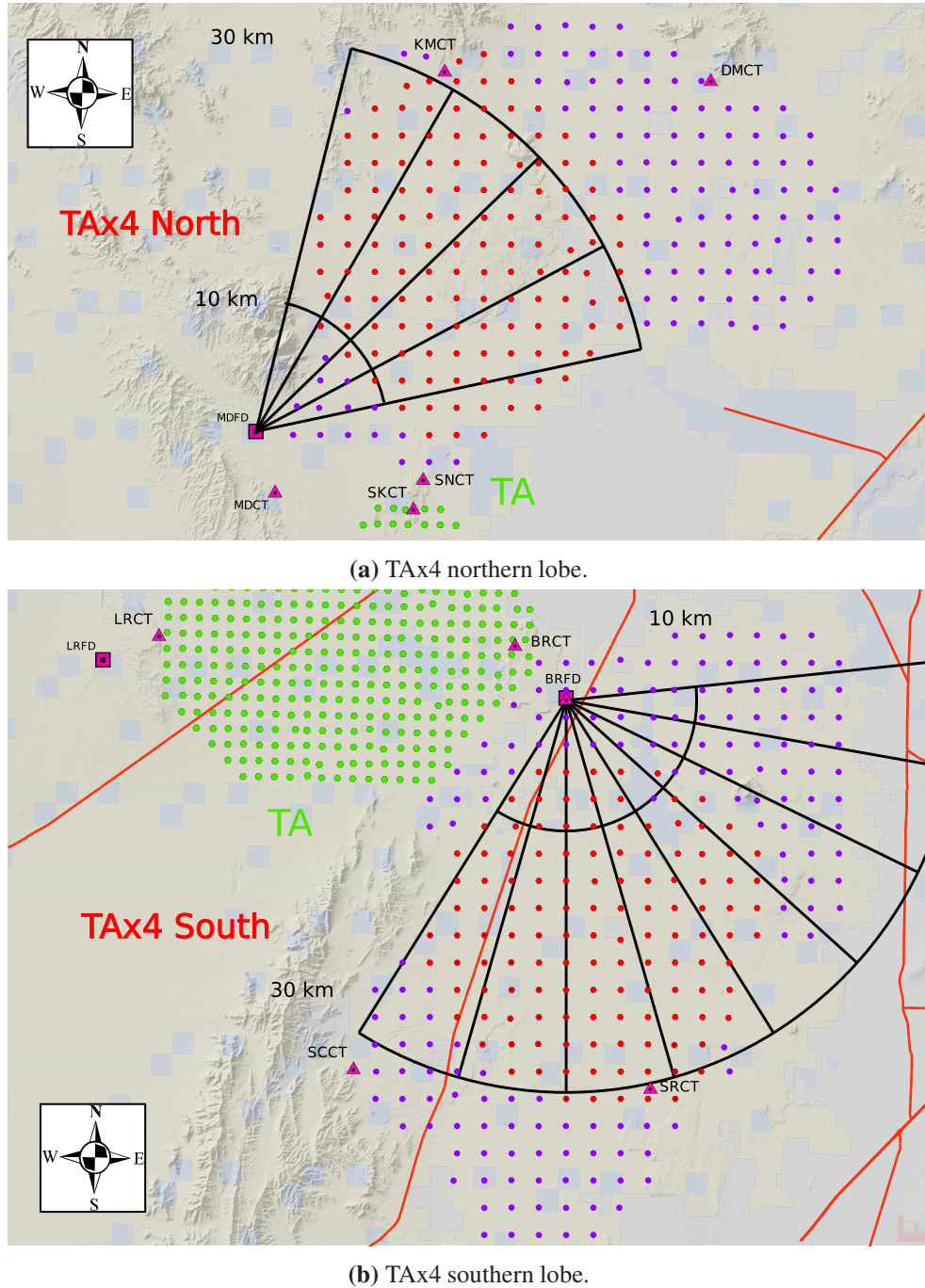
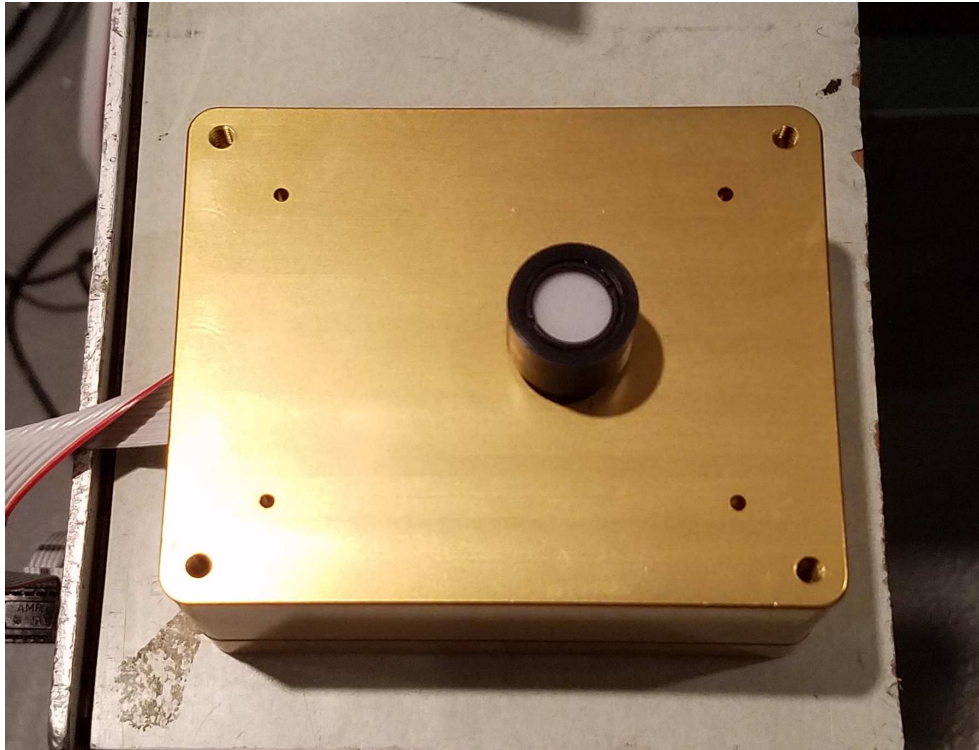


**Figure 2.11:** Political map of the two Telescope Array cosmic ray observatory expansion lobes. TA SD sites are green dots, TAx4 deployed sites in red, and TAx4 planned SD sites in purple. Radio WLAN antenna sites in pink triangles, FD sites in pink squares. The approximate FOV of the TAx4 FD sites with arcs to 10 and 30 km. Reproduced and adapted with permission from Stan Thomas. Adoptions to this map include cropping original map, removing the TALE array and moving labels.<sup>[57]</sup>



(a) A UV LED flasher that is pulsed to emit UV photons to test the response of the PMTs and FADC electronics.



(b) Example real time display of testing the PMT cluster or FADC electronics. A wooden cutout was made by Stan Thomas to spell TAX4 in the PMT pixels when placed in front of the pixels and tested in the UVLED gain balancing.

**Figure 2.12:** The HiRes PMT clusters and refurbished FADC electronic racks were tested with a UVLED gain balance to check the connections and performance.



(a) The MD FD Station with the MD TA, TALE, and MD TAX4 telescope bays.



(b) The BR FD Station with the BR TA, and BR TAX4 telescope bays.

**Figure 2.13:** Overhead image of the TAX4 FD station expansions. Reprinted and adapted with permission from Stan Thomas. Adapted by adding labels to each FD at a station.



(a) Installing a HiRes PMT cluster for MD TAx4 FD. Reprinted with permission of J.N. Matthews and Telescope Array.



(b) Wiring the PMT cluster to the refurbished HiRes FADC electronics. Reprinted with permission of J.N. Matthews and Telescope Array.



(c) The MD TAx4 FD 4 telescopes expansion at the MD FD stations.

**Figure 2.14:** Deployment of MD TAx4 FD.



**Figure 2.15:** Deployment of a TAx4 SD by helicopter. The author is pictured guiding the helicopter in to the GPS location of the SD site. Photos taken by ICRR PR Office in February, 2019.<sup>[58]</sup>

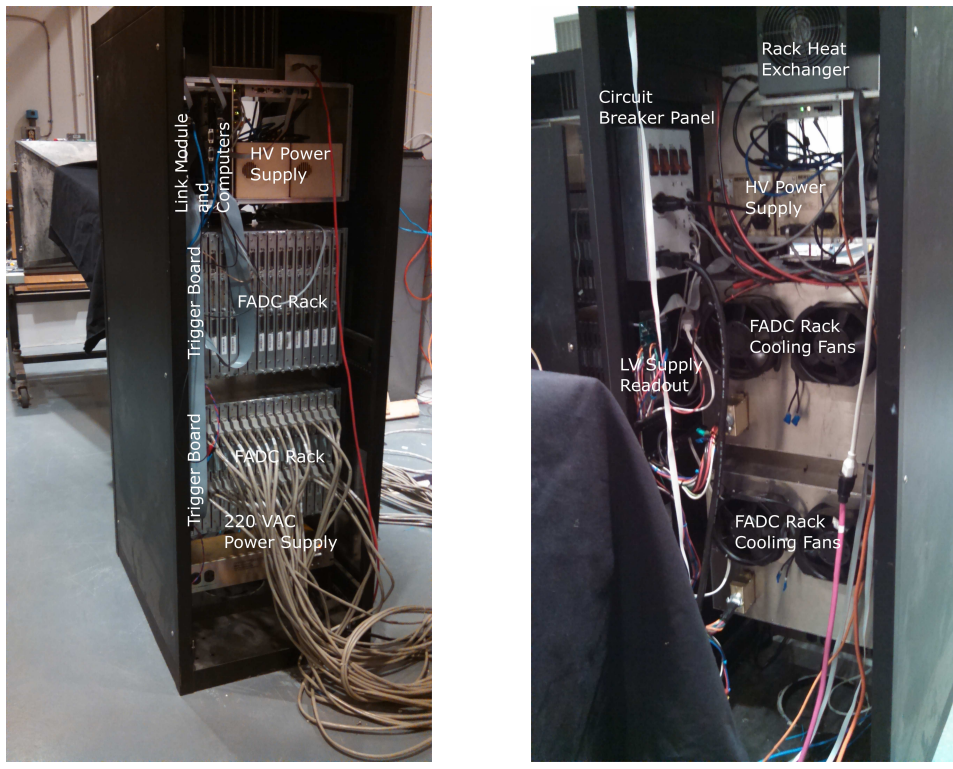


(a) Mirror comprised of 4 segments.



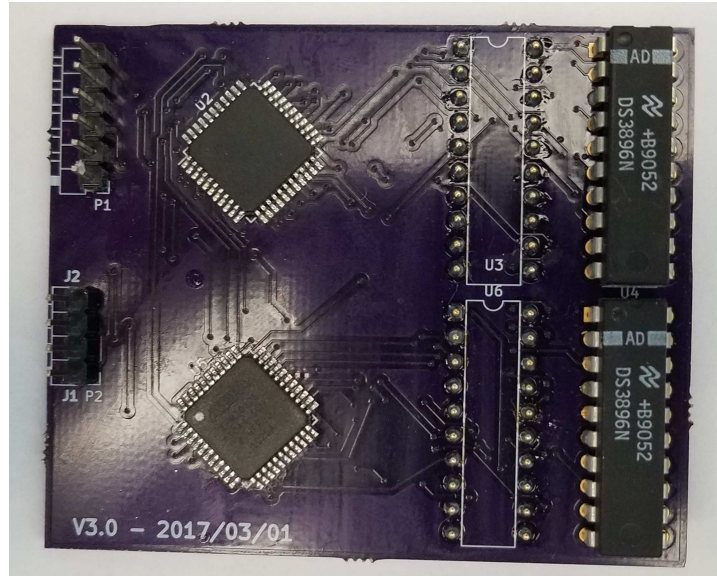
(b) 16x16 PMT cluster camera with a UV pass-band filter cover.

**Figure 2.16:** TAx4 fluorescence telescopes with the mirror collecting the fluorescence light from the atmosphere onto a 16x16 PMT cluster camera.



(a) Front side.

(b) Back side.

**Figure 2.17:** TAx4 refurbished HiRes-II FADC electronic rack.**Figure 2.18:** The TAx4 FD trigger daughter board to recover near vertical EAS tracks. P1 is the connectors for programming the daughter board. P2 is the connects for the jumpers which set the mode.

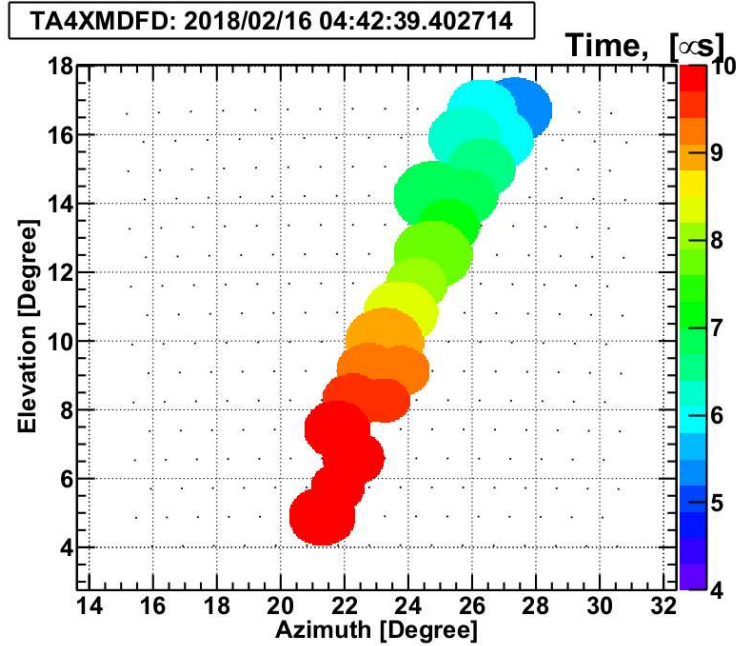


**Figure 2.19:** TA4 MD FD first light. The figure shows the EAS track through a camera. The black dots indicate the pointing direction of each PMT on the night sky. The filled circles represent the signal received by each PMT with their size. The timing of each tube is represented with the circle's color.

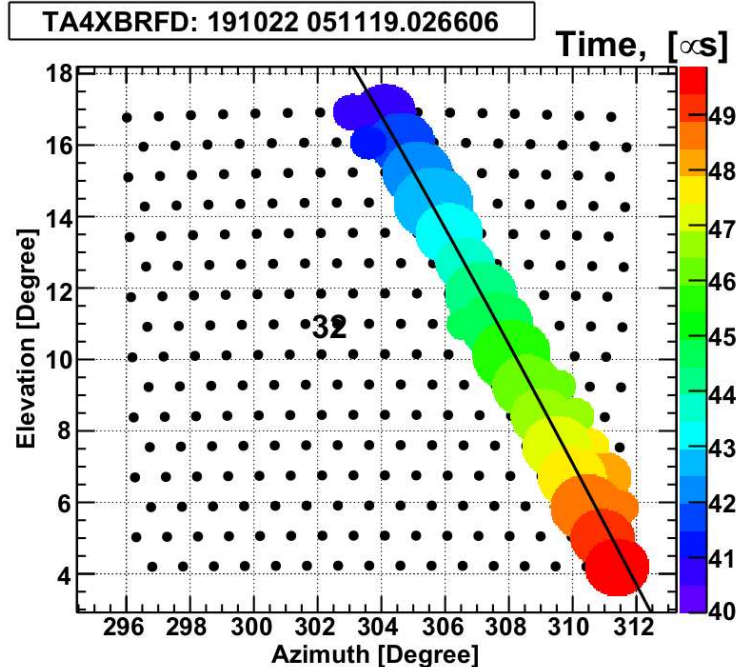


**Figure 2.20:** TA4 BR FD first light. The figure shows the EAS track through a camera. The black dots indicate the pointing direction of each PMT on the night sky. The filled circles represent the signal received by each PMT with their size. The timing of each tube is represented by the circle's color. The fitted shower detector profile, discussed in Chapter 3, is the solid black line.

# CHAPTER 3

## MONOCULAR RECONSTRUCTION OF COSMIC RAY FD EVENTS

Reconstructions scripts are run on the data to calculate important parameters of the EAS as it develops in the atmosphere to understand the FD cosmic ray events. The event reconstruction is typically staged with different scripts that handle different parts of the reconstruction. Some of these scripts handle cutting out events based on their qualities. Events are cut to reduce noise, or airplane flashers, atmospheric fluctuations, or muons passing through the PMT cluster that made it past the trigger of the detector or to cut events that are in a regime where the reconstruction of the event leads to huge uncertainties. Hence, the event is no longer considered for further analysis.

For this dissertation, events were reconstructed with only one FD station observing the cosmic ray event. This is called reconstruction in *monocular mode*, or shortened to *mono*, versus *stereo mode* where two FDs observe an event or *hybrid mode* where both a FD and a cluster of SDs observe the events. For this dissertation, two different sets of reconstruction scripts are covered, given the two different sets of FDs, the BR and LR FDs and the TAx4 MD FD. The reconstruction of TAx4 FD events is based on the same scripts of the TALE and MD FDs, which are traced back to the HiRes analysis.

### 3.1 DST Files

To store the data for analysis, TA utilizes a custom file type called *Data Storage Tapes (DSTs)*. The name goes back to the HiRes experiment, where the data was stored on magnetic tapes. A DST file contains a sequential list of *events*. Each event in the DST file stores information in *banks* which contain different elements or structures of information. Typically in the reconstruction scripts, a DST file is read in event by event, and given the information in the banks, new banks are generated from new reconstructed information. The existing DST file is copied to a new DST file with the addition of the new banks. This copying of old DST banks can cause DST files can become quite large after reconstruction.

TA has defined the structures of many DST banks over the past 11 years of operation. Some of these banks also store information for generating Monte Carlo Simulations, or information about the

weather, detector geometry, or calibration information. Banks used for the BR and LR FD analysis are in Table 3.1, while banks used for the TAx4 FD analysis are in Table 3.2. The different detectors use different DST banks depending on the detector type and electronics and the reconstruction scripts used.

## 3.2 Data Collection

On clear, moonless nights, the FD stations are operated to collect EAS events. The run lasts from astronomical dusk to astronomical dawn when the sun is  $18^\circ$  below the horizon, and the moon is below the horizon. This run period allows for optimal viewing of the night sky for the photo-sensitive PMTs not to be completely saturated or to breakdown. Because of LR’s remote location with respect to Delta, UT, LR is shut down an hour earlier than BR. This early shutdown is in case there is a shutdown issue with LR, the remote operators in Delta have enough time to make it to LR, which faces east towards the sunrise, and cover the mirrors before the sun’s rays could damage anything. TAx4 FD is currently operated by people onsite at the MD station. There are plans to run TAx4 BR remotely from the MD station.

The FDs store data from the DAQ buffer in a data file or *part*. The DAQ is stopped every so often to dump the data to storage before it resumes again. BR and LR write data to a part every 1000 triggers of the FDs, which can cause the data parts to be over variable duration given the night’s conditions, which can increase or decrease the trigger rate. Since TAx4 uses a similar operation script as TALE, TAx4 writes data to a part every 20 minutes of operation. Summing over the start and stop of these data parts allows for the calculation of the FDs *ontime*, which becomes important in calculating a cosmic ray energy spectrum as done in Chapters 6 and 7.

## 3.3 Intermirror Timing

The first step in the event reconstruction is converting the raw FADC waveforms into a DST file. For BR and LR FDs, this is handled by the TAMA (TA MAtching) program. For TAx4, this is handled by the TLFDP0 program.

### 3.3.1 BR and LR TAMA

BR and LR FDs each generate about 500 GB of data a month, more even in the winter when the nights get much longer. The data size is due to the trigger system reading out the waveforms for every PMT at a station for each trigger. BR and LR trigger approximately two times a second. The data size is greatly reduced after the conversion of the raw data to the DST format. TAMA first finds the cameras with tracks given the trigger codes. Next, TAMA reduces the data further by only keeping hit PMTs and rejecting noise PMTs. A hit PMT has is defined with a value that is  $3\sigma$  above

the background within 16 or 32 FADC samples of the waveform. This determination of the hit PMT is different from the trigger hit PMT discussed in Chapter 2. The PMT significance in TAMA is determined by

$$\sigma = \max \left( \frac{S_i - wBG_{\text{mean}}}{\sqrt{wBG_{\text{var}}}} \right), \quad S_i = \sum_{k=i}^{i+w} \text{FADC Count}_k \quad (3.1)$$

where  $BG_{\text{mean}}$  and  $BG_{\text{var}}$  are the FADC background mean and variance levels respectively,  $S_i$  is the summation over the FADC waveform over a sample bin size  $w$ . The index of  $S_i$  is increased by half of the sample bin size,  $w/2$  for each step of the summation. This method is an effective way to cut out noise within the trigger. TAMA reduces the data by about 90% of the raw data.

### 3.3.2 TAx4 TLFDP0

TAx4 has a reduced data size given the trigger pre-processing done by the electronics. TAx4 data is about .5 - 2 GB a night. TLFDP0 also searches for time matched FADC pulses between mirrors in a window of  $100 \mu\text{s}$  to group intermirror events. TLFDP0 stands for TALE FD Pass 0, but the program is used for TAx4, given their FADC electronics are identical.

## 3.4 Geometry Reconstruction

Once the event has been converted from the raw data and the good PMTs in the events are found, the next step is to determine the geometry of the EAS track. This is done for both TA FADC and TAx4 FDs by finding the *shower detector plane (SDP)* which is the plane defined by the EAS track at the point of the detector. The SDP is determined by minimizing the function

$$\chi^2 = \sum_{i=1}^{N_{\text{good}}} (\hat{n} \cdot \hat{v}_i)^2 N_{\text{pe},i} \quad (3.2)$$

to determine the best normal vector of the SDP,  $\hat{n}$ . This is calculated using the known pointing direction of all the hit PMTs for the event,  $\hat{v}_i$  weighted by the amount of photoelectrons,  $N_{\text{pe},i}$ , each hit PMT produces.

Within the SDP, the direction of the shower core in the SDP is determined by the timing fit of the good PMTs with the function

$$t_i = t_o + \frac{R_p}{c} \tan \left( \frac{\pi - \psi - \alpha_i}{2} \right) \quad (3.3)$$

where  $R_p$  is the impact parameter,  $\psi$  is the inclination angle between the shower core and the detector, and  $t_i$ ,  $\alpha_i$  are the respective best fit trigger time and pointing direction of each PMT in the event. These parameters are illustrated in Figure 3.1.

### 3.4.1 BR and LR FDPlane

BR and LR use the `FDPlane` program to fit the event geometry. `FDPlane` first determines the SDP by minimizing Equation 3.2, then determines the shower geometry by fitting Equation 3.3. To assist with good initial fit values of  $R_p$  in the fit minimization, `FDPlane` first computes a linear fit of the PMTs to make sure the event moves down with appropriate speed, then a pseudo-tangent fit where  $\psi = \pi/2$ , before finally fitting with Equation 3.3. `FDPlane` assigns an event a direction of either the event being noise, upward going, or downward going. Only the downward going events are kept for further analysis.

### 3.4.2 TAx4 STPS2, STPLN, and STGEO

Before TAx4 can determine the geometry, because of the design of the trigger, noise-like events with a strong signal, such as airplane flashers as they fly by, can be found. A Rayleigh filter in the `STPS2` program is used to distinguish these events from track-like events. This filter determines whether an event appears track-like with direction by the probability it is not a random walk. The Rayleigh probability density function for a random walk over a total displacement of  $r$  is

$$p(r) = \frac{r}{\sigma^2} \exp\left(-\frac{r^2}{2\sigma^2}\right). \quad (3.4)$$

For a random walk over  $N$  steps,  $\sigma^2 = N/2$ . To get the probability of a net displacement greater than observed displacement  $R$  is

$$\text{Prob}(r > R) = \int_R^\infty p(r)dr = \exp\left(-\frac{R^2}{N^2}\right). \quad (3.5)$$

A convenient way of expressing Equation 3.5 is the negative  $\log_{10}$  probability

$$P_{\log_{10}} = \frac{R^2}{N \ln(10)}. \quad (3.6)$$

With a  $P_{\log_{10}} = 2$ , there is a 1% chance a that a random walk over  $N$  steps would have a displacement of  $R$ . This is an effective filter for dropping non-track-like triggers.

The next step in TAx4 FD event reconstruction is determining the SDP with the `STPLN` program. The SDP is calculated with the same method used for the BR and LR FDs with minimizing Equation 3.2. The last step in the geometry reconstruction for TAx4 FD is in the `STGEO` program. `STGEO` determines the geometry using the same method as BR and LR FD geometry reconstruction, which is done minimizing Equation 3.3.

### 3.5 Calorimetric Energy Reconstruction

The next step in the monocular event reconstruction is the calorimetric energy which is the energy that the EAS deposited in the atmosphere. As discussed in Chapter 1, the profile charged particles generated with respect to the slant depth  $X$  can be described by the Gaisser-Hillas function

$$N_{\text{ch}}(X) = N_{\text{max}} \left( \frac{X - X_0}{X_{\text{max}} - X_0} \right)^{\frac{X_{\text{max}} - X_0}{\lambda}} \exp \left( \frac{X_{\text{max}} - X}{\lambda} \right).$$

The energy deposited in the atmosphere by the ionizing particles in the EAS is then determined with

$$\frac{dE_{\text{dep}}(X)}{dX} = \alpha(X)_{\text{eff}} N_{\text{ch}}(X).$$

where  $\alpha$  is the mean ionization loss rate of the particles in the EAS. The value of  $\alpha$  is in Section 1.7. Thus integrating over the above equation yields the calorimetric energy

$$E_{\text{cal}} = \int_{X_0}^{\infty} \frac{dE_{\text{dep}}(X)}{dX} dX. \quad (3.7)$$

In order to determine a good shower profile, accounting for the calibration of the electronics, and the effects on the light propagation in the atmosphere and around the detector, the light along the EAS track, given the reconstructed geometry, was binned according to the light received by each PMT. This binned profile is then compared to a light profile created by simulated cosmic ray EAS events with a known Gaisser-Hillas profile and energy. These simulated events are sometimes referred to as *thrown events*, given the action of generating them with a random direction out over the detector array. This profile is an *inverse Monte Carlo (IMC)* method, which compares an observed event to the best simulated event to determine the characteristics of the shower profile. To determine the best simulated shower, the following equation is minimized

$$\chi^2 = \sum_{i=1}^{N_{\text{Good PMTs}}} \frac{(S_i^{\text{Observed}} - S_i^{\text{Simulated}})^2}{\sigma_i^2}. \quad (3.8)$$

Equation 3.8 compares over all hit PMTs the difference in the amount of light received from the observed data in  $S_i^{\text{Observed}}$  to the simulated data in  $S_i^{\text{Simulated}}$ , divided by the variance in  $\sigma_i^2$ .

Given the determined shower profile of charged particles created by the EAS, the energy deposition of these ionizing particles is calculated by Equation 1.49. Lastly, integrating over this profile, accounting for the mean ionization loss, the calorimetric energy is reconstructed via Equation 3.7.

#### 3.5.1 BR and LR FDTubeProfile

Using the above process, BR and LR use the program `FDTubeProfile` to calculate the calorimetric energy.

### 3.5.2 TAx4 STPF12

For this dissertation, given that a preliminary spectrum as a proof-of-concept of the new TAx4 detector working condition, default calibration was used in the event reconstruction. Follow up analyses will need to incorporate more rigorous calibration methods. TAx4 FD uses the STPF12 program for the inverse Monte Carlo method of fitting the profile and then reconstructing the calorimetric energy.

## 3.6 Missing Energy Correction

The initial energy of the cosmic ray primary,  $E_0$ , can be determined from the calorimetric energy,  $E_{\text{cal}}$ , by accounting for the missing energy that does not get deposited in the atmosphere. As discussed in Chapter 1, the EAS develops a muonic component comprised of relativistic muons and neutrinos that continue to propagate undisturbed through the atmosphere. As shown by the Heitler-Matthews model, the number of charged pions that decay to muons and neutrinos is energy dependent. This missing component can account for up to 10% of the energy. To estimate the missing energy as a function of the energy that is deposited into the atmosphere, we turn to simulations of cosmic ray induced EAS. CORSIKA<sup>[59]</sup> is a program for simulating the particles generated in an EAS using *hadronic interaction models* such as EPOS, QGSJET, or SYBILL. Using many CORSIKA simulated EAS over a range of primary cosmic ray particle types and energy, by tracking the muonic component of the shower, a function for determining the missing energy of the shower can be developed.

For both FDs, for the missing energy correction, we apply the same energy correction as the TA FADC FD 3.5 year monocular spectrum<sup>[60,61]</sup>

$$\frac{E_{\text{cal}}}{E_0} = -0.5717 + 0.1416 \log_{10}(E_{\text{cal}}/\text{eV}) - 0.003328 \log_{10}(E_{\text{cal}}/\text{eV})^2. \quad (3.9)$$

This correction assumes a protonic primary, which for the further analysis in this dissertation is a good assumption<sup>[62]</sup>, since we mainly consider UHECRs with  $E > 10^{18}$  eV. The energy correction is plotted in Figure 3.2.

## 3.7 Data Selection and Quality Cuts

*Quality cuts*, also called selection cuts, are applied to eliminate events that do not reconstruct well and increase the quality of the data used in further analyses. These cuts are applied based on specific parameters in the event timing, geometry, or profile reconstruction. These cuts were developed to eliminate noncosmic ray events that passed the trigger or events which have parameters that make their energy estimate unreliable. However, there is a trade-off to these cuts as loose cuts allow for more events, but these events might have characteristics that skew the data in an

undesirable way. At the same time, severe cuts remove too many events so that the statistics limit further analysis greatly.

### 3.7.1 BR and LR FD Event Selection and Quality Cuts

For BR and LR, we applied the following quality cuts<sup>[60]</sup> to the geometry in Table 3.3 and profile in Table 3.4 of the cosmic ray event. These cuts were applied to the events using the programs `FilterFDPlane` and `FilterFDTubeProfile`.

### 3.7.2 TAx4 FD Event Selection and Quality Cuts

For the TAx4, we applied the quality cuts from HiRes I, which was also a one ring FD<sup>[63]</sup>. The quality cuts applied are in Table 3.5. These were either applied in the event reconstruction scripts above or after the events were fully reconstructed.

## 3.8 Python Processing Pipelines and Pandas DataFrames

Given the extensive amount of data from 10 years of operation for the BR and LR site, a pipeline using the reconstruction scripts above was created in `python`<sup>[64]</sup>. The process flow first found all nights of operation, found each FD data part per night, and then processed each part with the reconstruction scripts. This pipeline also tracked the metadata of events that got cut at certain stages. After the reconstruction of each data part, the `DST` files were converted into an aggregated database to increase the efficiency of the data analysis. Using `TDSTio`<sup>[65]</sup>, the events were converted from a `DST` file to `ROOT`<sup>[66]</sup> `TTree` structures which were then converted in `python` to a Pandas DataFrame. Pandas DataFrames are an indexed tabulated data structure optimized for querying and manipulation. The event database was stored in a Hierarchical Data Format (HDF)<sup>[67]</sup> file. Databases of weather information, night operation information, and FD data part information were also created to further the analysis.

Even though TAx4 had a small amount of data, for ease of processing, a `python` pipeline was again created using the TAx4 reconstruction scripts.

## 3.9 Distance to Shower Max, $R_{X_{\max}}$

Parts of this section follow from work presented at the ICRC 2019.<sup>[68]</sup>.

To better understand the response of the FDs to an event, we introduce a new parameter,  $R_{X_{\max}}$ . This parameter is the distance from the FD to the shower's maximum development,  $X_{\max}$ , along the shower core, as shown in Figure 3.3. Figure 3.3 also illustrates the difference between  $R_{X_{\max}}$  vs.  $R_p$ , which is a construct of the geometry reconstruction and not connected the development of the EAS.

To calculate  $R_{X_{\max}}$  we used the equation

$$h(X_{\max}, \theta_{\text{zen}}, h_o) = X^{-1}[X_{\text{top}} - X_{\max} \cos(\theta_{\text{zen}})] - h_o \quad (3.10)$$

where

$$X_{\text{top}} = 1033.223645 \text{ g/cm}^2, \quad (3.11)$$

$X^{-1}$  is the inverse function from slant depth to height calculated numerically using the density of the atmosphere from the US Standard Atmosphere 1976<sup>[69]</sup> discussed in Appendix A,  $\theta_{\text{zen}}$  is the zenith angle of the shower core,  $h_o$  is the FD site's ground level altitude above sea level. Using the azimuth angle and ground impact location of the shower core, the  $x$  and  $y$  projection of  $X_{\max}$  can be determined and then the radial distance between the detector site and  $X_{\max}$  to get  $R_{X_{\max}}$ .

Figure 3.4 displays how the height above the CLF varies with the observed  $X_{\max}$  and the zenith angle of the shower core. It illustrates the interesting regions where the model fails to account for the ground material as the shower path exits the atmosphere.

### 3.10 TAx4 MD FD Reconstructed Good Event

A TAx4 MD FD event that reconstructed well is shown in Figure 3.5. The intermirror EAS track is shown in Figure 3.5a. The pointing direction of the PMTs are the black dots. Hit PMTs' signal size is expressed by the size of the circle and the timing of the PMT by the circle's color. The SDP fit to the EAS track through the mirrors is the black line. The geometry reconstruction for the timing fit of  $\psi$  and  $R_p$  is shown in Figure 3.5b. The black lines are the hit PMTs' time and the angle along the fitted SDP. The red line is the best timing fit with the parameters in the upper right of the figure. The calorimetric energy reconstruction by fitting the event photoelectron flux profile is shown in Figure 3.5c. Each hit PMT is represented by a black point corresponding to the tube's photoelectron flux and the tube's viewing of the EAS development in slant depth. The important profile fit parameters are in the upper right. The profile matches the PMTs with less error in their signal, making it a good fit. This event represents a well reconstructed event for TAx4 MD FD.

### 3.11 LR Highest Energy Reconstructed Event

Rather than show a "typical" event, the highest energy reconstructed event for BR or LR is shown in Figure 3.6. This event is of interest as its energy is above the GZK suppression energy level and is a good comparison to the highest energy cosmic ray ever detected, the "Oh-My-God particle" observed by the Fly's Eye experiment<sup>[17]</sup>. The event reconstructed in monocular mode has the characteristics in Table 3.6.

The "Oh-My-God particle" particle had energy 2.7 times greater and the maximum development at 800 g/cm<sup>2</sup>. This event developed much shallower in the atmosphere, where higher composition

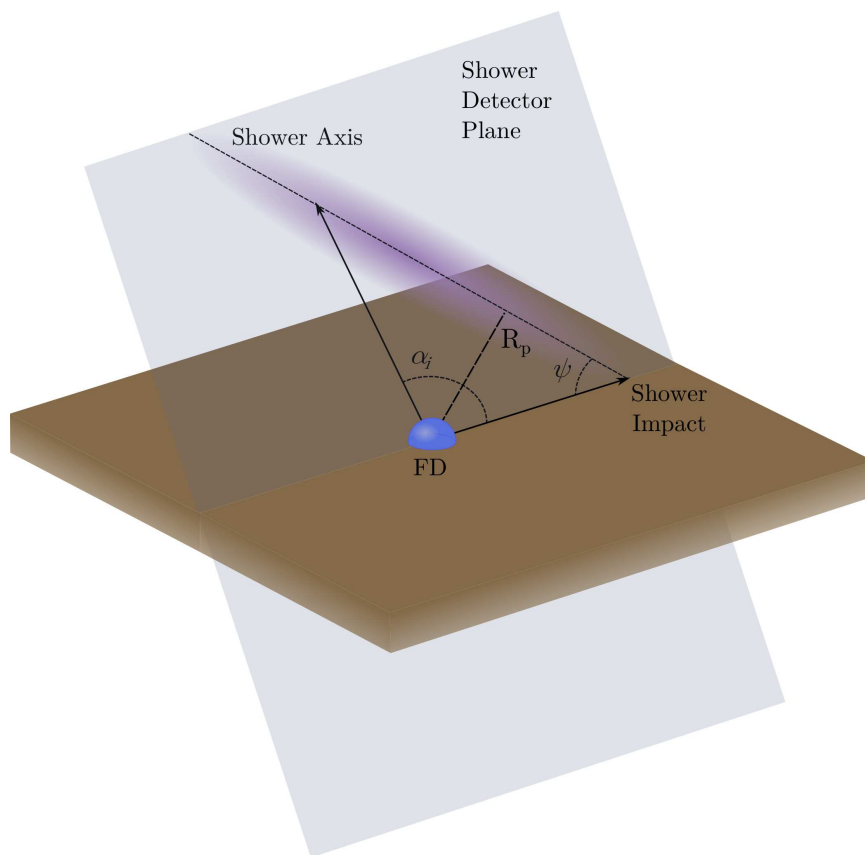
cosmic rays usually develop. Both events have a  $\psi$  value of  $\pm 15^\circ$  from  $90^\circ$ . Fly's Eye observed the event at about 18 km with  $R_p$  while this event was observed at about the edge of TA's detection area with  $R_p = 50.7 \pm 4$  km.

**Table 3.1:** BR and LR FD DST banks.

Bank Name	Generated By	Contents
<b>Processed Data Banks:</b>		
FDRaw	TAMA	Event raw FADC waveform and timing information.
FDTIME	TAMA	Event CTD timing information.
FDPlane	FDPlane	Event geometry reconstruction information.
FDTubeProfile	FDTubeProfile	Event profile reconstruction information.
TrumpMC	TRUMP	Simulated event information.
<b>TRUMP Simulations Input Banks:</b>		
ShowLib		Shower library of CORSIKA generated shower parameters.
ShowScale		Linear event scaling information for energy and angle in the shower library.
<b>Detector Geometry and Calibration Banks:</b>		
FDPed		Nightsky background mean and variance for each PMT at the station.
GeoFD		Station telescopes' geometry information.
FDMirrorRef		Station mirrors' reflectivity information.
FDParaglasTrans		Station Paraglas camera protectors' transmittance information.
FDBG3Trans		Station BG3 Filters' transmittance information.
FDPMTQECE		Station PMTs' quantum and collection efficiency information.
FDPMTUniformity		Station PMTs' uniformity information.
FDPMTGain		Station PMTs' gain information.
FDAtmosParam		Atmospheric condition information.
FDScat		Aerosol Scattering Information.
GDAS		NOAA GDAS (Global Data Assimilation System) database atmospheric conditions information.

**Table 3.2:** TAx4 FD DST banks.

Bank Name	Generated By	Contents
<b>Processed Data Banks:</b>		
FRAW1	TLFDP0	Event raw FADC waveform and timing information.
FTRIG1	TLFDP0	Event trigger information.
FPHO1	TLFDP0	Event FADC photoelectron count waveforms and timing information.
FSCN1	TLFDP0	Event waveform scan information.
STPS2	STPS2	Event tracklike probability information.
STPLN	STPLN	Event shower detector plane reconstruction information.
HCTIM	STPLN	Event geometry reconstruction information.
HCBIN	STGEO	Event profile reconstruction binned light information.
PRFC	STPF12	Event profile reconstruction fitting parameters.
MC04	MC2K12	Simulated event information.
<b>Weather Banks:</b>		
TLWEAT	TLFDP0	MD station night sky weather codes.

**Figure 3.1:** Reconstructing the EAS shower core geometry first using calculating the Shower Detector Plane (SDP) and then the geometry in the plane using the timing fit.

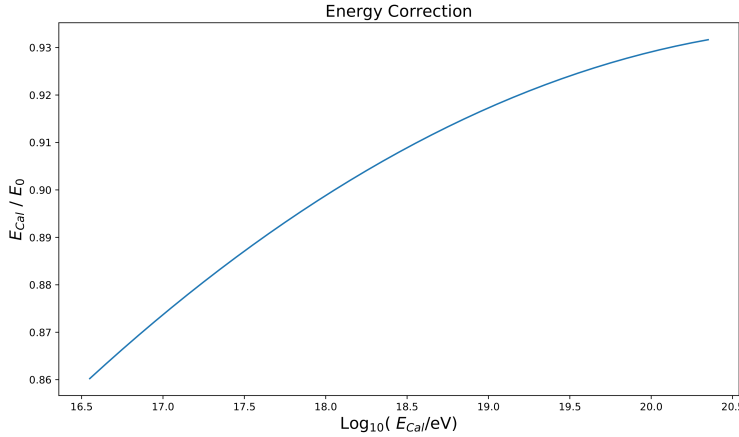


**Figure 3.2:** Missing energy correction applied to the calorimetric energy to get the primary cosmic ray energy assuming a protonic primary.

**Table 3.3:** BR and LR monocular event geometry reconstruction quality cuts.

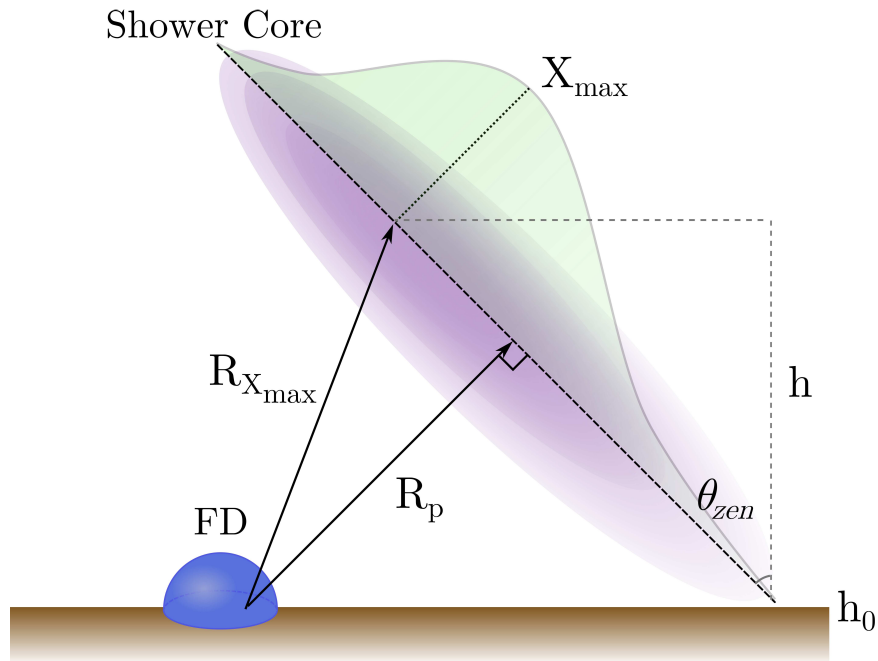
Event Geometry Reconstruction Cuts	
Good PMT Fraction	$N_{\text{Good PMT}}/N_{\text{PMTs}} \geq 3.5\%$
Number Good PMTs	$N_{\text{Good PMT}} \geq 6$ Tubes
NPE per Degree	$N_{\text{pe}}/\Delta\theta > 25$ NPE / deg.
Pseudo Distance (angular speed of EAS)	$r_p > 1.5$ km
SDP Angle	$\leq 80^\circ$
$R_p$	$R_p \geq .5$ km
$\psi$	$\psi < 130^\circ$
$\psi$ fit uncertainty	$\sigma_\psi < 36^\circ$
<i>Successful Timing Fit</i>	
Timing Fit	$\chi^2/\text{ndf} < 10$
Track Length 1 Ring	$\Delta\theta_{\text{Ring } 1} > 7^\circ$
Track Length 2 Ring	$\Delta\theta_{\text{Ring } 2} > 10^\circ$
Zenith Angle	$\theta_{\text{zen}} < 70^\circ$
Crossing Time	$t_0 < 25.6 \mu\text{s}$
Time Duration	$\Delta t > 6 \mu\text{s}$ (for $R_p < 5$ km)

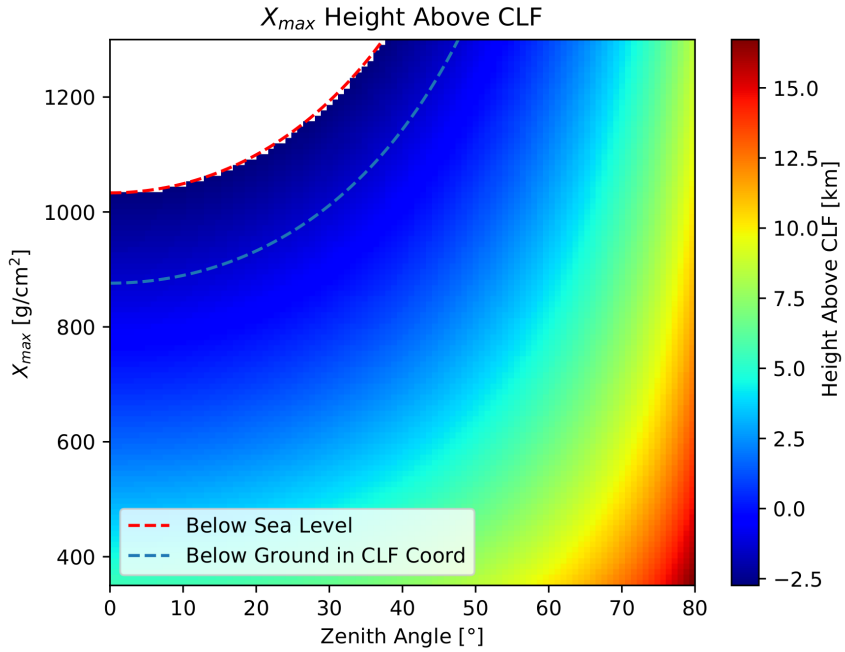
**Table 3.4:** BR and LR monocular event profile reconstruction quality cuts.

Event Profile Reconstruction Cuts	
<i>Successful Profile Fit</i>	
First Depth	$150 \text{ g/cm}^2 \leq X_1 \leq 1200 \text{ g/cm}^2$
Observed Depth Extent	$\Delta X \geq 150 \text{ g/cm}^2$
$X_{\text{max}}$ Bracketing	$X_{\text{max}}$ is contained within the FOV

**Table 3.5:** TAx4 monocular event reconstruction quality cuts.

Event Reconstruction Cuts	
Rayleigh Filter	$P_{\log_{10}} \geq 2$
Brightness Cut	$\Sigma N_\gamma / N_{\text{Good PMTs}} \geq 200$ $\Sigma N_{\text{pe}} / N_{\text{Good PMTs}} \geq 55$
Track Length	$\Delta\theta > 7.9^\circ$
Track Width RMS	$\theta_{\text{RMS}} \leq 1^\circ$
Angular Speed	$5.73^\circ/\mu\text{s}$
<i>Successful Geometry Fit</i>	
<i>Successful Profile Fit</i>	
Profile Fit	$\chi^2/\text{ndf} < 14$
Cerenkov Fraction	$f_{\text{Cerenkov}} < 20\%$
First Interaction	$X_1 \leq 1200 \text{ g/cm}^2$

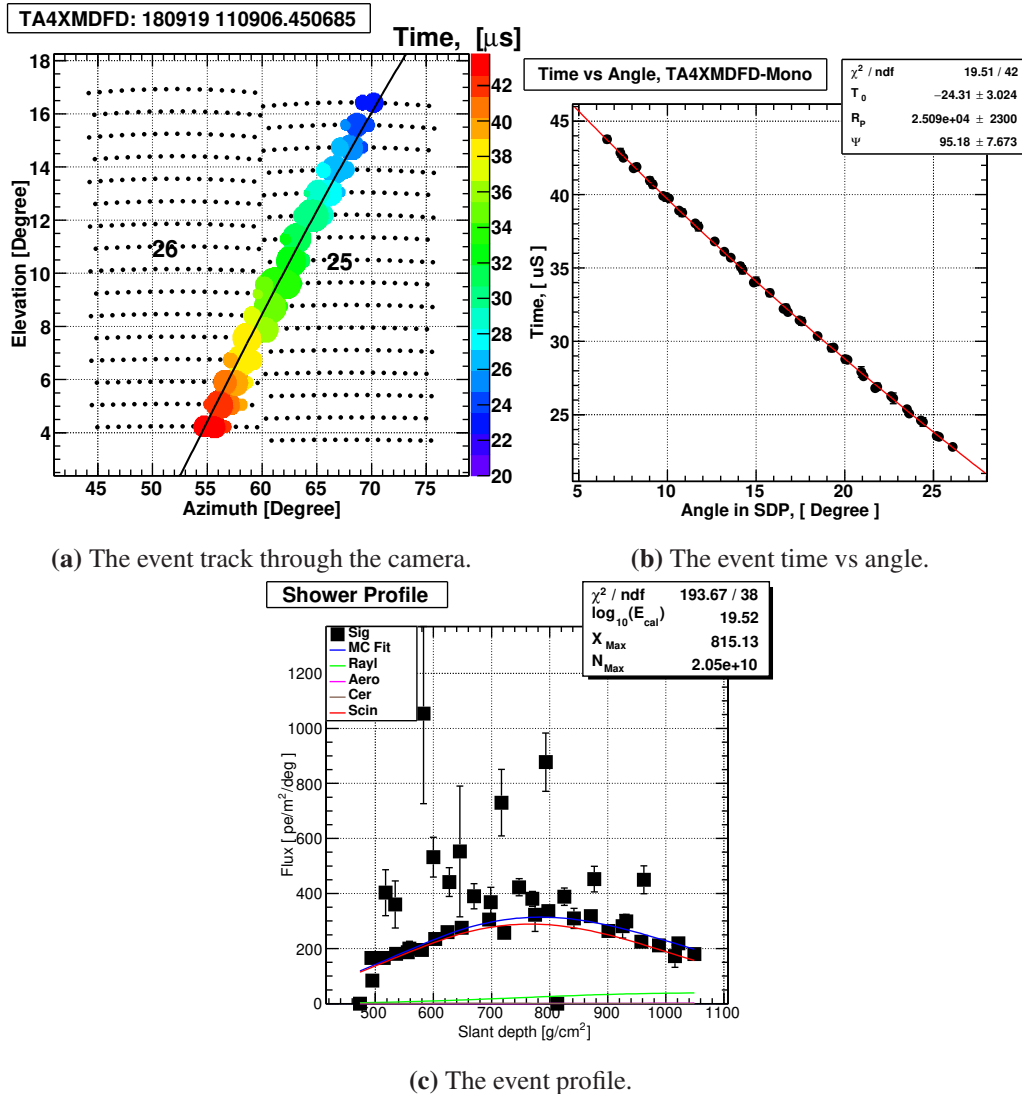
**Figure 3.3:** The  $R_{X_{\max}}$  parameter vs shower impact parameter,  $R_p$ , for a fluorescent event with the shower development overlaid on top of the shower core.



**Figure 3.4:** Height of  $X_{\max}$  above CLF at TA used to determine the radial distance from a FD station to  $X_{\max}$ .

**Table 3.6:** TA FADC highest energy monocular event reconstruction parameters.

Event Reconstruction Parameters	
Date	2013-04-11
Time	05:06:01.144682 UTC
Good Tubes	22 out of 222 PMTs
Track Length	$\Delta\theta = 16.515^\circ$
Time Extent	$\Delta t = 32.940 \mu\text{s}$
Impact Parameter	$R_p = 50.749 \pm 4.071 \text{ km}$
SDP Inclination Angle	$\psi = 105.453 \pm 7.731^\circ$
Shower Max	$X_{\max} = 555.7 \pm 6.5 \text{ g/cm}^2$
	$N_{\max} = (8.04 \pm .18) \times 10^{10}$
Calorimetric Energy	$E_{\text{cal}} = (1.089 \pm .031) \times 10^{20} \text{ eV}$
Primary Energy	$E_0 = (1.171 \pm .032) \times 10^{20} \text{ eV}$ $117 \pm 3.2 \text{ EeV}$ $18.7 \text{ J}$



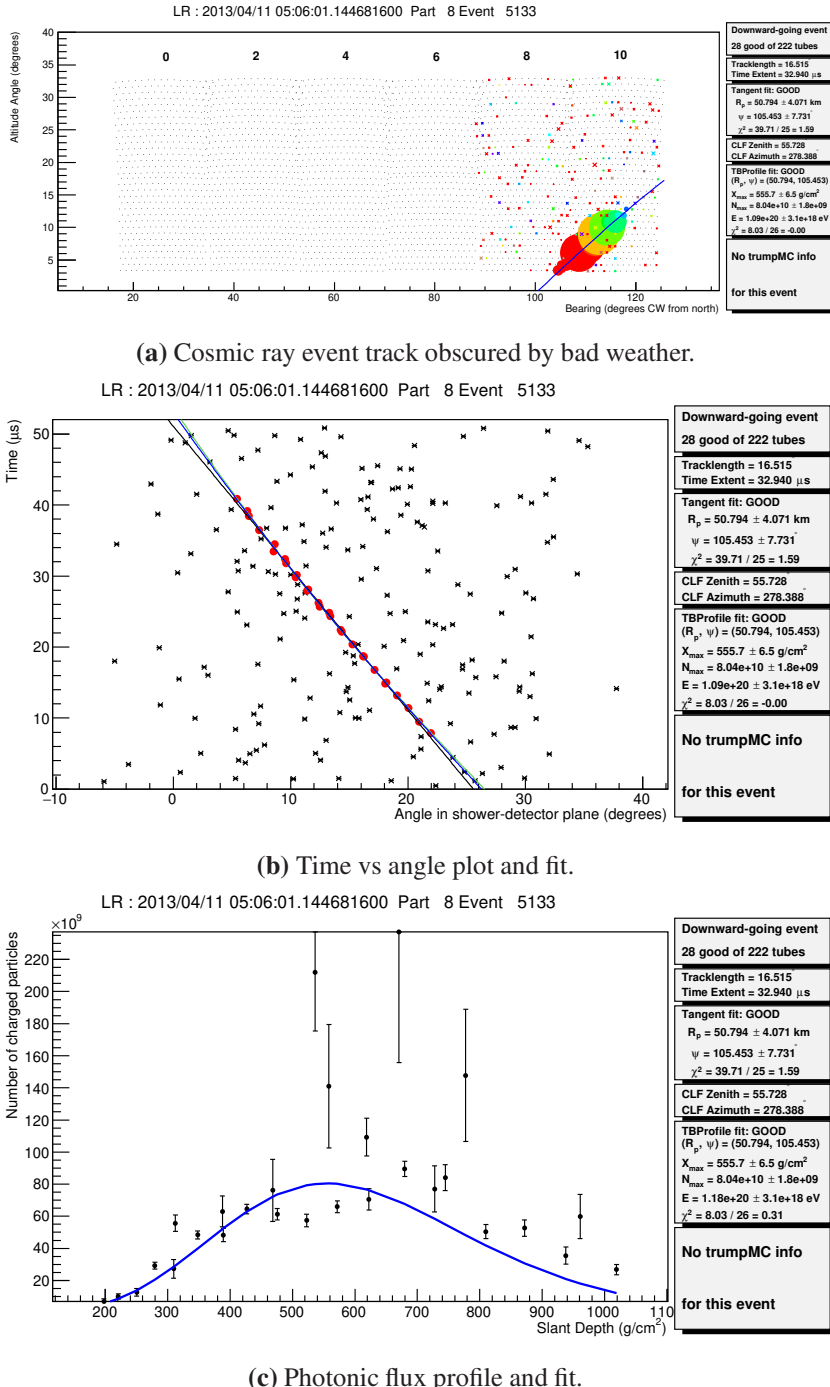


**Figure 3.6:** The highest energy event reconstructed in monocular mode. Event was seen by LR.

# CHAPTER 4

## WEATHER SELECTION CUTS USING MACHINE LEARNING

Parts of Chapter 4 follow from work presented at the ICRC 2019.<sup>[70]</sup>.

The FDs operate on clear, moonless nights, to best observe the cosmic ray EASs that excite the nitrogen molecules in the atmosphere. However, the FD stations have been operated when the weather is nonideal. Weather conditions affect the scattering of the fluorescence light in the atmosphere. Cloudy weather diminishes the ability to reconstruct or simulate the cosmic ray event accurately. The previous method of recording the weather had the MD station operators go outside every hour of operation and observe the night sky. This method is subjective as it depends on the opinions of the operators. This method also assumes that the conditions observed from the MD station are the same at LR and BR. We desired a more robust method of classifying weather in the FOV for the BR and LR stations.

We developed a novel method for classifying weather for the BR and LR FOV using neural networks trained on snapshot animations of the night sky created using the FADC pedestals of each PMT in an FD. Creating these pedestal animations was based on previous work at TA<sup>[71]</sup>. Starting with simple neural networks and building up complexity, we were able to achieve high accuracy in weather classification. This method also allowed for classifying each FD data part, which offers better time resolution of the night’s weather progression during FD operation. These results permit for the flagging of weather conditions that can be used in further analyses as done in the spectrum calculated in Chapter 7.

### 4.1 Impact of Weather on Observation and FD Event Reconstruction

The impact of weather on the FD event reconstruction is observed for an event that occurred during cloudy weather, as shown in Figure 4.1. The track of the event through the telescopes is seen in Figure 4.1a. A thick cloud in the FOV in Figure 4.1b obscures the center of the track in Figure 4.1a. The reconstruction of the event is seen with the timing fit in Figure 4.1c and the profile reconstruction in Figure 4.1d. We again see the obscured tubes in the timing fit and, most

importantly, in the profile fit. The profile fit does not match the signal well given the obscured portion in the middle. The profile is under reconstructed, which would lead to under reconstructing the energy of the cosmic ray event. Events like this are not desired in further analyses as they will skew the data.

## 4.2 Current Weather Recording at the MD Station

The previous method of recording the weather at TA was utilizing the weather recorded into what TA has named `weat codes`, which is a string of 7 digits. The values of the digits of the `weat codes` are in Table 4.1.

The weather is classified using the values of the `weat codes` in a defined function. A standard function for determining the weather classes of the array is given in Table 4.2.

These timestamped `weat codes` are stored in the MD station operation logs. A database of `weat codes` with timestamps was created by extracting all the `weat codes` patterns from the MD operation logs. Using the classification function in Table 4.2, the distribution from 11 years of weather classes from MD `weat codes` are displayed in Figure 4.2.

The preliminary cosmic ray spectrum analysis in Chapter 6 used these `weat codes` to assign weather classes to the data parts and events.

## 4.3 FD Pedestal Snapshots of the Night Sky

For every minute of operation, the pedestal average of each PMT is evaluated using all the triggered events within the minute and stored. The BR and LR FDs record data in file parts for every 1000 triggers of the detectors. The series of pedestal minute average values are stored corresponding to each part. Using these pedestal averages and the PMT's configuration of nominal pointing on the night sky, a snapshot, like those shown in Figure 4.3, can be produced. For each frame, all of the PMT values of the subsequent frame were subtracted from the corresponding PMT in the proceeding frame to enhance objects that were moving in the snapshots. For each data part, these snapshots can be used as a frame in a temporal sequence to animate the night sky progression. In these animations, we see stars move across the FOV or clouds obscuring them.

### 4.3.1 FD Pedestal Weather Classes

The BR and LR FD pedestal animations were classified into three distinct categories according to these qualities:

**Clear :** Multiple stars in a majority of the FOV were seen as they tracked across the sky as the Earth rotated (Figure 4.3a).

**Cloudy :** Nebulous clouds obscured the stars decreasing the pixel variation. Clouds had definable moving edges across the FOV (Figure 4.3b).

**Noisy :** A small fraction of the training set were distinguished from the other two classes. This class had random fluctuations across the FOV, giving a noisy appearance that made distinguishing either clouds or stars in the FOV difficult (Figure 4.3c). Lightning strikes in the FOV or the electronics not working properly could be the possible source of the parts. This class was more frequent around the beginning of the FDs operation in 2008 and less after that year.

## 4.4 Weather Classification Using Neural Networks

A series of neural networks with increasing complexity were designed to classify the weather using the FD pedestal data. The neural networks were trained to classify the weather using the FADC pedestal animations of each FD data part. The snapshots were fed into the neural network with their associated weather class. The neural network adjusted its weights over each training epoch to best match the mapping of the inputs to the desired outputs by optimizing its cost function<sup>[72,73]</sup>. These neural networks were constructed using the Keras machine learning framework<sup>[74]</sup> and run on a University of Utah Center for High Performance Computing GPU Node.

### 4.4.1 Training Data

Twenty percent of the FD data parts were sampled and selected uniformly throughout all operation nights to reduce bias from seasonal effects or other temporal effects to the FDs. This subsampled data is the training set. These sampled data parts were classified by eye using the snapshot animation according to the three weather categories; clear, cloudy, and noisy. There was also the issue that some FD data parts were missing. These data could be missing for two reasons. First, during the feature enhancement, if there was only one frame, there was an error in subtracting the sequential frame, and therefore an animation could not be generated. The second reason the FD pedestal data did not exist to begin with. The breakdown of classes in the training set is shown in Figure 4.4.

### 4.4.2 Neural Network Training and Performance

To evaluate the performance of the neural network, the training set was split further into two-thirds and one third. The one third was used as a validation set for the neural network. In each training epoch, the two-thirds subsample was fed through the neural network. The weights of each node in the neural network were adjusted via backpropagation to optimize the cost function. Backpropagation is a method for calculating the gradient of the cost function as a function of all

the variables in the neural network. The cost function is a measure of the difference between the neural network predictions from the true labels of the data. The performance of the neural network training is tracked by the accuracy of the training set predicted labels vs. the true labels and the cross entropy between the predicted classifications and the true classifications over each training epoch. Cross entropy is an information entropy measurement of the difference between the sets of the predicted labels and the true labels. Minimizing the cross entropy maximizes the log-likelihood that the two are indistinguishable.

Then the validation set was fed through the neural network, but the weights are not adjusted. The neural network validation set predicted classifications were compared to the true labels. Since the neural network does not train on the validation set, if it classifies this set well, then the neural network performs well. A good indicator of the neural network performance is comparing the training set accuracy and cross entropy vs. the validation set accuracy and cross entropy. If the values for the training set and validation set diverge, the neural network is over-training and will not perform well on data outside of the training.

Another metric of the neural network's ability is the validation data confusion matrix. The confusion matrix shows how the neural network predicted weather classes compare to the true labels classified by a human. The more the confusion matrix is diagonalized, the more agreement there is between the predicted labels and the true labels.

#### **4.4.3 Dense Neural Network**

The first attempt to classify the snapshots was using a simple deep neural network (DNN), which is useful for learning general patterns in a data set. The input for the DNN was the last frame of each data part flattened into a one-dimensional array where each PMT pedestal value corresponded to an input node. The inputs were processed through three hidden layers of densely connected nodes, where all the nodes in a layer fully are connected to all nodes in the preceding and succeeding layers, which were connected to three outputs corresponding to each of the three weather classes. The DNN architecture is displayed in Table 4.3.

The DNN showed the capacity for learning as its accuracy increased in Figure 4.5a and cross entropy decreased in Figure 4.5b. In Figure 4.5c, the validation data confusion matrix showed the DNN predicted most of the data parts were clear while they were labeled differently by a human. The DNN resulted in poor classification due to the limitation of the inputs being one dimensional with a flattened array of each PMT pedestal value for the last frame of the data part. The DNN could not take advantage of all the features of the data.

#### 4.4.4 Convolution Neural Network

The next neural network used was a convolution neural network (CNN), which is useful for learning patterns from a spatially correlated data set. A two-dimensional image can be input for this neural network, and a series of convolution filters are run across the input image to discern critical features in the image. Convolutions are used in image processing to distinguish features. In a CNN, the neural network is learning which image features are decisive and weights them accordingly. The last frame of each part was input through three convolution layers followed by three densely connected layers to three output nodes. The CNN architecture is displayed in Table 4.4.

The CNN showed better learning ability in the higher accuracy and lower cross entropy, as shown in Figures 4.6a and 4.6b. In Figure 4.6c, the validation data confusion matrix, the CNN started to distinguish between clear and not clear but was not yet achieving the desired diagonalization. The neural network was again limited to the last frame of each part but could recognize crucial spatial features. The CNN could be improved upon by including all snapshots of a data part.

#### 4.4.5 Recurrent Neural Network

A recurrent neural network (RNN) was constructed to include the temporal feature of the input data being a time series of snapshots. An RNN is useful for learning patterns from sequentially correlated inputs. It retains a state or memory as sequential data is feed through, and the RNN tries to optimize towards the desired classification. However, the sequential data is limited to a one-dimensional array like the DNN, but all the frames of the data part were flattened and padded to the same length of the max time steps,  $t_{\max} = 216$ . These flattened frames were fed through for the learning of the DNN. The flattened arrays of all frames in a data part were input through three Long Short Term Memory (LSTM) layers to three output nodes. The RNN architecture is displayed in Table 4.5.

Including the sequential reasoning by constructing a RNN lead to better results in the accuracy and cross entropy (Figures 4.7a and 4.7b). The validation data confusion matrix in Figure 4.7c shows further diagonalization where a majority of predicted classes matched their true labels.

#### 4.4.6 Recurrent Convolution Neural Network

We combined the features of the CNN and RNN to allow for spatial and temporal reasoning to take full advantage of the features of the training data set. The neural network can read in frame by frame and learn temporal and spatial patterns. The frames were padded with zeroed frames, so the four-dimensional data was all the same length. Then the padded array of frames were fed in by their time-sequential order into the RCNN. The RCNN architecture is displayed in Table 4.6.

The RCNN has good training accuracy and cross entropy in Figures 4.8a and 4.8b. The validation confusion matrix(Figure 4.8c) shows good diagonalization. The RCNN performs well and is therefore a good method for classifying weather.

## 4.5 BR Neural Network Weather Classification Results

The results of the different NN architectures are displayed in Table 4.7. The RCNN performed the best. The RCNN takes full advantage of the FADC pedestal snapshot animation features in learning to classify weather. The RCNN achieved accuracy higher than 90% with low cross entropy. A downside for the RCNN is that it was more computationally expensive as it takes much longer to iterate through its training epochs. Next in performance was the RNN, which took into account the temporal information but was limited to the flattened frames. After that in performance was the CNN, which took into account the spatial information but only for the first frame. Lastly, in performance was the DNN, which was substantially limited to the flattened first frame. The DNN was used as a proof of concept for using Keras with the FD pedestal data. The DNN was never expected to achieve any passable results.

## 4.6 LR RCNN Weather Classification Results

Once the RCNN was developed in Keras for the BR FD pedestal animations, the same neural network was trained on the LR animations instead. Again 20% of the pedestals were subsampled for the training set and classified. This breakdown of the classification is seen in Figure 4.9. The LR training set compared to the BR training set in Figure 4.4a has 10% more clear data parts. Again the noisy set was found to be significantly small but was again was a unique class given its visual difference from the other classes. The max time steps for LR was found as  $t_{\max} = 131$ .

The performance of training the RCNN with the LR data is shown in Figure 4.10. The RCNN again achieves very high accuracy as seen in Figure 4.10a and low cross entropy as seen in Figure 4.10a. Both of those plots exhibit an interesting sub plateau in the early training epochs and then progress further. This plateau is caused by the optimizer finding a local minimum before determining the global minimum. The normalized confusion plot shows that the RCNN performed well in classifying clear from nonclear. Its confusion between the cloudy and noisy is fine as both of those are not considered for further analysis, and the noisy parts in the training set were a significantly small subset in the training set. The results of the RCNN with LR are seen in Table 4.8.

## 4.7 Machine Learning Weather Cuts

With the proven RCNN, all of the FD pedestal animations for BR and were classified. The full classification for all FD data parts is seen in 4.11a. The data parts classification was then mapped to the events within the data part, and the breakdown by event classes is seen in 4.11b. We expect more clear events in the events break down than in the part break down. This breakdown discrepancy is from more successfully reconstructed events in a clear data part than in a cloudy data part where reconstruction of events would be poor. We also did observe a few missing or noisy, which is expected given the types of classes they are.

Most interestingly from this analysis is the difference of weather class breakdown between LR and BR seen in Figure 4.11. This difference between BR and LR will have a further effect on the spectrum analysis using these sites in Chapter 7 when calculating the ontime of the two detectors. The previous spectrum analysis with BR and LR<sup>[61]</sup> applied weather cuts using taking into account the MD weat codes and assuming the weather was the same between the MD, BR, and LR station. From Figure 4.2, we see that MD even has a different breakdown of its weather classes, but this is not a full direct comparison given the difference in these methods. The new machine learning method improves the timing resolution on weather cuts. Most importantly allows for weather determination at both LR and BR using data collected from the FDs. Whenever there is cosmic ray data collected for a site, there will be this pedestal data.

## 4.8 Other Interesting Optical Events Seen in FD Pedestals

Other exciting optical events were observed in the training sets while classifying the parts by eye. One event was the octocopter carrying a UVLED across the FOV for calibration purposes. Meteors, Meteor Showers, the Aurora Borealis, and a *transient luminous event (TLE)* whimsically named ELVES were seen in the FOV. Many of these events have not been studied much in the near UV spectrum of the FDs. These FD pedestal animations could shed new insight into these phenomena.

### 4.8.1 Octocopter

An octocopter with a UVLED was flown very close to the FD station in the FOV for calibration purposes<sup>[75]</sup>. The octocopter was noticed as a rapidly moving object covering large angular extents across the FOV of minutes, as seen in Figure 4.12. Airplanes are seen in the FD pedestal animations but mostly travel east to west as there is a civilian corridor out over the array. However, this event was moving faster and in multiple directions. Using the logs of when the octocopter was flown, this event was confirmed.

#### 4.8.2 Meteors and Meteor Showers

Bright transients that flashed across the FOV for one frame and disappeared were noticed. These transient flashes had an oblong track shape over a significant angular extent, as seen in Figure 4.13. Whatever caused these events were bright enough or remained long enough to impact the minute average of the PMTs' FADC pedestal. Nights with many of these transients were noticed, and the dates corresponded to meteor showers giving evidence to the source of these bright transient events. Many meteor showers or sporadic meteors were found in the training animations. The JEM-EUSO and Mini-EUSO space-based detectors have a proposed secondary mission of studying meteorites in the near UV as well.

#### 4.8.3 Aurora Borealis

Another exciting event seen in the animations was the event seen in Figure 4.14. This event was different from clouds given its pillar shapes and how it hovered in the northern portion of the FOV. There was a K 4+ geomagnetic storm reported that night by the Space Weather Prediction Center<sup>[76]</sup>.

#### 4.8.4 Elves, A Transient Luminous Event

ELVES are a whimsically named high atmospheric transient luminous event corresponding to lightning events. They produce an expanding luminous ring in the ionosphere. POA has been observing them as well with their FDs<sup>[77]</sup>. Mini-EUSO is also proposed to study TLEs such as ELVES. Quite a few of these were observed within the pedestal animations.

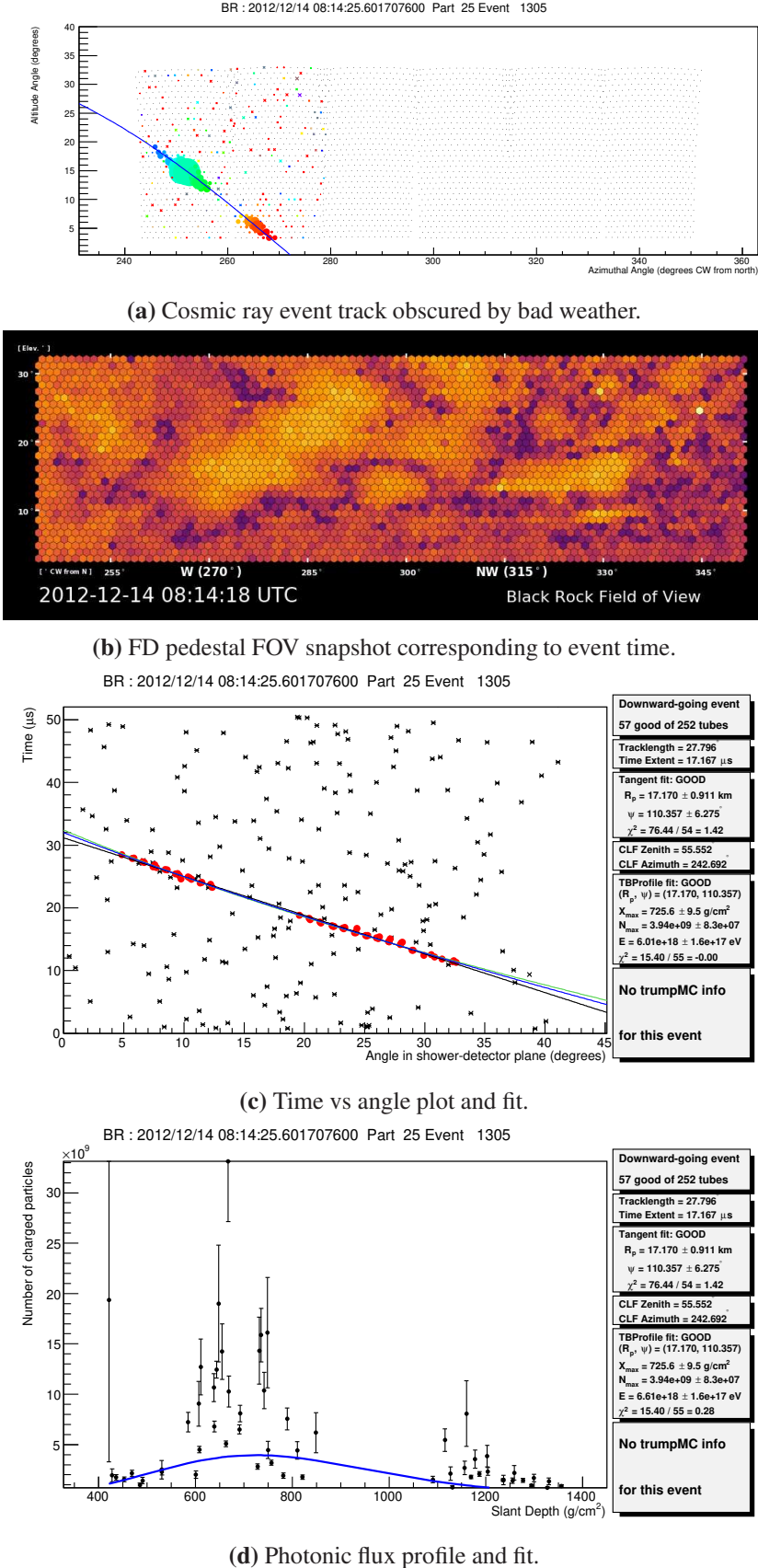


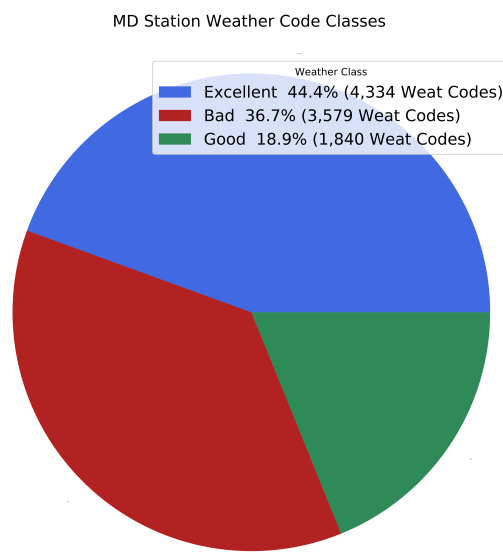
**Figure 4.1:** A fluorescence event obscured by dense clouds in the BR FOV.

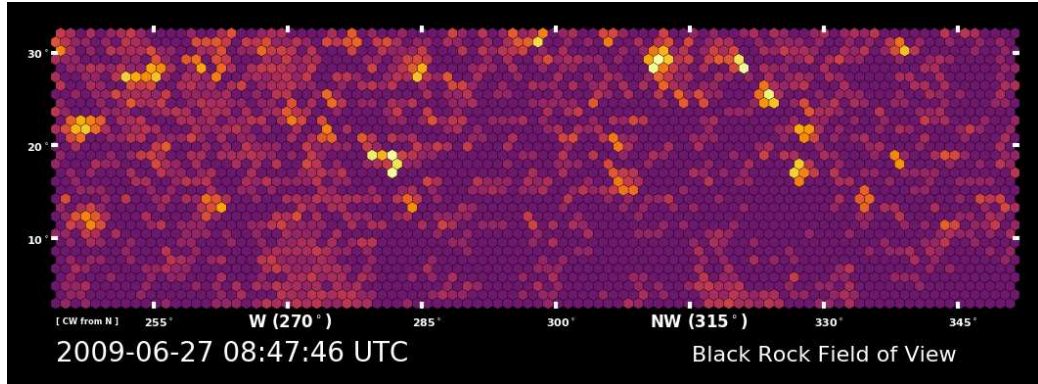
**Table 4.1:** MD weat code digits.

Digit	Attribute	Values
1	N - North	0 for clear, 1 for clouds
2	E - East	0 for clear, 1 for clouds
3	S - South	0 for clear, 1 for clouds
4	W - West	0 for clear, 1 for clouds
5	O - Overhead	0 for clear, 1 for clouds
6	T - Cloud Thickness	0-4 scale for 0 being clear and 4 being thick overcast
7	H - Haze	0 for clear, 1 for haze

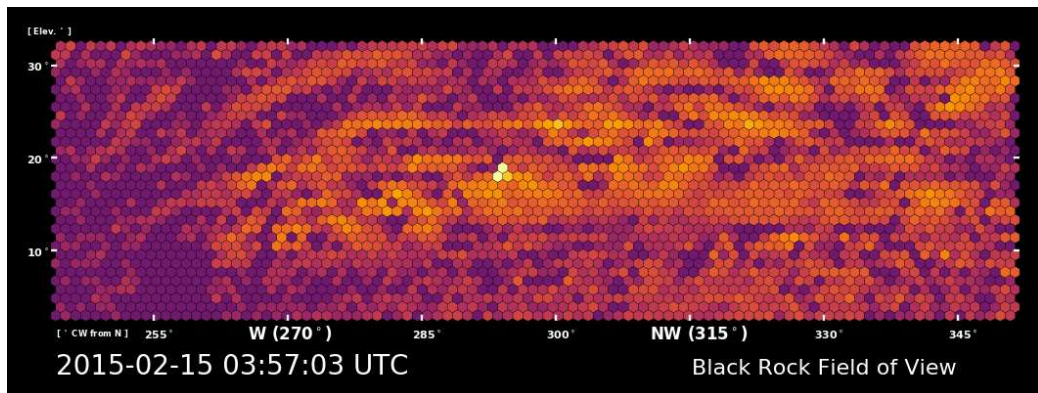
**Table 4.2:** Standard MD weat code weather classes.

Class	weat code Values
Excellent	Sum(NESWO) = 0
Good	Sum(NESWO) $\leq 2$
Bad	Everything Else

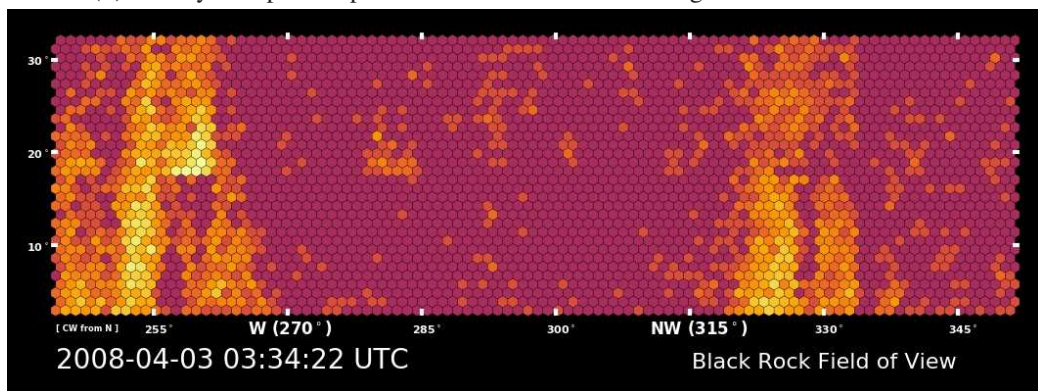
**Figure 4.2:** MD weat codes weather classes from 2008-01-03 - 2019-09-29.



(a) Clear data part snapshot. An asterism, the Big Dipper, is present in the upper right of the FOV.

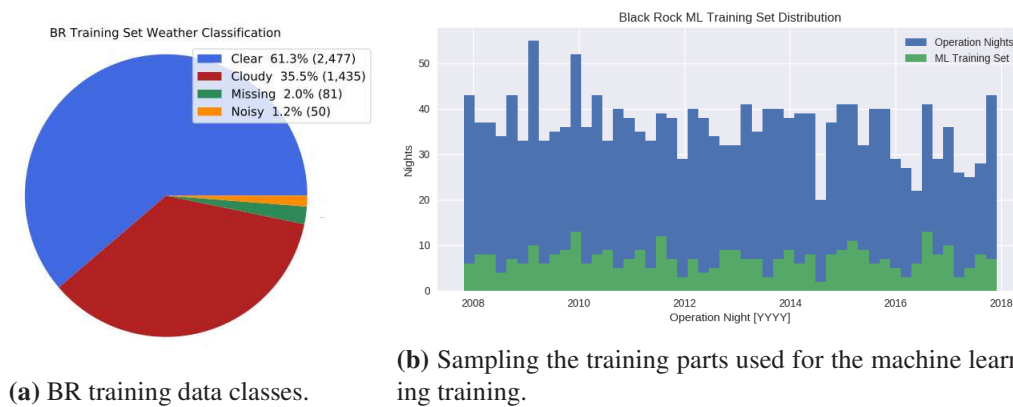


(b) Cloudy data part snapshot. No stars are visible through the clouds in the FOV.



(c) Noisy data part snapshot. No apparent points or edges.

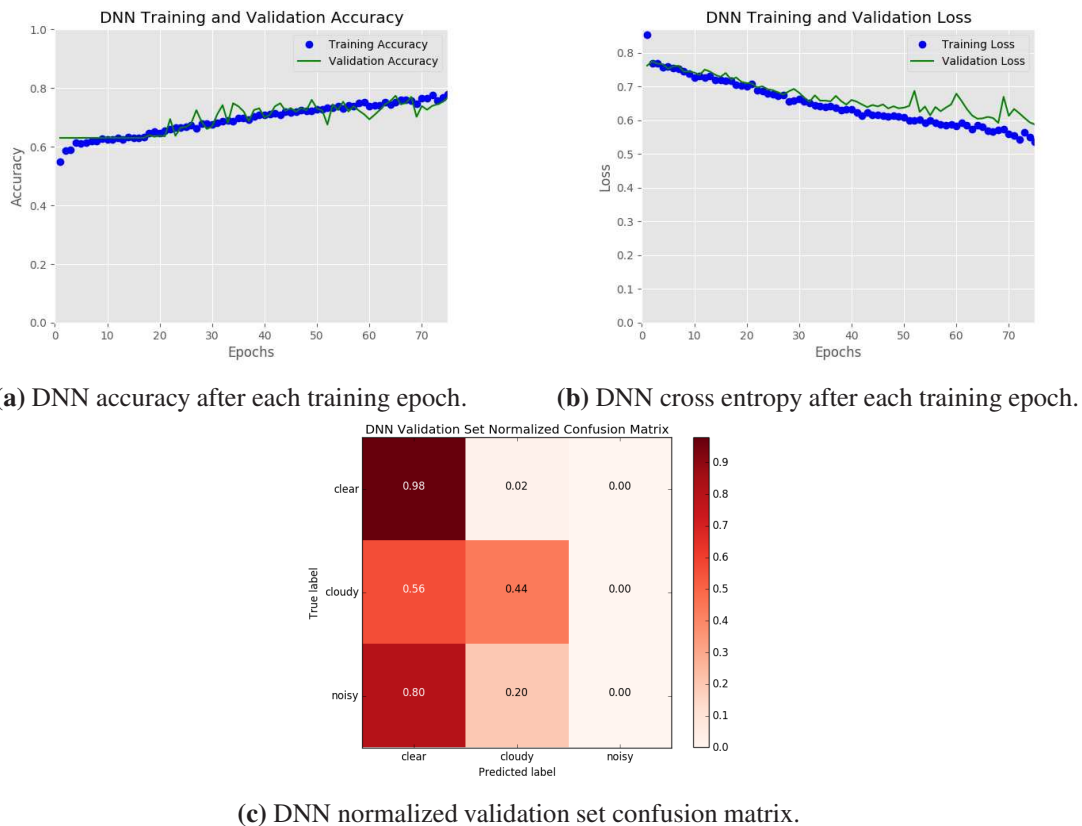
**Figure 4.3:** FD pedestal false color snapshots of the night sky in the FOV.



**Figure 4.4:** BR machine learning training data.

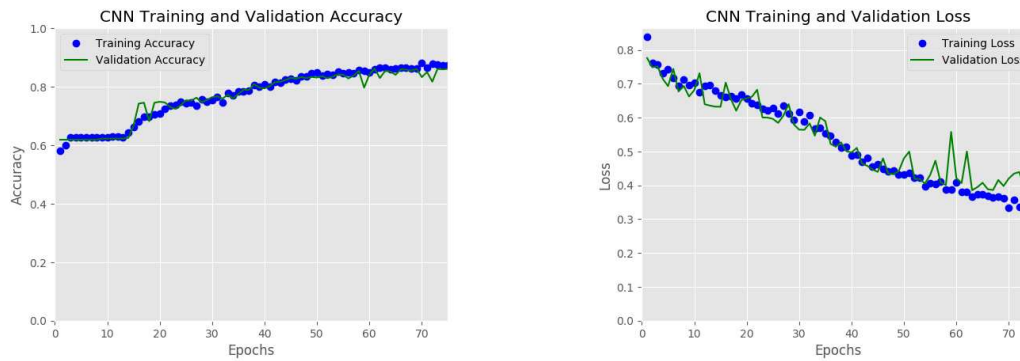
**Table 4.3:** DNN Architecture.

DNN Layers	
Input Layer	$\text{Input}_{\text{dim}} = 3072 \text{ pixels}$
1 <sup>st</sup> Hidden Layer	48 Nodes
2 <sup>nd</sup> Hidden Layer	12 Nodes
3 <sup>rd</sup> Hidden Layer	6 Nodes
Output Layer	3 Output Nodes

**Figure 4.5:** DNN performance.

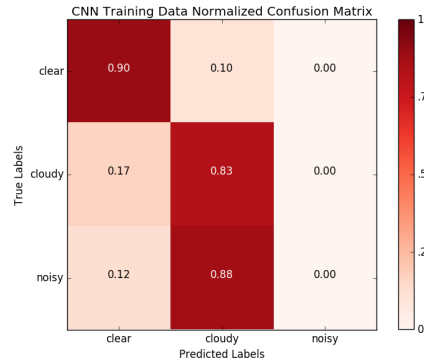
**Table 4.4:** CNN Architecture.

CNN Layers	
Input Layer	Input <sub>dim</sub> = 32 rows x 96 columns of pixels
1 <sup>st</sup> Convolution Layer	40 4x4 Convolution Filters
2 <sup>nd</sup> Convolution Layer	32 4x4 Convolution Filters
3 <sup>rd</sup> Convolution Layer	24 4x4 Convolution Filters
Flatten Layer	2D array to 1D array
1 <sup>st</sup> Hidden Layer	48 Nodes
2 <sup>nd</sup> Hidden Layer	12 Nodes
3 <sup>rd</sup> Hidden Layer	6 Nodes
Output Layer	3 Output Nodes, one for each class



(a) CNN accuracy after each training epoch.

(b) CNN cross entropy after each training epoch.

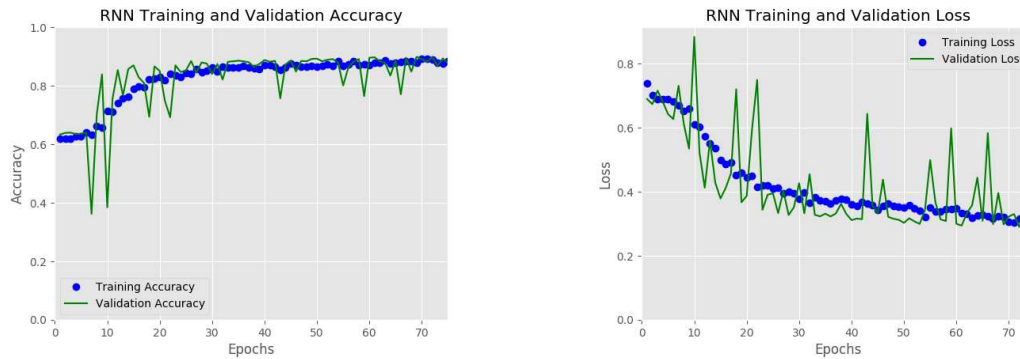


(c) CNN normalized validation set confusion matrix.

**Figure 4.6:** CNN performance.

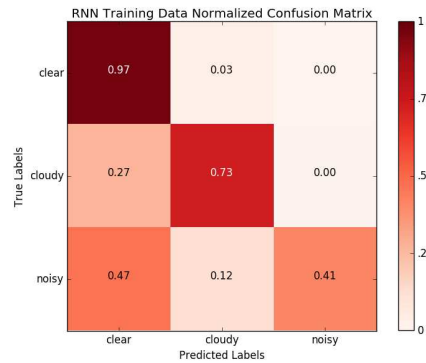
**Table 4.5:** RNN Architecture.

RNN Layers	
Input Layer	$\text{Input}_{\text{dim}} = t_{\max} \times 3072 \text{ pixels}$
1 <sup>st</sup> Long Short Term Memory (LSTM) Layer	48 Nodes
2 <sup>nd</sup> LSTM Layer	12 Nodes
3 <sup>rd</sup> LSTM Layer	6 Nodes
Output Layer	3 Output Nodes



(a) RNN accuracy after each training epoch.

(b) RNN cross entropy after each training epoch.



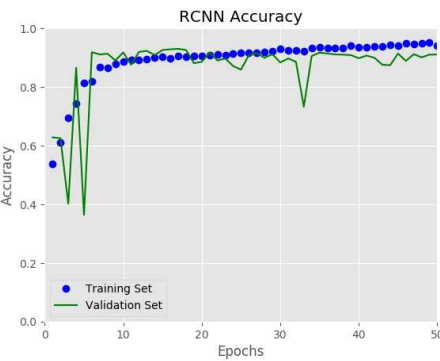
(c) RNN normalized validation set confusion matrix.

**Figure 4.7:** RNN performance.

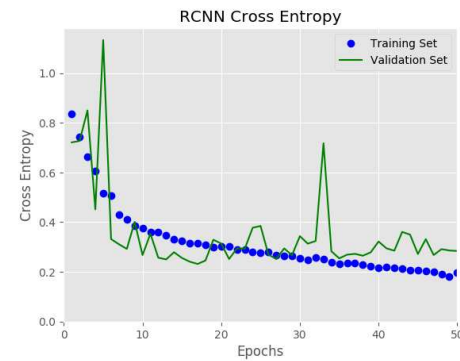
**Table 4.6:** RCNN Architecture.

## RCNN Layers

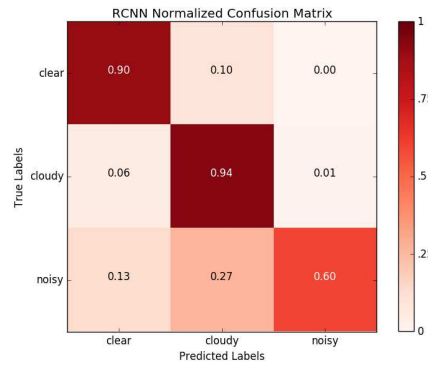
Input Layer	$\text{Input}_{\text{dim}} = t_{\max} \times 32 \text{ rows} \times 96 \text{ columns of pixels}$
1 <sup>st</sup> Time Distributed Convolution Layer	8 4x4 Convolution Filters
2 <sup>nd</sup> Time Distributed Convolution Layer	8 4x4 Convolution Filters
1 <sup>st</sup> LSTM Layer	48 Nodes
2 <sup>nd</sup> LSTM Layer	6 Nodes
Output Layer	3 Output Nodes



(a) RCNN accuracy after each training epoch.



(b) RCNN cross entropy after each training epoch.



(c) RCNN normalized validation set confusion matrix.

**Figure 4.8:** RCNN performance.

**Table 4.7:** Comparing the performance of each neural network model with the BR pedestal animations.

Model	Training Epochs	Optimizer	Computation Time	Validation Accuracy	Validation Cross Entropy
DNN	75	Adadelta	0:21:49 hours	76.79 %	0.58
CNN	75	Adadelta	0:09:06 hours	86.09 %	0.42
RNN	75	Adadelta	1:06:02 hours	87.65 %	0.35
RCNN	50	Adagrad	2:16:11 hours	90.93 %	0.29

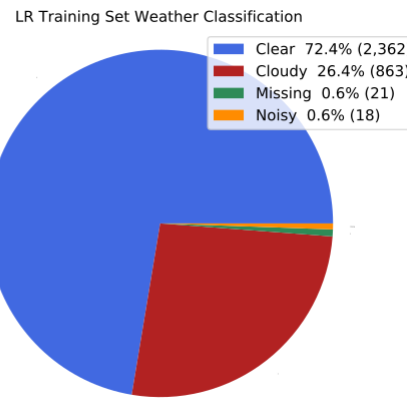
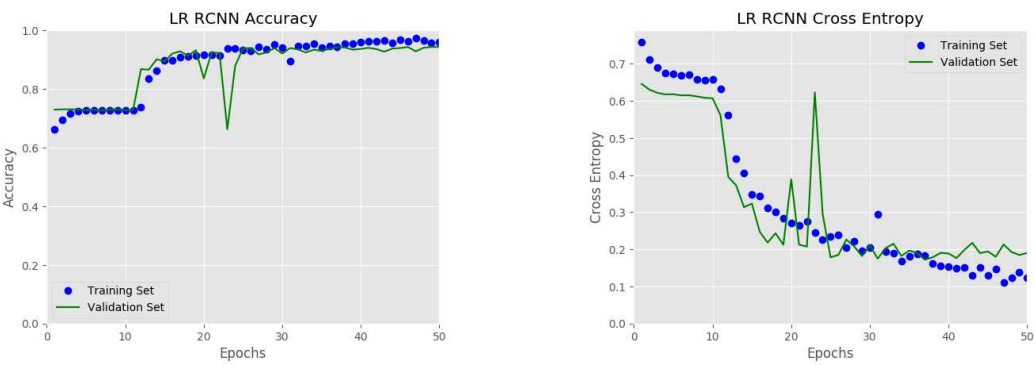


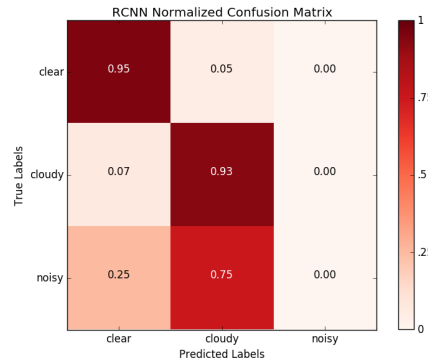
**Figure 4.9:** LR machine learning training data.

**Table 4.8:** LR RCNN weather classification results.

Model	Training Epochs	Optimizer	Computation Time	Validation Accuracy	Validation Cross Entropy
RCNN	50	Adagrad	0:36:57 hours	94.31 %	0.19

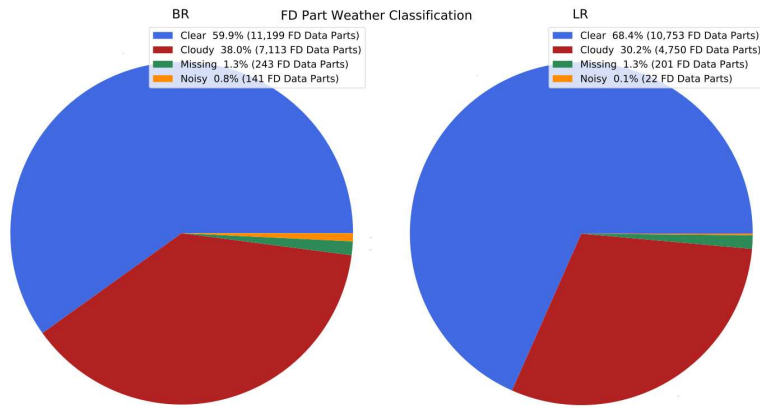


(a) LR RCNN accuracy after each training epoch. (b) LR RCNN cross entropy after each training epoch.

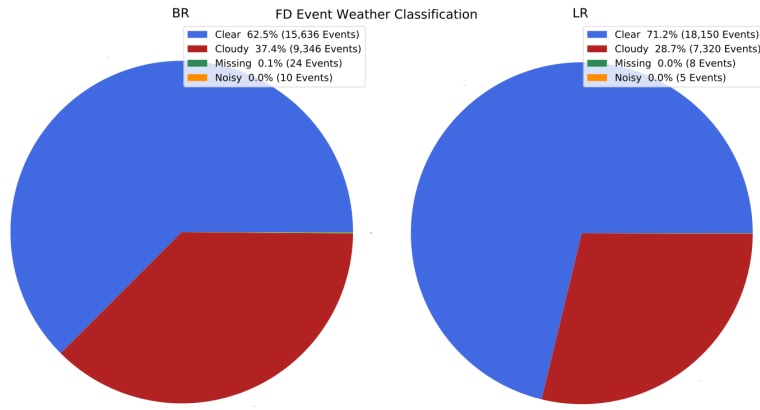


(c) LR RCNN normalized validation set confusion matrix.

**Figure 4.10:** LR RCNN performance.



(a) All FD data parts weather classification.



(b) All FD event weather classification.

**Figure 4.11:** All FD data weather classification using the RCNN neural network.

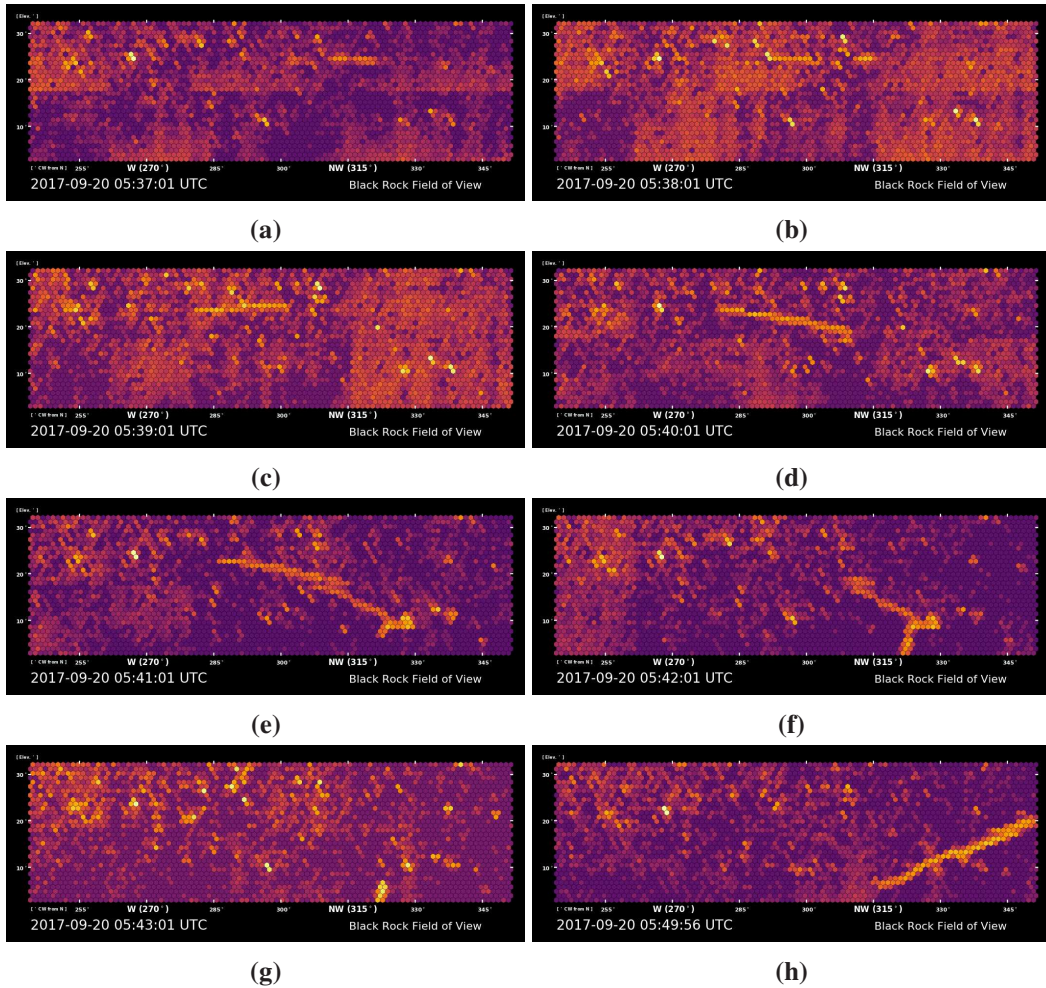


**Figure 4.12:** An Octocopter seen in the FD Pedestal Animations.

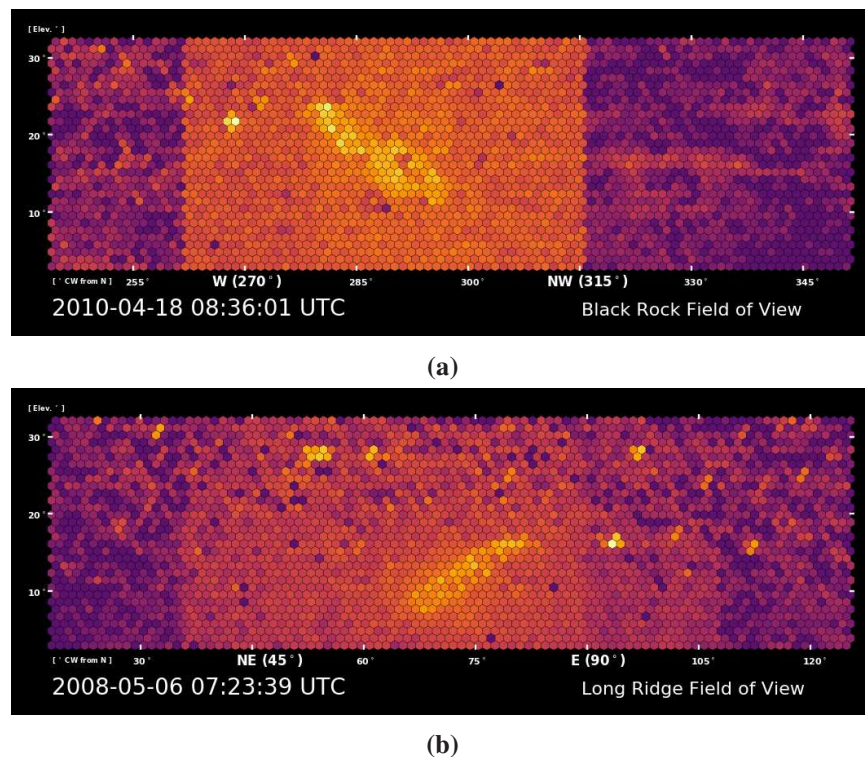


**Figure 4.13:** Meteors seen in the FD Pedestal Animations.

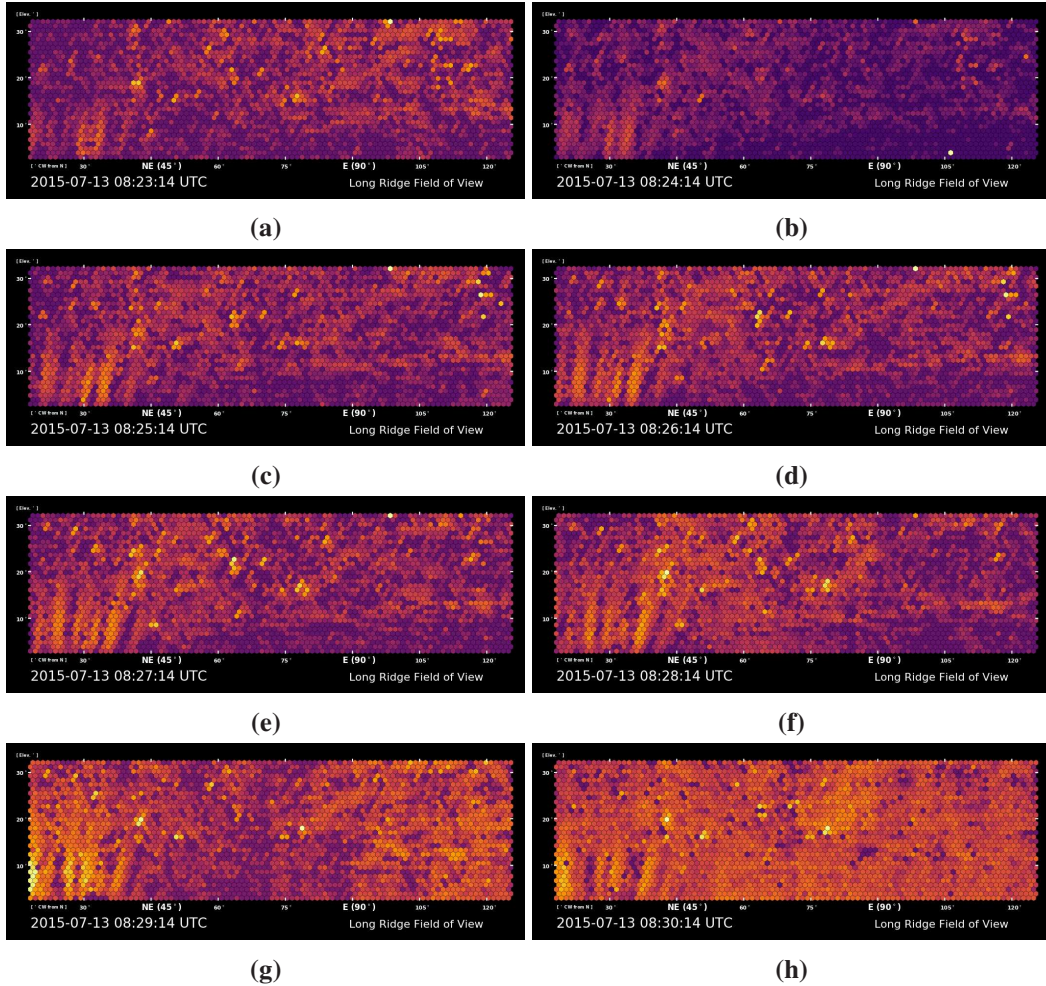


**Figure 4.14:** Aurora Borealis seen in the FD Pedestal Animations.

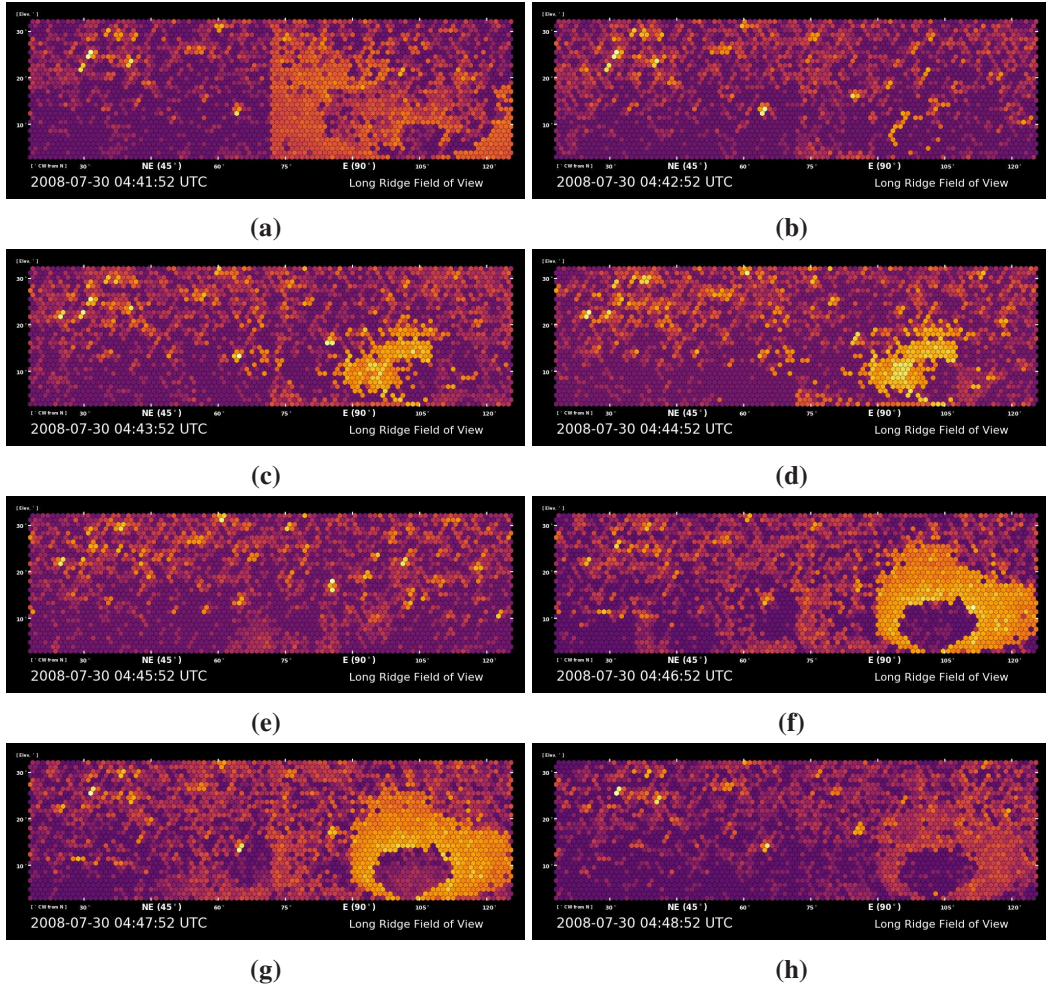


**Figure 4.15:** Transient Luminous Event called ELVES seen in the FD pedestal animations.

# CHAPTER 5

## COSMIC RAY EVENT MONTE CARLO SIMULATIONS

The purpose of *Monte Carlo (MC) simulations* of cosmic ray events is two-fold; to determine the detection aperture and the performance of the reconstruction of cosmic ray events. The MC's reconstructed event parameter distributions are compared with the reconstructed observed event parameter distributions to demonstrate that the MC represents the observed data well. The ratios of the binned data and MC histograms were calculated. A ratio with a horizontal line of unity shows good agreement. The ratios of each bin were fit with a linear function to check for an intercept of unity with no significant slope to test the data and MC agreement. These comparisons are coined a *Data/MC comparison*. It is essential to treat MC events in the same fashion as observed events in order to have an accurate Data/MC comparison. Thus, the same quality cuts described in Chapter 3 are applied.

The MC was used to determine the detection *aperture*,  $A\Omega$ , and *acceptance* of the FDs. The acceptance is a factor that incorporates the following FD sensitivity effects: the light generated by the shower development, the detector response, and the geometry of the shower around the detector. The acceptance is used as a correction factor. The acceptance is applied to the calculated geometric aperture the MC is simulated in. In this way, the MC is used to integrate the detection aperture, given the detector's sensitivity to the distance of an event and the thrown angle of the event. As the EAS development is dependent on the energy of the primary cosmic ray, the FDs sensitivity to and EAS will also be dependent on energy. The acceptance of the FDs is determined by the number of events fully reconstructed over the number of events thrown; (both binned by energy),

$$\text{Acceptance}(E) = \frac{N(E)_{\text{Recon.}}}{N(E)_{\text{Thrown}}} \quad (5.1)$$

Knowing the defined aperture that the MC events were thrown in,  $A_0\Omega_0$ , the corrected aperture of the FDs is calculated as

$$A\Omega(E) = A_0\Omega_0 \times \text{Acceptance}(E). \quad (5.2)$$

Another vital analysis done with the MC is determining the event reconstruction *resolution*. When the MC event is thrown, the initial parameters of the events are chosen at random. The MC

initial parameters are saved in a DST bank. The reconstructed value can be compared relatively or absolutely to the initial thrown parameters. The thrown value is sometimes referred to as the *true* value. Creating a distribution of the MC's thrown value compared to the reconstructed values for every reconstructed MC event shows the performance of the reconstruction. Taking the natural log of the relative difference distribution of for an example  $\zeta$  parameter allows for estimating the resolution of the reconstruction as a percentage as

$$\ln \left( \frac{\zeta_{\text{Recon.}}}{\zeta_{\text{Thrown}}} \right) = \ln(1 \pm \epsilon) \approx \pm \epsilon. \quad (5.3)$$

Using the natural log function in Equation 5.3 and assuming the relative difference is small the natural log can be approximated with its Taylor expansion. The resolution of variable  $\zeta$  is determined by fitting the distribution with a Gaussian function. The event reconstruction resolution is the Gaussian fit  $\sigma$  and the bias in reconstruction is the Gaussian fit  $\mu$ . If  $\mu \pm \sigma$  does not contain the origin, there is a significant bias of event reconstruction.

## 5.1 Telescope Array Monte Carlo Programs

Given the distinct difference and history between the BR and LR FADC FDs and the TAx4 FD, the two detector types have different MC simulation programs. BR and LR use the program TRUMP, the **Telescope Array Upgradable Monte Carlo Program**. TAx4 uses the `mc2k12` program. Both programs generate MC events in the following steps:

**Set configuration:** Important electronic calibration and atmospheric configuration files are set. The range or distribution of initial parameters such as energy, composition,  $R_p$ , and  $\theta_{\text{zen}}$  for the MC event are set. These parameters define the volume in which the MC events are thrown. The CORSIKA showers library from which events are sampled in the MC is defined. The program is then ready to start generating the specified showers.

**Set shower development and profile :** The program selects initial random parameters within the range set by the configuration (hence why the events are referred to as Monte Carlo). The event is scaled with the initial geometry and energy. A suitable event profile that matches the MC event is selected from the shower library and placed within the detection volume.

**Simulate light production:** Given the shower profile set in the previous step, the program calculates the light generated by the shower. The program accounts for the excited nitrogen fluorescence yield in the atmosphere due to the number of charged particles in the EM component of the EAS at a given slant depth, as discussed in Section 1.8.1.

**Simulate light propagation:** The light propagation is handled with ray tracing from the shower core to the detector. The effects of scattering and absorption are accounted for using the physics discussed in Section 1.8.2, given the atmospheric conditions set in the configuration file.

**Simulate detector optics:** The ray tracing and shadowing of the FD telescope system is calculated to determine the photon flux on the PMTs. The MC program accounts for the effects of the mirror reflectivity, and the transmission of the filters. The signal produced by the PMTs (given their QECE and gain balancing) is determined.

**Simulate detector electronics:** Given the PMT response from the previous step, the FADC electronic system’s conversion of the signal to ADC counts in a time series waveform is calculated. The triggering logic is simulated, and if the event passes, the MC event is recorded to a DST bank.

### 5.1.1 BR and LR MC Generation and TRUMP Configuration

The configuration parameters used by TRUMP for the MC events in this dissertation are given in Table 5.1. Figure 5.1 shows the proton dominated thrown composition. TRUMP can take two configuration files, one for BR and another for LR to throw events in tandem. Throwing events while simulating both stations allows for the simulation of stereo events that are reconstructed by both sites. Stereo events allow for a stereo acceptance calculation, which is critical for a combined energy spectrum from the BR and LR FD stations.

A python pipeline was written to generate MC events with TRUMP that corresponded to every night of observed data. The MC data was then reconstructed using the same BR and LR FD event reconstruction scripts. The reconstructed events were aggregated into an MC event database. All thrown events energies were recorded and aggregated into a thrown energy distribution,  $N(E)_{\text{Thrown}}$ , required to calculate the BR and LR FD acceptance.

### 5.1.2 mc2k12 Configuration

The configuration parameters used by mc2k12 for the MC events in this dissertation are given in Table 5.2. A python pipeline was written to generate all MC events mc2k12 with one master configuration file. Using default calibration can be improved upon, but for a preliminary result, using default calibration will give a suitable enough result. The MC data was then reconstructed using the TAx4 FD event reconstruction scripts. The reconstructed events were aggregated into an MC event database. All thrown events energies were recorded and aggregated into a thrown energy distribution,  $N(E)_{\text{Thrown}}$ , from which the TAx4 FD acceptance is calculated.

## 5.2 TAx4 FD Observed Data versus Monte Carlo Comparison

The TAx4 data and MC event comparison is a good exercise to perform. However, given the one year of runtime and the roughly  $90^\circ \times 15^\circ$  FOV, the analysis is greatly constrained by the statistics. Even with all roughly more than 1,000 reconstructed events, with quality cuts and weather cuts, the analysis is limited to 132 events. As seen in Figure 5.2b, very few events were observed above  $\log_{10}(E/\text{eV}) > 18.5$ . The energy of  $\log_{10}(E/\text{eV}) > 18.5$  is the lower energy bound in the preliminary energy spectrum in Chapter 6. The Data/MC comparison is not very robust as of yet. Future studies with the TAx4 FD will have to reexamine this.

The TAx4 Data/MC comparison is shown in two plots; The left plot in the Data/MC comparison shows the distribution of MC events, and the right plot shows the binned Data/MC ratio. The MC event distribution in blue and the observed events in black. The MC event distribution was normalized to allow for a direct comparison. The Data/MC ratio was fit with a linear function using ROOT. The fit result is shown as a dashed red line, and the fit statistics are shown in the red box.

The reconstructed energy Data/MC comparison, shown in Figure 5.2, shows that agreement with unity is within the fit error. For  $\log_{10}(E/\text{eV}) > 17$ , there is no significant offset or slope in Figure 5.2a. For  $\log_{10}(E/\text{eV}) > 18.5$  in 5.2b there is a significant offset below unity but no significant slope. Important parameters in the geometry reconstruction,  $R_p$  in Figure 5.3 has a significant slope and intercept while  $\psi$  in Figure 5.4 has a significant slope. The geometry of the shower in  $\phi_{\text{azimuth}}$  has good agreement overall in Figure 5.6 while  $\theta_{\text{zenith}}$  has significant disagreement from unity in the slope and intercept. Parameters from the profile reconstruction,  $X_{\text{max}}$  and  $N_{\text{max}}$  in Figures 5.7 and 5.8 show disagreement from unity with significant slopes and intercepts. More disagreement between the data and MC in  $\Delta\theta$ , Figure 5.9, and  $\Delta t_{\text{crossing}}$ , Figure 5.10. This analysis is greatly limited due to the low number of events.

## 5.3 TAx4 FD Monte Carlo Reconstruction Resolution

The distributions of the thrown versus reconstructed MC event parameters were calculated to evaluate how well the TAx4 reconstruction scripts performed. The  $x$ -axis label lists the calculated difference of the parameter, either absolute or relative. The ROOT Gaussian fit is the black dashed line. The fit statistics are listed in the black box. The plot on the left is all reconstructed MC events, the plot on the right is all MC with  $\log_{10}(E/\text{eV}) > 18.5$  as to match the lower limit of the preliminary spectrum. The FD event reconstruction resolution is listed in Table 5.3. These values are comparable to one ring monocular results of HiRes I<sup>[63]</sup>.

## 5.4 BR and LR FD Monte Carlo Weather Cuts

The machine learning weather cuts described in Chapter 4 were applied to the MC data generated for BR and LR. TRUMP used the `ONTIME` file and the MC event time to assign the corresponding FD data part identification to the MC events. The same weather classification mapping of BR and LR FD data parts for the observed data is used on the MC events. The breakdown of the MC weather classes is shown in Figure 5.18. While TRUMP does not simulate the clouds in the atmosphere, the pedestal data and GDAS atmospheric `DST` banks were used in the MC simulation. Those `DST` banks which were recorded during “bad” (nonideal) weather reflect the atmospheric conditions and therefore are not desired in further analysis. However, these bad weather MC events can also be used for bad weather observed event MC event data comparison. These bad weather Data/MC comparisons are calculated in Section 5.6 to illustrate the need for good weather cuts.

## 5.5 BR and LR FD Observed Data versus Monte Carlo Comparison

Data/MC comparisons were performed with the BR and LR FD events to show that the TRUMP MC describes the observed events well. For this analysis, events with  $\log_{10}(E/\text{eV}) < 17.5$  were cut as this was the lower bound of the combined spectrum generated in Chapter 7. The quality cuts applied to the BR and LR events in Tables 3.3 and 3.4 and weather cuts above were also applied to the MC events.

The Data/MC comparison plots for BR and LR reconstructed parameters are shown in Figures 5.19–5.30. In each figure, the BR Data/MC comparison is on the left, and the LR Data/MC is on the right. Underneath the Data/MC comparison is the bin-by-bin ratio of data to MC. The ratio is fit with a linear function to compare with unity. Only bins where the data had more than 0.1% of the events were included in the ratio fit. The fit statistics are reported to the right of the ratio plots. Some comparisons are shown with both linear and log axes.

The energy comparison, shown in Figure 5.19, shows good visual agreement between the data and MC distributions for both BR and LR. The ratio fits have slopes consistent with zero. The  $R_p$  distribution, shown in Figure 5.20, shows a slight disagreement for  $R_p$ s less than 5 km. However, there is a good visual agreement over the range of 5–20 km, where a significant portion of events occur. The slope of the ratio fit is not zero due to the events less than 5 km. The variable  $R_{X_{\max}}$ , shown later, is a more robust estimate of the distance to the shower.

The  $\psi$  Data/MC comparison, shown in Figure 5.21, shows excellent visual agreement in BR and mostly excellent visual agreement for LR, except for a few bins. For Data/MCs that are somewhat symmetric, as the  $\psi$  distribution is, it is more appropriate to fit the Data/MC ratio with a second-order polynomial as the disagreements in the Data/MC will create a curved line around a point of

symmetry and not a linear shift. The quadratic had three fit parameters, the height,  $y_0$ , the center of the parabola,  $x_0$ , and the curvature. The  $\psi$  ratio fit shows no significant curvature for BR and slight curvature for LR due to the few bins with excess data.

Next, we consider parameters related to the viewing of the EAS track. The number of photoelectrons per degree of the track,  $\log_{10}(\text{NPE}/\text{deg})$ , shown in Figure 5.22, shows good visual agreement. This is the brightness of the track, and the good agreement illustrates the accuracy of the photometric component of the simulation. The time extent,  $\Delta t$ , shown in Figure 5.23, also shows good agreement. However, the track length,  $\Delta\theta$ , shown in Figure 5.24, shows a shift with significant negative slope in the ratio fit. This disagreement is related to the SDP angle, discussed later.

The reconstructed shower axis zenith angle, shown in Figure 5.25, also shows a significant slope, again related to the SDP angle. The azimuthal angle of the shower axis was shifted to be relative to the center of the FOV, shown in Figure 5.26. This shows agreement between BR and LR FOV and also shows a preference of events coming toward the detector with peaks at  $\sim \pm 110^\circ$  where events track across the FOV. The azimuthal angle is symmetric at the origin; therefore, it was fitted with a parabolic fit function. The azimuthal angle shows a good Data/MC agreement. The SDP angle, the angle of the shower track across the FOV, shown in Figure 5.27, was also fitted with a parabolic fit and showed significant negative curvature in the ratio fit. This disagreement, with negative curvature, is evidence for the MC resolution being greater than what is observed. This causes events to spread from the center in the MC distribution, which results in negative curvature. This is a geometric effect that should be independent of the brightness or energy of the event. We will account for this disagreement as a systematic uncertainty in the aperture.

The Data/MC comparison for the profile parameters of  $N_{\max}$  and  $X_{\max}$  are shown in Figures 5.28 and 5.29 respectively.  $N_{\max}$  shows good Data/MC agreement, while  $X_{\max}$  does not. However,  $X_{\max}$  also does not impact further analysis as energy Data/MC comparison shows excellent agreement. However, in a composition study where  $X_{\max}$  is a key parameter, this would be an issue.

The Data/MC comparison for the new parameter,  $R_{X_{\max}}$ , introduced in this dissertation, is shown in Figure 5.30.  $R_{X_{\max}}$  being the distance to the maximum development of the EAS where the most light is generated is a better measure of the distance to the shower than  $R_p$ . The excellent agreement in the Data/MC comparisons of  $R_{X_{\max}}$  for both sites gives great confidence in the calculation of the detector aperture.

Figure 5.31 shows an indirect Data/MC comparison of the shower core impacts and  $X_{\max}$  positions out over the array with the FD FOV with a 30 km arc shaded. These figures illustrate the intersection of the detection area, which is important for stereo events. Figures 5.31c and 5.31d

illustrate the effect of requiring  $X_{\max}$  to be in the FOV. These plots show visual agreement in point positions between the data and MC.

Overall, the Data/MC comparisons for BR and LR show good agreement; therefore, the MC describes the observed data well. The acceptance depends on the distance to the thrown showers and the direction of the thrown showers. The agreement in  $R_{X_{\max}}$  shows that events are placed at appropriate distances from the detector.  $\psi$  and the *SDP* angle determine the appropriate direction.  $\psi$  has good Data/MC agreement while *SDP* shows a slightly wider distribution in MC than in data. We will account for this discrepancy as a systematic uncertainty with the overestimation of the aperture by 11%.

## 5.6 Bad Weather Observed Data versus Monte Carlo Comparison

The same Data/MC comparisons are performed using the bad weather data (as discussed in Section 5.5). Select comparisons of bad-weather Data/MC are shown in Figures 5.32–5.41. Events with  $\log_{10}(E/\text{eV}) < 17.5$  were also removed from the bad weather events. The captions of each figure refer to the corresponding good-weather Data/MC comparison. The bad-weather Data/MC comparisons illustrate the need for good weather cuts and how well we can determine the detector aperture.

The bad weather energy Data/MC comparison shows a shift with a significant  $y$ -intercept and slope in the ratios in Figure 5.32. The bad weather  $R_p$  also shows a shift, as shown in Figure 5.33, and there is no longer a flat region between 5–20 km as there was for the good weather Data/MC. A shift is shown in Figure 5.34 and Figure 5.35 for  $R_{X_{\max}}$  and  $N_{\max}$  respectively. This shift shows that bad weather affects the sensitivity to events that developed further away from the detector and the peak of profile development. The number of photoelectrons per degree also shifts significantly, as shown in Figure 5.36 as the bad weather impacts the amount of light that gets to the detector. The Data/MC comparison for  $\psi$ , shown in Figure 5.37, indicates significant curvature in the quadratic fit. The time extent, shown in Figure 5.38, shows a shift with bad weather. The track length shows a more significant shift in bad weather vs. good weather in Figure 5.39. The zenith angle shows a significant  $y$ -intercept and slope in the ratio fit in Figure 5.40. The SDP angle, shown in Figure 5.41, has more significant curvature and a significant offset at the point of symmetry.

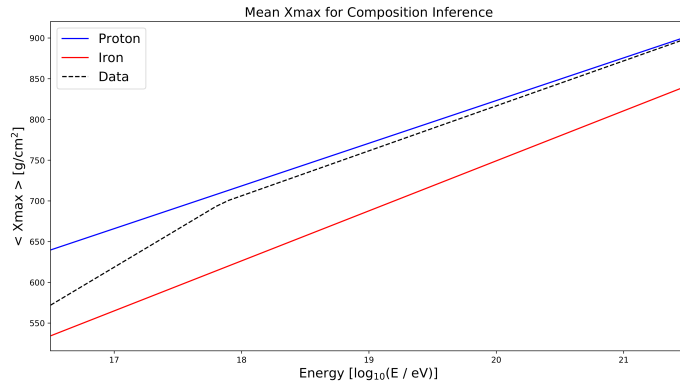
The selected Data/MC comparisons show a disagreement when considering only bad weather events and MC. Comparing the good weather to the bad weather shows the importance of good weather cuts and the benefits of the novel weather classification method produced in this dissertation.

## 5.7 BR and LR FD Monte Carlo Reconstruction Resolution

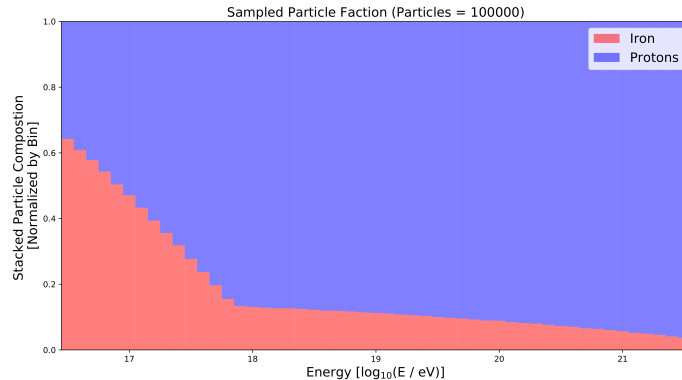
The BR and LR reconstruction resolution are done in the same fashion as the TAx4 resolution plots but with BR on the left and LR on the right. The resolution only considers events with  $\log_{10}(E/\text{eV}) \geq 17.5$ . The distribution of the parameter's reconstructed versus thrown relative or absolute difference is fit with a Gaussian distribution. The fit statistics are displayed in a box. The FD event reconstruction resolution is listed in Table 5.4. The reconstruction resolution of BR and LR performs well in monocular mode.

**Table 5.1:** TRUMP MC event generation configuration. Each BR and LR FD operation night has a corresponding MC thrown. Generated by `tax4_generate_mc.py`.

Parameter	Description	Value
<b>Out Files</b>		
FILE	output file name	{night}-{site}{instance}.dst.gz
<b>FD Station</b>		
SITEID	Station ID	0 = BR, 1 = LR
GEOFILE	Station geometry file	geobr_joint.dst.gz geolr_joint.dst.gz
<b>Events Configuration</b>		
SEED	Seed for event random generation	Hashed by night and instance using MD5
DTIME	Average time between thrown events [s]	0.016 (Roughly 5x MC)
<b>Thrown Primary Species</b>		
SPECIES	Cosmic ray composition	14 - protonic composition 5626 - iron composition
SHOWLIB	Composition CORSIKA shower library	tas-qgsjetii-04-prot.dst.gz tas-qgsjetii-04-iron.dst.gz
<b>Thrown Energy Spectrum - ICRC 2015<sup>[78]</sup></b>		
ENERGY	Energy bounds [ $\log_{10}(E/\text{eV})$ ]	17.0 21.5
NBREAK	Spectrum break points	4
EBREAK	Break point locations $\log_{10}(E/\text{eV})$	16.340 17.304 18.721 19.800
ESLOPE	Spectral indicies	3.133 2.943 3.226 2.663 4.670
<b>Thrown Volume and Shower Constraints</b>		
LAT	Latitude [ $^{\circ}$ ] around the CLF Pole	17.0 21.5
RP	$R_p$ bounds [m]	100.0 40000.0
PSI	$\psi$ bounds [ $^{\circ}$ ]	20.0 160.0
PHIIMP	$\phi_{\text{impact}}$ bounds [ $^{\circ}$ ]	-180.0 180.0
PHI	$\phi_{\text{azimuth}}$ bounds [ $^{\circ}$ ]	-180.0 180.0
THETA	$\theta_{\text{zenith}}$ bounds [ $^{\circ}$ ]	0.00 80.0
<b>Thrown Calibration and Ontime Parameters</b>		
SKYBG	Night sky background noise level [10 MHz]	9.00
MIRREF	Mirror reflectivity file	mirrorDSTBank.{yyyy}.dst.gz
PARAGLAS	Paraglas transmittance file	default fdparaglas_trans DST file
BG3	BG3 transmittance file	default default fdbg3_trans DST file
PMTQE	PMT QECE file	fdpmt_qece DST file
PMTGAIN	PMT gains file	pmtGainDSTBank.{yyyy}{mm}.dst.gz
PMTUNIF	PMT uniformity file	default fdpmt_uniformity DST file
PMTCAL	PMT gains file	black-rock/y{yyyy}m{mm}d{dd}.ped.dst.gz long-ridge/y{yyyy}m{mm}d{dd}.ped.dst.gz
ONTIME	Station Ontime file	black-rock/y{yyyy}m{mm}d{dd}.ped.dst.gz long-ridge/y{yyyy}m{mm}d{dd}.ped.dst.gz



(a) HiRes-Mia mean  $X_{\text{max}}$ <sup>[79]</sup> used to determine the proton fraction using the proton and iron rails.



(b) Trump composition sampling in each energy bin. Blue is protonic and red is iron. Above  $\log_{10}(E/\text{eV}) = 18$ , the composition is proton dominated.

**Figure 5.1:** TRUMP composition selection.

**Table 5.2:** mc2k12 MC event generation configuration. Generated by `mc_process_trump.py`.

Parameter	Description	Value
<b>FD Station</b>		
detfile	Station geometry file	ta_md_tax4.conf
shift origin	Set origin to FD site	YES
<b>Events Configuration</b>		
setNr	Night run number	2019062604
iseed	Seed for event random generation	-1908200101
nevt	Number of events thrown	5000000
event type	Number of events thrown	SHOWER
<b>Thrown Primary Species</b>		
primary	Cosmic ray composition CORSIKA shower library	qgsjetii-03, proton
<b>Thrown Energy Spectrum</b>		
gamma	Spectral index	2
minEnrgy	Minimum energy [eV]	1E+17.5
maxEnrgy	Maximum energy [eV]	1E+21
<b>Thrown Volume and Shower Constraints</b>		
rpmin	$R_p$ lower bound [m]	100.0
rpmaz	$R_p$ upper bound [m]	50000.0
thesh1	$\theta_{\text{zenith}}$ lower bound [radians]	0
thesh2	$\theta_{\text{zenith}}$ upper bound [radians]	1.22173048
phish1	$\phi_{\text{azimuth}}$ lower bound [radians]	-3.141592653589793
phish1	$\phi_{\text{azimuth}}$ upper bound [radians]	3.141592653589793
dxlim	Upper limit in slant depth [ $\text{g}/\text{cm}^2$ ]	2000.0
hceil	Atmosphere ceiling [m]	47000.0
<b>Thrown Calibration and Ontime Parameters</b>		
use DB	Use calibration database	No, default calibration

**Table 5.3:** TAx4 FD event reconstruction resolution.

Parameter	Resolution	Resolution	Figure
$(\log_{10}(E/\text{eV}) > 18.5)$			
$E$	21%	18%	5.11a
$R_p$	12%	10%	5.12
$\psi$	$6.8^\circ$	$6.1^\circ$	5.13
$X_{\text{max}}$	$70\text{g}/\text{cm}^2$	$65\text{g}/\text{cm}^2$	5.14
$N_{\text{max}}$	25%	21%	5.15
$\theta_{\text{zenith}}$	$2.6^\circ$	$2.3^\circ$	5.16
$\phi_{\text{azimuth}}$	$7.1^\circ$	$6.7^\circ$	5.17

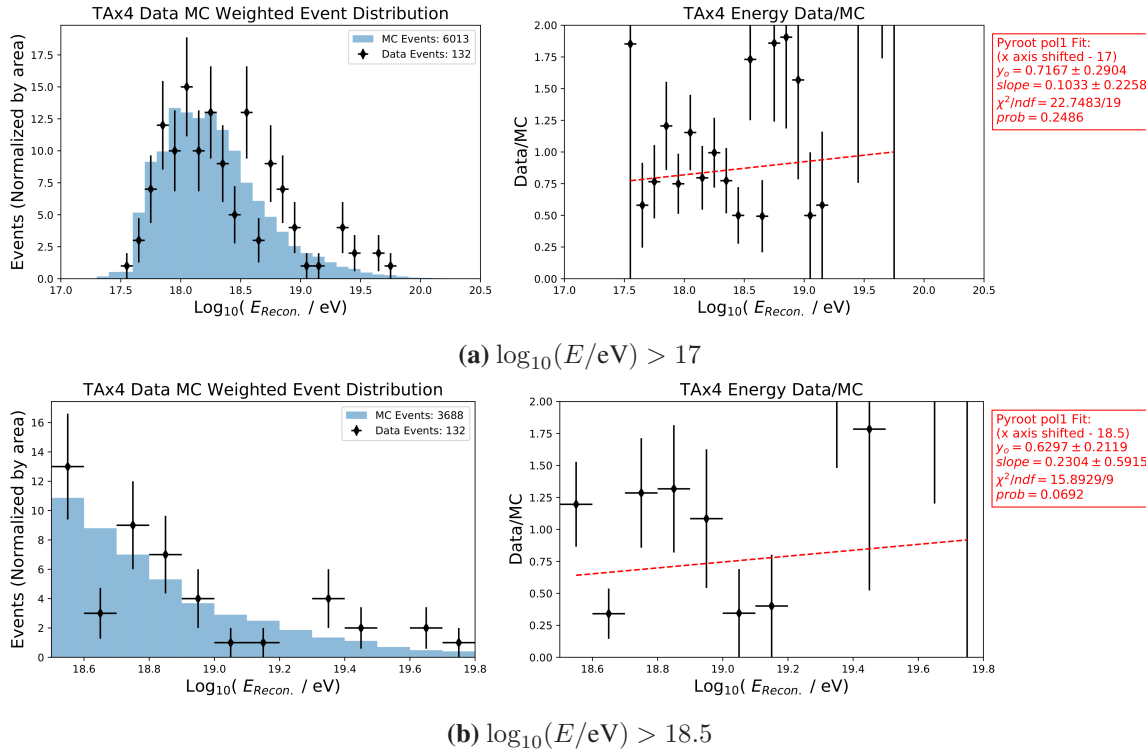


**Figure 5.2:** TAx4 reconstructed energy Data/MC comparison.

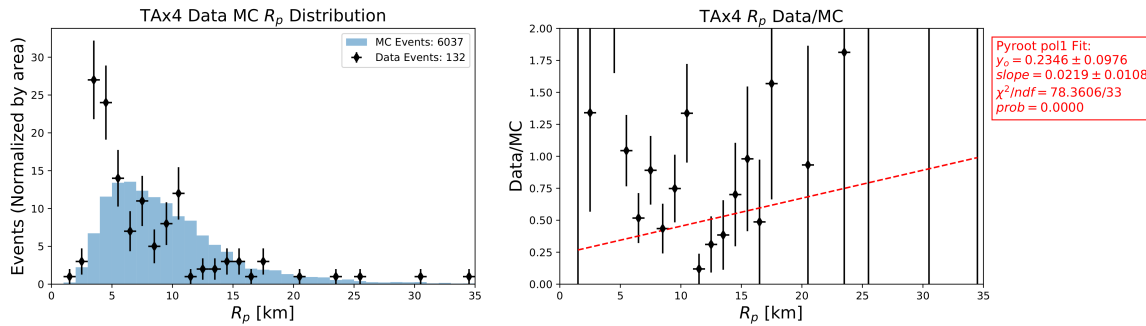


**Figure 5.3:** TAx4  $R_p$  Data/MC comparison.

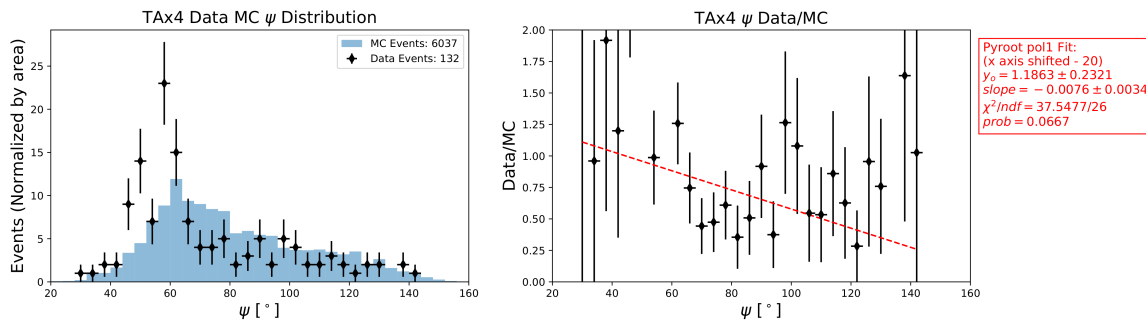


**Figure 5.4:** TAx4  $\psi$  Data/MC comparison.

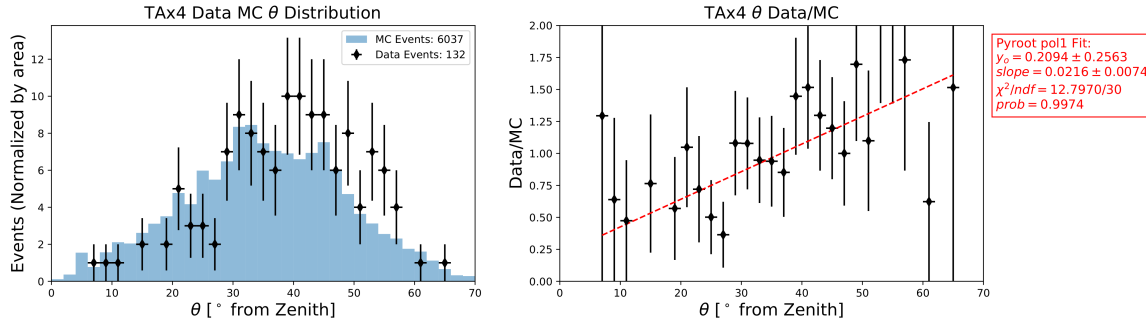


**Figure 5.5:** TAX4  $\theta_{\text{zenith}}$  Data/MC comparison.

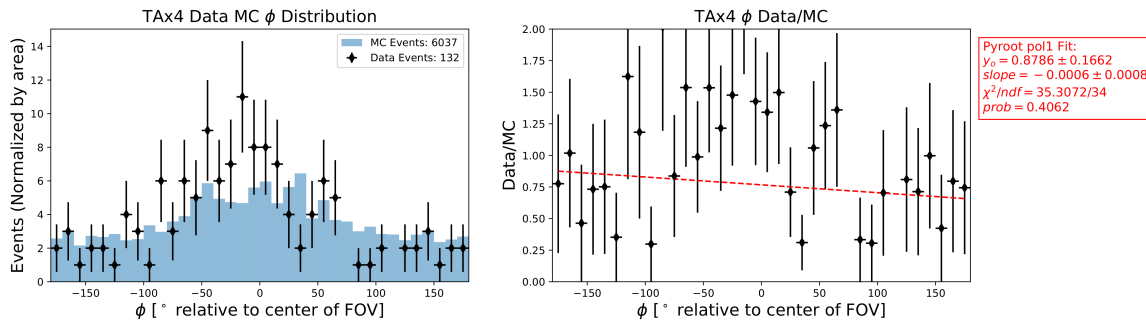


**Figure 5.6:** TAX4  $\phi_{\text{azimuth}}$  Data/MC comparison. Origin was shifted to the center of the TAX4 FOV.

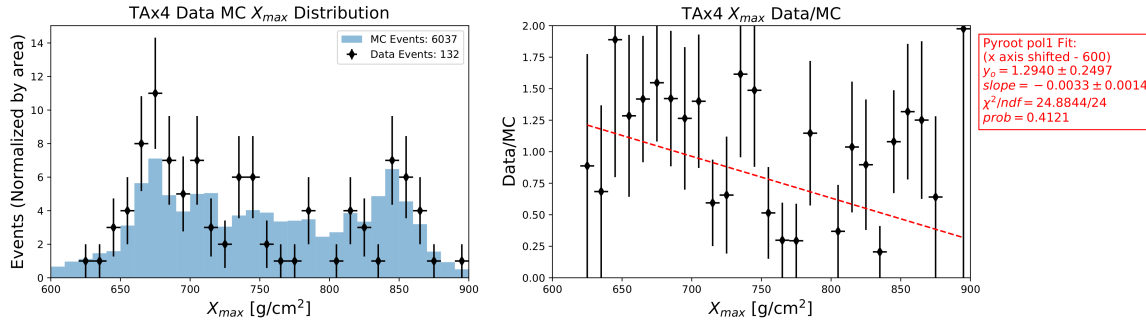


**Figure 5.7:** TAX4  $X_{\max}$  Data/MC comparison.

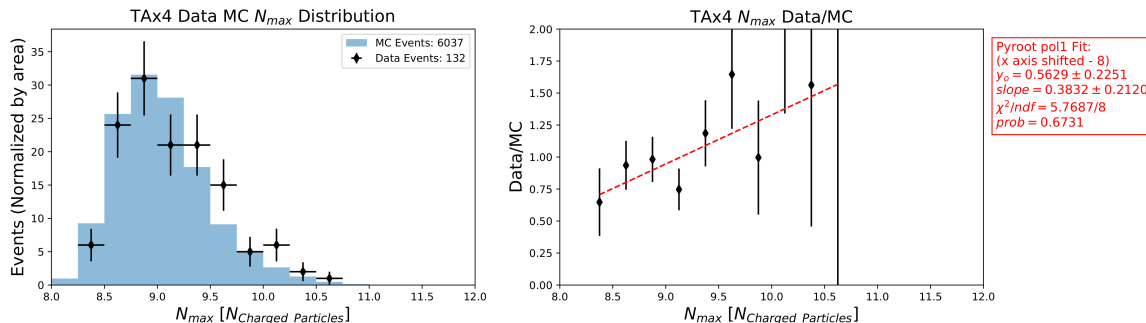


**Figure 5.8:** TAX4  $N_{\max}$  Data/MC comparison.

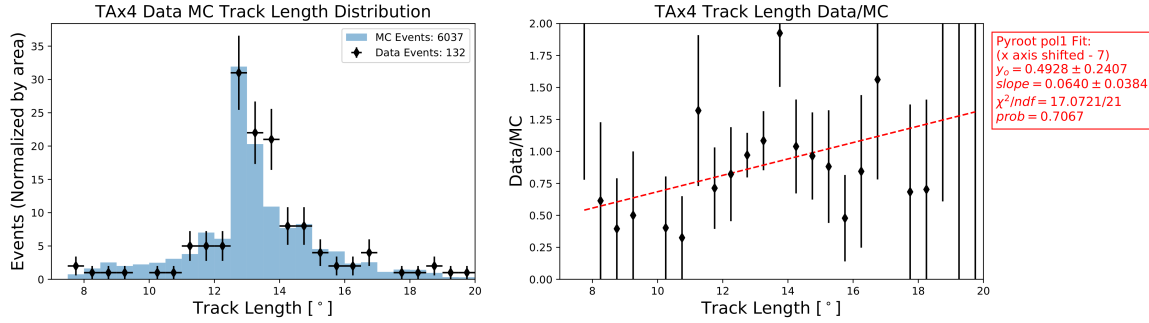


Figure 5.9: TAX4  $\Delta\theta$  Data/MC comparison.

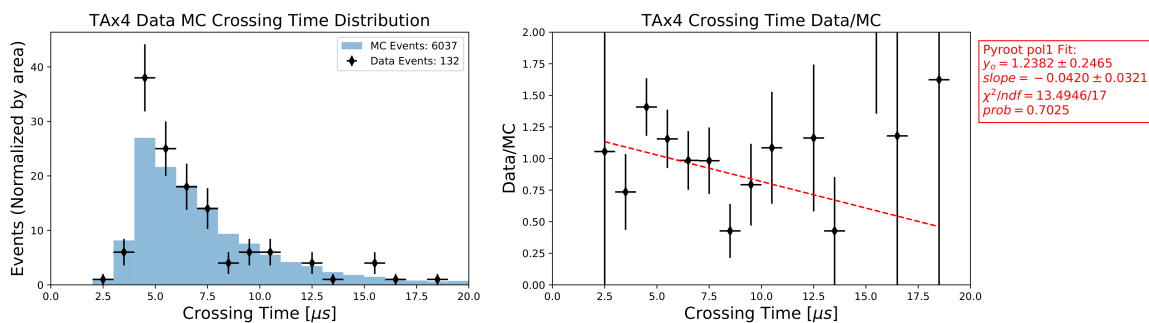
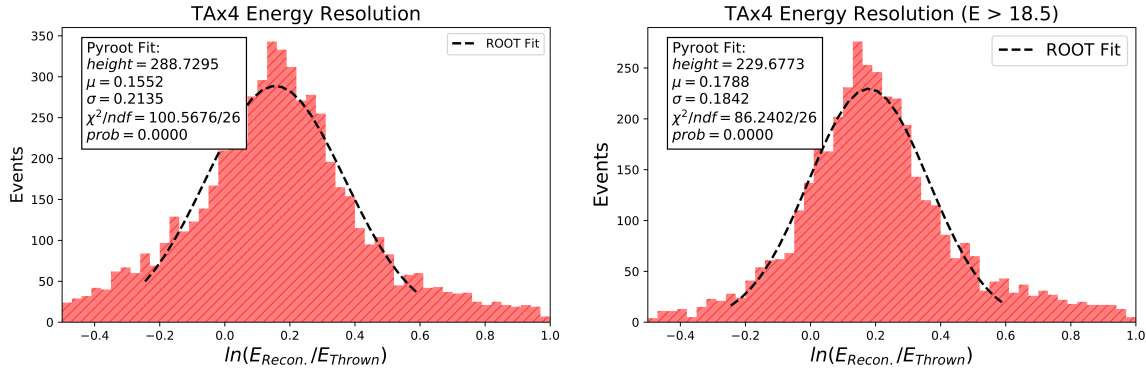
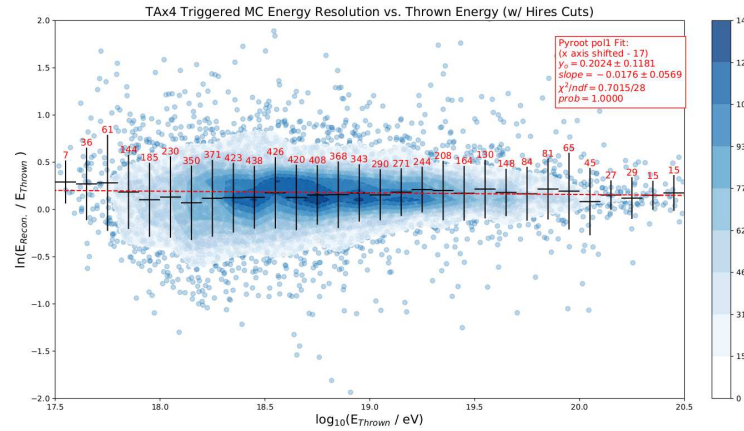


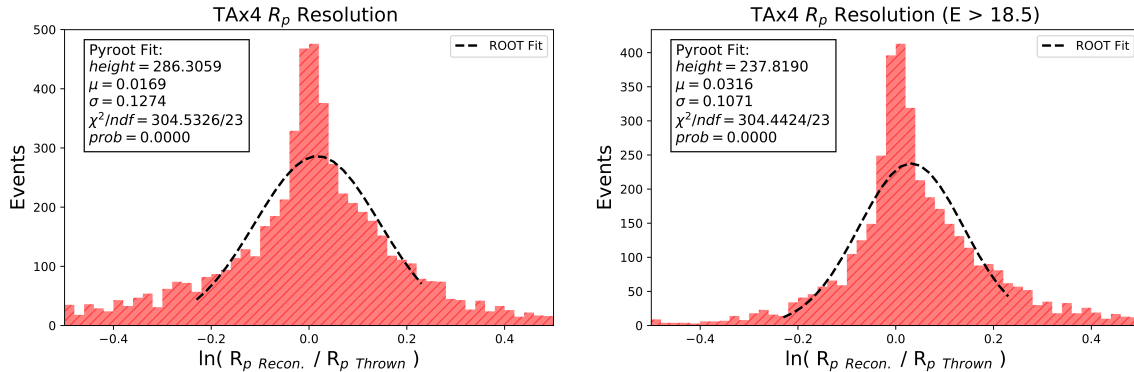
Figure 5.10: TAX4  $\Delta t_{\text{crossing}}$  Data/MC comparison.

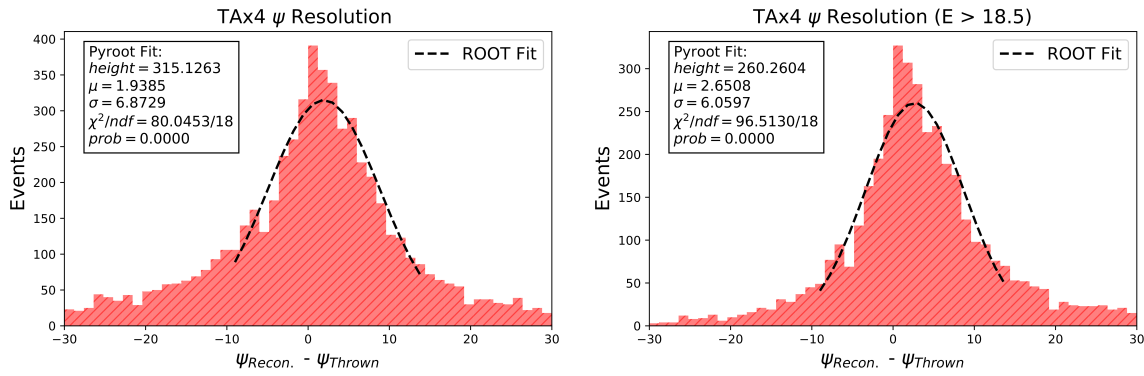


(a) TAX4 energy reconstruction resolution.

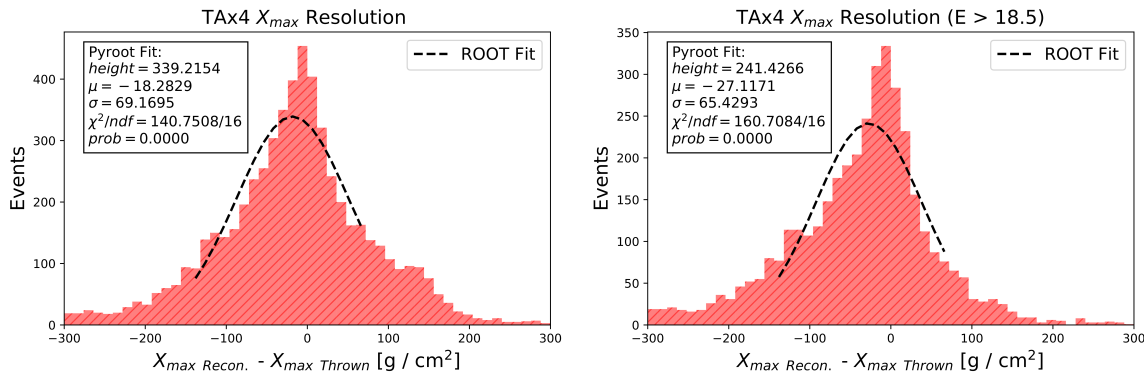


**(b) TAX4 energy reconstruction profile.** Each point represents an MC event and contours are add over high density regions of the profile. The energy reconstruction for all events is binned by the thrown energy. The mean and standard deviation of each bin as an estimation of the bin resolution is shown in black. A linear fit to the bin means was calculated. Each bin contains the origin within its standard deviation, thus, the values are considered to be of quality agreement despite the  $y$ -intercept in the linear fit.

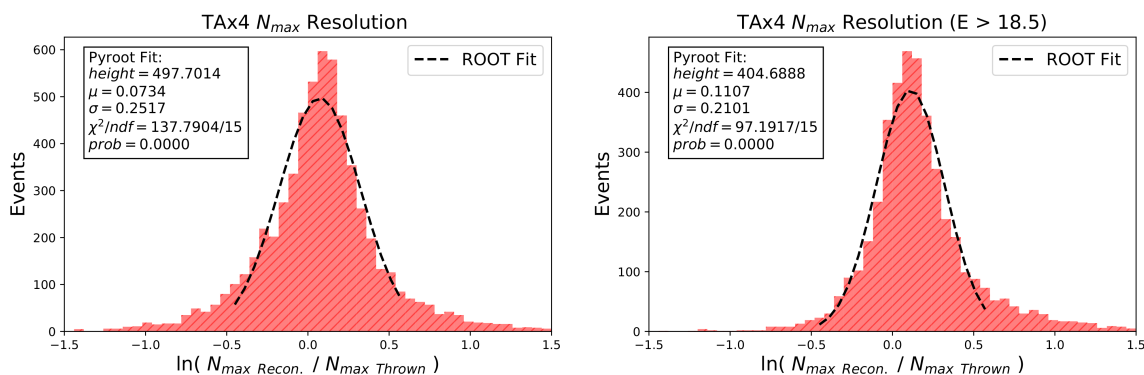
**Figure 5.11:** TAX4 energy reconstruction resolution.**Figure 5.12:** TAX4  $R_p$  reconstruction resolution.



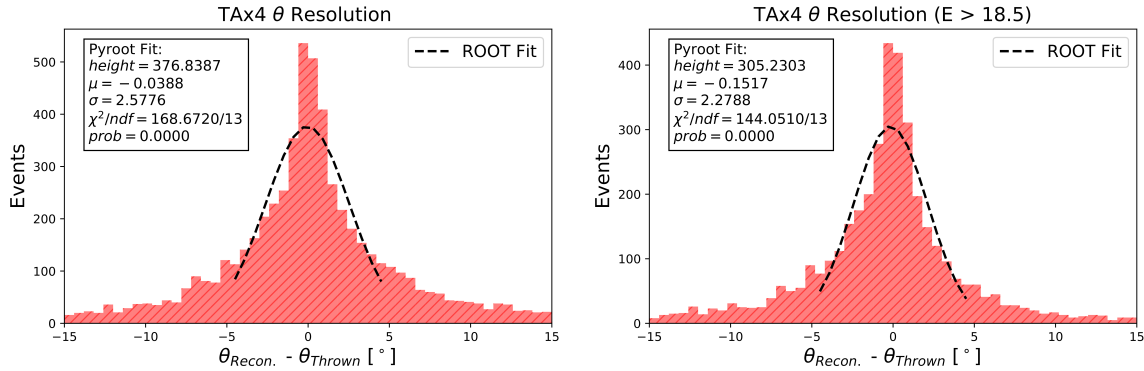
**Figure 5.13:** TAX4  $\psi$  reconstruction resolution.



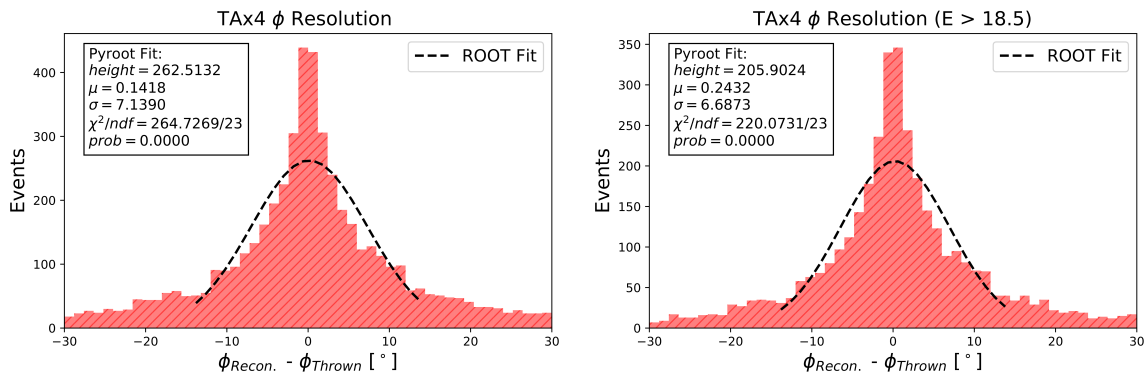
**Figure 5.14:** TAX4  $X_{\max}$  reconstruction resolution.



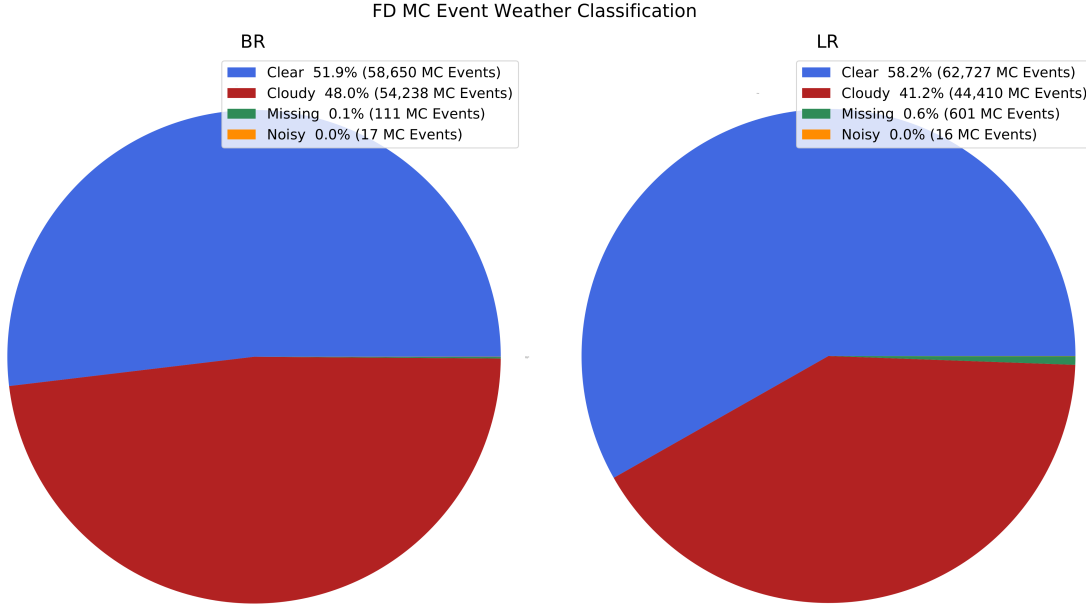
**Figure 5.15:** TAX4  $N_{\max}$  reconstruction resolution.



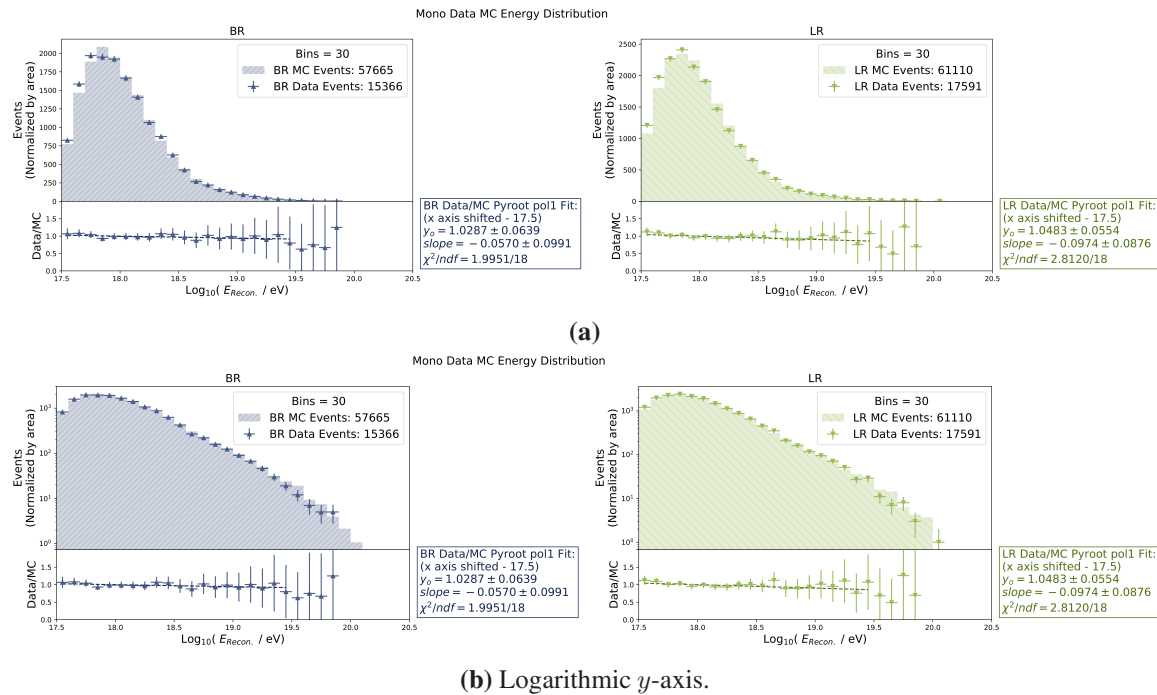
**Figure 5.16:** TAx4  $\theta_{\text{zenith}}$  reconstruction resolution.



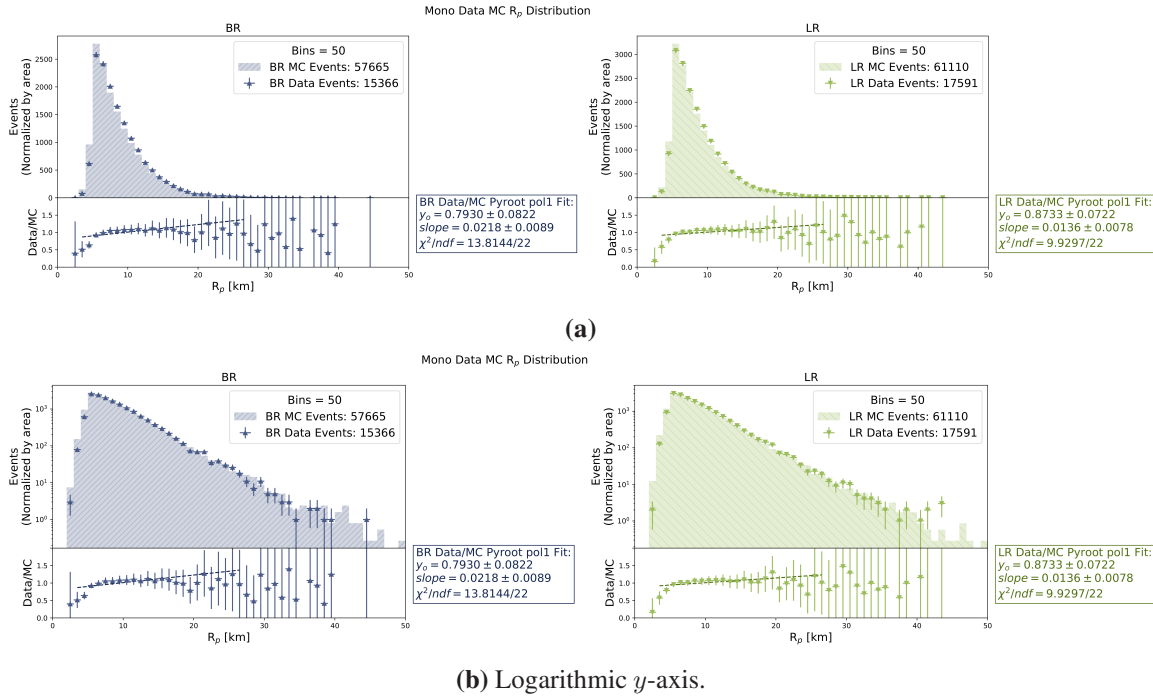
**Figure 5.17:** TAx4  $\phi_{\text{azimuth}}$  reconstruction resolution.



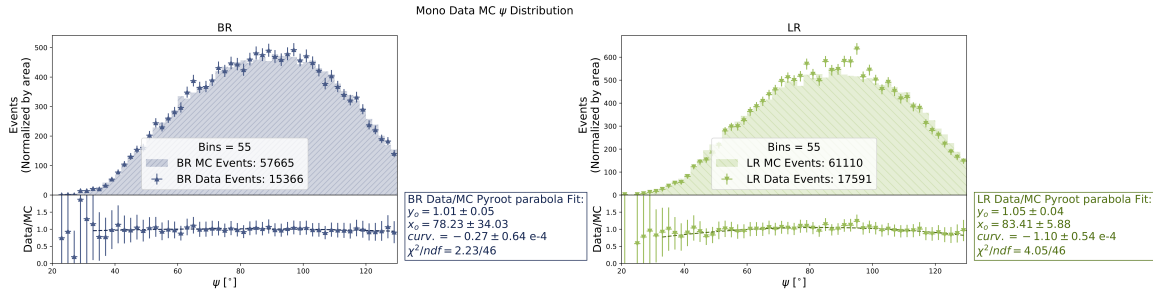
**Figure 5.18:** All BR and LR MC FD event weather classification using the RCNN neural network weather cuts from Chapter 4.



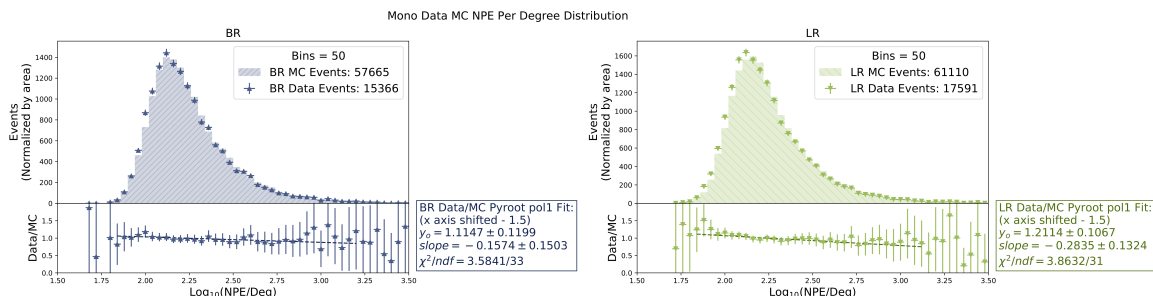
**Figure 5.19:** BR and LR reconstructed energy Data/MC comparison.



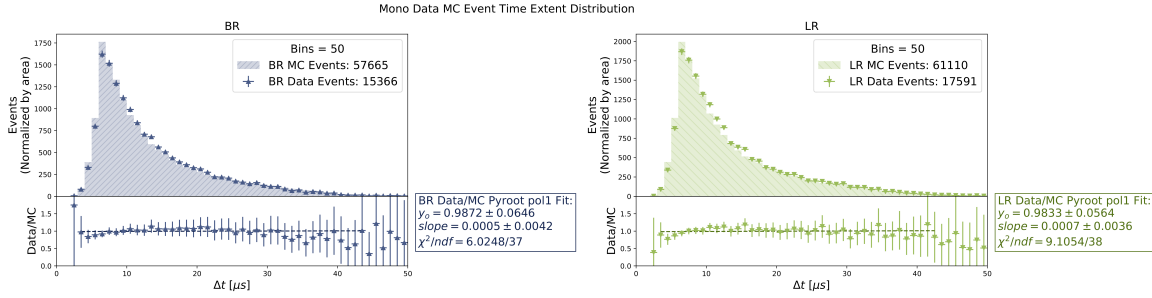
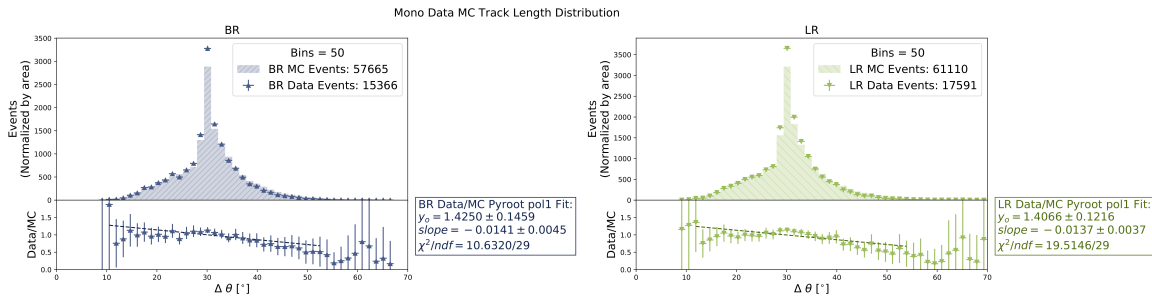
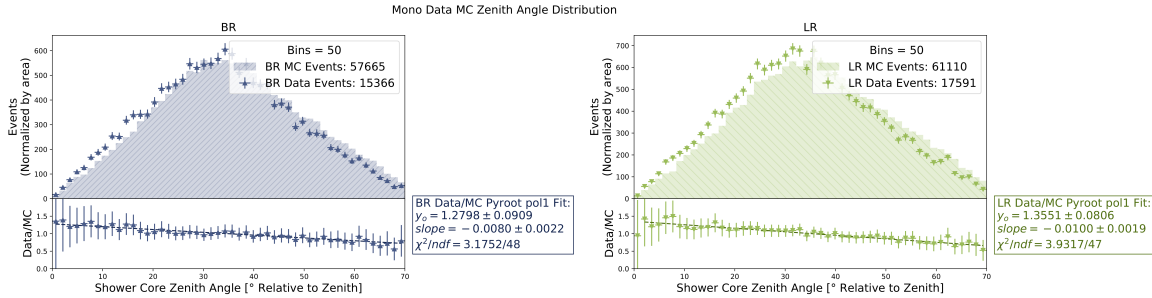
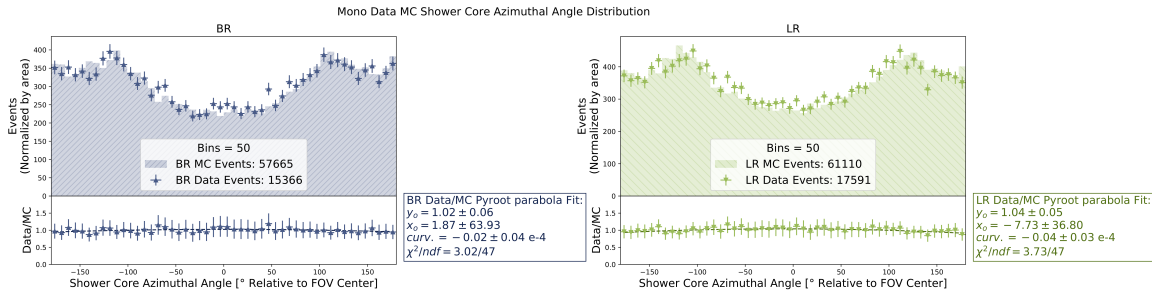
**Figure 5.20:** BR and LR  $R_p$  Data/MC comparison.



**Figure 5.21:** BR and LR  $\psi$  Data/MC comparison.



**Figure 5.22:** BR and LR  $\log_{10}(\text{NPE}/\text{deg})$  Data/MC comparison.

Figure 5.23: BR and LR  $\Delta t$  Data/MC comparison.Figure 5.24: BR and LR  $\Delta\theta$  Data/MC comparison.Figure 5.25: BR and LR  $\theta_{\text{zenith}}$  Data/MC comparison.Figure 5.26: BR and LR  $\phi_{\text{azimuth}}$  Data/MC comparison.

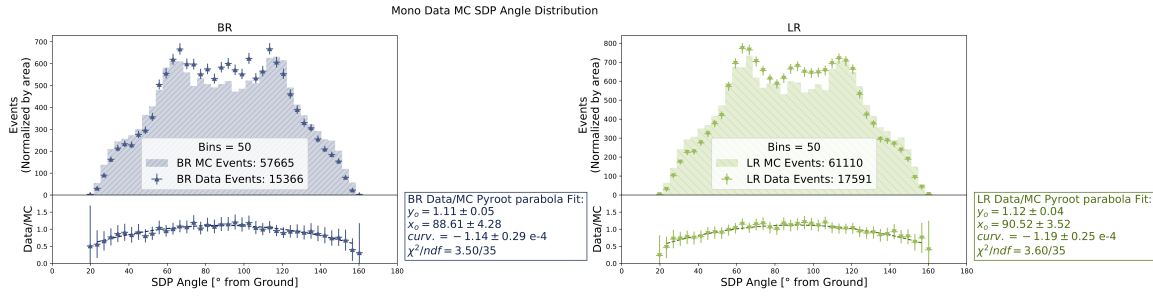


Figure 5.27: BR and LR  $\theta_{\text{SDP}}$  Data/MC comparison.

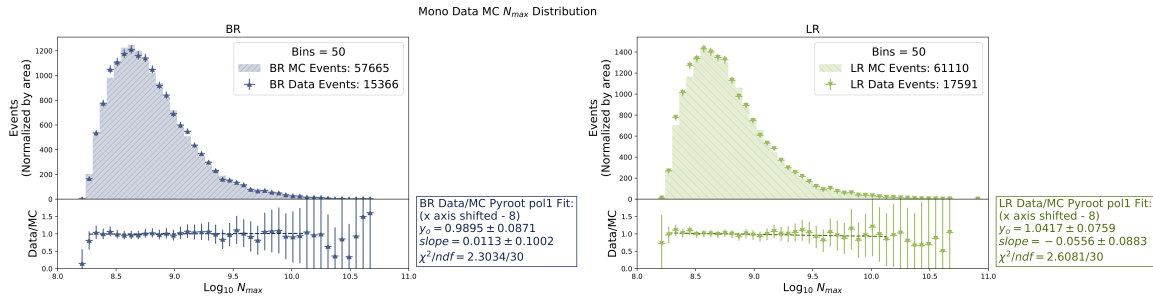


Figure 5.28: BR and LR  $N_{\text{max}}$  Data/MC comparison.

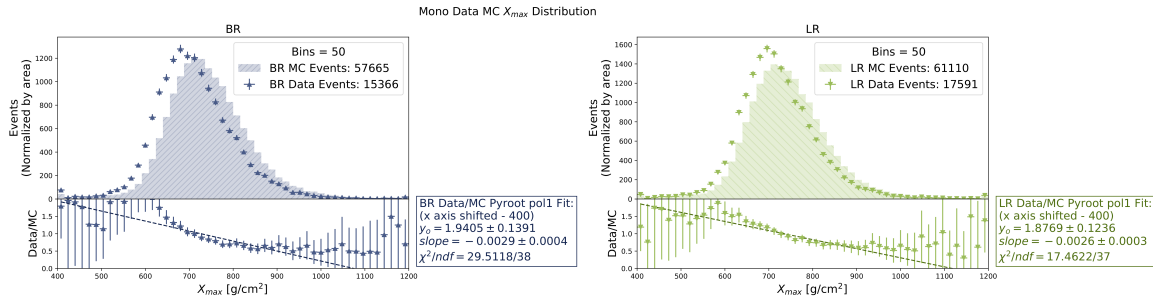


Figure 5.29: BR and LR  $X_{\text{max}}$  Data/MC comparison.

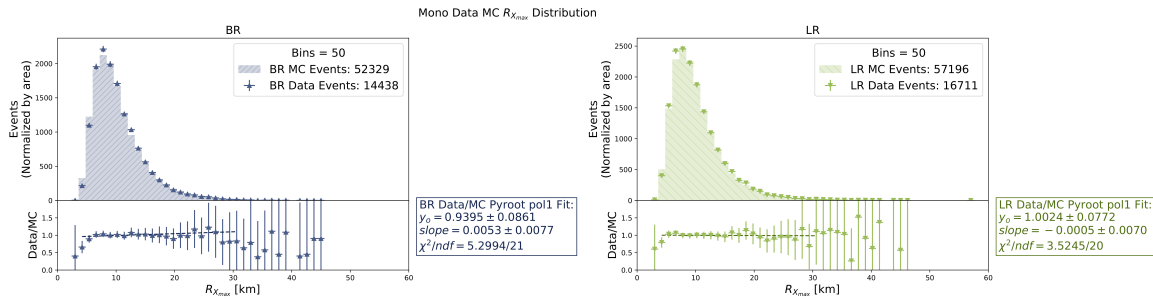
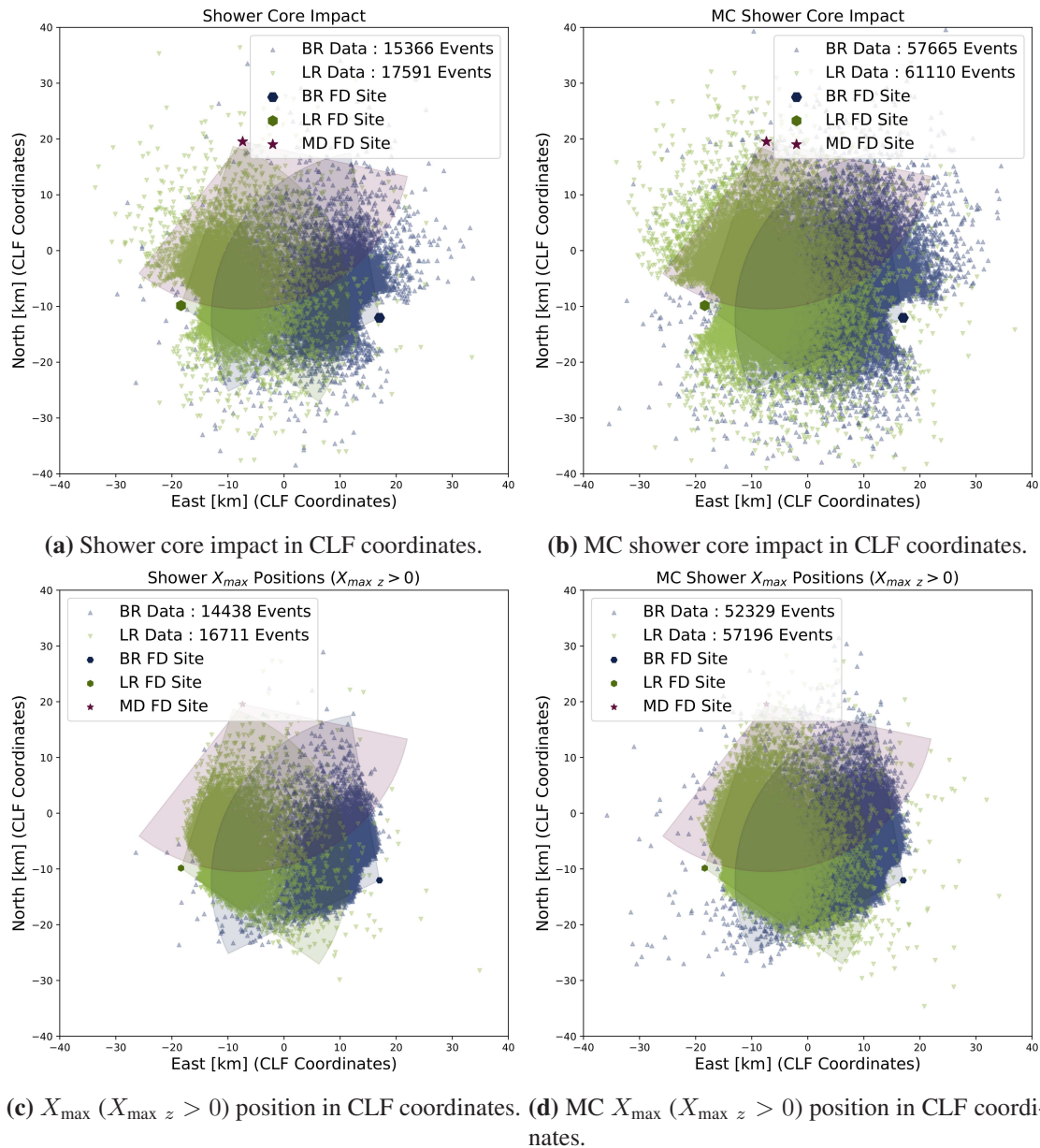
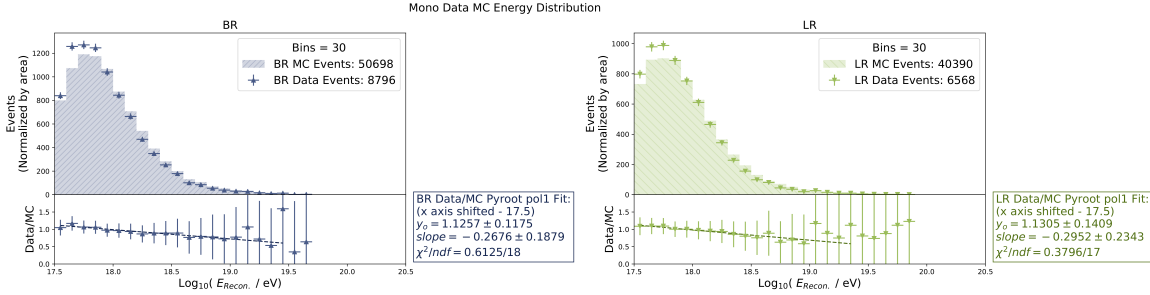


Figure 5.30: BR and LR  $R_{X_{\text{max}}}$  Data/MC comparison.



**Figure 5.31:** BR and LR  $X_{\max}$  and shower core impact positions.



**Figure 5.32:** Bad weather BR and LR  $X_{\max}$  Data/MC comparison. Compare with Figure 5.19a.

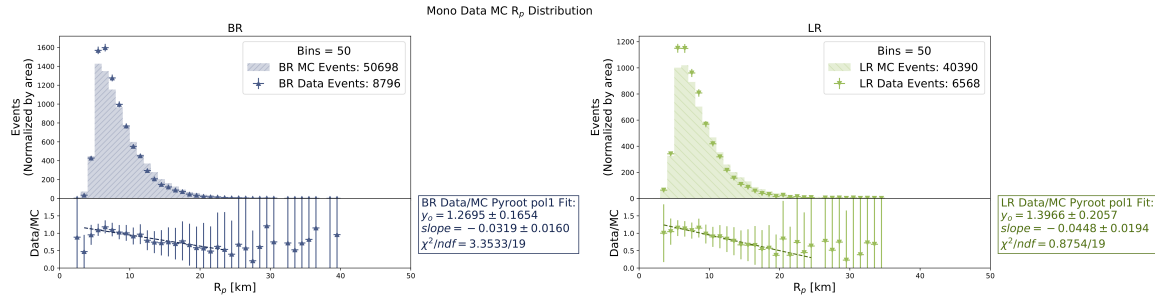


**Figure 5.33:** Bad weather BR and LR  $R_p$  Data/MC comparison. Compare with Figure 5.20a.

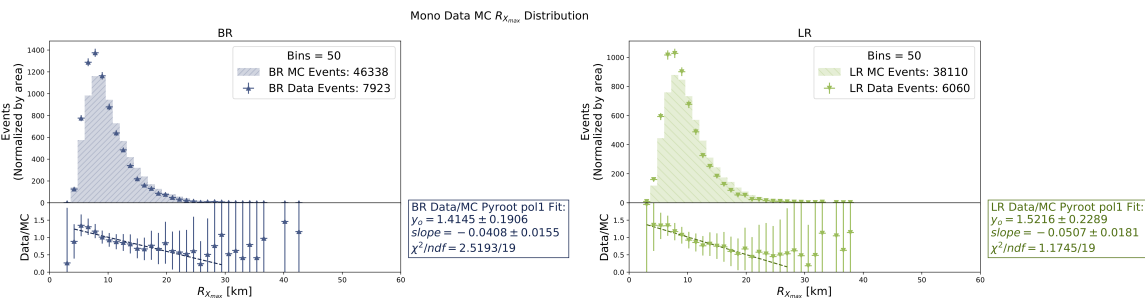


**Figure 5.34:** Bad weather BR and LR  $R_{X_{\max}}$  Data/MC comparison. Compare with Figure 5.30.

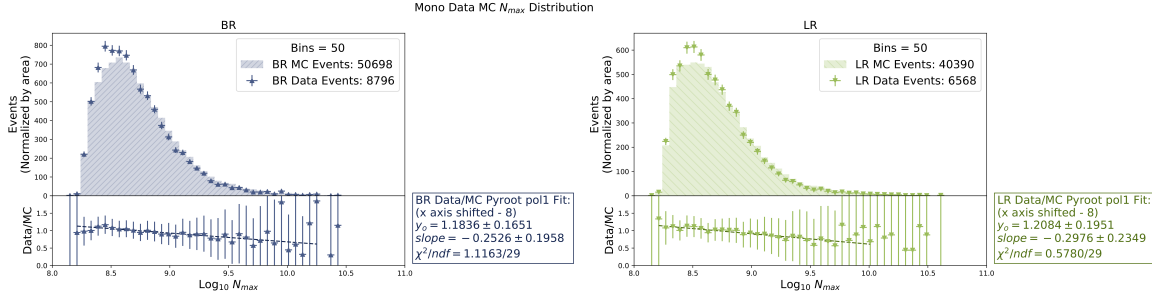


**Figure 5.35:** Bad weather BR and LR  $N_{\max}$  Data/MC comparison. Compare with Figure 5.28.

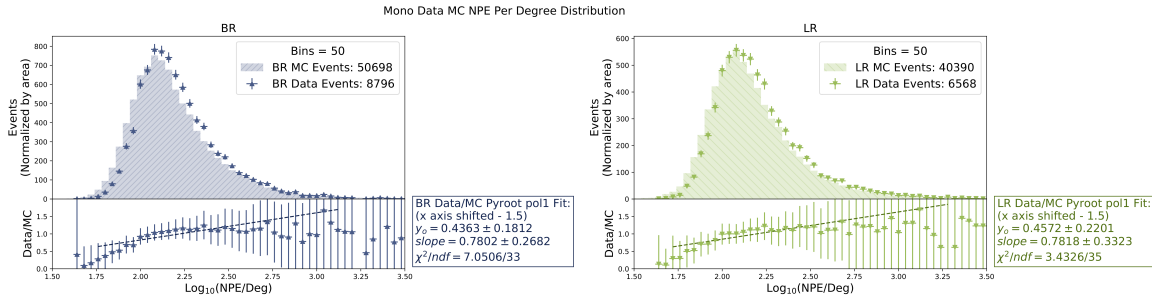


**Figure 5.36:** Bad weather BR and LR  $\log_{10}(\text{NPE}/\text{deg})$  Data/MC comparison. Compare with Figure 5.22.

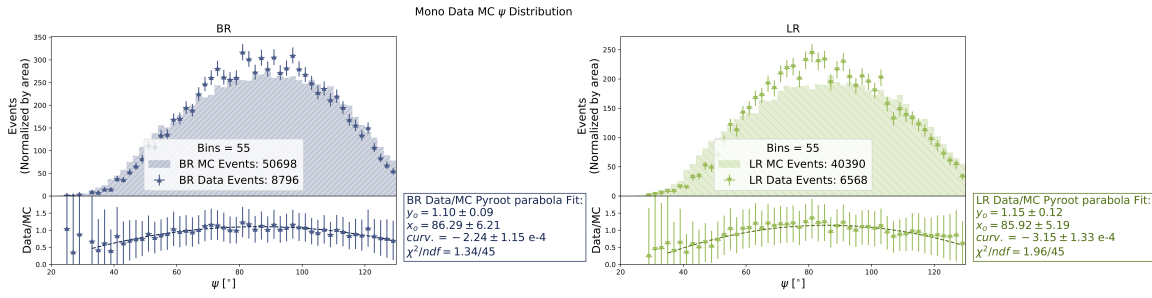


**Figure 5.37:** Bad weather BR and LR  $\psi$  Data/MC comparison. Compare with Figure 5.21.

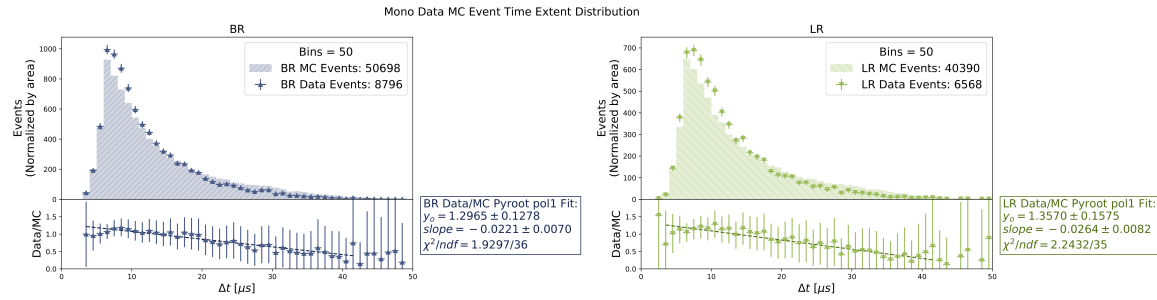


**Figure 5.38:** Bad weather BR and LR  $\Delta t$  Data/MC comparison. Compare with Figure 5.23.

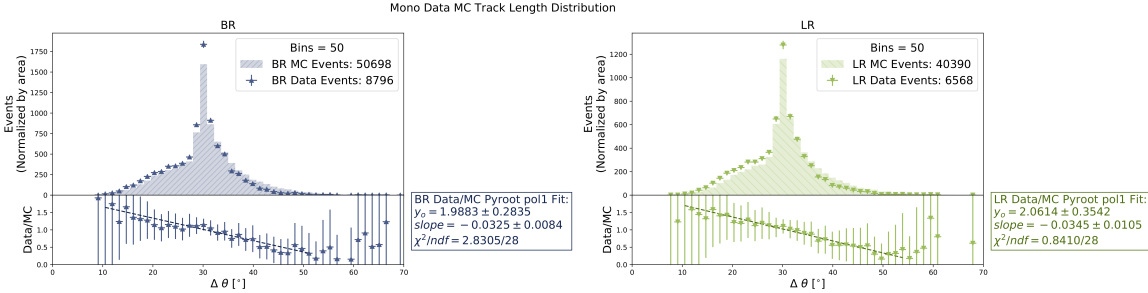


**Figure 5.39:** Bad weather BR and LR  $\Delta\theta$  Data/MC comparison. Compare with Figure 5.24.

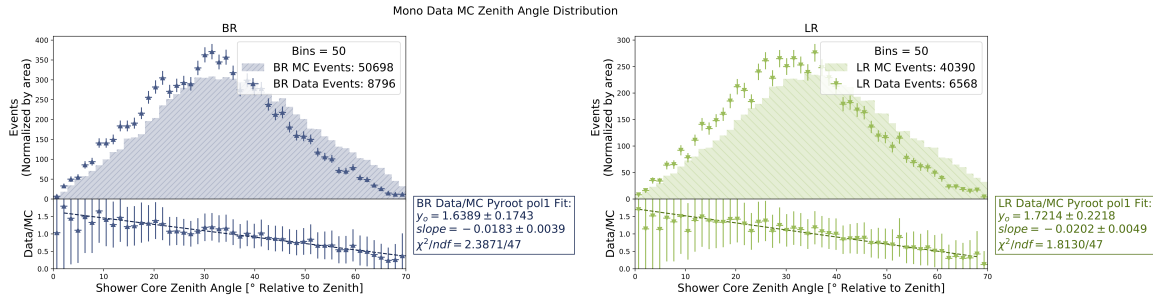


**Figure 5.40:** Bad weather BR and LR  $\theta_{\text{zenith}}$  Data/MC comparison. Compare with Figure 5.25.

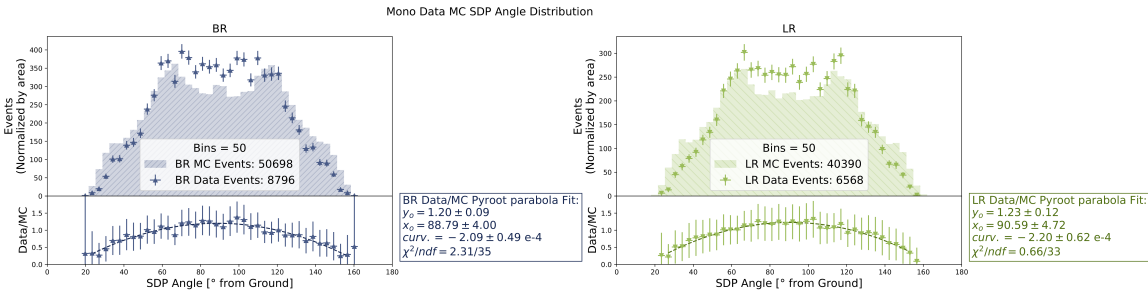
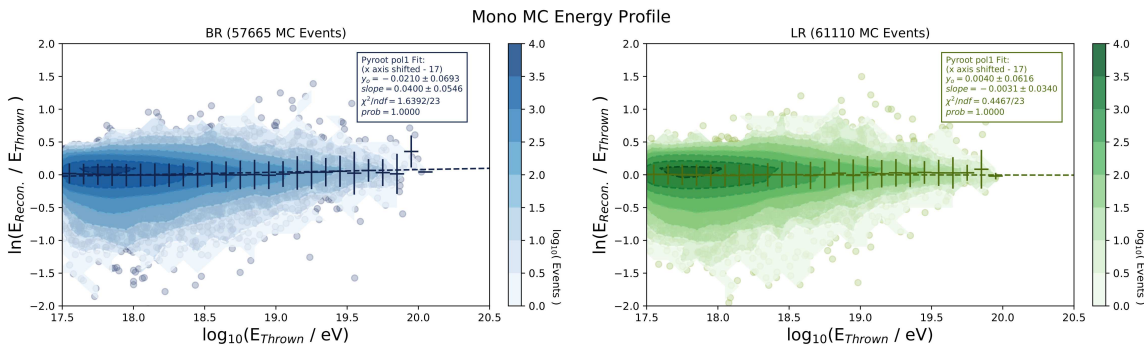
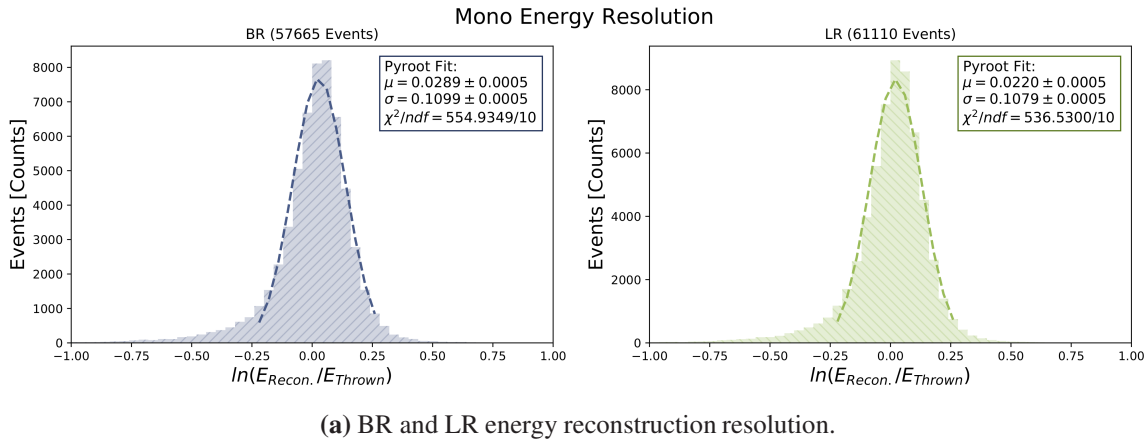


**Figure 5.41:** Bad weather BR and LR  $\theta_{\text{SDP}}$  zenith Data/MC comparison. Compare with Figure 5.27.

**Table 5.4:** BR and LR FD event monocular reconstruction resolution.

Parameter	BR Resolution	LR Resolution	Figure
$E$	11%	11%	5.42a
$R_p$	3.9%	3.8%	5.43
$\psi$	$3.6^\circ$	$3.6^\circ$	5.44
$X_{\max}$	$37\text{g/cm}^2$	$38\text{g/cm}^2$	5.45
$N_{\max}$	11%	11%	5.46
$\theta_{\text{zenith}}$	$1.5^\circ$	$1.6^\circ$	5.47
$\phi_{\text{azimuth}}$	$4.5^\circ$	$4.3^\circ$	5.48
$R_{X_{\max}}$	6.9%	6.9%	5.49



(b) BR and LR energy reconstruction profile. Each point represents an MC event and contours are add over high density regions of the profile. The energy reconstruction for all events is binned by the thrown energy. The mean and standard deviation of each bin as an estimation of the bin resolution is shown in black. A linear fit to the bin means was calculated.

Figure 5.42: BR and LR energy reconstruction resolution.

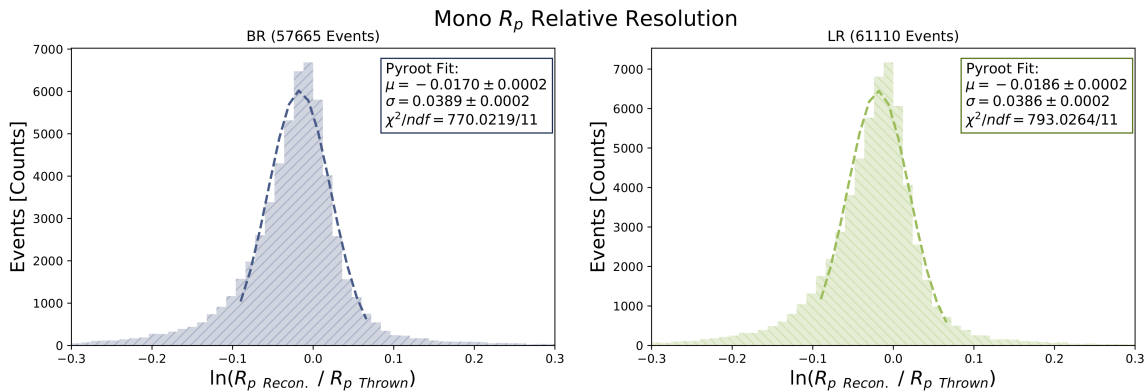
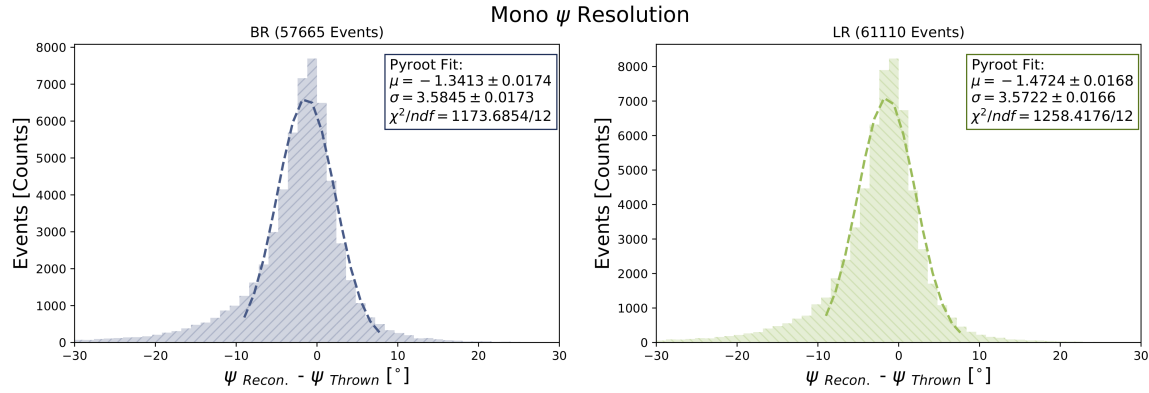
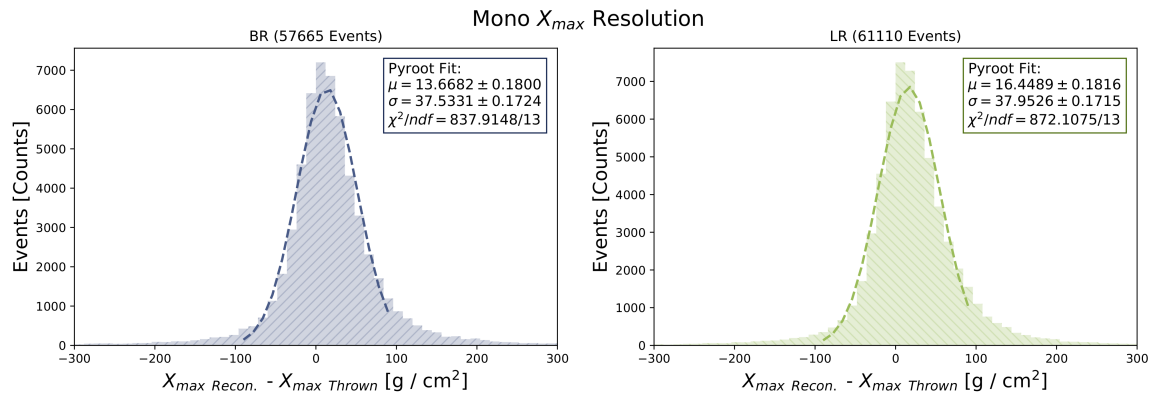


Figure 5.43: BR and LR  $R_p$  reconstruction resolution.



**Figure 5.44:** BR and LR  $\psi$  reconstruction resolution.



**Figure 5.45:** BR and LR  $X_{\max}$  reconstruction resolution.

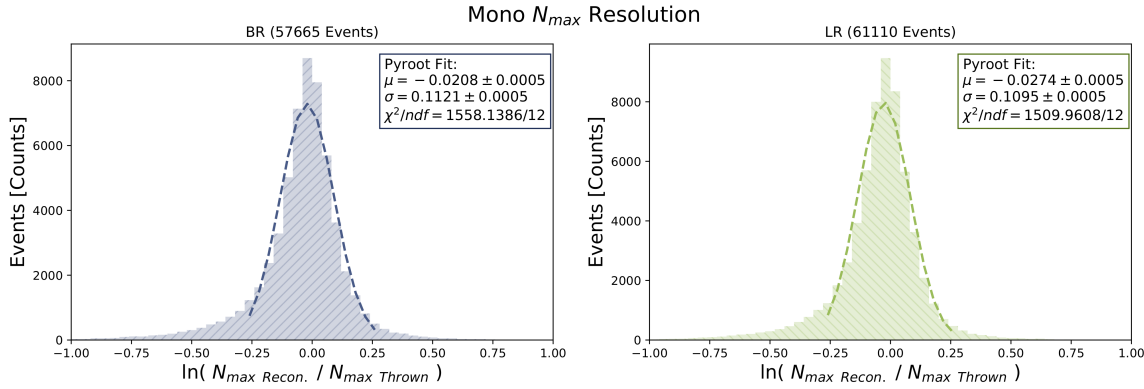


**Figure 5.46:** BR and LR  $N_{\max}$  reconstruction resolution.

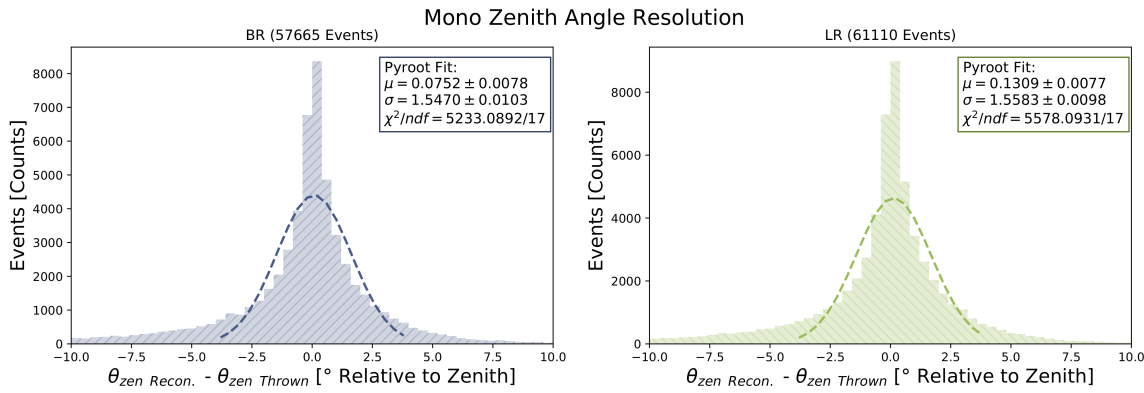


**Figure 5.47:** BR and LR  $\theta_{\text{zenith}}$  reconstruction resolution.

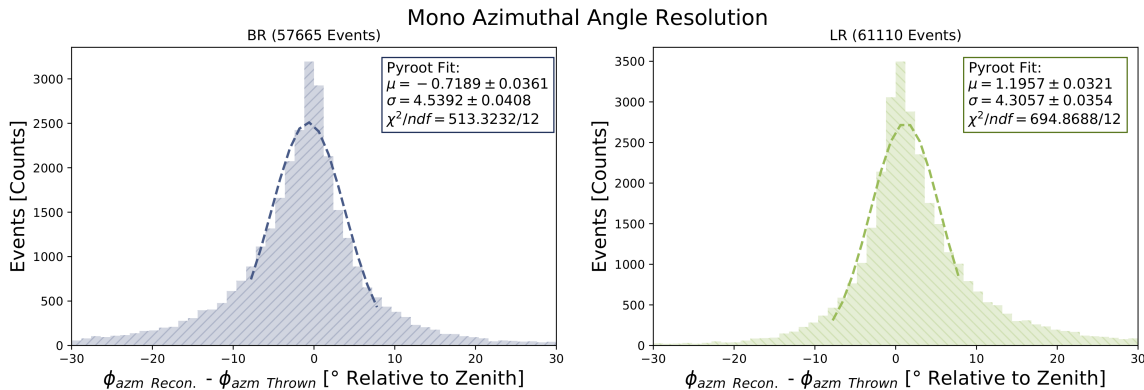


**Figure 5.48:** BR and LR  $\phi_{\text{azimuth}}$  reconstruction resolution.

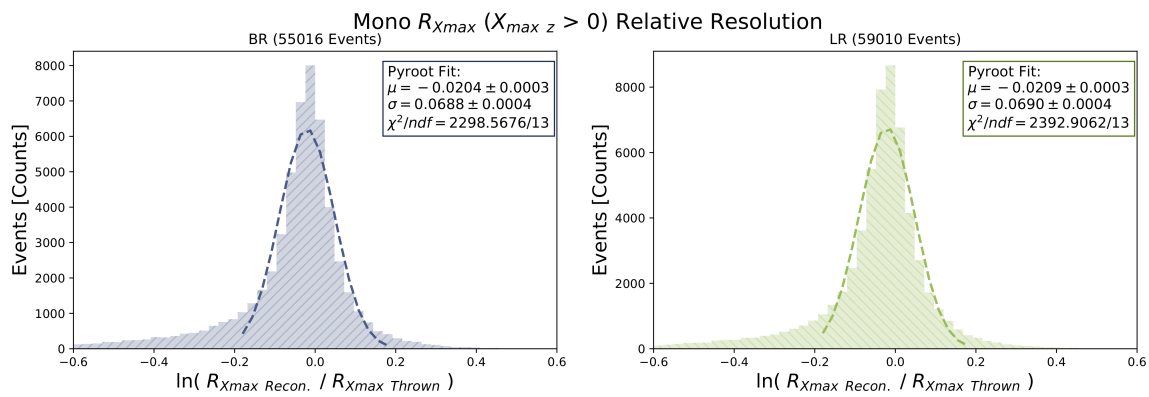


**Figure 5.49:** BR and LR  $R_{X_{\max}}$  reconstruction resolution.

# CHAPTER 6

## TAX4 MD FD PRELIMINARY COSMIC RAY ENERGY SPECTRUM

The amount of events,  $N(E_i)$ , that a cosmic ray detector observes at energy  $E_i$  within an energy bin  $\Delta E_i$  is

$$N(E_i) \Big|_{E_i}^{E_i + \Delta E_i} = \int_{E_i}^{E_i + \Delta E_i} J(E') A\Omega(E') T dE' \quad (6.1)$$

$$\approx J(E_i) A\Omega(E_i) T \Delta E_i \quad (6.2)$$

where  $J(E_i)$  is the cosmic ray energy spectrum,  $A\Omega(E_i)$  is the detector aperture, and  $T$  is the detector livetime. The cosmic ray energy spectrum is the differential flux of particles per area per solid angle per time as a function of energy. The cosmic ray energy spectrum can be calculated using the detected events as

$$J(E_i) = \frac{N(E_i)}{\Delta E_i A\Omega(E_i) T}. \quad (6.3)$$

The MC was used to determine the TAX4 MD aperture as a function of the cosmic ray energy,  $A\Omega(E_i)$ . The length of each FD data part was used to determine the detector livetime  $T$ . A preliminary TAX4 MD FD cosmic ray energy spectrum was calculated using the observed events in epochs 0 and I and the calculated livetime and exposure.

### 6.1 Event Distribution

The event distribution for the reconstructed events observed by TAX4 is shown in Figure 6.1. Only 132 events passed reconstruction and quality cuts and weather cuts. The quality cuts reduce the events by about 80%, which is reflected in the weighted MC event distribution used for the aperture calculation. The weather selection cuts reduce the events by another 50 % to a total of a 90 % reduction. Reconstructed events with  $\log_{10}(E/\text{eV}) < 17.4$  were completely removed by the quality cuts. The statistics of the number of events that triggered and then passed each stage of the reconstruction are listed in Table 6.1. The number of triggers in the FD increase between epoch I compared to epoch 0 as the column thickener was installed on the TAX4 trigger boards.

### 6.1.1 TAx4 Comparison with HiRes-I

The TAx4 event distribution was compared to that of the HiRes-I experiment<sup>[63]</sup>. This comparison is suitable as both are ring 1 FD telescope systems with the same elevation angle coverage. However, HiRes-I looked roughly a full  $360^\circ$  in azimuth while TAx4 MD FD looks over about  $90^\circ$ . Both event distributions (with  $\log_{10}(E/\text{eV}) \leq 18$ ) were normalized by the total number of events observed. The weather cuts were not applied to the TAx4 events, boosting the number of events. The two distributions, shown in Figure 6.2, are in agreement except at the highest energies. This difference in the highest energy bins can be attributed to the limited exposure of TAx4 for epochs 0 and I. The quality cuts of the HiRes analysis were updated after the cited HiRes result used in the comparison. The updated quality cuts removed the excess of high energy events in the later HiRes analyses. TAx4 MD FD compares well to the HiRes-I distribution. This result is a good indication that TAx4 MD FD is working as expected.

## 6.2 Thrown Monte Carlo Event Distribution

As stated in Chapter 5, one of the purposes of the MC is to determine the aperture of the detector. 5 million events were thrown using mc2k12 with a spectral index of  $\gamma = 2$ . However, the observed cosmic ray flux follows a  $\gamma \approx 3$ . A  $\gamma = 2$  was chosen to fill out events at the highest energies with increased statistics. Both the thrown and reconstructed events with quality cuts were weighted according to TA combined spectrum from the ICRC 2015<sup>[78]</sup> to have the thrown distribution then match the form of the observed spectrum. The results of the reweighting of the thrown and reconstructed event distributions are shown in Figure 6.3. Much like the observed events, the reconstructed MC cuts off at  $\log_{10}(E/\text{eV}) = 17.3$ . The spectral breaks of the ankle at  $\log_{10}(E/\text{eV}) = 18.7$  and the second break beyond the ankle which is attributed to the GZK suppression (discussed in Section 1.3) at  $\log_{10}(E/\text{eV}) = 19.8$  are seen in the thrown distribution. The MC events and reconstruction statistics are given in Table 6.2.

## 6.3 Weather Cuts

The weather cuts applied to the TAx4 events are based on the MD weat codes described in Section 4.2. The weather classes based on these weat codes were modified slightly from Table 4.2 as TAx4 MD FD looks northeast. Table 6.3 lists the weather classes defined for the TAx4 MD FD analysis. A weat code was assigned to every event processed through TLFDP0 by reading the corresponding time-stamped code from the MD FD operations logs. The weather classification breakdown for TAx4 by data part, total ontime, and by events are in Figure 6.4.

## 6.4 Ontime

For TAx4, the ontime and livetime of the detector are interchangeable as the trigger system was designed to be deadtimeless. TLFDP0 reports the start and stop of each TAx4 FD data part. The total ontime is calculated by summing over the time duration of each data part. Figure 6.5a shows the accumulated ontime of TAx4 MD FD. The MD station is only operated for any night with more than 3 hours of operation given the lunar phase and the season. The shift between the summer and winter night lengths is seen in the accumulated ontime. The *duty cycle* (the total accumulated operation time over the total time elapsed since the operation began) for TAx4 MD FD is 7.19%. The accumulated ontime with the weather cuts applied is shown in Figure 6.5b. For epoch 0 and I, TAx4 MD FD operated for 366 hours of good and excellent weather data out of 629 hours of total operation.

## 6.5 Detector Acceptance and Aperture

Using the MC generated in `mc2k12` and the weighted thrown and reconstructed MC events in Figure 6.3 were used to calculate TAx4 MD FD acceptance using Equation 5.1.

The volume into which events were thrown in using `mc2k12` is calculated as, using the bounds of  $R_p$  and  $\theta_{\text{zenith}}$  defined in Table 5.2,

$$A_0 = \pi(R_p^2_{\max} - R_p^2_{\min}) \quad (6.4)$$

$$\Omega_0 = 2\pi(1 - \cos(\theta_{\text{zenith max}})) \quad (6.5)$$

$$A_0\Omega_0 = 3.24698 \times 10^{10} \text{ m}^2 \text{ sr.} \quad (6.6)$$

The aperture of the detector, shown in Figure 6.6, was calculated using  $A_0\Omega_0$  and the acceptance in Equation 5.2.

## 6.6 Detector Exposure

The detector *exposure*,  $\xi(E)$ , is the aperture multiplied by the livetime of the detector,

$$\xi(E) = A\Omega T. \quad (6.7)$$

The spectrum can be calculated using the exposure as

$$J(E_i) = \frac{N(E_i)}{\Delta E_i \xi(E)}. \quad (6.8)$$

We fit the calculated exposure, shown in Figure 6.7a, to combined MC statistics over several bins to provide a smoother exposure for the spectrum calculation. The exposure fit function is

$$\log_{10} \xi(E) = p_1 \left( 1 - \exp \left[ -\frac{\varepsilon - p_2}{p_3} \right] \right) \quad (6.9)$$

where  $\varepsilon = \log_{10}(E/\text{eV})$ .  $p_1$  is the constant that represents the max height of the fit,  $p_2$  is the fit activation energy where the exposure starts to turn on, and  $p_3$  is the scale factor of the exponential. The exposure is plotted in Figure 6.7b and the fit results for Equation 6.9 are in Table 6.4.

## 6.7 Preliminary Cosmic Ray Energy Spectrum

Using the binned reconstructed events from Figure 6.1, binned,  $\Delta E_i$ , by one-tenth of a decade in logspace, and the exposure fit, the preliminary TAx4 MD FD spectrum was calculated. The preliminary TAx4 MD FD spectrum is shown in Figure 6.8. The preliminary spectrum shows an agreement with the TA combined ICRC 2019 spectrum<sup>[80]</sup>.

Since the cosmic ray energy spectrum follows  $\gamma \approx 3$ , to bring out the features of the spectrum that are indicative of the cosmic ray populations, the spectrum is multiplied by  $E^3$ , as shown in Figure 6.9. Again the preliminary spectrum shows an agreement with the TA combined ICRC 2019 measurement in  $JxE^3$ , but the preliminary measurement is constrained by the number of observed events in epoch 0 and I. Only 47 events were observed above  $\log_{10}(E/\text{eV}) > 18.5$ . Most importantly, the preliminary spectrum is, on average, the correct order of magnitude compared to the more robust spectrum. This result indicates that the TAx4 MD FD observed and reconstructed these initial cosmic ray events well. Thus the TAx4 FDs are dependable for the future hybrid analysis of events, which will reconstruct events using both the FDs and SDs to set the energy scale on the SD events.

**Table 6.1:** TAx4 epoch 0 and I events statistics.

Epoch 0	
122 Run Nights (20180608 - 20190409)	
Raw Triggers	366102 Events
Pass 0 (TLFDP0)	315053 Events
Pass 3 (SDP Fit)	47527 Events
Pass 2 (Rayleigh Filter)	3352 Events
Pass 4 (Geometry Recon.)	3352 Events
Pass 5 (Profile Recon.)	887 Events
Epoch I	
25 Run Nights (20190424 - 20190608)	
Raw Triggers	408785 Events
Pass 0 (TLFDP0)	396942 Events
Pass 3 (SDP Fit)	23872 Events
Pass 2 (Rayleigh Filter)	291 Events
Pass 4 (Geometry Recon.)	291 Events
Pass 5 (Profile Recon.)	254 Events
Epoch II Preliminary	
27 Run Nights (20190625 - 20190908)	
Raw Triggers	476590 Events
Pass 0 (TLFDP0)	218371 Events
Pass 3 (SDP Fit)	15635 Events
Pass 2 (Rayleigh Filter)	268 Events
Pass 4 (Geometry Recon.)	268 Events
Pass 5 (Profile Recon.)	229 Events

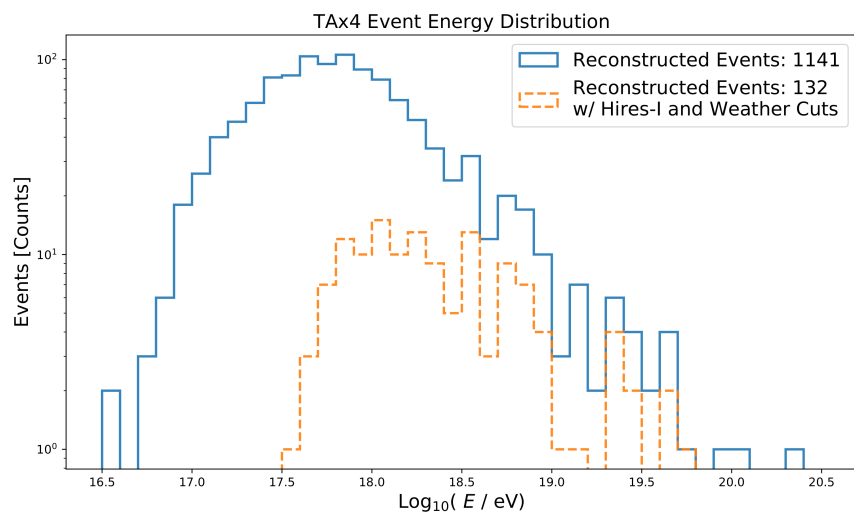


**Figure 6.1:** TAX4 reconstructed event distribution. Blue is all of the reconstructed events and orange is the reconstructed events with weather and selection cuts applied.

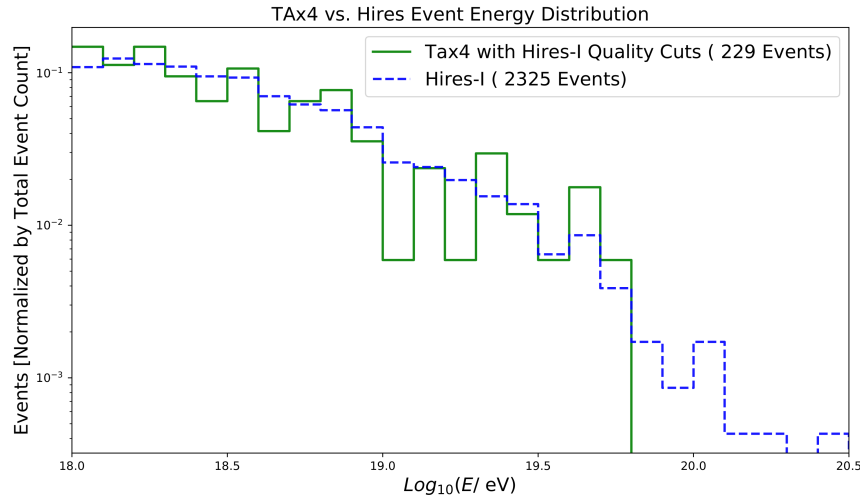


**Figure 6.2:** TAX4 vs HiRes-I<sup>[63]</sup> event distribution from May 1997 to June 1999.

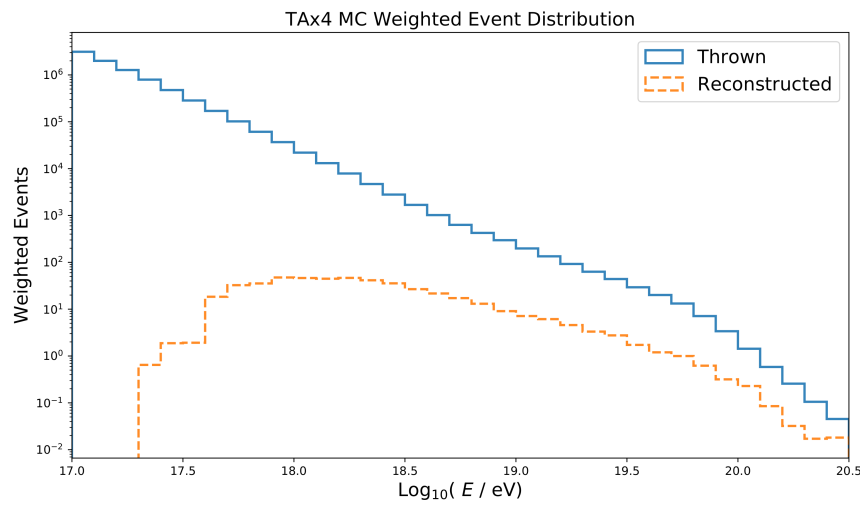


**Figure 6.3:** TAX4 reweighted MC event distribution.

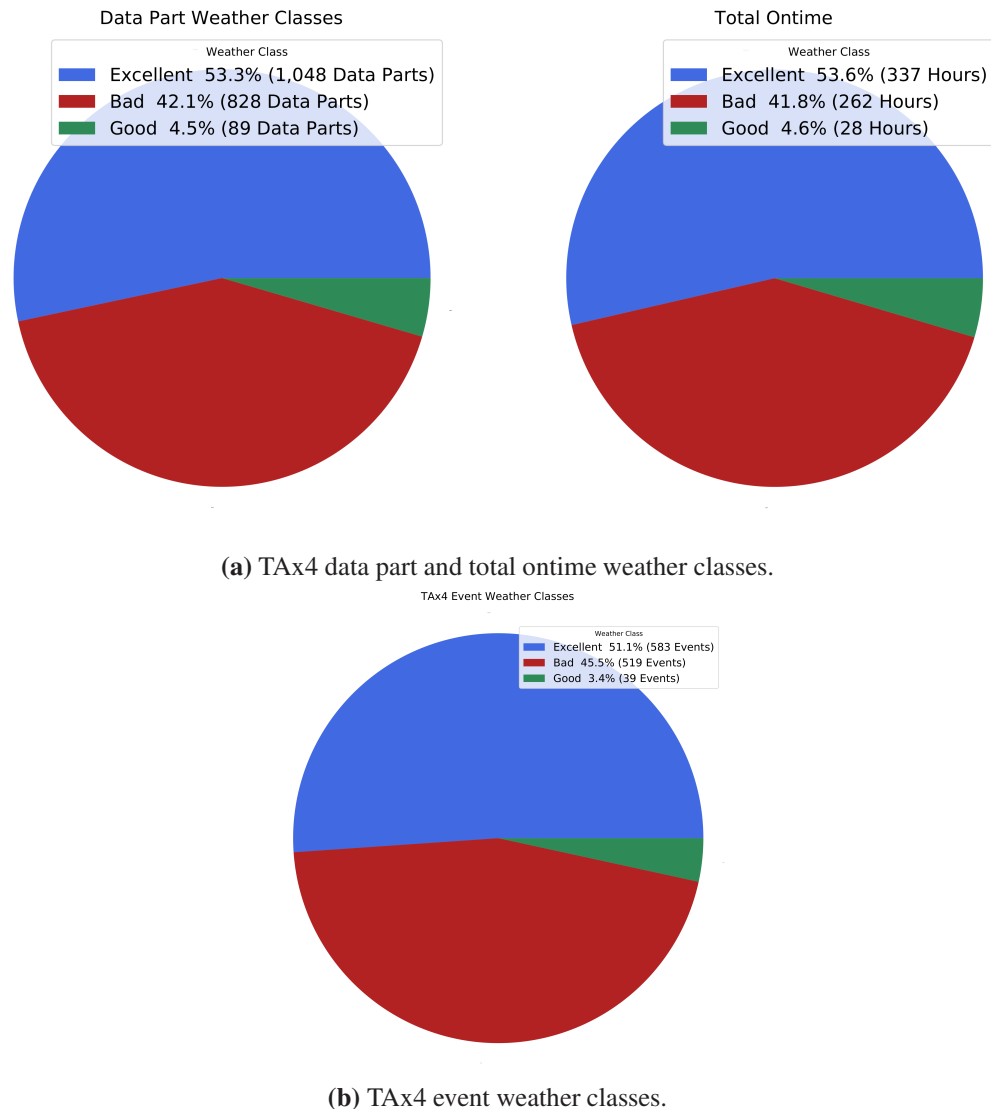
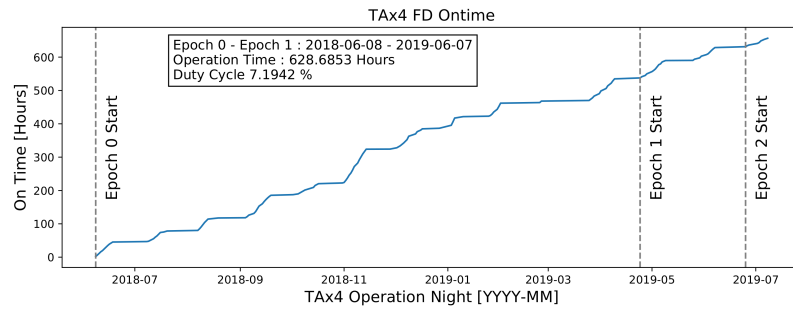
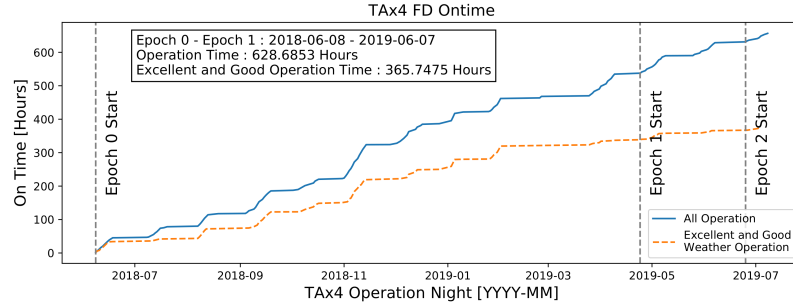


**Figure 6.4:** TAx4 weather classes from the `weat` codes.



(a) TAx4 ontine for Epoch 0 and I.



(b) TAx4 ontine with weather cuts.

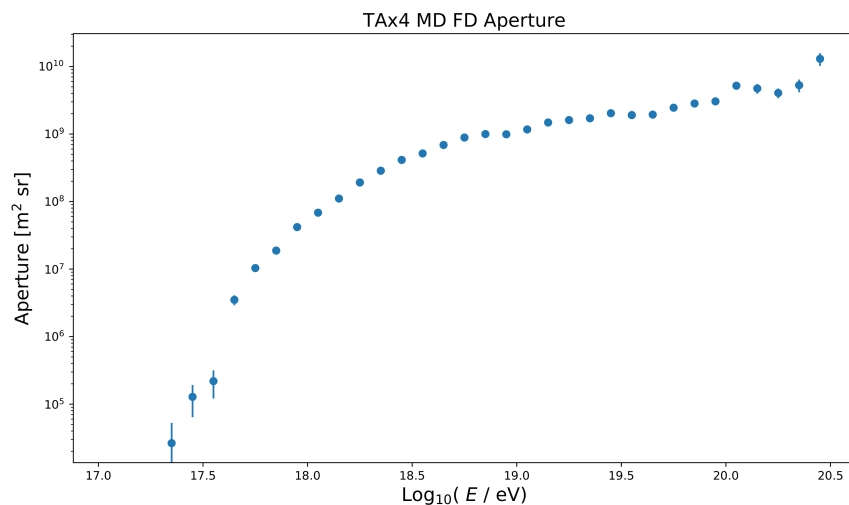
**Figure 6.5:** TAx4 accumulated ontine. The vertical dashed gray lines show the dates of the TAx4 MD FD epoch starts. The horizontal periods in the ontine accumulation are dates between a *run* when the moon and sun are in positions that make the observation time in a night less than 3 hours. On these nights with less than 3 hours of observation time, the detectors are not run. The winter vs. the summer season is seen when more data is accumulated in a run given the length of winter vs. summer nights.

**Table 6.2:** TAx4 thrown and reconstructed MC events statistics.

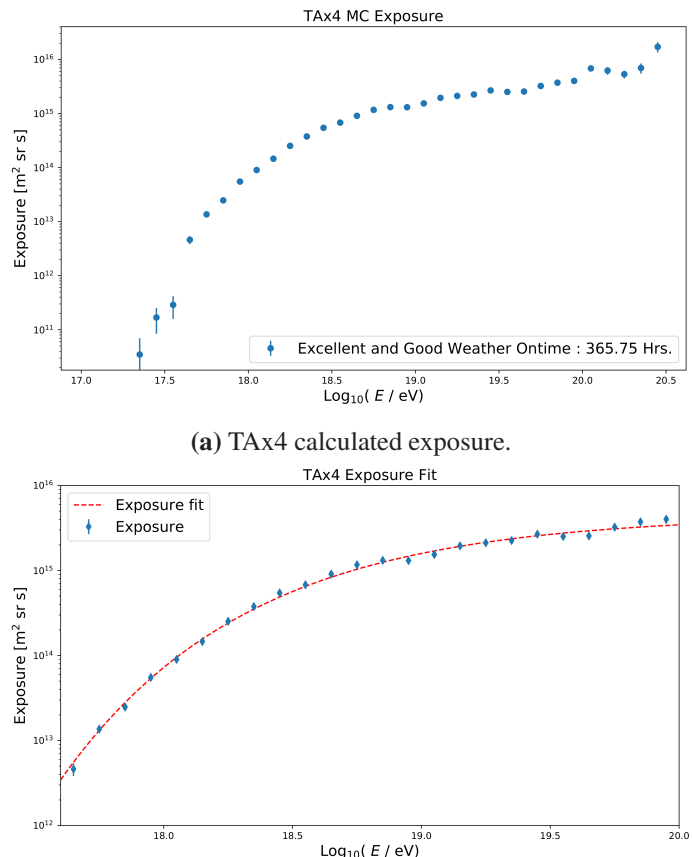
	Events
Thrown	5000000
Triggered	12532
Pass 3 (SDP Fit)	12084
Pass 2 (Rayleigh Filter)	11834
Pass 4 (Geometry Recon.)	11825
Pass 5 (Profile Recon.)	11366

**Table 6.3:** TAx4 defined weat code classes.

Class	weat code Values
Excellent	Sum(NESWO) = 0
Good	Sum(NEO) = 0
Bad	Everything Else

**Figure 6.6:** TAx4 aperture.**Table 6.4:** TAx4 ROOT exposure fit results.

Parameter	Value
$p_1$	$15.6503 \pm 0.0397$
$p_2$	$16.4318 \pm 0.0915$
$p_3$	$0.7235 \pm 0.0446$
$\chi^2 / \text{ndf}$	$14.0866 / 21$
Probability	0.8658



**(b) TAx4 exposure fit.** The dashed red line is the exposure fit.

**Figure 6.7:** TAx4 calculated exposure and exposure fit.

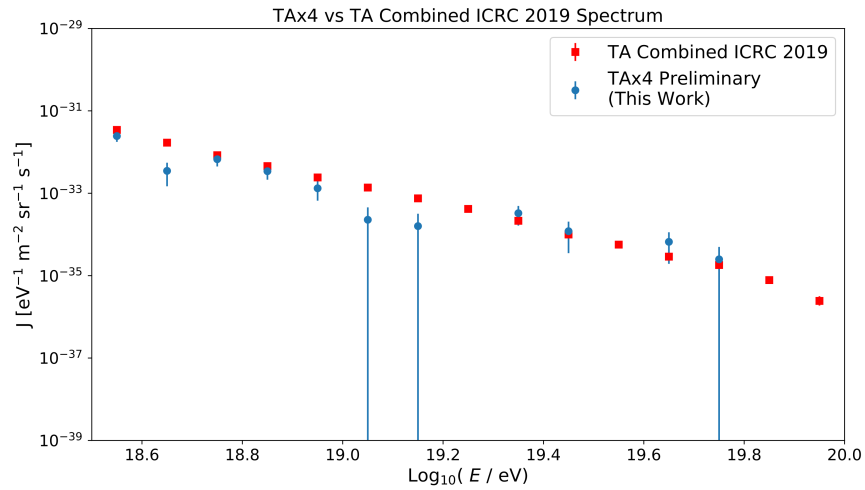


**Figure 6.8:** TAX4 MD FD epoch 0 and I spectrum.

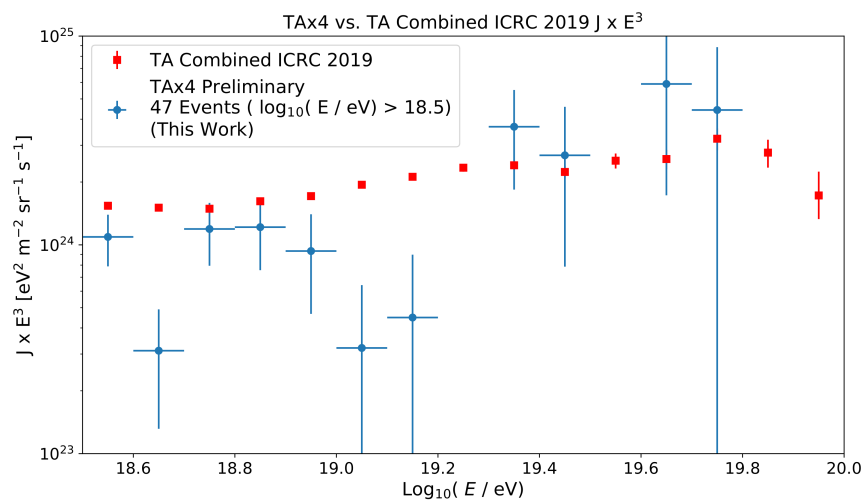


**Figure 6.9:** TAX4 MD FD epoch 0 and I  $J(E) \times E^3$ .

# CHAPTER 7

## TA 10-YEAR MONOCULAR FD COSMIC RAY ENERGY SPECTRUM

The observed events for both the BR and LR FD stations in monocular mode are combined to increase the statistics for a spectrum calculation. The mono combined spectrum is calculated as

$$J(E_i)_{\text{Combined}} = \frac{N(E_i)_{\text{Combined}}}{\Delta E_i \xi(E_i)_{\text{Combined}}} \quad (7.1)$$

where  $N(E_i)_{\text{Combined}}$  is the combined event distribution, and  $\xi(E_i)_{\text{Combined}}$  is the combined exposure. A mono combined spectrum was calculated with the events collected from 2008/04/01 - 2017/11/28, just under 10 years.

### 7.1 Coincidence FD Events between the BR and LR Stations

Stereo events<sup>1</sup> were searched for to ensure that FD events are not double-counted if both BR and LR stations observe the same event. These stereo events were found by the timing coincidence of each station's events. If two events were within a 26-microsecond time window, the two events were flagged as a single stereo event. The two reconstructions were paired into a database of stereo events. The stereo event energy was calculated as the geometric mean of both stations

$$E_{\text{Stereo}} = E_{\text{BR} \cap \text{LR}} = \sqrt{E_{\text{BR}} \times E_{\text{LR}}}. \quad (7.2)$$

Stereo events in the MC were also searched for to calculate the stereo acceptance, aperture, and exposure. After quality and weather cuts, 416 stereo events were found. The stereo event energy distribution compares well with the BR and LR energy distributions of the stereo events, as shown in Figure 7.1a. The energy profile of BR energy vs. LR energy, shown in Figure 7.1b, shows good agreement across all observed stereo energies as the linear fit shows no significant offset or slope from zero. Both BR and LR are in good agreement on the stereo event energy over the range of energies.

---

<sup>1</sup>This is not the same analysis as a full stereo analysis, which reconstructs the event geometry using the intersection of both station's SDP.<sup>[81]</sup>

## 7.2 Event Distribution

Accounting for the stereo events, the combined BR and LR event distribution is

$$N(E_i)_{\text{Combined}} = N(E_i)_{\text{BR}} + N(E_i)_{\text{LR}} - N(E_i)_{\text{BR} \cap \text{LR}}. \quad (7.3)$$

The 10-year event distribution with events that passed reconstruction, quality cuts, and weather cuts is shown in Figure 7.2. LR sees more low-energy events as it is roughly 100 m higher in elevation, which places it closer to low-energy events that develop shallower in the atmosphere. Otherwise, the BR and LR event distributions follow the same form at the higher energies. The stereo distribution starts above  $\log_{10}(E/\text{eV}) = 18.0$ , which indicates a rough threshold incorporating the quality cuts to at which both BR and LR can observe the same event.

## 7.3 Monte Carlo Event Distribution

The event distributions for the TRUMP-generated MC events that pass reconstruction, quality cuts, and weather cuts are shown in Figure 7.3. The thrown event distribution was scaled by the ratio of MC events reduced by the weather cuts to calculate the acceptance accurately. The reconstructed MC consists of roughly five times the number of reconstructed events in the data.

## 7.4 Ontime

The BR, LR, and stereo ontine statistics are listed in Table 7.1. Using the machine learning weather cuts discussed in Chapter 4, the ontine statistics are reduced to the values in Table 7.2. The LR station ends operation an hour before the BR station, given its remoteness as explained in Section 3.2. The stereo ontine was calculated using the overlap of the BR and LR data parts' start and stop times. The duty cycle was calculated from the time elapsed from the FD's first data part start on 2008/04/01 and the stop of the last FD data part on 2017/11/28. BR and LR have a duty cycle of 11% and 9%, respectively, again reflecting LR's early shutdown on each night of operation. The DAQ for both BR and LR is stopped after each trigger to allow for the data buffers to be recorded. Each pause, or *deadtime*, of the DAQ for BR and LR is recorded with the CTD. The deadtimes for each FD data part were summed and recorded in a deadtime database. The aggregate ontine,  $t_{\text{Ontime}}$ , and deadtime,  $t_{\text{Deadtime}}$ , for both detectors were calculated using only the clear weather FD data parts. The total *livetime* is when the FD was able to observe and trigger on FD events and is the correct time to be used in the exposure calculation. The total livetime was calculated as

$$T_{\text{Livetime}} = t_{\text{Ontime}} - t_{\text{Deadtime}} \quad (7.4)$$

$$= t_{\text{Ontime}} (1 - f_{\text{Deadtime}}) \quad (7.5)$$

where  $f_{\text{Deadtime}}$  is the deadtime fraction. The deadtime fraction is calculated as

$$f_{\text{Deadtime}} = \frac{t_{\text{Deadtime}}}{t_{\text{Ontime}}}. \quad (7.6)$$

The deadtime fraction is convenient for determining the stereo deadtime fraction. It is possible but computationally expensive to calculate exact stereo deadtime. The task requires given that the task requires tracking the overlaps of BR and LR FD data parts (which is done for stereo ontime), and then also summing both station's deadtimes and accounting for the overlaps in deadtimes between the stations. It is easier and nearly as accurate to approximate the stereo livetime using the BR and LR deadtime fractions,

$$T_{\text{Stereo}} = t_{\text{Stereo}} (1 - f_{\text{Stereo}}) \approx t_{\text{Stereo}} (1 - f_{\text{BR}})(1 - f_{\text{LR}}). \quad (7.7)$$

With BR, LR, and the stereo livetime, the exposure of all three can be determined and used to calculate the combined exposure which is discussed further in Section 7.7.

## 7.5 Detector Acceptance

Using the distributions of the reconstructed and thrown MC events in Equation 5.1, the acceptances for BR, LR, and stereo are calculated. These acceptance as a function of energy are shown in Figure 7.5a. The combined acceptance, shown in Figure 7.5b, is calculated in the same fashion as the combined event distribution to remove the intersection of stereo events,

$$\text{Acceptance}(E_i)_{\text{Combined}} = \text{Acceptance}(E_i)_{\text{BR}} + \text{Acceptance}(E_i)_{\text{LR}} - \text{Acceptance}(E_i)_{\text{BR} \cap \text{LR}}. \quad (7.8)$$

This combined acceptance is not used in this analysis, but it allows us to compare BR, LR, and stereo acceptance. The combined exposure includes the different livetimes of BR, LR, and stereo.

## 7.6 Detector Aperture

The detection volume into which MC events are thrown is defined as

$$A_0 = 2\pi \int_{0^\circ}^{1^\circ} R_{\text{Earth}}^2 \sin(\alpha) d\alpha \quad (7.9)$$

$$\Omega_0 = 2\pi \int_{0^\circ}^{80^\circ} \sin(\theta) \cos(\theta) d\theta, \quad (7.10)$$

where  $R_{\text{Earth}} = 6370.984$  km which is the mean radius of the earth at TA (roughly  $39.3^\circ$  N latitude), and  $\alpha$  is treating the CLF as a pole on the surface of the earth and integrating over  $1^\circ$  in latitude around the pole. The solid angle of the detection aperture comes from the zenith angle limits in  $\theta$  rotated over  $2\pi$ . This volume definition allows for BR and LR stations to be simulated in tandem for stereo events. The detection aperture for this monocular analysis is  $A_0 \Omega_0 = 1.18348 \times 10^{11} \text{ m}^2 \text{ sr}$ . The mono apertures, using Equation 5.2, is shown in Figure 7.6.

## 7.7 Detector Exposure

The monocular combined exposure using the aperture and livetime of BR, LR, and the stereo intersection is calculated as

$$\xi(E)_{\text{Combined}} = A\Omega(E_i)_{\text{BR}} T_{\text{BR}} + A\Omega(E_i)_{\text{LR}} T_{\text{LR}} - A\Omega(E_i)_{\text{BR} \cap \text{LR}} T_{\text{BR} \cap \text{LR}}. \quad (7.11)$$

The BR, LR, and stereo exposures are calculated with Equation 6.7. The exposures shown in Figure 7.7 were fit with Equation 6.9. For BR, LR and the mono combined fit, the lower energy bound was  $\log_{10}(E/\text{eV}) = 17.6$ , while for the stereo fit, the lower bound was  $\log_{10}(E/\text{eV}) = 18.5$ . The exposure fit results are listed in Table 7.3. To extend the exposure to lower energies, a joint exposure was calculated by joining the fit exposures with the calculated exposure values below  $\log_{10}(E/\text{eV}) = 17.6$  for the BR, LR, and combined exposure and the calculated stereo exposure below  $\log_{10}(E/\text{eV}) = 18.5$ . This joint exposure gives a smooth exposure for the higher energies but also allows for lower energies where the fit does not handle the rapid decline of the calculated exposure. The MC has a greater number of events at lower energies which allows for a better exposure calculation without using the fit. The joint exposures are shown in Figure 7.8.

## 7.8 Combined Cosmic Ray Spectrum

The mono spectra for BR, LR, and stereo, shown in Figure 7.9, are calculated using Equation 6.8. The ankle feature is apparent in all three spectra. The LR spectrum is offset above the BR spectrum, but the spectra are parallel as a function of energy, agreeing on the ankle position and spectral slopes of the spectrum each other well from  $\log_{10}(E/\text{eV}) = 17.5$  to  $\log_{10}(E/\text{eV}) = 19.3$  where the statistics are low. Even though BR and LR are identical stations, there are environmental factors that are different. The weather classification using machine learning showed a 10% difference in the number of clear weather data parts. BR and LR are separated by 30 km, and LR is 100 m higher in altitude. As seen with weather classification, the assumption that conditions at both sites are identical may not hold. Given that the spectra are parallel to each other, it is suggestive that factors in the exposure could be investigated and improved. However, the mono combined spectrum, by its construction, averages the BR and LR event distributions and exposures, giving a better representation of the true spectrum than the individual spectra.

By combining the measurements of both stations, the event statistics will improve, especially at the higher energies where events are rare. The mono combined spectrum was calculated using Equation 7.1 and it is shown in Figure 7.10 compared to the individual spectra. The mono combined spectrum compares well with the other individual spectra as they visually follow the same form and match breakpoints. The BR and LR spectra are brought into agreement by shifting BR up 5% and

LR down 5%, thus we estimate the mono combined spectra has a 5% systematic uncertainty from the BR and LR offset.

The mono combined spectrum measurement compares well with other previous spectrum measurements. The mono combined spectrum measurement agrees within the statistical errors with the TA combined ICRC 2019 spectrum, which used the TA SD array and the TALE fluorescence detectors. The mono combined spectrum result also agrees within the statistical errors with the HiRes experiment mono FD spectra of HiRes-I and -II. These spectra match well with form and breaks.

### 7.8.1 Systematic Uncertainty

The contributions to the systematic uncertainty of the mono combined spectrum are listed in Table 7.5. The energy measurement systematic uncertainty accounts for the effects of the experimental apparatus, the experimental apparatus environment, and the physics models employed in the fluorescence event reconstruction, as discussed in the 3.5 year mono combined spectrum<sup>[60]</sup>. All these uncertainties are added in quadrature for the total energy measurement systematic uncertainty. The mono combined spectrum systematic uncertainty depends on the energy measurement, the aperture systematic uncertainty estimated from the  $\theta_{SDP}$  Data/MC comparison, and the offset between the BR and LR spectra. The energy uncertainty contribution to the spectrum is estimated from the observed spectrum following a roughly  $J(E) \approx E^{-2.7}$ . The energy uncertainty is multiplied by 1.7 before being added to all the other contributions to spectrum uncertainty in quadrature to determine the total systematic uncertainty of the mono combined flux measurement.

## 7.9 Broken Power Fits to the Combined Spectrum

The spectrum has been observed to roughly follow a broken power law. Different populations of cosmic rays and acceleration mechanisms in the universe create features in the cosmic-ray energy spectrum. These features are brought out by fitting the spectrum with broken power law functions. The first fit is a simple once-broken power law in Equation 7.12, where  $A$  is the power-law normalization constant. For ease of comparing  $A$  with other results,  $A$  is used to calculate  $J(E = 10^{18} \text{ eV})$ .  $E_i$  represents the location of breakpoints in  $\log_{10}(E/\text{eV})$ , and  $\gamma_i$  represents the spectral indices.

$$J(E)_{\text{Once Broken}} = A \begin{cases} E^{\gamma_1} & E < E_1 \\ E_1^{\gamma_1 - \gamma_2} E^{\gamma_2} & E_1 \leq E \end{cases} \quad (7.12)$$

Since the spectrum is calculated using observed events, it is proper to minimize the Poisson fit deviance,  $D_{\text{Poisson}}$ , rather than  $\chi^2$ . By minimizing the Poisson deviance, we are maximizing the binned likelihood. The Poisson fit deviance is calculated as

$$D_{\text{Poisson}} = 2 \sum_i \left[ N(E_i)_{\text{Expected}} - N(E_i)_{\text{Observed}} + N(E_i)_{\text{Observed}} \ln \left( \frac{N(E_i)_{\text{Observed}}}{N(E_i)_{\text{Expected}}} \right) \right]. \quad (7.13)$$

The expected events are calculated as with the measured mono combined exposure and adjusting the spectrum fit function.

$$N(E_i)_{\text{Expected}} = J(E_i)_{\text{Fit}} \Delta E_i \xi(E) \quad (7.14)$$

Above  $\log_{10}(E/\text{eV}) = 17.5$ , the most prominent break feature is the ankle, thus  $E_1$  represents  $E_{\text{Ankle}}$ . To search for other higher breaks, the spectrum can also be fit with a twice-broken fit as in Equation 7.15 or a thrice-broken fit as in Equation 7.16.

$$J(E)_{\text{Twice Broken}} = A \begin{cases} E^{\gamma_1} & E < E_1 \\ E_1^{\gamma_1 - \gamma_2} E^{\gamma_2} & E_1 \leq E < E_2 \\ E_1^{\gamma_1 - \gamma_2} E_2^{\gamma_2 - \gamma_3} E^{\gamma_3} & E_2 \leq E \end{cases} \quad (7.15)$$

$$J(E)_{\text{Thrice Broken}} = A \begin{cases} E^{\gamma_1} & E < E_1 \\ E_1^{\gamma_1 - \gamma_2} E^{\gamma_2} & E_1 \leq E < E_2 \\ E_1^{\gamma_1 - \gamma_2} E_2^{\gamma_2 - \gamma_3} E^{\gamma_3} & E_2 \leq E < E_3 \\ E_1^{\gamma_1 - \gamma_2} E_2^{\gamma_2 - \gamma_3} E_3^{\gamma_3 - \gamma_4} E^{\gamma_4} & E_3 \leq E \end{cases} \quad (7.16)$$

The results of the series of broken power law fits, as shown in Figure 7.12, are listed in Table 7.6 with the position of the breaks, the spectral indices, and the fit statistics. Two twice-broken fits with comparable fit deviance were found with a lower and higher second break energy. Scanning the position of the second break in the twice-broken fit reveals two minima in the fit deviance, as shown in Figure 7.13. All of the broken power law fits have a agreement within the uncertainty for the ankle position, with the exception of the once-broken fit, which calculated  $\log_{10}(E_1 / \text{eV}) = 18.7$ . The lower  $E_2$  twice-broken fit is positioned between the  $E_2$  and  $E_3$  positions of the thrice-broken fit, possibly because the twice-broken fit was picking up on the presence of both breaks. The higher  $E_2$  twice-broken fit lines up with the thrice-broken fit so that the fits overlap beyond  $E_3$  in the thrice-broken fit. The higher  $E_2$  twice-broken fit is in agreement with the previous results of TA SD ICRC 2019 and the HiRes results listed in Table 7.7. Adding each break in the fit improves the deviance compared to the number of degrees of freedom (ndf) significantly. The thrice-broken compared to both twice-broken drops 2 ndf and drops five in deviance. Since the drop in deviance is greater than the drop in ndf, the thrice-broken power fit is significantly better. Thus, the mono combined spectrum suggests two breaks beyond the ankle. The last break in the thrice-broken fit can still be attributed to the GZK suppression.

## 7.10 Observation of the GZK Suppression

The mono combined spectrum is used to evaluate the significance of the GZK suppression of cosmic rays at the highest energies. This significance is determined by assuming that the spectral

index after the ankle,  $\gamma_2$ , does not break at  $E_2$  in the twice-broken power fit. Both twice-broken fits with the assumed continuation past the second break are shown in Figure 7.14. The number of events expected assuming the spectrum continues unbroken beyond  $E_2$  is calculated using Equation 7.14 for each energy bin beyond  $E_2$  to  $E \rightarrow \infty$ . This calculation is done for both twice-broken power law fits. The distribution of expected events vs. observed events is shown in Figure 7.15. To determine if the observed number of events is statistically significant compared to the expected number of events of the unbroken flux, the cumulative Poisson probability of observed events vs. expected events is

$$P_{\text{GZK}} = \sum_{n=0}^{N_{\text{Observed}}} P_{\text{Poisson}}(n, N_{\text{Expected}}). \quad (7.17)$$

This method evaluates the chance probability of the GZK suppression. The Poisson discrete distribution in the above equation is

$$P_{\text{Poisson}}(n, \mu) = \frac{\mu^n e^{-\mu}}{n!}. \quad (7.18)$$

The sigma significance of the chance probability of the GZK suppression is evaluated as

$$1 - P_{\text{GZK}} = F(\mu + n\sigma) - F(\mu - n\sigma) = \text{erf}\left(\frac{n}{\sqrt{2}}\right) \quad (7.19)$$

where  $F$  is a normal distribution with mean,  $\mu$ , and standard deviation,  $\sigma$ , and  $\text{erf}()$  is the error function. The lower second break twice-broken fit has a  $5.42\sigma$  significance while the higher second break twice-broken fit has a  $4.15\sigma$  significance.

## 7.11 Integral Flux and $E_{1/2}$

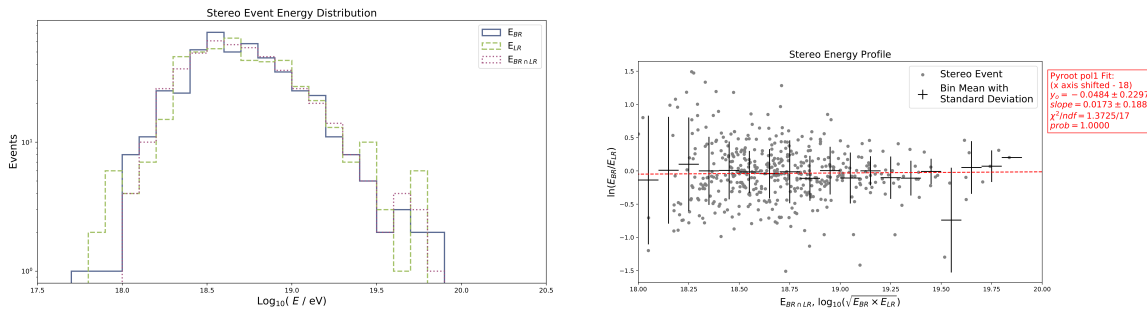
To evaluate the effective energy of the GZK suppression for an astrophysical interpretation, we use the  $E_{1/2}$  method<sup>[82]</sup> for calculating the position when the integral flux is half what would be compared to the integral flux if the spectrum continues unbroken at the second break. The integral cosmic ray flux is calculated, using the differential cosmic ray flux, as

$$I(E) = \int_E^\infty J(E') dE'. \quad (7.20)$$

The integral flux was calculated from the measured differential flux and for each twice-broken power law fits to the differential flux with values from Table 7.6. The calculated integral fluxes are shown in Figure 7.16. We calculate  $E_{1/2}$  as<sup>[83]</sup>

$$\log_{10}(E_{1/2} / \text{eV}) = \log_{10}(E_2 / \text{eV}) + \frac{1}{\gamma_2 - \gamma_3} \log_{10}\left(2 \frac{\gamma_2 + 1}{\gamma_3 + 1}\right). \quad (7.21)$$

The calculated  $E_{1/2}$  values compared to the TA SD ICRC 2019 and the HiRes experiment results are listed in Table 7.9. The higher second break twice-broken fit agrees within uncertainty with the previous results.



(a) The energy distributions for the BR, LR, and the geometric mean energies of the stereo events.

(b) The stereo energy profile with a linear fit in red dashed line.

**Figure 7.1:** Stereo FD events observed by both BR and LR.

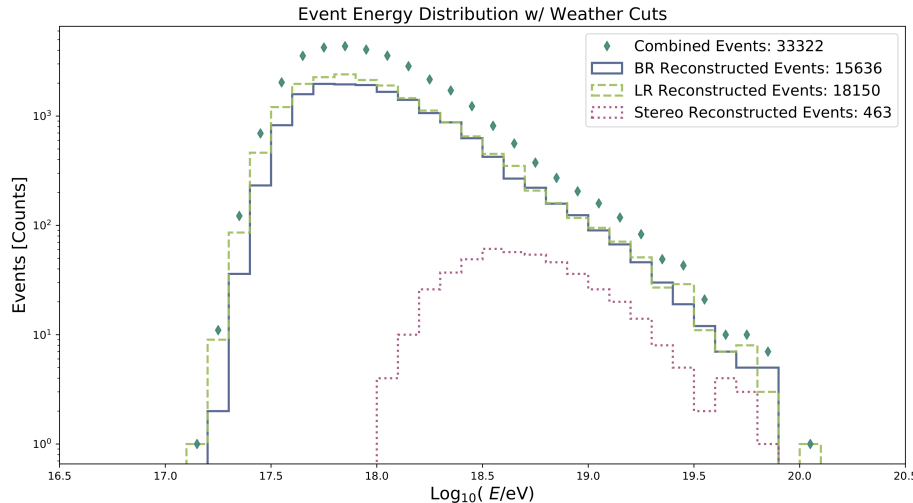


**Figure 7.2:** BR, LR, stereo, and combined event distributions.

**Table 7.1:** BR, LR, and stereo accumulated ontimes between 2008/04/01 - 2017/11/28.

	Operation Nights	Duty Cycle [%]	Ontime [h]	Deadtime [h]	Deadtime Fraction [%]	Livetime [h]
BR	1593	10.97	9288.19	574.16	6.18	8714.03
LR	1493	9.03	7647.41	555.79	7.26	7091.63
Stereo	1378	-	6876.40	-	13.00	5982.47

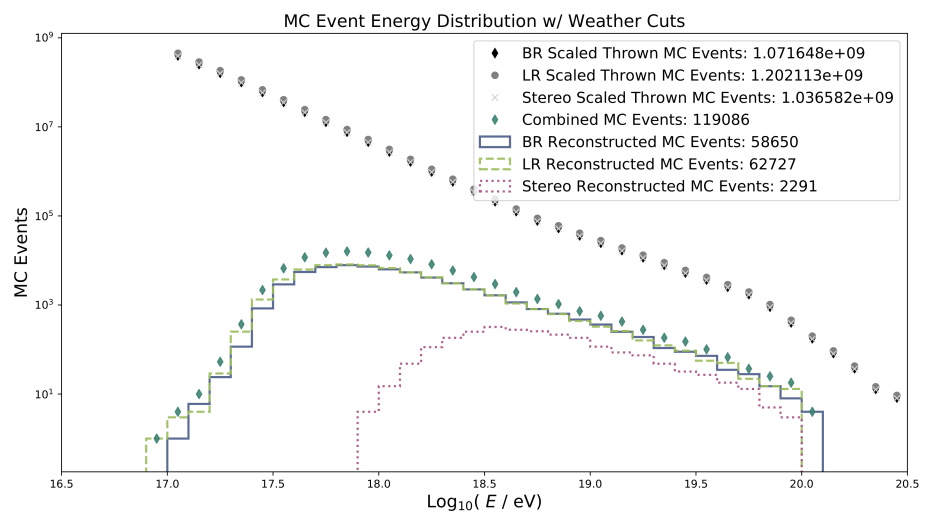


**Figure 7.3:** BR, LR, stereo, and combined MC event distributions.

**Table 7.2:** BR, LR, and stereo accumulated ontime between 2008/04/01 - 2017/11/28 using only the clear FD data part classified with the RCNNs in Chapter 4.

	Ontime [h]	Deadtime [h]	Deadtime Fraction [%]	Livetime [h]
BR	5542.60	369.06	6.66	5173.54
LR	5277.10	394.56	7.48	4882.54
Stereo	4090.03	-	13.64	3532.25

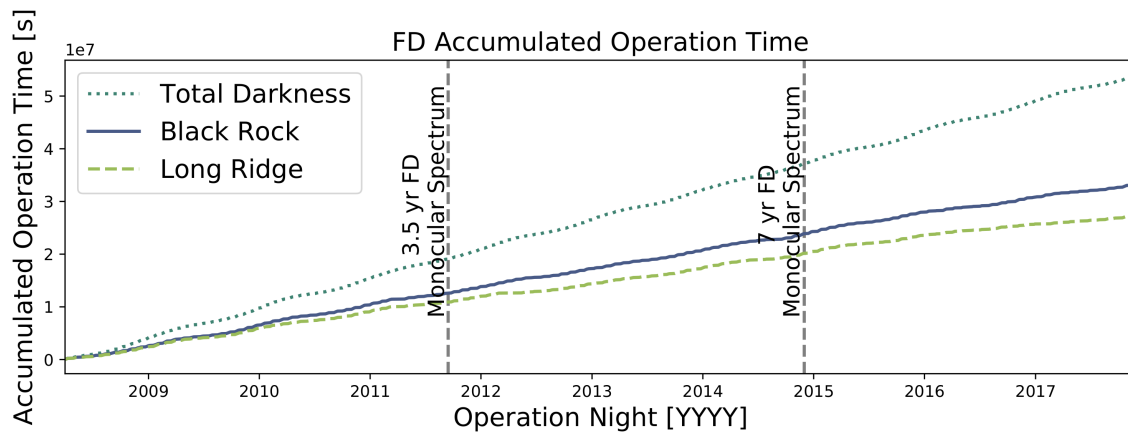
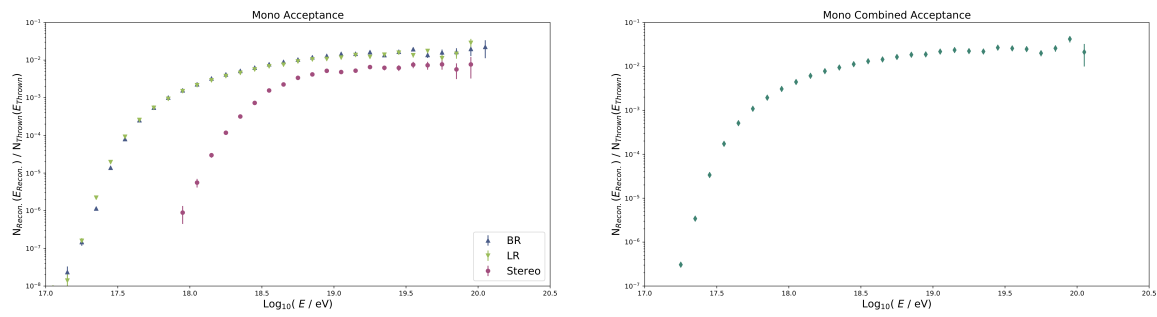


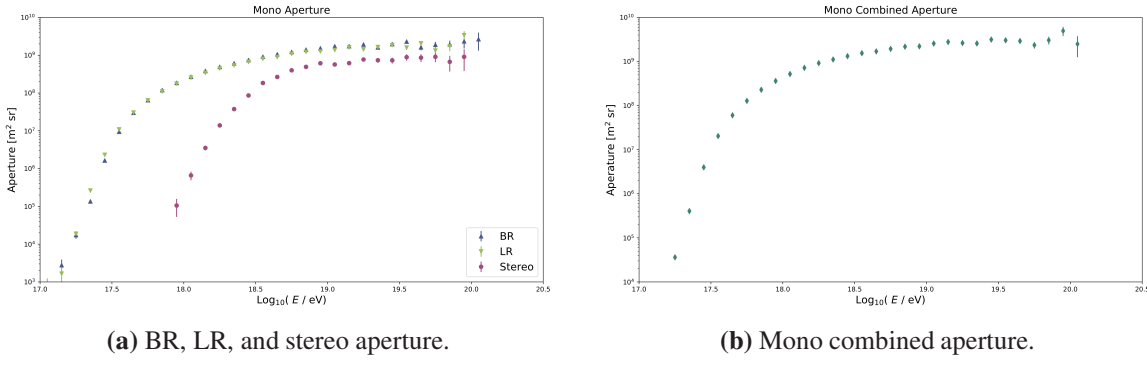
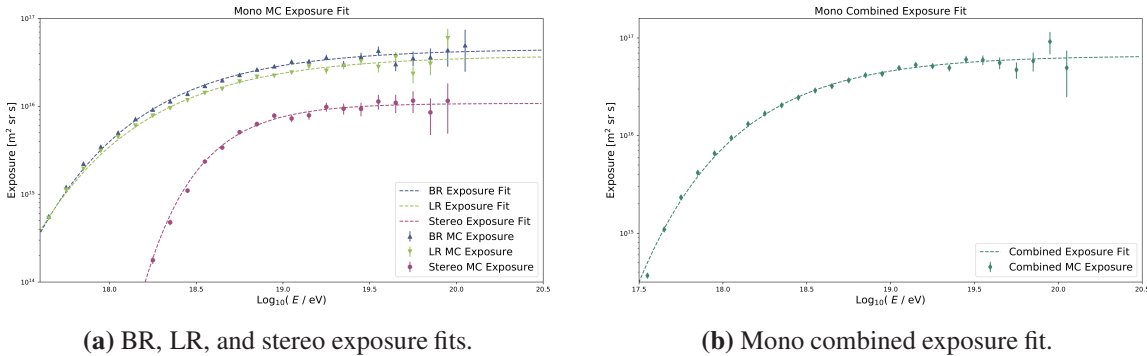
**Figure 7.4:** BR and LR accumulated ontime between 2008/04/01 - 2017/11/28. The dark green dashed line indicates the accumulated total darkness where the sun and moon are 18% below the horizon. The horizontal lines indicate past BR and LR mono combined spectra: the 3.5 year<sup>[61]</sup>, and the 7 year<sup>[84]</sup> results.



(a) BR, LR, and stereo acceptance.

(b) Mono combined acceptance.

**Figure 7.5:** BR, LR, stereo, and the mono combined acceptances.

**Figure 7.6:** Calculated mono apertures.**Figure 7.7:** Monocular exposure fits.**Table 7.3:** Monocular exposure fits.

	$p_1$	$p_2$	$p_3$	$\chi^2 / \text{ndf}$
BR	$16.65 \pm 0.03$	$16.40 \pm 0.09$	$0.58 \pm 0.04$	$10.64 / 23$
LR	$16.58 \pm 0.03$	$16.31 \pm 0.10$	$0.61 \pm 0.04$	$13.64 / 22$
Stereo	$16.03 \pm 0.05$	$17.57 \pm 0.28$	$0.32 \pm 0.29$	$3.91 / 12$
Combined	$16.82 \pm 0.02$	$16.39 \pm 0.09$	$0.56 \pm 0.03$	$9.83 / 23$

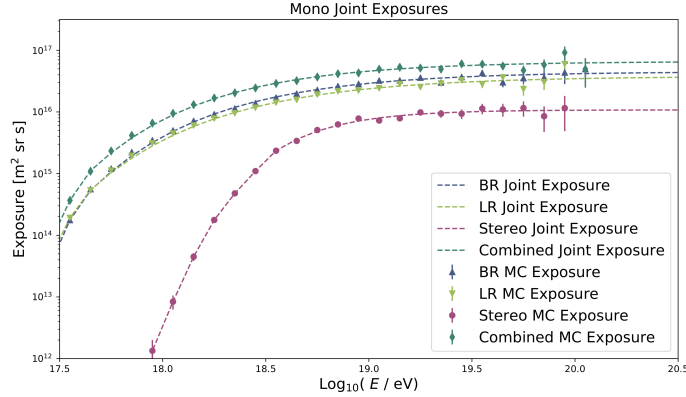
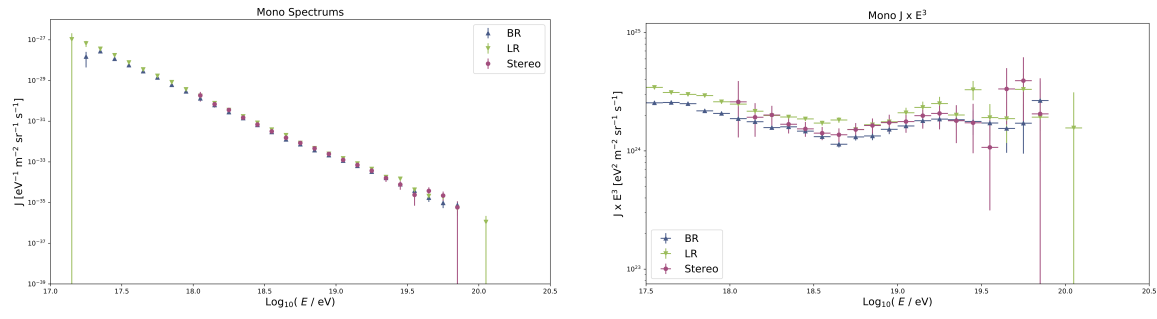


**Figure 7.8:** BR, LR, stereo, and the mono combined joint exposures. The joint exposure joins the calculated exposure with the exposure fits in Table 7.3.



(a) BR, LR, and stereo spectrum.

(b) BR, LR, and stereo  $J \times E^3$ .

**Figure 7.9:** BR, LR, and stereo spectrum and  $J \times E^3$ .

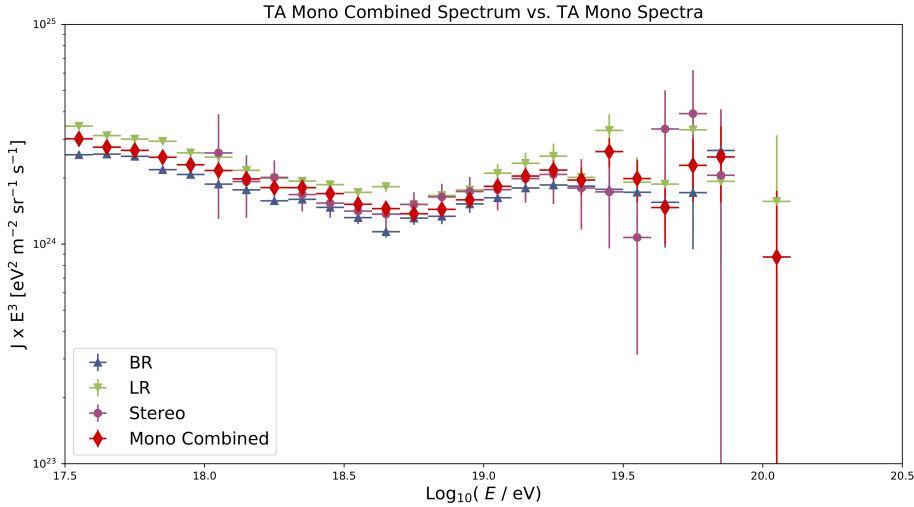
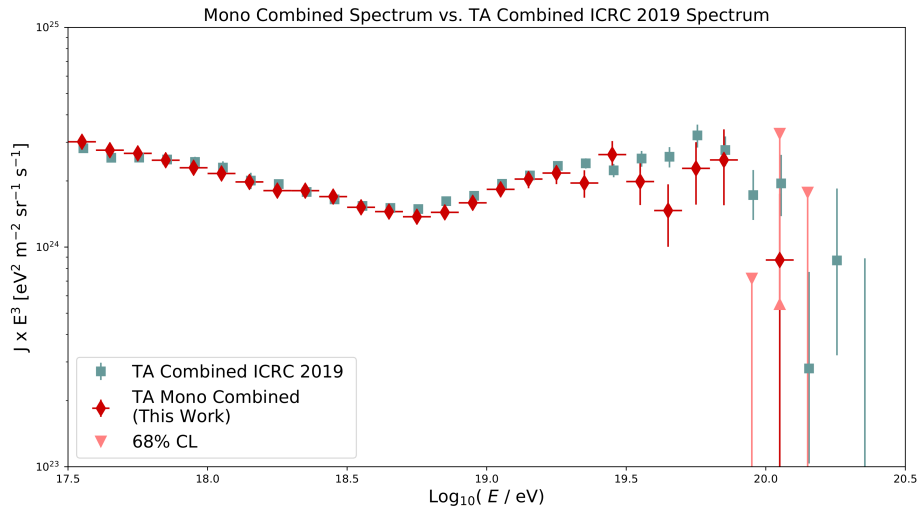


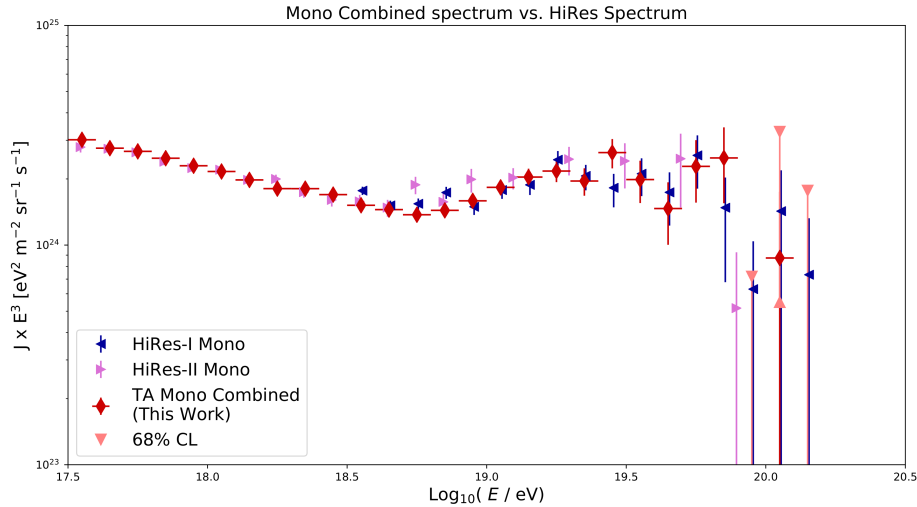
**Figure 7.10:** BR, LR, stereo, and mono combined  $J(E) \times E^3$ .

**Table 7.4:** Mono combined spectrum measurements by each bin for bin centers with  $\log_{10}(E/\text{eV}) \geq 17.5$ . Each bin has a size of .1 in  $\log_{10}(E/\text{eV})$ . The event counts for the BR, LR, stereo, and the mono combined are listed. The measured spectrum,  $J(E)$ , is listed with the lower and upper Poisson errors with units of  $[\text{eV}^{-1} \text{m}^{-2} \text{sr}^{-1} \text{s}^{-1}]$ .

Bin Center	$N_{\text{BR}}$	$N_{\text{LR}}$	$N_{\text{BR} \cap \text{LR}}$	$N_{\text{Combined}}$	$\xi(E)_{\text{Combined Joint}}$	$J(E)_{\text{Combined}}$	$\sigma_{J \text{ lower}}^{\text{stat}}$	$\sigma_{J \text{ upper}}^{\text{stat}}$
17.55	825	1208	0	2033	3.68e+14	6.75e-29	1.50e-30	1.50e-30
17.65	1585	1969	0	3554	1.11e+15	3.10e-29	5.20e-31	5.20e-31
17.75	1969	2269	0	4238	2.17e+15	1.50e-29	2.31e-31	2.31e-31
17.85	1949	2408	0	4357	3.81e+15	7.00e-30	1.06e-31	1.06e-31
17.95	1922	2135	0	4057	6.08e+15	3.24e-30	5.09e-32	5.09e-32
18.05	1665	1904	4	3565	8.99e+15	1.53e-30	2.56e-32	2.56e-32
18.15	1407	1459	10	2856	1.25e+16	7.02e-31	1.31e-32	1.31e-32
18.25	1065	1123	26	2162	1.64e+16	3.21e-31	6.91e-33	6.91e-33
18.35	876	875	37	1714	2.06e+16	1.61e-31	3.89e-33	3.89e-33
18.45	627	652	49	1230	2.49e+16	7.58e-32	2.16e-33	2.16e-33
18.55	424	451	61	814	2.93e+16	3.40e-32	1.19e-33	1.19e-33
18.65	268	350	57	561	3.34e+16	1.63e-32	6.87e-34	6.87e-34
18.75	221	208	54	375	3.74e+16	7.73e-33	3.99e-34	3.99e-34
18.85	158	160	46	272	4.10e+16	4.06e-33	2.46e-34	2.46e-34
18.95	124	117	36	205	4.44e+16	2.25e-33	1.57e-34	1.57e-34
19.05	90	95	26	159	4.74e+16	1.30e-33	1.03e-34	1.03e-34
19.15	67	71	20	118	5.00e+16	7.24e-34	6.66e-35	6.66e-35
19.25	46	51	14	83	5.23e+16	3.86e-34	4.24e-35	4.24e-35
19.35	30	27	8	49	5.44e+16	1.74e-34	2.49e-35	2.49e-35
19.45	19	29	5	43	5.61e+16	1.18e-34	1.80e-35	1.80e-35
19.55	12	11	2	21	5.77e+16	4.45e-35	9.71e-36	9.71e-36
19.65	7	7	4	10	5.89e+16	1.65e-35	5.20e-36	5.20e-36
19.75	5	8	3	10	6.01e+16	1.28e-35	4.06e-36	4.06e-36
19.85	5	3	1	7	6.10e+16	7.02e-36	2.66e-36	2.66e-36
19.95	0	0	0	0	6.18e+16	0.00e+00	0.00e+00	0.00e+00
20.05	0	1	0	1	6.25e+16	6.18e-37	6.18e-37	6.18e-37
20.15	0	0	0	0	6.30e+16	0.00e+00	0.00e+00	0.00e+00
20.25	0	0	0	0	6.35e+16	0.00e+00	0.00e+00	0.00e+00
20.35	0	0	0	0	6.39e+16	0.00e+00	0.00e+00	0.00e+00
20.45	0	0	0	0	6.43e+16	0.00e+00	0.00e+00	0.00e+00



(a) Mono combined spectrum vs. TA combined ICRC 2019<sup>[80]</sup> spectrum. The 68% Feldman-Cousins confidence levels (CL) are overlayed on the combined spectrum for the 19.95, 20.05, and 20.15  $\log_{10}(E/\text{eV})$  bins. The TA combined ICRC 2019 spectrum is offset slightly on the  $x$ -axis for ease of viewing.

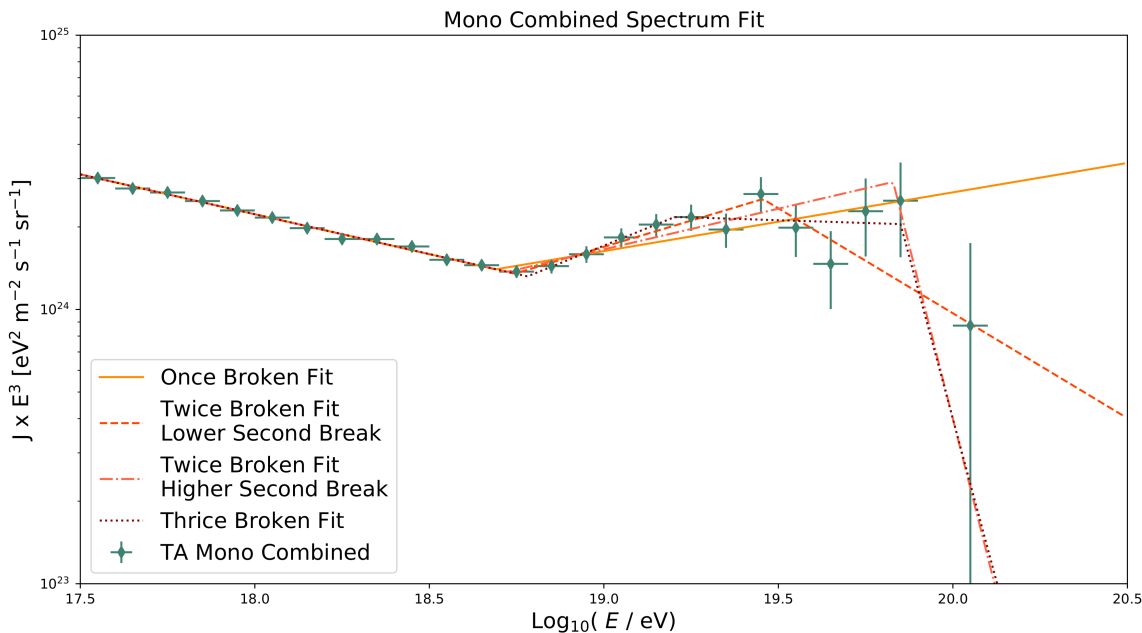


(b) Mono combined spectrum vs. the HiRes I and II<sup>[85]</sup> monocular spectrum. The 68% Feldman-Cousins confidence levels (CL) are overlayed on the combined spectrum for the 19.95, 20.05, and 20.15  $\log_{10}(E/\text{eV})$  bins. The HiRes I and II spectrum is offset slightly on the  $x$ -axis for ease of viewing.

**Figure 7.11:** Mono combined  $J(E) \times E^3$  vs. previous measurements.

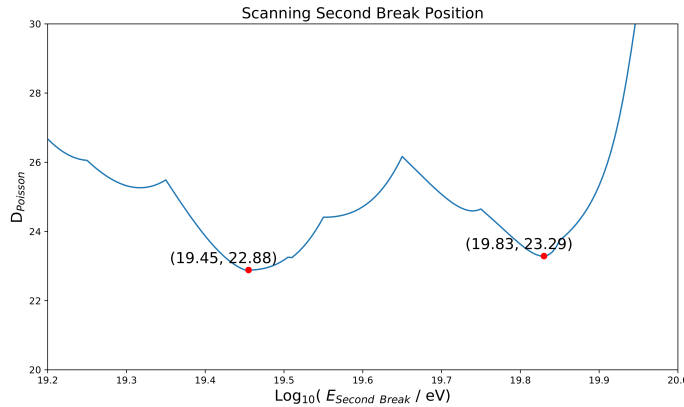
**Table 7.5:** Contributions to the systematic uncertainty to the mono combined spectrum.

Uncertainty from Experimental Apparatus <sup>[60]</sup>	
Detector Optics and Fluorescence Telescope Geometry	10 %
Electronics	10 %
Detector Onetime	1 %
Uncertainty from Experimental Apparatus Environment <sup>[60]</sup>	
Attenuation by Aerosols	10 %
Uncertainty from Physics Models <sup>[60]</sup>	
Fluorescence Yield <sup>[86]</sup>	10 %
Mean $dE/dX$ <sup>[23]</sup>	1 %
Missing Energy Correction	5 %
Systematic Uncertainty to Energy Measurement <sup>[60]</sup>	21 %
Systematic Uncertainty to Aperture (This Work)	11 %
Systematic Uncertainty from BR and LR Spectra Offset (This Work)	5 %
Systematic Uncertainty to Mono Combined Flux Measurement	37 %

**Figure 7.12:** Mono combined spectrum with a once, twice, and thrice-broken power fit above  $\log_{10}(E/\text{eV}) = 17.5$ .

**Table 7.6:** Mono combined spectrum broken power law fits above  $\log_{10}(E/\text{eV}) = 17.5$ . The mono combined spectrum was fit with a once, twice, and thrice-broken power law. Two twice-broken fits with comparable fit deviances at a lower and higher second break position are reported.

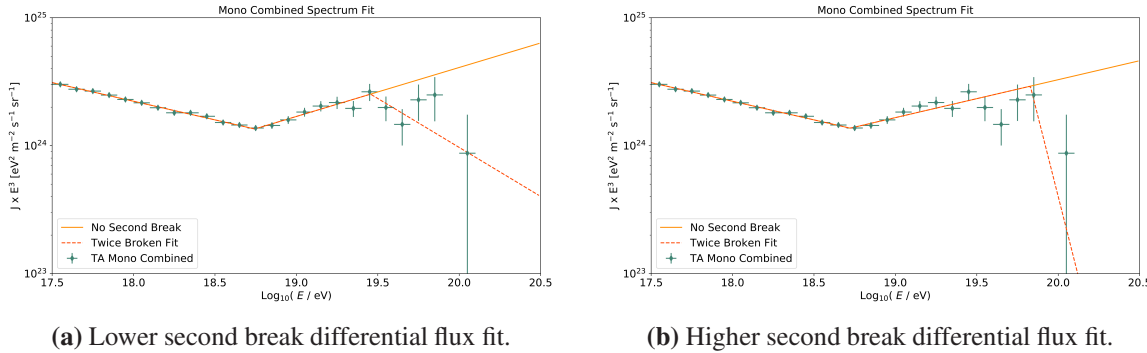
	$J(E)$ Once Broken	$J(E)$ Twice Broken, Lower $E_2$	$J(E)$ Twice Broken, Higher $E_2$	$J(E)$ Thrice Broken
$J(E = 10^{18} \text{ eV})$	$2.22 \pm 0.01$	$2.22 \pm 0.01$	$2.22 \pm 0.01$	$2.23 \pm 0.01$
$\times 10^{-30} \text{ eV}^{-1} \text{ m}^{-2} \text{ sr}^{-1} \text{ s}^{-1}$				
$\gamma_1$	$-3.29 \pm 0.01$	$-3.29 \pm 0.01$	$-3.29 \pm 0.01$	$-3.29 \pm 0.01$
$\log_{10}(E_1 / \text{eV})$	$18.68 \pm 0.04$	$18.74 \pm 0.03$	$18.72 \pm 0.05$	$18.78 \pm 0.04$
$\gamma_2$	$-2.79 \pm 0.05$	$-2.62 \pm 0.06$	$-2.70 \pm 0.05$	$-2.49 \pm 0.15$
$\log_{10}(E_2 / \text{eV})$	-	$19.46 \pm 0.10$	$19.83 \pm 0.04$	$19.20 \pm 0.11$
$\gamma_3$	-	$-3.77 \pm 0.41$	$-8.04 \pm 2.74$	$-3.04 \pm 0.19$
$\log_{10}(E_3 / \text{eV})$	-	-	-	$19.850 \pm 0.001$
$\gamma_4$	-	-	-	$-7.74 \pm 2.43$
D <sub>Poisson</sub> / ndf	43.45 / 26	22.69 / 24	23.29 / 24	17.74 / 22



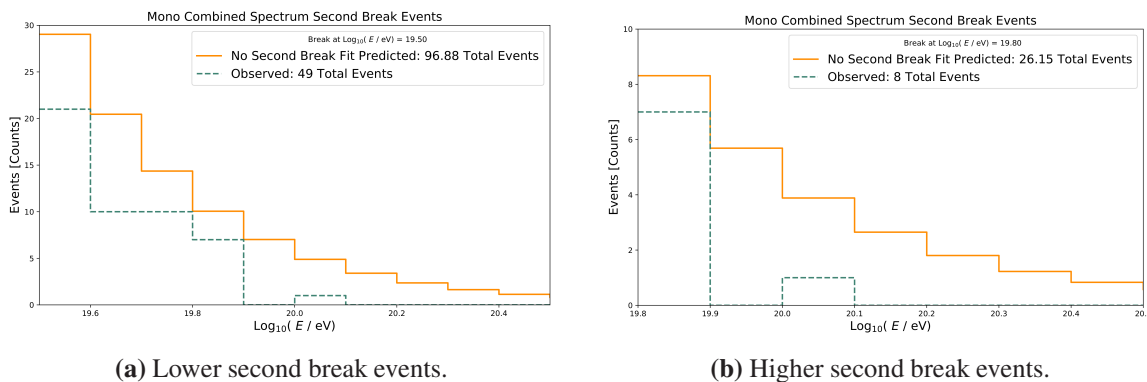
**Figure 7.13:** Scanning the fit deviance value of the second break position above the ankle in the mono combined spectrum twice-broken power law fit. Two significant minima in the deviance were found.

**Table 7.7:** Mono Combined vs. HiRes<sup>[86]</sup> and TA SD ICRC 2019<sup>[80]</sup>  $J(E)$ Twice Broken Fits. HiRes and TA SD ICRC 2019 are comparable to the higher break  $J(E)$ Twice Broken.

	This Work, Higher $E_2$	HiRes	TA SD ICRC 2019
$J(E = 10^{18} \text{ eV})$	$2.22 \pm 0.01$	-	$2.24 \pm 0.06$
$\times 10^{-30} \text{ eV}^{-1} \text{ m}^{-2} \text{ sr}^{-1} \text{ s}^{-1}$			
$\gamma_1$	$-3.29 \pm 0.01$	$-3.25 \pm 0.01$	$-3.28 \pm 0.02$
$\log_{10}(E_1 / \text{eV})$	$18.72 \pm 0.05$	$18.65 \pm 0.05$	$18.69 \pm 0.01$
$\gamma_2$	$-2.70 \pm 0.05$	$-2.81 \pm 0.03$	$-2.68 \pm 0.02$
$\log_{10}(E_2 / \text{eV})$	$19.83 \pm 0.04$	$19.75 \pm 0.04$	$19.81 \pm 0.03$
$\gamma_3$	$-8.04 \pm 2.74$	$-5.1 \pm 0.7$	$-4.84 \pm 0.48$



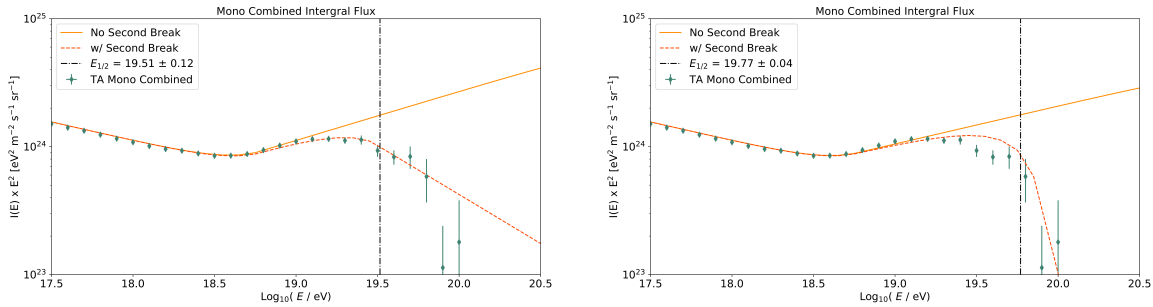
**Figure 7.14:** Twice-broken power law fits to the mono combined spectrum. The solid orange line shows the continuation of the spectral index,  $\gamma_2$ , past the second break  $E_2$  used to calculate the expect number of events if the spectrum remains unbroken above the ankle. The red dashed line shows the full twice-broken power law fit.



**Figure 7.15:** The observed events vs. expected events without the GZK suppression. The solid orange line shows the expected events calculated from a spectrum with no second break using Equation 7.14 vs. the observed number events in dashed dark green lines.

**Table 7.8:** Mono combined GZK significance.

	$J(E)$ Twice Broken Lower $E_2$	$J(E)$ Twice Broken Higher $E_2$
$\log_{10}(E_2 / \text{eV})$	$19.46 \pm 0.10$	$19.83 \pm 0.04$
$N_{\text{Expected}}$	96.88	26.15
$N_{\text{Observed}}$	49	8
$P_{\text{GZK}}$	$5.82 \times 10^{-8}$	$3.37 \times 10^{-5}$
$\sigma_{\text{GZK}}$	5.42	4.15

**(a)** Mono combined integral flux vs. the integral flux calculated from the lower second break twice-broken power law fit to the differential flux.**(b)** Mono combined integral flux vs. the integral flux calculated from the higher second break twice-broken power law fit to the differential flux.**Figure 7.16:** Mono combined integral flux,  $I(E)$ , vs. calculated integral fluxes for the twice-broken power law fits to the differential flux. The solid orange line shows integral flux calculated from the twice-broken fits to the differential flux if the spectrum continued with  $\gamma_2$  past  $E_2$ , while the dashed red line shows the integral flux calculated using the full twice-broken fit to the differential flux.**Table 7.9:** Mono combined  $E_{1/2}$  calculated using twice-broken fit spectral indecies from Table 7.6 in Equation 7.21. The statistical error is included. The results are compared to the HiRes experiment and TA SD ICRC 2019.

	$J(E)$ Twice Broken Lower $E_2$	$J(E)$ Twice Broken Higher $E_2$	TA SD ICRC 2019	HiRes
$\log_{10}(E_{1/2} / \text{eV})$	$19.51 \pm 0.12$	$19.77 \pm 0.04$	$19.79 \pm 0.04$	$19.73 \pm 0.07$

## CHAPTER 8

## CONCLUSIONS

Ultra high energy cosmic rays are the highest energy particles observed in the universe. The populations of cosmic rays can be studied from the cosmic ray energy spectrum, which is a flux measurement. Information concerning cosmic ray composition, their sources and acceleration mechanisms, are reflected in the features of the spectrum. This dissertation calculated two UHECR spectra using two different sets of fluorescence detectors: a preliminary spectrum of the expansion of TA (known as TAx4), and a 10-year monocular combined spectrum with the BR and LR FDs.

TA has observed a possible anisotropy of cosmic rays at the highest energy levels in the clustering of their arrival direction on the sky. TA is expanding the detection area by a factor of four to increase the observed amount of cosmic ray events. The expansion of TA includes quadrupling the array of surface detectors and the addition of refurbished FDs at the BR and MD stations that look out over the new surface arrays to allow for hybrid event reconstruction using both detector types. The new fluorescence telescopes at BR and MD have both achieved first light in observing cosmic ray events. TAx4 MD FD is fully operational and has been collecting data for over a year. TAx4 BR FD is not yet fully operational but is expected to be fully operational later in 2020.

Using epoch 0 and I of the TAx4 MD FD events (roughly a year of data), we calculated a preliminary cosmic ray energy spectrum. This preliminary spectrum is limited by the number of events observed in epoch 0 and I. However, even with vast statistical fluctuations, on average, this preliminary measurement shows an agreement in the correct order of magnitude when compared to previous TA spectrum results. We show the TAx4 FDs are correctly collecting and reconstructing cosmic ray events. Thus, the TAx4 FD will work well for setting the energy scale of the SDs in the TAx4 surface array. Setting the SD energy scale is important for understanding the correct energy reconstruction of the SD events and is instrumental for future analyses done with the new SD array.

We implemented a novel weather classification method for the BR and LR FDs using machine learning. Animations of the night sky were created using the minute average pedestals of each PMT to create a series of false-color snapshots to represent the night sky in the field of view. These animations allowed for classification of the weather for each FD data part, which improved the tracking of weather progression through a night. The animations were fed through a trained

recurrent convolution neural network for both BR and LR. We achieved greater than 90% accuracy on the training data with the neural network. These results showed a 10% discrepancy between the weather seen by BR and LR, showing the assumption that the weather is the same at both sites does not hold. These weather classifications were used for weather cuts in the BR and LR FD analysis.

We calculated a 10-year monocular combined cosmic ray energy spectrum using the BR and LR FDs for energies above  $10^{17.5}$  eV. The combined spectrum was in excellent agreement with the previous TA SD and HiRes spectra measurements. The combined spectrum was fit with a series of once, twice, and thrice broken power laws. Two comparable twice broken fits with the fit deviance were found with a lower  $\log_{10}(E_2/\text{eV}) = 19.46$  and higher  $\log_{10}(E_2/\text{eV}) = 19.83$ . The position of the higher  $E_2$  twice broken power law fit agrees within uncertainty with the TA SD and HiRes results. The thrice broken power law fit has significant improvement in the fit deviance over both of the twice broken fits. This thrice broken fit suggests another break at  $\log_{10}(E/\text{eV}) = 19.2$ .

We observe the GZK suppression at  $\log_{10}(E_2/\text{eV}) = 19.46$  with a  $5.46\sigma$  significance and at  $\log_{10}(E_2/\text{eV}) = 19.83$  at  $4.15\sigma$  significance for both comparable twice broken power law fits to the monocular combined spectrum. We claim the fourth observation of the GZK suppression after the HiRes experiment, TA SDs, and Peirre Auger Observatory SDs. This is the second observation of the GZK using FDs. We observe the effective energy of the GZK suppression of  $E_{1/2}$  at  $\log_{10}(E_2/\text{eV}) = 19.46$  with  $\log_{10}(E_{1/2}/\text{eV}) = 19.51$  and at  $\log_{10}(E_2/\text{eV}) = 19.83$  with  $\log_{10}(E_{1/2}/\text{eV}) = 19.77$  for both comparable twice broken fits. The higher second break is within uncertainty of previous results showing excellent agreement.

## APPENDIX A

### US STANDARD ATMOSPHERE 1976

The density profile of the atmosphere as a function of height for the US Standard Atmosphere 1976<sup>[69]</sup> is given by

$$\rho(h) = \rho_b \begin{cases} \exp\left(\frac{-gM(h-h_b)}{R^*T_b}\right) & L_b = 0 \\ \left(\frac{T_b}{T}\right)^{\left(1+\frac{gM}{R^*L_b}\right)} & L_b \neq 0 \end{cases}, \quad (\text{A.1})$$

where the  $T$  is

$$T = T_b + L_b(h - h_b). \quad (\text{A.2})$$

The variables in Equations A.1 and A.2 are given in Table A.1. The atmospheric density profile is divided into different layers with the layer values in Table A.2 to be used in Equations A.1 and A.2.

**Table A.1:** US Standard Atmosphere 1976 variables

Variable	Symbol	Units
Atmospheric Density	$\rho$	kg/m <sup>3</sup>
Atmospheric Temperature	$T$	K
Atmospheric Temperature Lapse Rate	$L_b$	K/m
Altitude	$h$	m
Molar mass of air	$M = 0.0289644$	Kg/mol
Universal Gas Constant	$R^* = 8.3144598$	N m / (mol K)
Gravitational acceleration	$g = 9.8066$	m/s <sup>2</sup>

**Table A.2:** US Standard Atmosphere 1976<sup>[69]</sup>.

Atmospheric Layer <i>b</i>	Altitude (m)	Relative Pressure (Pa/Pa)	Temperature (K)	Temperature Lapse Rate (K/m)
0	0	101325.00	288.15	-6.5e-3
1	11000	2.233e-1	216.65	0.0
2	20000	5.403e-2	216.65	1.0e-3
3	32000	8.566e-3	228.65	2.8e-3
4	47000	1.094e-3	270.65	0.0
5	51000	6.606e-4	270.65	-2.8e-3
6	71000	3.904e-5	214.65	-2.0e-3
7	84852	3.685e-6	186.946	0.0

## APPENDIX B

### TA TOPOGRAPHIC AND RELIEF MAPS

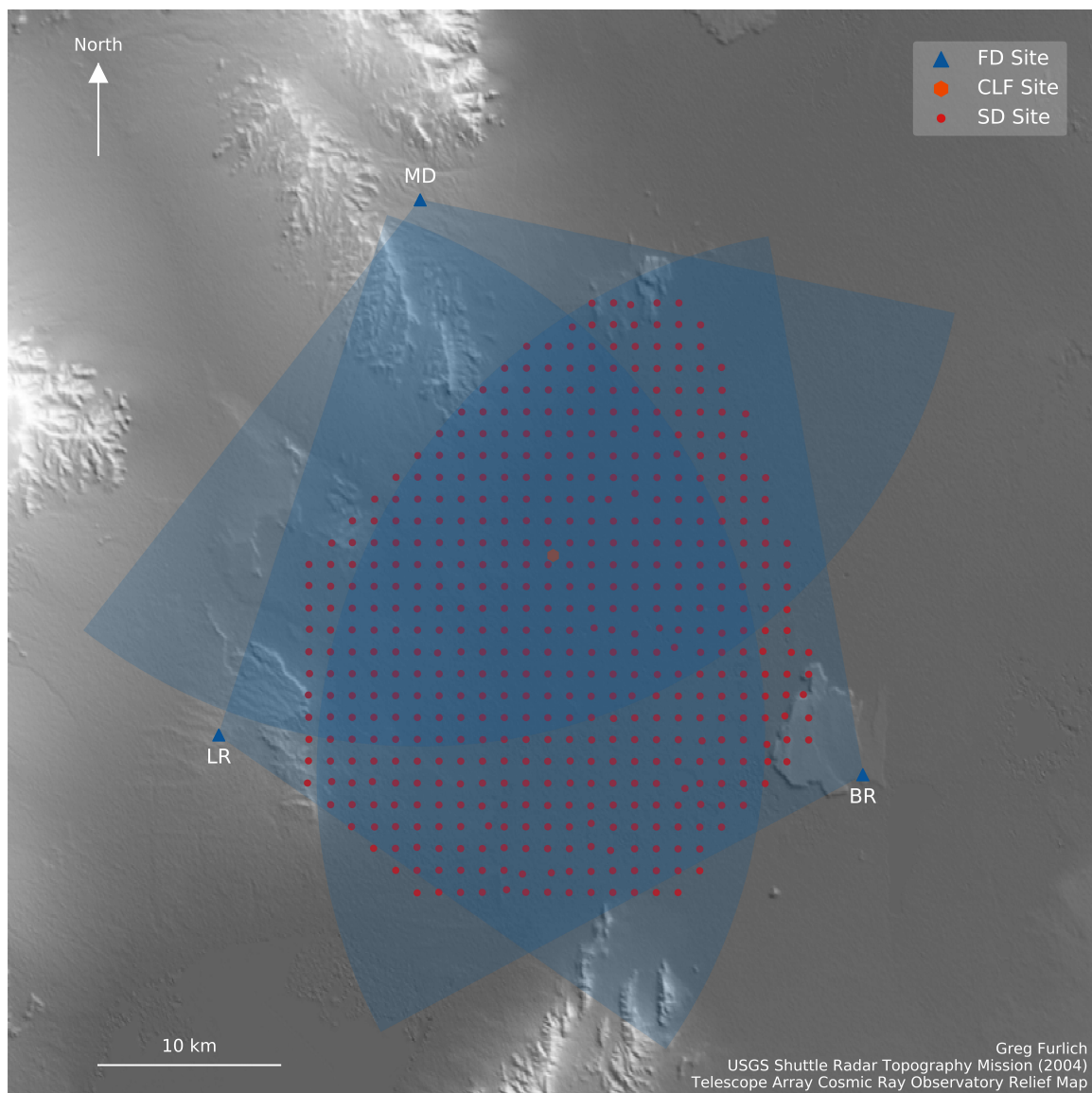


**Figure B.1:** Topographical shaded relief map of the Telescope Array detectors.

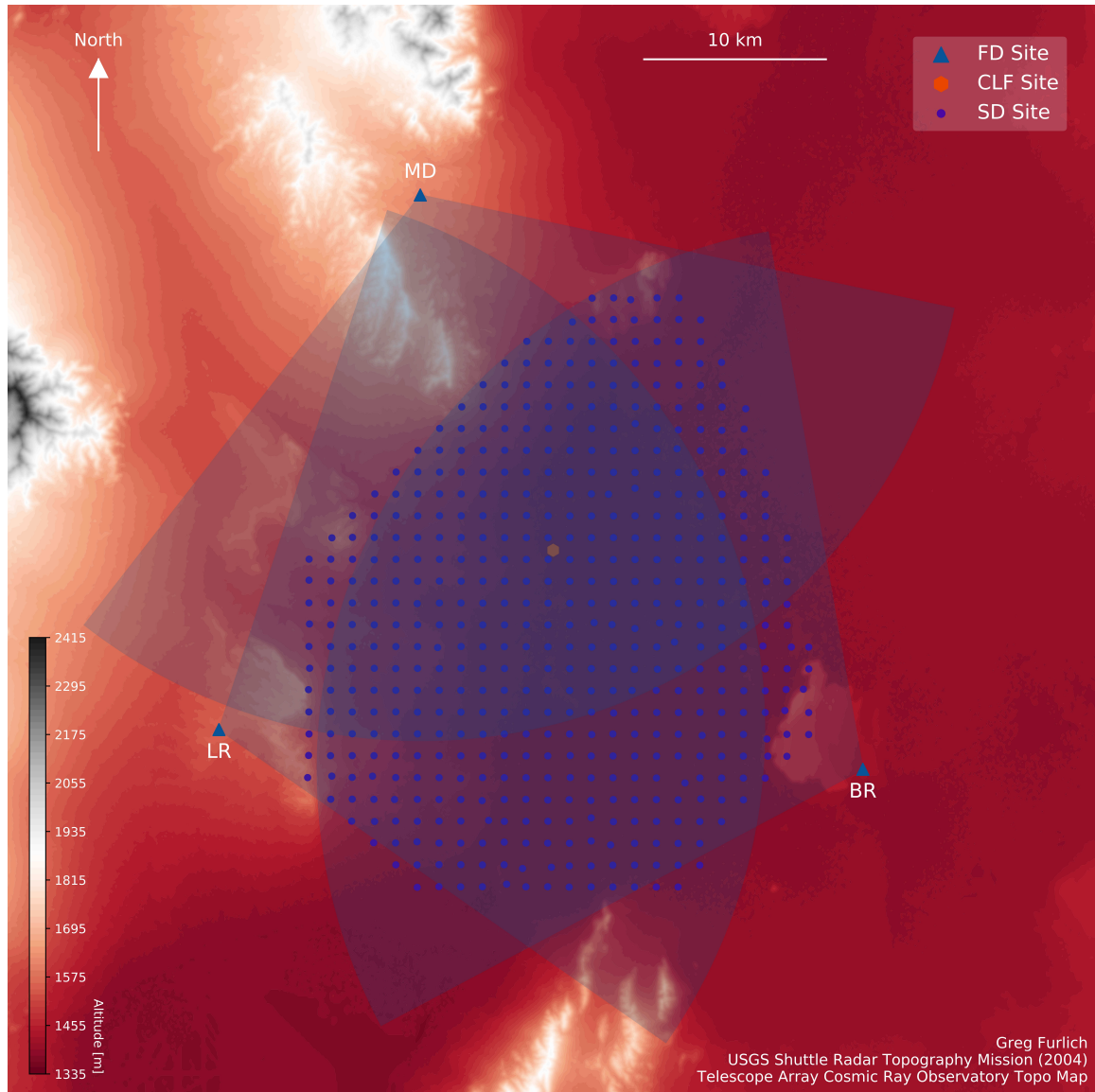


**Figure B.2:** Topographical map of the Telescope Array detectors.

## REFERENCES

- [1] Telescope Array Collaboration. [http://telescopearray.org/images/papers/TA\\_Collaboration\\_ICRC2017.pdf](http://telescopearray.org/images/papers/TA_Collaboration_ICRC2017.pdf), (2017). Accessed 2020-04-03.
- [2] Hess, V. F. *Constable & Company* (1928).
- [3] Rossi, B. *High-energy Particles*. Prentice-Hall physics series. Prentice-Hall, (1952).
- [4] Auger, P., Ehrenfest, P., Maze, R., Daudin, J., and Fréon, R. A. *Rev. Mod. Phys.* **11**(3-4), 288–291 Jul (1939).
- [5] Bunner, A. N. *Cosmic Ray Detection by Atmospheric Fluorescence*. PhD thesis, Cornell University, (1967).
- [6] *Physics Today* **27** (1974).
- [7] Bergeson, H. E., Cassiday, G. L., Chiu, T. W., Cooper, D. A., Elbert, J. W., Loh, E. C., Steck, D., West, W. J., Linsley, J., and Mason, G. W. *Phys. Rev. Lett.* **39**, 847–849 September (1977).
- [8] Baltrusaitis, R. M., Cady, R., Cassiday, G. L., Cooperv, R., Elbert, J. W., Gerhardy, P. R., Ko, S., Loh, E. C., Salamon, M., Steck, D., and Sokolsky, P. *Nucl. Instrum. Methods Phys. Res.* **240**(2), 410–428 October (1985).
- [9] Abu-Zayyad, T. et al. *Nucl. Instrum. Methods Phys. Res.* **450**(2), 253 – 269 (2000).
- [10] Hillas, A. M. *ARA&A* **22**, 425–444 Jan (1984).
- [11] Fermi, E. *Phys. Rev.* **75**(8), 1169–1174 Apr (1949).
- [12] Stanev, T. *High Energy Cosmic Rays*. Springer Praxis Books. Springer Berlin Heidelberg, (2010).
- [13] Patrignani, C. et al. *Chin. Phys.* **C40**(10), 100001 (2016).
- [14] Penzias, A. A. and Wilson, R. W. *ApJ* **142**, 419–421 Jul (1965).
- [15] Greisen, K. *Phys. Rev. Lett.* **16**, 748–750 Apr (1966).
- [16] Zatsepin, G. T. and Kuz'min, V. A. *J. Exp. Theor. Phys.* **4**, 78 Aug (1966).
- [17] Bird, D. J. et al. *ApJ* **441**, 144 Mar (1995).
- [18] O'Dowd, M., Ward, R., Ross, K., and Brown, K. Youtube <https://www.youtube.com/watch?v=osvOr5wbkUw>, (2017). Accessed 2020-01-29.
- [19] Heitler, W. *The Quantum Theory of Radiation*. Dover Books on Physics. Dover Publications, (1984).
- [20] Matthews, J. *Astropart. Phys.* **22**(5), 387 – 397 (2005).

- [21] Gaisser, T. K., Engel, R., and Resconi, E. *Cosmic Rays and Particle Physics*. UK: Cambridge University Press, June (2016).
- [22] Gaisser, T. K. and Hillas, A. M. In *15th International Cosmic Ray Conference (ICRC1977)*, volume 8 of *International Cosmic Ray Conference*, 353–357, (1977).
- [23] Nerling, F., Blmer, J., Engel, R., and Risse, M. *Astropart. Phys.* **24**(6), 421 – 437 (2006).
- [24] Kakimoto, F., Loh, E., Nagano, M., Okuno, H., Teshima, M., and Ueno, S. *Nucl. Instrum. Methods Phys. Res.* **372**(3), 527 – 533 (1996).
- [25] Abbasi, R. et al. *Nucl. Instrum. Methods Phys. Res.* **597**(1), 32 – 36 (2008). Proceedings of the 5th Fluorescence Workshop.
- [26] Abbasi, R. et al. *Nucl. Instrum. Methods Phys. Res.* **597**(1), 37 – 40 (2008). Proceedings of the 5th Fluorescence Workshop.
- [27] Nagano, M., Kobayakawa, K., Sakaki, N., and Ando, K. *Astropart. Phys.* **20**(3), 293 – 309 (2003).
- [28] Nozka, L., Hrabovsky, M., Ridky, J., Bohacova, M., Schovanek, P., Palatka, M., Pech, M., and Mandat, D. *Optik* **120**(12), 619 – 622 (2009).
- [29] Hanlon, W. F. *The energy spectrum of ultra high energy cosmic rays measured by the High Resolution Fly's Eye observatory in stereoscopic mode*. PhD thesis, University of Utah, (2008).
- [30] Binns, W. R. et al. *Astrophys. J.* **788**(1), 18 may (2014).
- [31] Adriani, O. et al. *Phys. Rev. Lett.* **122**, 181102 May (2019).
- [32] Aguilar, M. et al. *Phys. Rev. Lett.* **110**, 141102 Apr (2013).
- [33] Ahn, H. et al. *Nucl. Instrum. Methods Phys. Res.* **579**(3), 1034 – 1053 (2007).
- [34] Stone, E. C., Vogt, R. E., McDonald, F. B., Teegarden, B. J., Trainor, J. H., Jokipii, J. R., and Webber, W. R. *Space Sci. Rev.* **21**(3), 355–376 December (1977).
- [35] Abeysekara, A. U. et al. *Astropart. Phys.* **35**(10), 641–650 May (2012).
- [36] Achterberg, A. et al. *Astropart. Phys.* **26**(3), 155 – 173 (2006).
- [37] Adams, J. H. et al. *Exp. Astron.* **40**(1), 3–17 November (2015).
- [38] Capel, F., Belov, A., Casolino, M., Klimov, P., and JEM-EUSO Collaboration. *Adv. Space Res.* **62**(10), 2954–2965 November (2018).
- [39] Kawai, H. et al. *Nucl. Phys.* **175-176**, 221 – 226 (2008). Proceedings of the XIV International Symposium on Very High Energy Cosmic Ray Interactions.
- [40] Shinozaki, K. and Teshima, M. *Nucl. Phys.* **136**, 18 – 27 (2004). CRIS 2004 Proceedings of the Cosmic Ray International Seminars: GZK and Surroundings.
- [41] Abraham, J. et al. *Nucl. Instrum. Methods Phys. Res.* **523**(1), 50 – 95 (2004).
- [42] Abu-Zayyad, T. et al. *Nucl. Instrum. Methods Phys. Res.* **689**, 87 – 97 (2012).
- [43] Tokuno, H. et al. *Nucl. Instrum. Methods Phys. Res.* **676**, 54 – 65 (2012).

- [44] Telescope Array Collaboration, Kakimoto, F., Tsunesada, Y., Azuma, R., Ogio, S., Fukushima, M., Taketa, A., Tokuno, H., Hiyama, K., Smith, J. D., Thomas, S. B., Tanaka, M., Matsuda, T., and Kadota, K. *Physica E Low Dimens. Syst. Nanostruct.* **40**(2), 430–433 December (2007).
- [45] Tokuno, H. et al. *Nucl. Instrum. Methods Phys. Res.* **601**(3), 364 – 371 (2009).
- [46] Kawana, S. et al. *Nucl. Instrum. Methods Phys. Res.* **681**, 68 – 77 (2012).
- [47] Abbasi, R. U. et al. *Astrophys. J. Lett.* **790**(2), L21 August (2014).
- [48] Kido, E. and Telescope Array Collaboration. In *35th International Cosmic Ray Conference (ICRC2017)*, volume 301 of *International Cosmic Ray Conference*, 386, January (2017).
- [49] Kido, E. In *36th International Cosmic Ray Conference (ICRC2019)*, volume 36 of *International Cosmic Ray Conference*, 312, July (2019).
- [50] Zundel, Z. J. *Spectrum measurement with the telescope array low energy extension (TALE) fluorescence detector*. PhD thesis, University of Utah, (2016).
- [51] Boyer, J. H., Knapp, B. C., Mannel, E. J., and Seman, M. *Nucl. Instrum. Methods Phys. Res.* **482**(1), 457 – 474 (2002).
- [52] Peterson, J. and Zvirzdin, J. TAwiki [http://www.telescopearray.org/tawiki/index.php/TA\\_Star\\_Photography](http://www.telescopearray.org/tawiki/index.php/TA_Star_Photography), (2019). Accessed 2020-03-05.
- [53] Jui, C. private communication, (2020).
- [54] Smith, J. TAwiki [http://www.telescopearray.org/tawiki/index.php/TALE/TAX4\\_Gain\\_Balancing](http://www.telescopearray.org/tawiki/index.php/TALE/TAX4_Gain_Balancing), (2020). Accessed 2020-03-10.
- [55] Adams, J. H. et al. *Exp. Astron.* **40**(1), 301–314 November (2015).
- [56] Cady, R. TAwiki [http://www.telescopearray.org/tawiki/images/4/45/TAX4\\_555\\_FoV.pdf](http://www.telescopearray.org/tawiki/images/4/45/TAX4_555_FoV.pdf), (2015). URL links to a more recent version of what was modified. Accessed 2020-01-29.
- [57] Thomas, S. TAwiki [http://www.telescopearray.org/tawiki/images/9/92/TAX4\\_20190422\\_DepVsNon.pdf](http://www.telescopearray.org/tawiki/images/9/92/TAX4_20190422_DepVsNon.pdf), (2019). Accessed 2020-01-29.
- [58] Insitute of Cosmic Ray Research (ICRR), University of Tokyo. Flickr <https://www.flickr.com/photos/142880279@N06/albums/72157689940402503>, (2019). Accessed 2020-03-10.
- [59] Heck, D. and Pierog, T. <https://www.ikp.kit.edu/corsika/70.php>, (2020). Accessed 2020-03-07.
- [60] Stratton, S. R. *Measurement of the Flux of Ultra-High Energy Cosmic Rays by the Telescope Array FADC Fluorescence Detectors*. PhD thesis, Rutgers University, (2012).
- [61] Abu-Zayyad, T. et al. *Astropart. Phys.* **48**, 16 – 24 (2013).
- [62] Abbasi, R. U. et al. *Phys. Rev. Lett.* **104**(16), 161101 April (2010).
- [63] Abu Zayyad, T. Z. *The Energy Spectrum of Ultra High Energy Cosmic Rays*. PhD thesis, University of Utah, (2000).
- [64] Rossum, G. and the Python Software Foundation. <https://www.python.org/>. Accessed 2020-03-07.
- [65] Ivanov, D. TAwiki <http://telescopearray.org/tawiki/index.php/TDSTio>, (2015). Accessed 2020-03-07.

- [66] Brun, R. and Rademakers, F. <https://root.cern.ch/>, (1996). Accessed 2020-03-07.
- [67] The HDF Group. <https://www.hdfgroup.org/>. Accessed 2020-03-07.
- [68] Furlich, G. and Bergman, D. R. In *36th International Cosmic Ray Conference (ICRC2019)*, volume 36 of *International Cosmic Ray Conference*, 260, July (2019).
- [69] Oceanic, U. S. N., Administration, A., Aeronautics, U. S. N., Administration, S., on Extension to the Standard Atmosphere, U. S. C., and of the Air Force, U. S. D. *U.S. Standard Atmosphere, 1976*. NOAA - SIT 76-1562. National Oceanic and Atmospheric [sic] Administration, (1976).
- [70] Furlich, G. In *36th International Cosmic Ray Conference (ICRC2019)*, volume 36 of *International Cosmic Ray Conference*, 261, July (2019).
- [71] Stroman, T. A. TAwiki [http://www.telescopearray.org/tawiki/index.php/FDPED\\_animation\\_for\\_cloud\\_detection](http://www.telescopearray.org/tawiki/index.php/FDPED_animation_for_cloud_detection), (2016). Accessed 2020-03-13.
- [72] Chollet, F. *Deep Learning with Python*. Manning Publishing Co., (2018).
- [73] Bishop, C. M. *Pattern Recognition and Machine Learning*. Springer, (2006).
- [74] Chollet, F. et al. <https://keras.io>, (2015).
- [75] Tomida, T., Sano, K., Okub, Y., Tameda, Y., Inadomi, T., Nakazawa, A., and Ikeda, D. In *36th International Cosmic Ray Conference (ICRC2019)*, volume 36 of *International Cosmic Ray Conference*, 441, July (2019).
- [76] Space Weather Prediction Center (SWPC), NOAA, T. **SWPC PRF 2081**, 4 (2015).
- [77] Mussa, R. In *36th International Cosmic Ray Conference (ICRC2019)*, volume 36 of *International Cosmic Ray Conference*, 1131, July (2019).
- [78] Ivanov, D. In *34th International Cosmic Ray Conference (ICRC2015)*, volume 34 of *International Cosmic Ray Conference*, 349, July (2015).
- [79] Abu-Zayyad, T. et al. *Phys. Rev. Lett.* **84**(19), 4276–4279 May (2000).
- [80] Ivanov, D. In *36th International Cosmic Ray Conference (ICRC2019)*, volume 36 of *International Cosmic Ray Conference*, 298, July (2019).
- [81] Bergman, D. and Stroman, T. A. In *36th International Cosmic Ray Conference (ICRC2019)*, volume 36 of *International Cosmic Ray Conference*, 191, July (2019).
- [82] Berezinsky, V., Gazizov, A., and Grigorieva, S. *Phys. Rev. D* **74**(4), 043005 August (2006).
- [83] Ivanov, D. *Energy Spectrum Measured by the Telescope Array Surface Detector*. PhD thesis, University of Utah, (2012).
- [84] Fujii, T. *Measurements of the Energy Spectrum and the Mass Composition of Ultra-High Energy Cosmic Rays with Telescope Array Fluorescence Detectors in Monocular Mode*. PhD thesis, Osaka City University, (2012).
- [85] Bergman, D. R. <http://www.physics.rutgers.edu/~dbergman/HiRes-Monocular-Spectra-200702.html>, (2007). URL is now inactive, results provided by Douglas Bergman via private communication.
- [86] Abbasi, R. U. et al. *Phys. Rev. Lett.* **100**, 101101 Mar (2008).